TORNADOES AND WINDBORNE DEBRIS:
AN EXPERIMENTAL AND NUMERICAL APPROACH

by

Frederick Bourriez

UNIVERSITY OF BIRMINGHAM



A thesis submitted to the

University of Birmingham

for the degree of

Doctor of Philosophy

School of Engineering

Department of Civil Engineering

University of Birmingham

April 2020

Copyright © Frederick Bourriez, 2020

UNIVERSITY OF
BIRMINGHAM

University of Birmingham Research Archive

e-theses repository

This unpublished thesis/dissertation is copyright of the author and/or third parties. The intellectual property rights of the author or third parties in respect of this work are as defined by The Copyright Designs and Patents Act 1988 or as modified by any successor legislation.

Any use made of information contained in this thesis/dissertation must be in accordance with that legislation and must be properly acknowledged. Further distribution or reproduction in any format is prohibited without the permission of the copyright holder.

To Sophia...
...born three days...
...after submitting this thesis.

Abstract

Windborne debris during severe weather events such as hurricanes or tornadoes can seriously damage engineering and non-engineering structures. Building failures, whether induced by strong winds or debris impact, can generate significant amounts of airborne debris, increasing the risk of damage to surrounding buildings. To date, the interaction between tornado winds and windborne debris is poorly understood. Analytical models and numerical simulations have previously been used to examine debris flight, but those models are by nature highly simplified and still lack experimental or full-scale validation.

This research investigates the flight of debris in tornado-like flow fields using physical and analytical models. Physical simulations were carried out using a tornado simulator, and experimental results of the flight of single or multiple debris showed some good agreement with full-scale observations. Debris trajectories were also compared with numerically calculated debris trajectories based on experimental velocity and particle tracking data and the methodology developed showed good agreements with experimental data. Finally, the flight of debris was examined using velocity fields from analytical vortex models and demonstrates the limitations of these models to reproduce similar experimental flow fields or debris trajectories. One model showed good potential, but additional research and data are still needed before validating and using it further.

Acknowledgments

Firstly, I would like to express my sincere gratitude to my supervisors Prof Mark Sterling and Prof Chris Baker for giving me the opportunity to undertake this project and supporting me throughout this research. Their wisdom, knowledge and advice have had a considerable impact on my personal and professional development during the past four years. I am also very thankful to them for providing the opportunity to undertake one year of research within the wind engineering group. The experience certainly allowed me to deepen my knowledge and understanding about wind engineering. On that note, I would like to thank everybody in the wind engineering group for sharing their valuable knowledge and experience during meetings, conferences or social events. A big thank you to Dr David Soper for being a brilliant line manager - his passion for trains is unquestionable and the way he shares this passion with others is remarkable. I would like to thank him for his support during the long, freezing days at the TRAIN rig but also for the great discussions had during our traditional Fish Fridays.

I would like to acknowledge the University of Birmingham for funding my PhD studies and giving me the opportunity to carry out some teaching. A sincere thank you to the staff from the Civil Engineering laboratories for their invaluable help and important contribution to the success of my experimental work. I am aware that

I have often been quite the troublemaker with my crazy ideas, but I equally know you enjoyed the challenges. I would like to personally thank Mike Vanderstam, Luis Portela and David Allsop, a.k.a Mad Dave, for making me feel integrated into the team and for some memorable banter during the countless hours and lunch breaks spent in the lab.

Thank you also to the fantastic people that I have had the chance to meet during my time at the University of Birmingham... for the long break lunches or late night drinks at the Staff House, or simply for any fun or discussions we may have had together. Special thanks to Dr Stefanie Gillmeier, Dr Nick Tzavios and Dr Giulio Vita. I am grateful to Steffi for the countless hours spent in the lab playing with the tornado simulator and some great fun we have had in Birmingham and at conferences. That laughter in a pub in Liège was probably one of the highlights of my PhD. I am grateful to Nick for all the hours spent at The Hawthorns and the great times spent together both in and out of the university. I am deeply grateful to Giulio, "my boyfriend", for his craziness and continuous support during our studies which made my time spent in Birmingham and around the world with him so memorable. I hope we will have another chance to travel somewhere together, and hopefully this time you will be at the gate before the final call.

Lastly, I would like to thank my family and friends for believing in me and supporting me throughout the past four years. Finally, my thanks go to one particular person, Grace, for accepting to move to Birmingham and supporting me during the good and hard times. I guess it has not been easy to listen to all my nonsense during these years, and I know proofreading this thesis has not helped at all, but I am eternally grateful for all your efforts. This ends our Birmingham chapter but only starts a great journey with our little Sophia.

Table of Contents

Chapter 1: Introduction **1**

1.1 Motivation 1

1.2 Aims and objectives 6

1.3 Thesis outline 6

Chapter 2: Background and literature review to tornadoes and debris **8**

2.1 Introduction 8

2.2 Tornadoes: a meteorological point of view 9

2.2.1 Meteorology generalities 9

2.2.2 From clouds to tornadogenesis 11

2.2.3 The flow structure inside a tornado 14

2.2.4 Obtaining data at full-scale 18

2.2.5 Climatology 21

2.3 Tornadoes: an engineering point of view 25

2.3.1 Can we reproduce tornadoes in laboratories? 25

2.3.2 Can tornadoes be modelled analytically? 36

2.3.3 Debris in tornadoes 48

2.4 Research gap 61

Chapter 3: Physical simulation of tornado-like vortices at the University of Birmingham 62

3.1 Introduction 62

3.2 University of Birmingham Tornado-like Vortex Generator (UoB-TVG) 63

3.3 Flow visualisation 65

3.4 Mapping methodology 68

3.4.1 Cobra probe 68

3.4.2 Traverse system 69

3.5 Flow rate and radial Reynolds number 72

3.6 Tornado-like vortex flow field and structure 74

3.7 Horizontal velocity profiles 79

3.8 Vertical velocity profiles 83

3.9 Concluding remarks 89

Chapter 4: Experimental investigation of the flight of debris in tornado-like vortices 90

4.1 Introduction 90

4.2 Experimental set up 90

4.2.1 High-speed camera 91

4.2.2 Camera triggering device 93

4.3 Calibration 94

4.3.1 Calibration target 95

4.3.2 Camera arrangement 96

4.3.3 Validation . . . 100
4.4 Debris . . . 102
4.5 Data pre-processing . . . 110
4.6 Data post-processing . . . 112
4.6.1 OpenPTV software . . . 112
4.6.2 Particle trajectories . . . 115
4.6.3 Vortex wandering . . . 116
4.6.4 Debris path . . . 118
4.7 Camera validation . . . 122
4.7.1 Static validation and positioning errors . . . 124
4.7.2 Dynamic validation and velocity errors . . . 129
4.8 2D-PTV . . . 132
4.8.1 Single debris . . . 132
4.8.2 Vortex wandering . . . 137
4.9 3D-PTV . . . 140
4.9.1 Floor seeding . . . 140
4.9.2 Building model seeding . . . 150
4.10 Concluding remarks . . . 157

Chapter 5: Comparison between physical and numerical approaches to debris flight in tornado-like winds 159

5.1 Introduction . . . 159
5.2 Numerical methodology . . . 160
5.2.1 Debris equations . . . 160
5.2.2 Equations discretisation . . . 161

5.2.3 Data incorporation . . . 162
5.2.4 Elastic collision . . . 163
5.2.5 Validation . . . 164
5.3 Results . . . 166
5.3.1 Numerical validation . . . 166
5.3.2 Low-rise building located at $1r_c$ for $S = 0.3$ . . . 167
5.3.3 Floor seeding at $0r_c$ for $S = 0.7$ . . . 173
5.3.4 Single debris with vortex wandering . . . 175
5.4 Concluding remarks . . . 180

Chapter 6: Analytical modelling of debris flight in tornado-like flow field 182

6.1 Introduction . . . 182
6.2 Numerical methodology . . . 182
6.2.1 Baker and Sterling two-cell vortex model . . . 183
6.2.2 Debris flight equations with Tachikawa numbers . . . 184
6.2.3 Simulated vortex wandering . . . 185
6.3 Effects of vortex wandering on velocity flow fields . . . 186
6.3.1 Averaged tangential velocity profiles . . . 186
6.3.2 Variation in core radius size and maximum tangential velocity 188
6.3.3 Tangential velocities at the vortex core centre . . . 190
6.4 Tachikawa number effect on debris flight . . . 191
6.5 Debris flight in Baker and Sterling's two-cell model . . . 198
6.5.1 Effect of Tachikawa numbers on impact velocity . . . 198
6.5.2 Effect of turbulence intensity and vortex wandering . . . 200

6.6 Concluding remarks 204

Chapter 7: Conclusions and recommendations for further work 206

7.1 Introduction 206

7.2 Conclusion 206

7.3 Recommendations for further work 211

References 214

List of Tables

1.1 Estimated tornado wind speeds and scales based on damage surveys. 3

2.1 Vortex structure description as a function of the swirl ratio (Davies-Jones, 1973) . . . 27

3.1 Vane angles and corresponding swirl ratios used to simulate tornado-like vortices in the UoB-TVG. . . . 65

4.1 Summary of the different triggering modes available on the Sony FS700RH camera. . . . 93

4.2 Summary of the three-dimensional coordinates for different arrangements of the cameras used to perform the calibration of the 3D-PTV system. . . . 102

4.3 Swirl ratio tested and arbitrary full-scale equivalent core radius and maximum wind speed. . . . 105

4.4 Calculated full-scale equivalent debris characteristics from different swirl ratios and debris sizes tested in the simulator. . . . 108

4.5 3D position RMS errors (RMS_x;RMS_y;RMS_z) of the calibration target using the 3D calibration for the three different camera arrangements. . . . 126

4.6 3D position RMS errors (RMS_x;RMS_y;RMS_z) of the calibration target using the planar calibration for the three different camera arrangements. . . . 127

4.7 Percentage of calibration precision increase between the different camera arrangements and calibration targets, relative to planar and 3D targets with arrangement 3B. . . . 128

4.8 Real and reconstructed radial position, height and velocity of a circular moving target. . . . 131

4.9 Normalised average and maximal velocity magnitude of single debris for different swirl ratios and debris sizes. . . . 136

4.10 Estimated error between core radius sizes estimated from wind measurement and particle tracking. 138

4.11 Debris flight analysis of (a) mean normalised radial distance at impact, (b) mean normalised flight distance at impact, (c) normalised impacting debris area and (d) mean normalised maximal velocity magnitude for different swirl ratios and release locations. 145

4.12 Relative standard deviation of the repeated mean radial distance and travelling distance of debris released from the core radius location for $S = 0.13$, 0.30 and 0.70. 149

4.13 (a) Debris flight analysis for the building model and (b) the difference without the building model for $S = 0.30$. 155

5.1 Comparison between wind and initial debris velocities, pitch and yaw angles, when the building model was included and not included in the simulations. 171

5.2 Debris flight analysis and comparison between experimental and computed trajectories released from the vortex centre ($0r_c$) for $S = 0.7$. 175

6.1 Brief review of Tachikawa numbers and associated debris types used in tornado and wind tunnel studies. 192

6.2 Normalised mean flight distance and standard deviation for different turbulence intensities and vortex wandering. 203

List of Figures

1.1 Windborne debris chain (from Kakimpa et al. (2012)). 2

1.2 Aerial view of the 2011 Joplin EF5 tornado's path which caused 158 casualties (NOAA, 2016). 3

2.1 (a) Conceptual view of the atmospheric circulation – (b) Jet-streak quadrant and associated large-scale atmospheric forcing (Rose et al., 2004). 10

2.2 Structure of a tornadic supercell thunderstorm (Markowski, 2019) . 12

2.3 Conceptual view of a tornado (Snow, 1982). 16

2.4 Evolution of a tornado vortex structure as a function of the swirl ratio (Rotunno, 2013). The swirl ratio S measures the strength of a vortex and is fully defined in section 2.3. 17

2.5 (a) Doppler on Wheel (DOW) scanning a full-scale tornado (Wurman et al., 2013) - (b) The Tornado Intercept Vehicle (TIV) is positioned in the path of a tornado to measure in-situ pressure, temperature and wind data. 18

2.6 Axisymmetric cross-section of the May 25, 2012, Russel, Kansas tornado from a Rapid-Scan Doppler on Wheels (RSDOW) (Kosiba and Wurman, 2013). The colour contours denote the tangential velocity and the arrows the 2D vector field of radial and vertical velocities. 19

2.7 Tornado in-situ (a) wind data (Wurman et al., 2013) and (b) surface pressure data (Karstens et al., 2010). 20

2.8 Worldwide areas of tornado occurrences (NOAA, 1995). 22

2.9 Tornado climatology in Europe between 1950 and 2015 (Antonescu et al., 2016). 23

2.10 Evolution of vortex structure as a function of swirl ratio in a Ward-type tornado simulator from a laminar vortex to multiple vortices (Church et al., 1977) 27

2.11 Schematic of a Ward-type tornado generator (adapted from Davies-Jones (1973)) . . . 29
2.12 Swirl ratio as a function of radial Reynolds number for a Ward-type tornado simulator and different aspect ratios (adapted from Church et al. (1979)). . . . 29
2.13 Different tornado generator designs from (a) Ward (1972), (b) Church et al. (1977), (c) Mishra et al. (2008*a*), (d) Haan et al. (2008), (e) Refan and Hangan (2018) and (f) Tang et al. (2018) . . . 31
2.14 Cylindrical coordinate system and velocity vectors denotations. . . . 36
2.15 Variation of the ratio of suction strength and eddy viscosity as a function of the square of the core radius to determine the constant K_M as defined in Wood and White (2011). . . . 44
2.16 Radial profile of radial, tangential and vertical velocities at $z/r_c = 1$ for Rankine, modified Rankine, Burgers-Rott, Sullivan and Baker and Sterling analytical vortex models. . . . 47
2.17 Stereoscopic system and epipolar lines. . . . 50
2.18 Debris classification (Wills et al., 2002). . . . 53
2.19 Debris flight trajectories using Baker and Sterling's model for (a&c) flying and (b&d) falling debris, (e) Flying and falling Φ_T parameter as a function of the swirl ratio S (adapted from Baker and Sterling (2017). . . . 57
3.1 (a) Vertical-cross section and (b) iso-view of the University of Birmingham Tornado-like Vortex Generator (UoB-TVG) . . . 63
3.2 Guide vane angle θ . . . 64
3.3 Flow visualisation for different swirl ratio (a) $\theta = 30°$ - $S = 0.13$ (b) $\theta = 50°$ - $S = 0.30$ (c) $\theta = 70°$ - $S = 0.70$ . . . 66
3.4 Flow visualisation using soap bubbles depicting the turbulent core for $S = 0.70$. . . . 67
3.5 (a) Schematic and description of a TFI Cobra probe – (b) Wind velocity coordinates with a TFI Cobra probe (TFI, 2011). . . . 69
3.6 (a) Sketch of the simulator's upper half with the traverse system mounted to measure the outflow - (b) Traverse system inside the simulator while at prototype stage. . . . 73

3.7 Outflow velocities profiles at the top of the convection chamber for $\theta = 0°$ (plain), $30°$ (dotted), $50°$ (dashed) and $70°$ (dash-dotted). The red colour outlines when the data quality is lower than 75%. . 74

3.8 3D velocity flow fields for (a) $S = 0.13$, (b) $S = 0.3$ and (c) $S = 0.7$. The white contour outlines the normalised tangential velocities, and the arrows show the 2D vector field of radial and vertical velocities. 76

3.9 Turbulence intensity of the velocity vector for different swirl ratios of (a) $S = 0.13$, (b) $S = 0.3$ and (c) $S = 0.7$. The white contour outlines the data quality defined as the ratio of non-zero to the total number of measured points. 77

3.10 Horizontal profiles of tangential velocity for different heights, analytical vortex models and for different swirl ratios of (a) $S = 0.13$, (b) $S = 0.3$ and (c) $S = 0.7$. 80

3.11 Horizontal profiles of radial velocity for different heights, analytical vortex models and for different swirl ratios of (a) $S = 0.13$, (b) $S = 0.3$ and (c) $S = 0.7$. 81

3.12 Horizontal profiles of vertical velocity for different heights, analytical vortex models and for different swirl ratios of (a) $S = 0.13$, (b) $S = 0.3$ and (c) $S = 0.7$. 82

3.13 Vertical profiles of (a) normalised local maximum tangential velocity and (b) local core radius for swirl ratios of $S = 0.13$, 0.3 and 0.7 . . 84

3.14 Vertical profiles of the tangential velocity components for different swirl ratios of (a) $S = 0.13$, (b) 0.3 and (c) 0.7 and at different core radius locations ($r = 0,\ 0.5,\ 1.0$ and $1.5r_c$) 85

3.15 Vertical profiles of the radial velocity components for different swirl ratios of ((a) $S = 0.13$, (b) 0.3 and (c) 0.7 and at different core radius locations ($r = 0,\ 0.5,\ 1.0$ and $1.5r_c$) 86

3.16 Vertical profiles of the vertical velocity components for different swirl ratios of ((a) $S = 0.13$, (b) 0.3 and (c) 0.7 and at different core radius locations ($r = 0,\ 0.5,\ 1.0$ and $1.5r_c$) 87

4.1 Particle tracking velocimetry coordinate system. 91

4.2 Sony FS700RH camera and SELP18200 (18–200mm F3.5–6.3 OSS) 11x zoom E-Mount lens used for Particle Tracking Velocimetry. . . 91

4.3 Multi-Camera LANC Controller ALE718, developed by Applied Logic Technology, used to trigger three cameras Sony FS700RH. . . 94

4.4 Planar calibration target. Each dot is spaced every 0.04m covering 1.05m × 0.75m. 97
4.5 3D calibrated target with the CAD design (left) and the 3D printed target (right). 98
4.6 Camera used in a one-camera arrangement to perform 2D-PTV and mounted at the centre of the simulator (in x-direction but off-centre in y-direction) pointing downward. 99
4.7 Example of a three-camera arrangement mounted inside the simulator and used to perform 3D-PTV. 100
4.8 Schematic of the different arrangements used with three cameras #1, #2 and #3. (a) All three cameras #1, #2 and #3 are placed at equal Y and Z positions but are evenly spaced along X direction from the centre of the simulator. (b) Positions of camera #1 and #3 remain unchanged but camera #2 is placed slightly above. (c) Positions of camera #1 and #3 remain unchanged but camera #2 is placed at the top of the convection chamber. 101
4.9 Calibration validation using the 3D calibration target placed at different locations inside the simulator. 103
4.10 Calibration validation using a moving target mounted on a motor. . 104
4.11 Device used to release Styrofoam spheres inside the simulator. The device is mounted under the simulator and can be placed at different positions (left) and consists of a perforated wheel loaded with Styrofoam spheres (right). 109
4.12 Example of epipolar lines displayed for each camera for a specific particle on OpenPTV software. The closer the intersection from the particle centroid, the better the calibration. 114
4.13 Circle fitting in scattered data. 117
4.14 Step by step procedure to calculate the debris path width from trajectory data. 121
4.15 Real and reconstructed target points using the planar calibration target. 122
4.16 Real and reconstructed target points using the 3D calibration target. 123
4.17 Top (a) – Side (b & c) and isometric view of the reconstructed moving target used during dynamic calibration validation. 130
4.18 Single debris trajectories subjected to tornado-like winds for different swirl ratios (columns) and debris sizes (rows). 133

4.19 Distribution of the vortex centre picturing the vortex wandering for (a) $S = 0.13$, (b) $S = 0.30$ and (c) $S = 0.7$. The dashed line outlines the size of the normalised core radius determined from the wind velocity mappings. 137

4.20 3D representation of debris trajectories when released from (a) the core radius for $S = 0.30$ and (b) the vortex centre for $S = 0.7$. The colours depict the normalised velocities of the debris. 141

4.21 Horizontal view of debris trajectories released from different distances from the origin (row) in tornado-like flow with different swirl ratios (column). The red line denotes the mean debris trajectory. . 143

4.22 Early flight trajectories and wind velocity vectors for S = 0.3. . . . 144

4.23 Evolution of the debris path width with flight distance for different swirl ratios. 148

4.24 Vertical velocity profiles at the core radius location ($r = r_c$) of normalised – (a) tangential, (b) radial, (c) vertical velocity, (d) yaw angle and (e) pitch angle. The black line denotes when the building model is not included in the flow field, and the grey line when it is included. The horizontal capped lines denote the measurement uncertainties. 151

4.25 Mean debris trajectories for $S = 0.30$ initiated with and without a building model. 153

4.26 (a) 3D representation of the flight of debris from a low-rise building at the core radius (r_c) location. The dashed line denotes the size of the core radius, the arrows denote the idealised flow-field the building is subjected to. 154

4.27 Comparison of the debris path width evolution with and without the building model for $S = 0.30$. 156

5.1 Sub-grid wind determination using bilinear interpolation. 162

5.2 Perfect elastic collision model. 163

5.3 PTV set up for single debris tracking in the wind tunnel. 165

5.4 Comparison between experimental debris trajectories and different numerical methods subjected to uni-directional winds. 166

5.5 Top view of the experimental and numerical debris trajectories. Left column denotes the experimental trajectories (a-c), right column the computed trajectories (b-d). The top row denotes the trajectories when the building model is not included (a-b), the bottom row the trajectories when the building model is included (c-d). 169

5.6 Distribution of debris initial tangential (a), radial (b), vertical (c) velocities, yaw (d) and pitch (e) angle, when the low-rise building model is and is not included in the tornado-like flow field. 170

5.7 Debris flight analysis – the red cross denotes the mean value, the box the interquartile range, the vertical line the median and the whiskers the range from minimal to maximal values. 172

5.8 Comparison between experimental and computed trajectories released from the vortex centre ($0r_c$) for $S = 0.7$. 174

5.9 Single debris trajectories (a) experimental for $S = 0.30$, (b) computed and (c) computed included vortex wandering. 176

5.10 Vertical view (XZ plan) of single debris trajectories for $S = 0.30$ computed with vortex wandering. 178

5.11 Evolution of (a) radial and (b) vertical position of single debris subjected to vertical wind velocities (c). 179

6.1 Averaged tangential velocities at $z/r_c = 1$ with vortex wandering up to $1r_c$ for (a) Rankine, (b) modified Rankine, (c) Burgers-Rott, (d) Sullivan and (e) Baker and Sterling analytical vortex models. . . 187

6.2 Effect of maximal fluctuation Δr_c of the vortex centre position on (a) the maximal tangential velocity and (b) the core radius. 189

6.3 Effect of maximal fluctuation Δr_c of the vortex centre position on the tangential velocity at $r/r_c = 0$. 190

6.4 Estimated debris diameter based on the EF-scale for different debris types and Tachikawa numbers. Wood debris are more likely to become windborne with EF0-1 tornadoes (light grey), gravel with EF2-3 tornadoes (grey) and steel debris with EFF4-5 tornadoes (dark grey). 193

6.5 Debris released from $r/r_c = 1$ and $z/r_c = 1$ with K = 1, 2, 5, 10, 20. 40, 60, 80 and 100 and with (a) Burgers-Rott, (b) Sullivan, (c) Baker and Sterling one-cell and (d) Baker and Sterling two-cell vortex models. 194

6.6 Comparison between different vortex models of the ranges of Tachikawa numbers when the debris is released for different radial and height positions and impacting the ground within one revolution. 197

6.7 Relation between normalised initial impact debris velocities and Tachikawa number for Baker and Sterling's (a) one-cell and (b) two-cell vortex models and for debris impacting the ground within one revolution. The velocities are normalised by the wind velocity at the release location ($\boldsymbol{V}^0_{wind}$). 199

6.8 Effect of turbulence intensity and vortex wandering on 100 debris computed using Baker and Sterling's two-cell model and released from $r/r_c = 1$ and $z/r_c = 1$. 201

Nomenclature

Γ	Circulation
Γ_{max}	Maximum circulation at the core radius
λ_K	Tachikawa scale factor
ν	Kinematic viscosity of air
ν_e	Eddy viscosity
ρ_a	Air density
ρ_d	Debris density
θ	Guide vane angle
a	Aspect ratio
$\tilde{a}$	Suction strength in normalised Burgers-Rott and Sullivan models
A	Debris frontal area
C_D	Drag coefficient
g	Gravity acceleration
h_0	Height of inflow
k	Buoyancy parameter in Holmes' equations

K	Tachikawa number
K_M	Constant in normalised Burgers-Rott and Sullivan models
l	Debris characteristic length
m	Debris mass
P	Static pressure
$\overline{P}$	Normalised static pressure
Q	Volumetric flow rate through the updraft hole
r	Radial distance
$\overline{r}$	Normalised radial distance
r_c	Core radius
r_0	Radius of updraft hole
Re_r	Radial Reynolds number
S	Swirl ratio
t	Time
$\overline{t}$	Normalised time
U	Reference wind speed
V	Wind velocity vector
$\mathbf{V}$	Vector of the relative velocity between the wind and debris
V_θ	Tangential velocity component
$V_{\theta,max}$	Tangential velocity maximum

$\overline{V_\theta}$	Normalised tangential velocity
V_R	Radial velocity component
$\overline{V_R}$	Normalised radial velocity
V_W	Vertical velocity component
$\overline{V_W}$	Normliased vertical velocity
z	Vertical distance
z_{max}	Height where $V_{\theta,max}$ occurs
$\overline{z}$	Normalised vertical distance

Acronyms

AGL Above Ground Level

CAPE Convective Available Potential Energy

CIN Convective Inhibition

DOW Doppler On Wheels

HFSB Helium-filled soap bubbles

ISU Iowa State Univeristy

LFC Level of Free Convection

LIDAR LIght Detection And Ranging

NOAA National Oceanic and Atmospheric Administration

PIV Particle Image Velocimetry

PTV Particle Tracking Velocimetry

RFD Rear Flank Downdraft

RMS Root mean square

RSDOW Rapid-Scan Doppler on Wheels

TFI Turbulent Flow Instrumentation Ltd.

TIV Tornado Intercept Vehicle

TTU Texas Tech University

UoB-TVG University of Birmingham Tornado-like Vortex Generator

Chapter 1

Introduction

1.1 Motivation

Tornadoes account for the strongest and most devastating natural wind phenomenon observed on Earth. Lasting from a few minutes up to several hours, these fast vertical-swirling columns of air developed between the cloud base of a supercell thunderstorm and the ground and can generate wind speeds up to 500km/h. Visually frightening, tornadoes can also reach considerable sizes, such as the 2013 El Reno tornado which grew to a width of 4.2km (Bluestein et al., 2015). Under such extreme conditions, failure of engineering and non-engineering structures due to tornadoes can mainly be attributed to the high wind speeds, the low pressure inside the core vortex and windborne debris (Brooks and Doswell, 2001), which all increase the risk of damage for surrounding buildings. Single debris impacting a building can lead to a variation of its internal pressure and ultimately cause more structural damage (Minor et al., 1977), resulting in what is known as a debris chain (Figure 1.1). Therefore, potential damage during tornadoes is not only related to wind speed but also debris loading (Wills et al., 2002). Although an effort can be made to design buildings resistant to tornado winds,

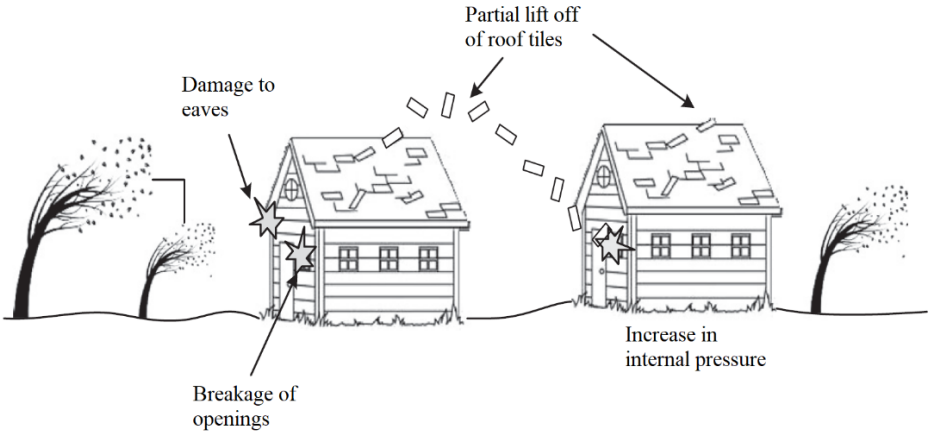


Figure 1.1: Windborne debris chain (from Kakimpa et al. (2012)).

their structures can rarely sustain significant debris loading; thus, urban areas can be severely affected by a violent tornado. In 2011, the city of Joplin (U.S.) was struck by the costliest tornado in U.S. history, causing about $2.8 billion worth of damage (Kuligowski et al., 2014). Figure 1.2 shows an aerial view of the tornado's path where it travelled approximately 35km across Joplin city and killed 158 people.

To estimate the intensity and wind speed of a tornado, Ted Fujita introduced the Fujita Scale based on different damage levels (Fujita, 1971). Post-tornado damage surveys are carried out to establish the intensity of the tornado, which is then ranged from 0 to 5 on the Fujita Scale, representing little damage to total destruction. To take into account the evolution of building construction techniques and standards over the years, the Fujita Scale was revised by the U.S. National Weather Service in 2006. It then became operational in 2007 as the Enhanced Fujita Scale. Table 1.1 shows the different scales and differences in terms of 3-second wind gust between the F-Scale and EF-Scale. In the United Kingdom, a similar tornado intensity scale was proposed in 1975 by the Tornado and Storm



Figure 1.2: Aerial view of the 2011 Joplin EF5 tornado's path which caused 158 casualties (NOAA, 2016).

Research Organisation (TORRO), known as the TORRO scale (TORRO, 1975). The TORRO scale contains 12 categories going from T0 to T11 and is an extension of the Beaufort scale. The Beaufort scale is an empirical wind force scale which initially estimated wind speeds based on observed sea conditions but is also generally used to describe wind intensity on land. Nevertheless, the EF-Scale is primarily used to evaluate and describe the severity of a tornadic event.

Table 1.1: Estimated tornado wind speeds and scales based on damage surveys.

Fujita Scale		Enhanced Fujita Scale	
F-Scale	3-second wind gust [m/s]	EF-Scale	3-second wind gust [m/s]
0	20-35	0	29-38
1	35-52	1	38-49
2	53-72	2	50-60
3	72-93	3	61-74
4	94-117	4	74-89
5	117-142	5	>89

To date, such extreme events are hard to forecast with reasonable accuracy; however, numerical weather prediction models can anticipate whether the environment is favourable or not to develop supercell thunderstorms. But in reality, only a small percentage of supercell thunderstorms produce tornadoes (Jones et al., 2004, Trapp et al., 2005). Therefore, operational weather services in the U.S. rely on weather radars and observers to monitor these severe weather events. When a tornado occurs, the U.S. National Weather Service alerts the population with a tornado warning. To trigger such a warning, weather radars must indicate strong rotation inside the thunderstorm or observers must report a tornado on the ground. Following the recent development of weather radars and understanding of the environmental conditions before a tornado, residents in tornado-prone regions are typically warned 13 minutes before a tornado strikes (NOAA, 2011). Tornado shelters or safe rooms provide a safe place for occupants to protect themselves. Nevertheless, 1200 tornadoes (Mulder and Schultz, 2015) and 80 casualties directly related to them are reported on average each year in the U.S. In Europe, where tornadoes are less inclined to occur, about 84 tornadoes occur annually, with 5478 tornadoes reported between 1950 and 2015 (Antonescu et al., 2016). However, fewer tornadoes do not necessarily mean weaker tornadoes, with for instance the 1967 tornado outbreak which saw an F4 and an F5 tornado in France (Antonescu et al., 2018), or more recently an F4 tornado that also struck France in August 2008 (Wesolek and Mahieu, 2011).

To safely study tornadoes, physical simulations have been undertaken over the past few decades to improve our understanding of the complex flow field of a tornado. Ward (1972) pioneered the tornado generator that could generate realistic

tornado-like vortices and sub-vortices. Since then, different tornado generators have emerged, leading to the characterisation of tornado-like vortex flow fields and wind loading studies on buildings. However, due to the earth's curvature and weather radar limitations, no full-scale data is usually obtained below 30m AGL (Wurman et al., 2013), which is usually more than standard low-rise building heights. Therefore, validating physical simulations against full-scale data can be problematic. In addition to physical simulations, analytical vortex models can also be used. Although very simplistic in their formulations with significant assumptions taken, they can be used to provide useful information on wind and debris impact loading (Baker and Sterling, 2018) or debris flight (Baker and Sterling, 2017).

Although great effort has been made over the past few decades to model and understand the flow field of a tornado, the flight of debris in a tornado flow field is still poorly understood. A better understanding of wind-debris interaction in tornadoes could ultimately lead to better tornado warnings, as weather services could estimate where the debris is likely to fall. Research showed that debris can fall at distances up to 300km from where it originated (Anderson, 1985*a*,*b*, Snow et al., 1995, Knox et al., 2013). Therefore, the motivation behind this research is to explore the flight of debris in tornadoes using physical simulations and analytical vortex models.

1.2 Aims and objectives

This research aims to investigate and characterise tornado-like flow fields and the flight of debris within a tornado using physical and numerical simulations. To accomplish these aims, the University of Birmingham Tornado-like Vortex Generator was used, and the following objectives were developed and carried out:

1. Characterise the vortex structure within the tornado simulator, using a velocity mapping with high spatial resolution for different swirl ratios,

2. Develop a methodology to investigate the flight of debris using high-speed cameras and the Particle Tracking Velocimetry technique,

3. Develop a methodology to numerically simulate the flight of debris, using analytical vortex models.

1.3 Thesis outline

Following this introductory chapter, Chapter 2 presents the relevant background knowledge and reviews the relevant literature on tornadoes from a meteorological and engineering point of view. The meteorological point of view introduces the fundamentals of meteorology to understand the formation of tornadoes, as well as some background on full-scale data and climatology. On the other hand, the engineering point of view introduces the different physical and analytical techniques employed to investigate tornado-like vortices and debris in laboratories. In Chapter 3, the investigation of tornado-like flow fields using the University of Birmingham Tornado-like Vortex Generator is introduced. In this chapter, the experimental

methodology is detailed, and wind measurements are discussed. Chapter 4 examines the flight of debris in tornado-like flow fields experimentally. The methodology based on the particle tracking velocimetry technique is detailed, and 2D and 3D debris trajectories are shown and discussed. In Chapter 5, the numerical methodology to compute debris trajectories using experimental data is introduced, and results are compared with experimental data. Chapter 6 examines the flight of debris using analytical vortex models. The influence of different vortex models on debris flight is investigated in this chapter. Finally, Chapter 7 concludes with the main findings of this research work and gives some recommendations for further work.

Chapter 2

Background and literature review to tornadoes and debris

2.1 Introduction

This chapter presents the general background and relevant literature to this thesis which sets the foundation to understand and investigate the flight of debris in tornadoes. Section 2.2 introduces the general concepts of meteorology which are relevant to understand the environment needed to develop tornadic thunderstorms, as well as a thorough description of the tornado structure, the technique to obtain wind data and the climatology of tornadoes around the world. It then follows in section 2.3 with the engineering research undertaken in order to improve our understanding of tornadoes. The background and relevant literature regarding the modelling of tornado-like vortices both physically and analytically are first described. Then, the background and literature related to debris is introduced. In order to investigate the flight of debris in tornadoes, the technique called Particle Tracking Velocimetry (PTV) is used. Therefore, the technique and the relevant literature to apply this technique to the current work is detailed. Since the PTV

technique is used to reconstruct the motion of debris, an overview of the literature related to the flight of debris is given. Since tornadoes are modelled, whether using physical, analytical or even numerical method, it is important to reflect on the scale of this model to the real world. Therefore, this section finishes by assessing the scaling issues between modelled and full-scale tornadoes. Finally, a description of the research gap motivating this research work is given in section 2.4.

2.2 Tornadoes: a meteorological point of view

2.2.1 Meteorology generalities

Wind is an air mass movement caused by the unbalanced heating of the surface of the Earth from the sun. When receiving solar energy, the surface of the Earth is heated and emits heat radiation back to the atmosphere. Due to the inclination of the Earth, more solar energy is received near the Equator than the Poles throughout the year. As a result of that contrast and in order to balance it, this excess of energy is distributed in the atmosphere by air mass movements. Hadley (1735) was the first to propose an atmospheric circulation model, describing one cell in each hemisphere with what would be termed 'trade winds', consisting of moving masses of air towards the equator in the lower atmosphere. Based on Hadley's theory, Ferrel (1861) identified secondary, thermally indirect circulation cells in midlatitudes, known as Ferrel cells. The Ferrel cells, usually located between 30 and 60 degrees of latitude, are the region where the strongest contrast exists with warm, tropical air moving northward and cold air moving southward. Strong temperature gradients result in strong pressure gradients which, associated with the Earth's rotation, generate strong winds at an altitude of around 10km:

the jet-stream (Figure 2.1 (b)). The jet-stream extends all around the Earth, and its shape depends on the low-pressure systems moving westerly. In Europe, the jet-stream is a key component and significantly influences the weather as it can bring cold air from the North Pole regions or warm air from North Africa. The oscillatory motion of the jet-stream can result in a local region of intense winds, known as jet-streak. A jet-streak is characterised by four regions, left entrance/exit and right entrance/exit (Figure 2.1 (b)). The right entrance and left exit account for regions of flow convergence while the left entrance and right exit for regions of flow divergence. Regions of convergence in the upper atmosphere account for downward synoptic-scale winds while regions of divergence account for synoptic-scale upward winds (Rose et al., 2004). As described in section 2.2.2, the upward forcing plays an important role in the formation of thunderstorms.

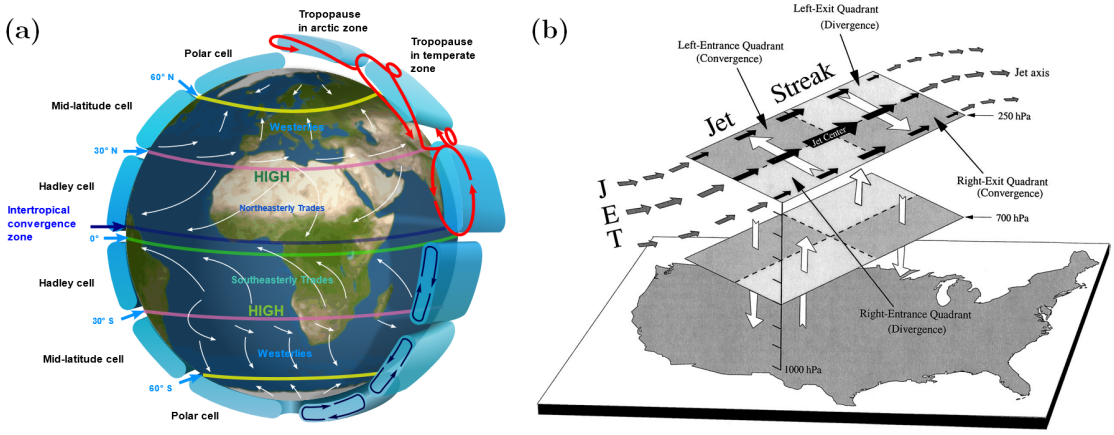


Figure 2.1: (a) Conceptual view of the atmospheric circulation – (b) Jet-streak quadrant and associated large-scale atmospheric forcing (Rose et al., 2004).

2.2.2 From clouds to tornadogenesis

A thunderstorm is a convective cloud almost always associated with heavy rain, lightning activities, and sometimes hail. When the cloud reaches a vertical extension up to about 12-15km, it is is typically called a cumulonimbus (Houze, 2014). A thunderstorm cloud generally needs three ingredients to develop: warmth, moist air, and instability. The instability can be thermally caused when the surface of the Earth is heated and initiates natural convection, or dynamically caused, such as introduced in the previous section. Such atmospheric instability can be defined by two major parameters, the Convective Available Potential Energy (CAPE) [J/kg] (Moncrieff and Miller, 1976) and the Convective Inhibition (CIN) [J/kg] (Colby, 1984). CAPE is the potential energy an air parcel would have if lifted to its Level of Free Convection (LFC). The LFC is the height where a rising air parcel becomes warmer than the ambient environment. Once past its LFC, the air parcel is convectively buoyant and freely rises upwards until reaching the Equilibrium Level. The equilibrium level is the level where the air parcel and the ambient environment have the same temperature and where buoyancy forces are becoming neutral. However, due to its momentum, the air parcel commonly travels further than the equilibrium level and forms an overshooting top. An overshooting top helps to easily identify strong convection and updraft inside a cumulonimbus. The intensity of the updraft (w) can be roughly estimated from the CAPE, with $w = \sqrt{2\text{CAPE}}$ [m/s] (Bluestein, 2013). The larger the CAPE, the stronger the probability of observing an intense convective event. However, the CIN plays a major role in the convection initiation. The CIN is the energy needed by an air parcel to reach the level of free convection. This energy can be given to the air parcel from surface

heat flux, low-level wind convergence or synoptic-scale forcing. CAPE and CIN are usually estimated by radio sounding, where temperature, humidity and pressure are measured vertically through the atmosphere with a radiosonde (Bluestein, 2013). Once fully developed, a convective cloud is characterised by an updraft due to the upward air parcel motion and a downdraft due to precipitation. Wind shear plays a crucial role in the next stage of the convective storm. The wind shear is the difference in wind speed and/or direction with height. If the wind shear is low, the downdraft counteracts with the updraft. The convective cloud weakens and dissipates. However, if the wind shear is of sufficient strength, the updraft and downdraft are separated, and the convective cloud reaches a mature and structured form (Figure 2.2).

If all conditions are favourable, i.e. high instability and strong wind shear, a convective storm can evolve into a more complex storm, a supercell. A supercell is a long-life storm due to the separation of rotating updraft and the downdraft.

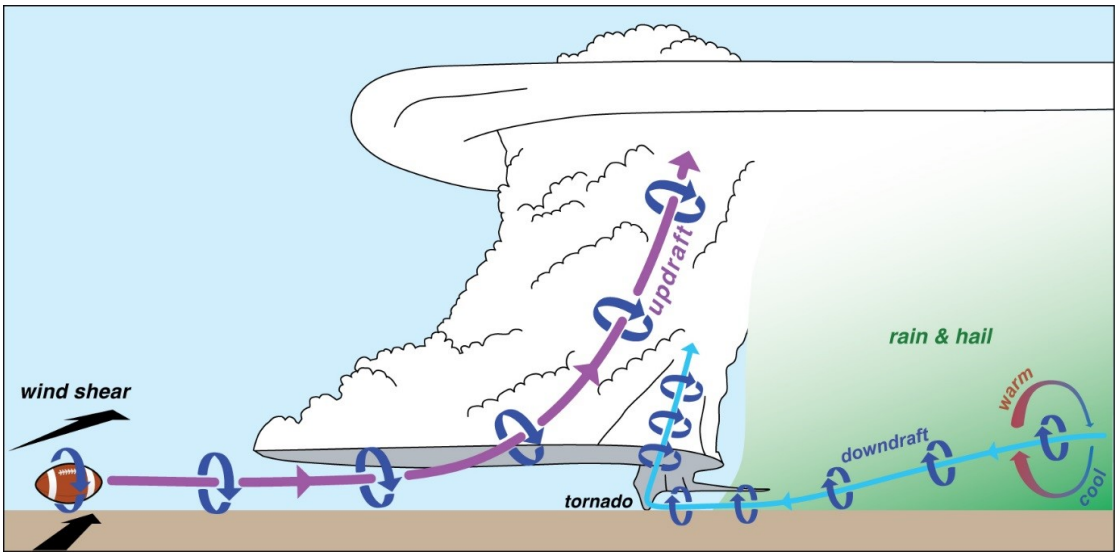


Figure 2.2: Structure of a tornadic supercell thunderstorm (Markowski, 2019)

The supercell thunderstorm can generate significant amounts of precipitation, large hail, strong winds and sometimes tornadoes. To form a tornado, three essential ingredients are required to form a tornadic supercell:

- A strong rotating updraft that can reach up to 50m/s,
- A downdraft forming behind the updraft, known as Rear Flank Downdraft (RFD),
- Near ground wind convergence.

First, strong vertical wind shear generates large-scale horizontal vortices near the surface. When a convective cell is initiated, these horizontal vortices can be embedded within the updraft resulting in tilted vorticity. Two vertical vortices are then created, one rotating clockwise and the other anticlockwise. In mid-latitude regions, the vertical wind shear is predominantly varying clockwise with altitude so, as a result, cyclonic vertical vorticity is enhanced while anticyclonic vorticity is suppressed. Cyclonic rotation is counter-clockwise in the Northern hemisphere whereas anticyclonic rotation is clockwise. Therefore, vertical vorticity is initiated and maintained at mid-level altitude inside the thunderstorm, around 3 and 6km AGL, and is known as a mesocyclone. At this stage, the supercell thunderstorm is formed and can potentially live several hours if the conditions are maintained.

Although vertical vorticity is generated within the mesocyclone, its strength is not sufficient to form a tornado and radar measurements showed that it would take up to 20 minutes to bring the vertical vorticity down to ground-level (Trapp and Davies-Jones, 1997). However, rapid-scan observations showed that tornadogenesis usually occurs within a minute (French et al., 2013). At this point, extra

vorticity is required to intensify the low-level rotation. The RFD most likely plays a significant role in transporting vertical vorticity back to the ground-level, and its interaction with the updraft increases low-level rotation (Markowski et al., 2002, Markowski and Richardson, 2009, Davies-Jones, 2015). However, uncertainties remain on the processes leading to tornadogenesis and in particular why some supercells produce tornadoes and others do not. This led meteorologists to discover that the temperature of the downdraft also plays a role during its interaction with the rotating updraft, with temperature deficit up to 2 to 3 times higher in weak tornadoes (F0-F1) than in more intense tornadoes (F2) (Markowski et al., 2002). More recently, meteorologists and storms chasers have started examining the Forward-Flank Downdraft, i.e. the downdraft region where the precipitations are located, and its potential role in also transporting vorticity (Schueth and Weiss, 2018). This shows that all the processes leading to tornadogenesis are still not fully understood.

2.2.3 The flow structure inside a tornado

Each tornado is generally different, in terms of shape, wind intensity and structure, but it is possible to describe a general, idealised axisymmetric tornado. Snow (1982) described the idealised vortex as consisting of five distinct regions (Figure 2.3):

I. The Outer Flow: the flow spirals inward and updraft around the core region is present. Tangential velocities increase towards the core region due to the conservation of angular momentum.

II. The Core: water condensation and debris are lifted in the core region, making

the vortex visible with its characteristic shape - the funnel. In this region, maximum tangential velocities occur due to the cyclostrophic equilibrium between pressure and centrifugal forces.

III. The Corner: converging horizontal winds from the inflow region are deflected upward into the core region. This is the region where the most intense winds are observed.

IV. The Inflow: this surface boundary layer region fuels the storm with unstable air characterised by a strong radial inflow.

V. Upper flow: the vortex core merges with the ambient environment where the mesocyclone is located. This region plays a crucial role in maintaining the tornado lifetime.

Although the above gives a conceptual description of a tornado, the actual flow structure of the tornado core vortex varies considerably, and the structure can evolve due to the intensity of the core vortex, as illustrated in Figure 2.4 (Snow, 1982, Rotunno, 2013). A low-intensity tornado is characterised by a single-cell vortex structure with a low turbulence updraft, usually referred to as laminar, and radial flow. With increasing vorticity, a downdraft is formed and shows a negative vertical velocity and a radial outflow in the centre of the vortex. Consequently, the flow becomes turbulent and broadens around a stagnation point; this reveals a transition from a one to two-cell vortex structure, also known as vortex breakdown. As the rotation increases more and the stagnation moves down to reach the surface, the vortex evolves to a fully developed two-cell vortex structure. Finally, with more rotation, the two-celled vortex loses its asymmetry, and local vortices are formed

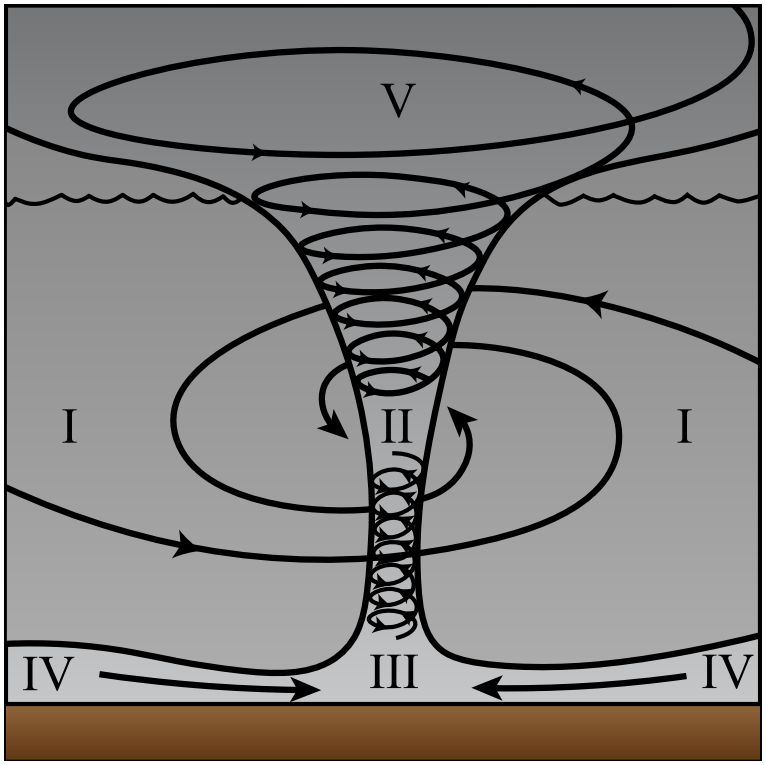


Figure 2.3: Conceptual view of a tornado (Snow, 1982).

(Fujita, 1971). The vortex then evolves into a multiple vortex structure with a strong downdraft in the centre. Local wind speeds associated with these local vortices can be higher than the maximum wind speed observed at the core vortex region and therefore explains the extreme wind speed, e.g. 509km/h, measured during the 1999 Oklahoma City tornado (Wurman et al., 2007).

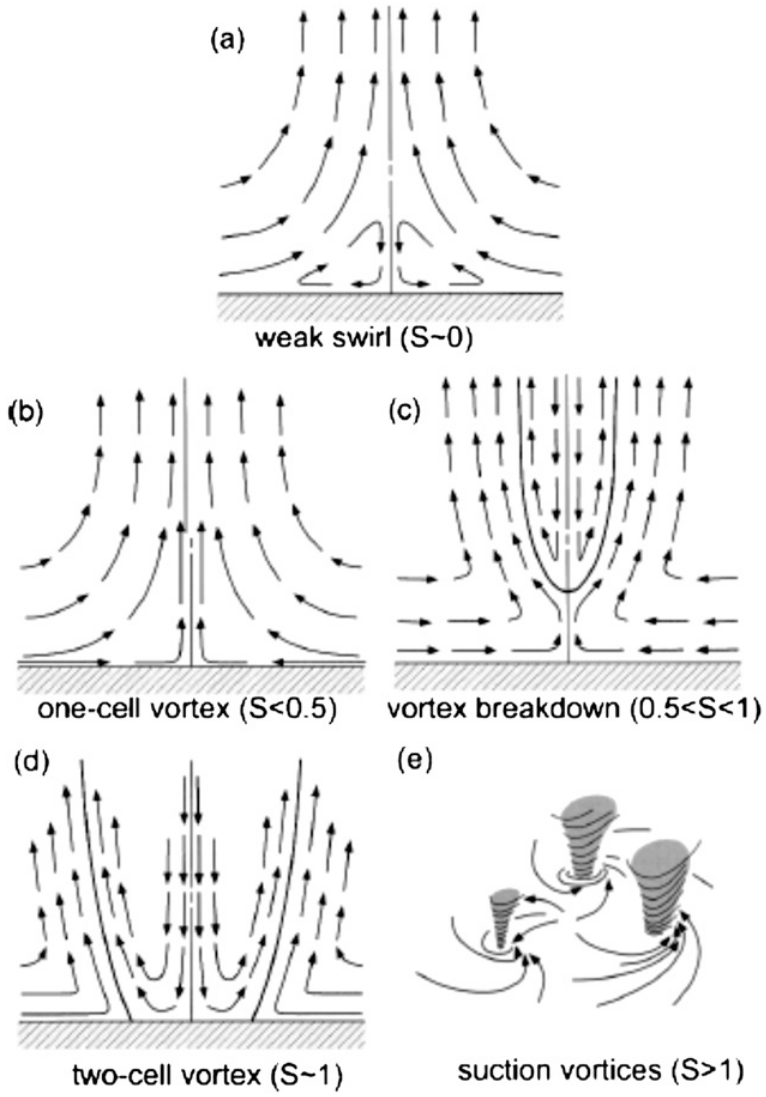


Figure 2.4: Evolution of a tornado vortex structure as a function of the swirl ratio (Rotunno, 2013). The swirl ratio S measures the strength of a vortex and is fully defined in section 2.3.

2.2.4 Obtaining data at full-scale

Due to their unpredictability and their hazardous nature, in-situ data are difficult to obtain in full-scale tornadoes. Over the past decades, the development of weather radars has increasingly helped in understanding and picturing the environment leading to a tornado and its wind characteristics. Zrnic et al. (1977) managed to determine core radii and maximum wind speeds of tornadoes measured with a Doppler radar. Although advantageous, weather Doppler radars can be limited in obtaining data close to the ground due to the earth curvature or urban/vegetated areas. To overcome this limitation, Bluestein and Unruh (1989) used a Portable Doppler radar to intercept and get as close as 10km distance from a tornado. As a result, between 1995 and 2008, 150 tornadoes have been measured using Doppler On Wheels (DOWs) (Alexander and Wurman, 2008) with measurements within 20m Above Ground Level (AGL) (Wurman et al., 1997, Wurman,

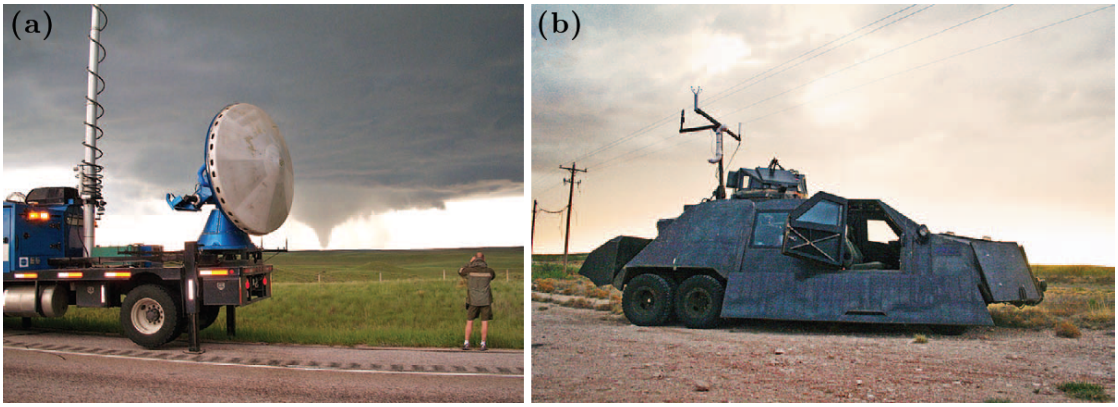


Figure 2.5: (a) Doppler on Wheel (DOW) scanning a full-scale tornado (Wurman et al., 2013) - (b) The Tornado Intercept Vehicle (TIV) is positioned in the path of a tornado to measure in-situ pressure, temperature and wind data.

1999, 2011). DOWs have been used in numerous important field campaigns (Figure 2.5 (a)) that have improved our understanding of tornadogenesis such as the Radar Observations of Tornadoes And Thunderstorms Experiment (ROTATE) project, the Tactical Weather-Instrumented Sampling in/near Tornadoes Experiment (TWISTEX) project, the Verification of Rotation in Tornadoes EXperiment (VORTEX) project, or more recently the Targeted Observation by Radars and UAS of Supercells (TORUS) project. Wurman et al. (2013) derived the DOW data to obtain the 3D velocity flow field of a full-scale event and radial profiles of tangential velocity to estimate the core radius of the tornado. However, data are only available from 50m AGL upwards, which limits its purpose for wind loading applications. Nevertheless, Kosiba and Wurman (2013) managed to map the three-dimensional structure of the boundary-layer of a tornado (Figure 2.6) and its temporal evolution using a Rapid-Scan Doppler On Wheels (RSDOW).

Data were collected near the surface with heights as low as 4m AGL and showed that the tornado winds are more intense near the surface than above. However, the

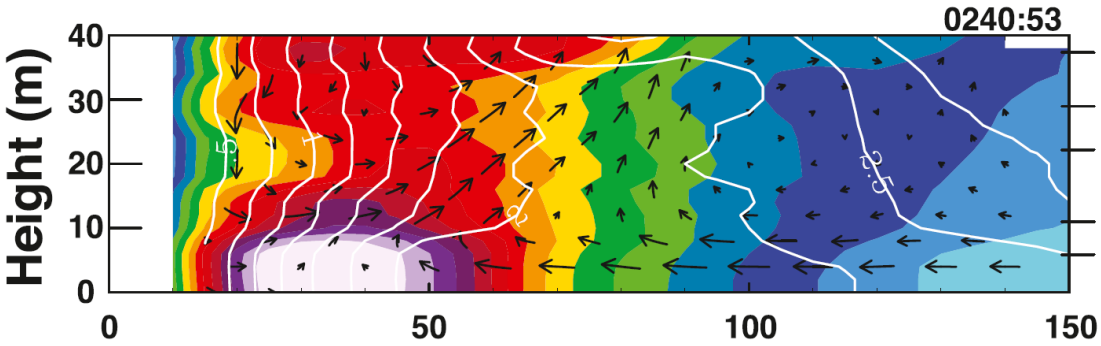


Figure 2.6: Axisymmetric cross-section of the May 25, 2012, Russel, Kansas tornado from a Rapid-Scan Doppler on Wheels (RSDOW) (Kosiba and Wurman, 2013). The colour contours denote the tangential velocity and the arrows the 2D vector field of radial and vertical velocities.

RSDOW needs to be in close vicinity to be able to obtain such high-resolution data. During 2019 and 2020, the TORUS project aims to try to better understand the relationship between severe thunderstorms and tornadogenesis (NOAA, 2019). In addition to using a DOW and other meteorological instrumentations, the TORUS team will be using a LiDAR (LIght Detection And Ranging) system that will provide wind data. This will help in investigating the environment as well as the development of tornadoes in severe thunderstorms.

In recent years, more audacious and radical methods have been used to obtain full-scale data in tornadoes. Wurman et al. (2007) used a Tornado Intercept Vehicle (TIV) (Figure 2.5 (b)), an instrumented and armoured truck that can sustain strong winds and be driven inside a tornado. On-board meteorological instrumentation as well as an anemometer at 3.5m AGL were used to obtain wind data right inside the core of an EF2 tornado (Figure 2.7 (a)) (Wurman et al., 2013).

Figure 2.7 (a) shows the wind speed estimated from the RSDOW and reveals

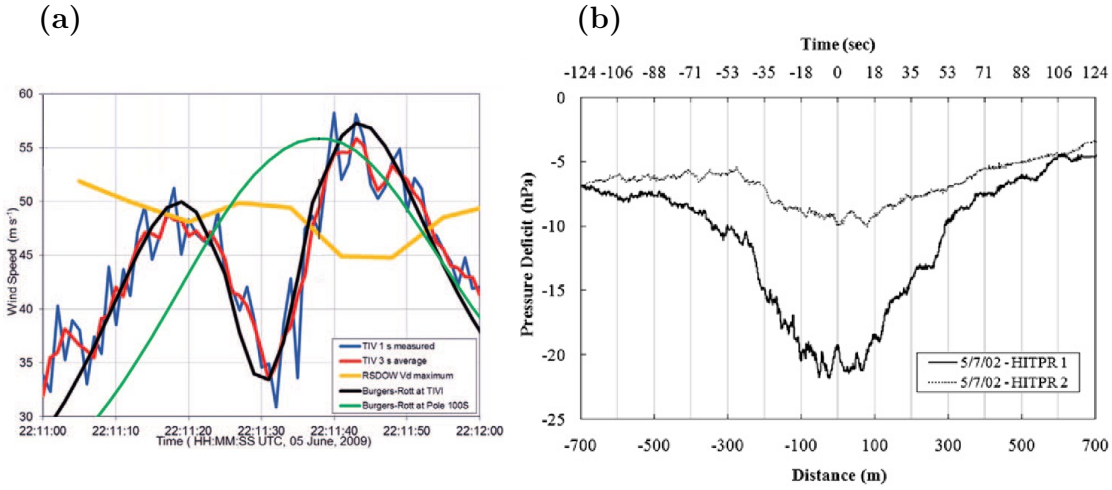


Figure 2.7: Tornado in-situ (a) wind data (Wurman et al., 2013) and (b) surface pressure data (Karstens et al., 2010).

the limitation of Doppler radars in measuring high-frequency wind fluctuations. Another way to obtain in-situ data is to deploy surface pressure probes in the path of a tornado. This technique can be very dangerous but also difficult to set up due to the unpredictability of the tornado and the inability to predict the tornado path. This technique has been used for several occasions leading to a dataset of surface pressure inside tornadoes (Winn et al., 1999, Lee and Samaras, 2004, Karstens et al., 2010). However, Figure 2.7 (b) shows the difference between two surface pressure probes from two nearby locations but with significantly different signals (Karstens et al., 2010). In this case, the tornado core diameter was estimated between 400 and 450m from a DOW radar. Although it gives an idea of the surface pressure within a tornado, F0-F1 tornadoes are the most common with much smaller core sizes. Furthermore, pressure measurements are typically made on landscaped grounds with no surrounding buildings. It is unclear what the surface pressure at ground level would be and how the pressure distribution within the tornado, and indirectly the wind loading, would be affected in urban areas.

2.2.5 Climatology

Theoretically, tornadoes can occur anywhere on the planet except within Antarctica, where the temperature and moisture level are too low for convective storms to occur. Figure 2.8 shows where tornadoes frequently occur. As discussed in section 2.2.1, severe weather usually happens where strong temperature gradients are observed. Therefore, mid-latitude regions are the most favourable environment to develop thunderstorms and tornadoes (Fujita, 1973) (Figure 2.8). In the U.S.A, the Great Plains, covering a large area of North America's mid-continent,

are the region where most tornadoes are observed. Every year, about 1200 tornadoes occur in the U.S.A (Mulder and Schultz, 2015), mainly in the so-called Tornado Alley. The Tornado Alley is the region with most tornadoes in the world due to a very particular meteorological environment. Cold air is travelling down from the Canadian Prairies while warm most air is travelling up from the Gulf of Mexico. This leads to the formation of the most spectacular and violent storms. Fortunately, only 3% (Jones et al., 2004) to 25% (Trapp et al., 2005) of the supercell thunderstorms observed in the U.S. produce a tornado. Tornado climatology showed that they could occur at any time during the year; however, the tornado season in the U.S. is usually from April to August (Brooks, Lee and Craven, 2003). Tornadoes are also relatively common in Europe, as shown in Figure 2.9. Similarly to North America, tornadoes can generally occur at any time, although a peak is

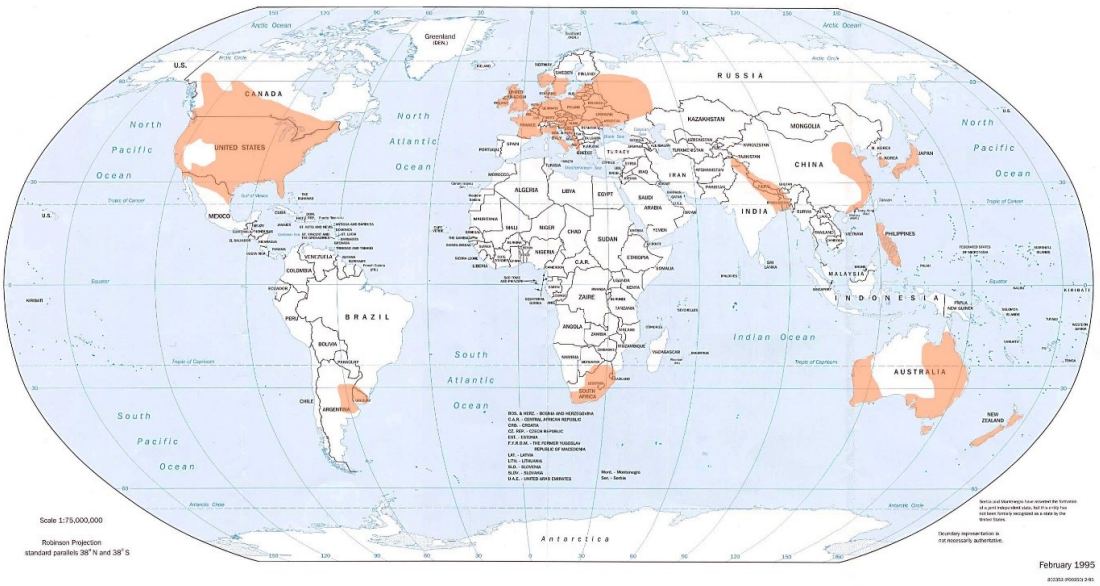


Figure 2.8: Worldwide areas of tornado occurrences (NOAA, 1995).

observed between May and August (Antonescu et al., 2016). In 2018, 628 tornadoes were reported in Europe. Regarding the geographic distribution, Germany and the United Kingdom are the most affected. In the United Kingdom, about 30 tornadoes are reported every year, with 2.2 tornadoes per year per 10,000 km sq. on average. This is more than in the U.S. with 1.3 tornadoes per year per 10,000km (Mulder and Schultz, 2015). The most recent and intense tornado in Europe occurred in 2008 in Northern France, with winds estimated up to 300 km/h (Wesolek and Mahieu, 2011).

Although tornadoes seem to occur in limited regions, as shown in Figure 2.8, it is still unclear if other regions are indeed affected. Tornado reports seem to have

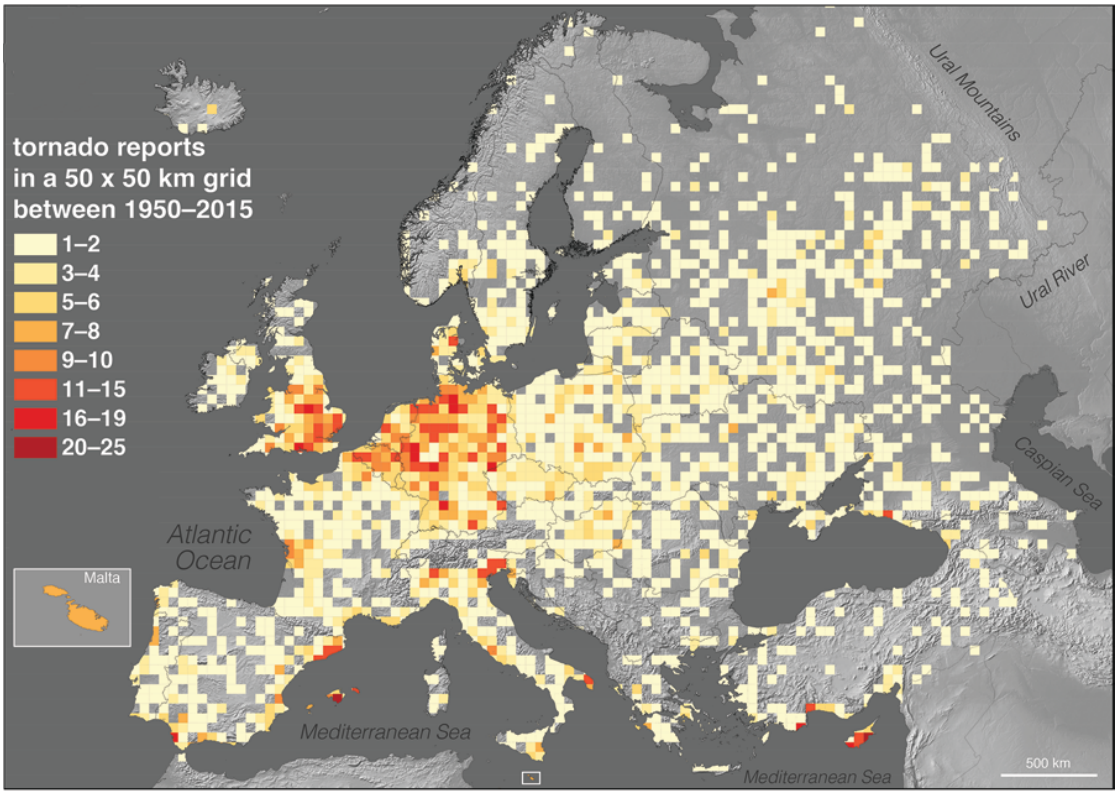


Figure 2.9: Tornado climatology in Europe between 1950 and 2015 (Antonescu et al., 2016).

risen with the global increase in population and the evolution of the Internet and television in rural regions (Dias, 2011), as well as with the popularisation of camera phones. Until the mid-19th century in the U.S.A., tornado reports were approximatively ten times lower than nowadays (Doswell et al., 1999). Therefore, it is most likely that on a global scale, many tornadoes occurring in remote regions are still unreported. The development of Doppler radar and detection algorithms (Brown et al., 1978, Bodine and Kurdzo, 2018) as well as research undertaken on tornado damage on crops (Rhee and Lombardo, 2017, Baker et al., 2020) may enhance the number of reported tornadoes worldwide in the future.

2.3 Tornadoes: an engineering point of view

The lack of data regarding the flow field and structure of a tornado has stimulated the development of apparatus and models to investigate tornado-like flow fields physically and numerically. This research presents several advantages to simulate scaled tornadoes by controlling geometric, kinematic and dynamic parameters. It also allows flow field characterisation in an easy and safe environment and generally gives good similarities with full-scale tornadoes. However, as a simplified model of a tornado, they can fail in reproducing a realistic scale version of a real tornado. Analytical vortex models are even more simplified models and therefore fail to reproduce the complexity of either a physically modelled or full-scale tornado but allow to consider different concepts easily. Section 2.3.1 introduces the major tornado simulators and the controlling parameters to physically model tornado-like vortices, while section 2.3.2 introduces the different analytical vortex models developed to date.

2.3.1 Can we reproduce tornadoes in laboratories?

Over the past 40 years, several different approaches have been used to physically simulate tornado-like vortices. This section introduces the major tornado-like vortex generators that have been used to experimentally characterise and investigate tornadoes. However, are these tornado simulators really reproducing full-scale tornadoes and/or are they comparable with each other? Baker and Sterling (2019) recently questioned the efficacy of tornado simulators in reproducing full-scale tornadoes. The authors looked at various dimensionless groups to evaluate the performance of several tornado simulators with regards to dynamic, kinematic

and geometric similarities. The main conclusion drawn from this analysis is that some are able to match geometric similarity for some tornadoes, some are able to match kinematic similarity, but none of the current tornado simulators are able to show all similarities with full-scale tornadoes and therefore are not fit for purpose. Nevertheless, the research undertaken throughout the years has helped to identify key parameters for the physical modelling of tornadoes.

Governing parameters

To physically generate a tornado-like vortex, it is necessary to define parameters controlling the flow dynamics of the simulated vortex. Three important non-dimensional parameters governing the tornado flow have been introduced by Lewellen (1962): the aspect ratio, the swirl ratio and the radial Reynolds number. The aspect ratio, a, is a geometric parameter that defines the ratio between the height of the inflow (h_0) and the radius of the updraft hole (r_0). The swirl ratio, S, is a kinematic parameter that measures the circulation strength relative to the updraft and is defined as:

$$S = \frac{r_0 \Gamma}{2 Q' h_0} \tag{2.1}$$

where Γ is the circulation and Q' the volumetric flow rate through the updraft hole per unit length. The swirl ratio is an important parameter that characterises the vortex structure evolution (Davies-Jones, 1973) as discussed in section 2.2.3 and shown in Table 2.1.

The radial Reynolds number is a dynamic parameter defined as:

$$Re_r = \frac{Q'}{2\pi\nu} \tag{2.2}$$

where ν is the kinematic viscosity of air.

Table 2.1: Vortex structure description as a function of the swirl ratio (Davies-Jones, 1973)

Swirl ratio	Vortex structure
$S = 0$	Vertical updraft
$S < 0.5$	One cell vortex
$0.5 < S < 1$	Vortex breakdown (VDB) appearance
$S = 1$	Two cell vortex structure
$S > 1$	Multiple vortex structure

Early in the experimental work on tornado simulators, Ward (1972) identified the swirl ratio to be one of the key factors for designing tornado simulators. When varying the swirl ratio, Ward's simulator could produce different vortex structures and particularly multiple vortex formations as observed during extreme tornadic events (Figure 2.10).

Even if the swirl ratio is mainly accepted as the main parameter to describe the vortex, its definition can be complicated to apply to full-scale tornadoes or depend

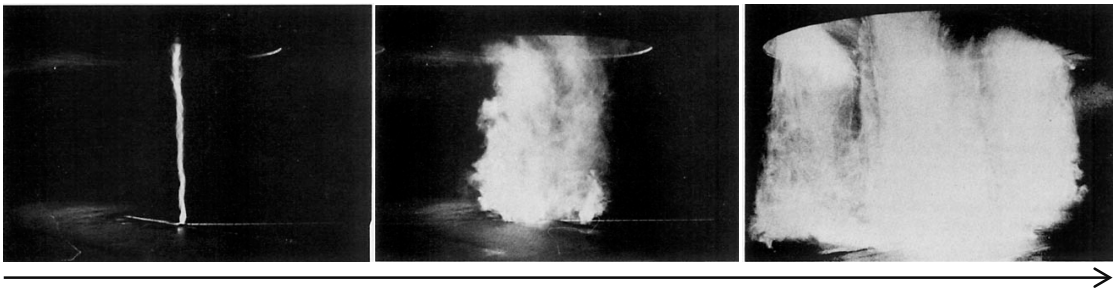


Figure 2.10: Evolution of vortex structure as a function of swirl ratio in a Ward-type tornado simulator from a laminar vortex to multiple vortices (Church et al., 1977)

on the simulator configurations (Haan et al., 2008). Hangan and Kim (2008) showed that a swirl ratio of 2.0 would be equivalent to a Fujita scale F4 tornado by comparing full-scale data from the Spencer South Dakota tornado. However, it was specific to one particular full-scale tornado and cannot be generalised to all tornadoes. Moreover, it appears unsuitable to compare a dimensionless parameter such as the swirl ratio to an estimation of wind speed. Mishra et al. (2008*a*) and Baker and Sterling (2017) defined the swirl ratio as the ratio of the tangential to the radial velocity. Whilst these velocities can be measured in tornado simulators, they are more difficult to obtain in full-scale tornadoes as they are located near the ground (see section 2.2.4). Therefore, defining a geometric or kinematic swirl ratio for a full-scale tornado appears to be fraught with difficulties, if not impractical.

Davies-Jones (1973) showed the core radius (r_c) to be solely swirl ratio dependent. He also performed a dimensionless analysis and suggested the flow structure to be swirl ratio (S) and Reynolds number (Re) dependent, as well as four dimensionless geometric parameters, $r_o/r_s, r_w/r_s, l/r_0, h/r_0$, as defined in Figure 2.11. Further investigation on swirl ratio, aspect ratio and Reynolds numbers effects using a Ward-type simulator showed that the flow fields of tornado-like vortices are supposedly Reynolds number independent, under the considered range of radial Reynolds number and above a certain critical value of radial Reynolds number (Church et al., 1977, 1979) (Figure 2.12). Therefore, the flow characteristics are considered Reynolds number independent if the radial Reynolds numbers achieved are high enough to ensure turbulent flow. However, it is unclear if the flow characteristics would behave similarly at low radial Reynolds number. Furthermore, the swirl ratio is asymptotically dependent on the radial Reynolds number (Figure

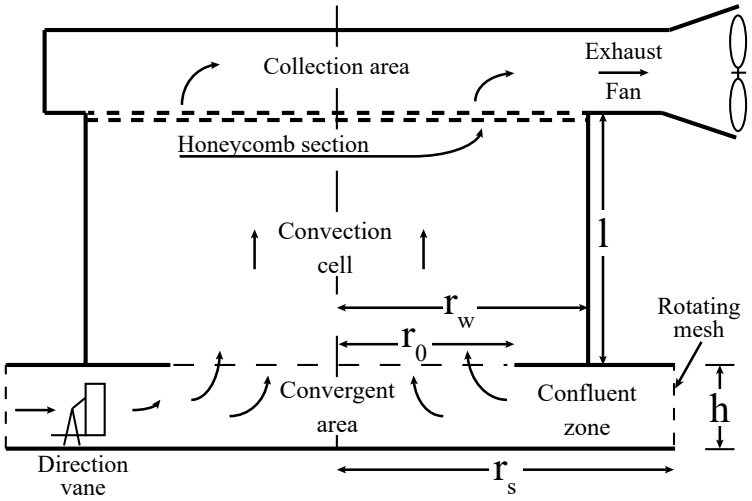


Figure 2.11: Schematic of a Ward-type tornado generator (adapted from Davies-Jones (1973))

2.12) and would probably lead to unrealistic swirl ratio at low Reynolds number.

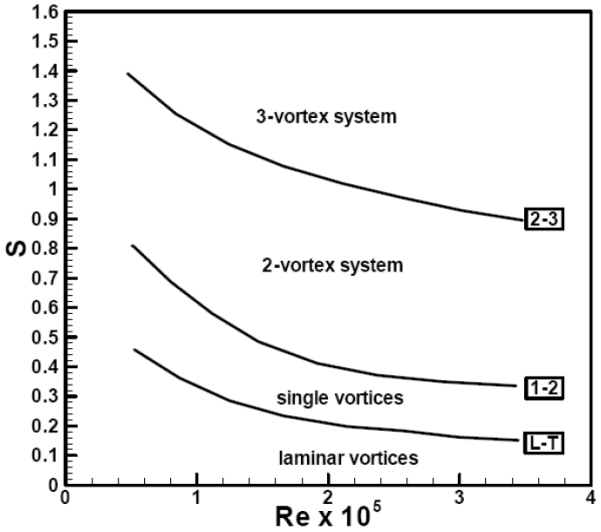


Figure 2.12: Swirl ratio as a function of radial Reynolds number for a Ward-type tornado simulator and different aspect ratios (adapted from Church et al. (1979)).

The analysis also showed that an aspect ratio between 0.5 and 1.5 has little effect on the generated flow field, which differs from the early suggestions of vortex structure dependences on aspect ratios (Ward, 1972).

Tornado-like vortex generators

Ying and Chang (1970) were the first to initiate an experimental investigation of tornado-like vortices with a physical simulator. Their simulator consisted of a rotating mesh screen to produce a horizontal circulation and an exhaust fan to generate an axial flow. By controlling those two parameters, they managed to generate different tornado-like vortices. Later, Ward (1972) developed a generator based on Ying and Chang's design and pioneered what became the standard Ward-type generator (Figure 2.13 (a)). A Ward-type generator consists of a convergence chamber characterised by a radial inflow simulating the low-level convergence observed in supercell thunderstorms. A cylindrical rotating mesh, located around the convergence chamber, was used to control the inflow angular momentum by its rotation and therefore the horizontal vorticity inside the convergence region. A wind vane was also used to measure the inflow angle. A fan located at the top of the apparatus stretches the vertical vorticity present in the convergence chamber into a swirling flow in the convection chamber. The convection region is considered to be analogous to the convection core of the thunderstorm. At the top of the convection chamber, a fine mesh honeycomb was used to straighten the outflow and remove vortices created by the fan.

Church et al. (1977) built at Purdue University a large-scale generator based on Ward's design which more easily controls the aspect ratio, swirl ratio and radial Reynolds number (Figure 2.13 (b)). The aspect ratio is controlled by varying the

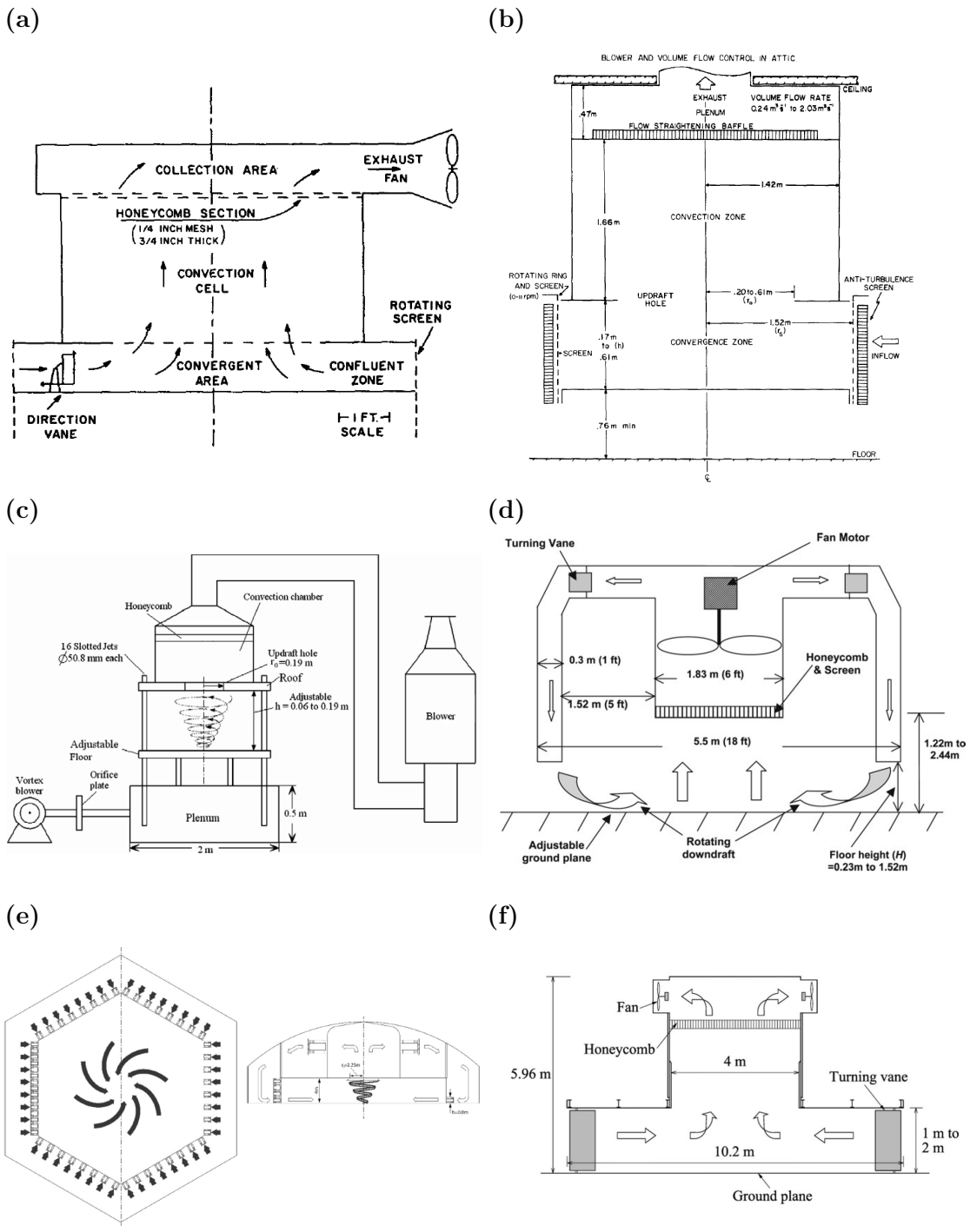


Figure 2.13: Different tornado generator designs from (a) Ward (1972), (b) Church et al. (1977), (c) Mishra et al. (2008*a*), (d) Haan et al. (2008), (e) Refan and Hangan (2018) and (f) Tang et al. (2018)

height of the inflow and/or the size of the updraft hole. The control of the swirl ratio allowed the formation of different vortex structures, from a single laminar vortex to a four vortices configuration.

To attempt to simulate moving tornadoes, Diamond and Wilkins (1984) modified a Ward-type simulator to reproduce translating tornado-like vortices. To do so, they installed a translating ground plate inside the simulator chamber to simulate the tornado translation. They showed that the ground translation generates secondary vortices as a result of the interaction with the rough surface. They also showed that to generate multiple vortices with a rough surface, higher swirl ratios needed to be reached. Smooth surfaces were previously found to help the formation of multiple vortices (Leslie, 1977). Fiedler and Rotunno (1986) developed a physical model to estimate the maximum tangential velocities in tornadoes. They compared the model with the experimental data obtained in the Purdue tornado simulator (Church et al., 1977) and found that maximum tangential velocities in the laminar regions can be up to 1.7× higher than inside the turbulent regions associated with a vortex breakdown.

Mishra et al. (2008*a*,*b*) constructed at Texas Tech University (TTU) another Ward-type generator; however, they adopted a different approach to introducing angular flow. In the TTU vortex generator, the circulation is introduced by means of 16 slotted jets, which enables independent control of the circulation and makes flow and pressure measurement easier in the vortex chamber (Mishra et al., 2008*a*). A blower connected to the top of the convection chamber was used to generate the updraft. Although it is stated that it allows independent control of the flow, it is unclear what effects these slotted jets have on the generation of tornado-like vortices. However, the surface pressure measurements in the TTU simulator matches

the surface pressure data from the May 30, 1998, Manchester and June 24, 2003, Spencer tornadoes.

In recent years, new large-scale tornado simulator designs emerged, with the view of reproducing more realistic tornadoes in laboratories and accommodating larger structural models. The Iowa State University (ISU) research group designed and built in 2004 a new tornado simulator that aimed to realistically simulate a tornado for wind engineering applications (Sarkar PP, Haan FL, Gallus WA, Kuai L, 2005, Haan et al., 2008). The simulator consists of a central fan producing an updraft which is then deflected by means of guide vanes, giving angular momentum to the flow, before it is recirculated downward using a circular duct. The simulator is suspended and mounted on a crane that allows a translation of the simulator along a 10m ground plane. The height of the ground plane is also adjustable, which allows the aspect ratio to be changed. The ISU tornado simulator recreates the RFD typically observed in tornadic thunderstorms as well as allows translation (Haan et al., 2008). The simulator has shown the ability to generate one-cell and two-cell vortex structures with corresponding swirl ratios from 0.08 to 1.14, as well as matching the May 30, 1998, Spencer (Wurman and Alexander, 2005) and May 3, 1999, Mulhall tornadoes (Lee and Wurman, 2005). The range of tornado-like vortices generated in the ISU simulator also allows the investigation of tornado-induced wind loads on models of 1:100 to 1:500 scale. Haan et al. (2010) looked at the wind loads on a 1:100 scale gable-roof building with the ISU simulator and found that peak values were generally exceeding the recommended design loads for buildings located in the U.S.A. 'Tornado Alley'. Hu et al. (2011) further examined the interaction between tornado winds and the same gable-roof building using PIV and found that the flow field around the building and related

wake vortices was different from what is usually observed during wind events, such as downbursts. Similar conclusions have also been drawn for a 1:3500 scale cubical building model (Mishra et al., 2008*b*).

Using a 1:3 scale version of the ISU tornado simulator, the mini ISU simulator, Zhang and Sarkar (2012) performed PIV measurements of the near-ground tornado flow field and showed that the lower the swirl ratio, the higher the vortex wandering. Instantaneous flow fields also show the existence of small-scale vortices inside the swirling flow. These multiple vortices are usually observed in intense EF5 tornadoes and can potentially cause more severe damage due to higher local instantaneous velocities.

Constructed in 2009 at Texas Tech University, the large-scale simulator VorTECH is a Ward-type design simulator (Tang et al., 2018). Compared to previous Ward-type simulators (e.g. Ward, 1972, Church et al., 1977, Diamond and Wilkins, 1984, Mishra et al., 2008*a*), the updraft hole and honeycomb cover the whole section of the convection chamber. It is unclear what effects this does have on the tornado-like flow field, but the vortex wandering appears to be low compared to other tornado simulators (Tang et al., 2018, personnal communication). A large number of guide vanes (e.g. 64 vanes) with a symmetric airfoil shape could also possibly explain the low wandering due to a less disturbed inflow. Combining wind measurements using a Cobra probe (TFI, 2011) and a 12-hole Omniprobe (Aeroprobe Corporation) showed the ability of the VorTECH simulator to generate one-cell and two-cell vortices as well as catching the transition between the vortex structures. Surface pressure measurements were also matched with surface pressure data from three full-scale tornadoes with a range of swirl ratios ($0.11 < S < 0.78$). The Wind Engineering, Energy and Environment (WindEEE) Research Institute

at the University of Western Ontario (Canada) built in 2011 a three-dimensional testing chamber that can generate tornadoes (Refan and Hangan, 2018). The chamber has a hexagonal-shape configuration and is fitted with 100 fans. For tornado simulations, eight fans at the bottom of each wall are used, and vanes are placed in front of each individual fan to introduce circulation. The updraft is created through a suction hole by means of six fans located at the top of the facility. The WindEEE dome is currently the largest facility to study tornado-like vortices but an investigation was initially carried out using a 1:11 scale version of the WindEEE dome. Refan et al. (2014) performed PIV measurements for different swirl ratios and compared with full-scale tornado data measurements from a Doppler radar. They suggested that the mini WindEEE dome (MWD) could supposedly generate tornado-like vortices similar to full-scale EF0 to EF3 tornadoes. However, as discussed by Baker and Sterling (2019), proper scaling cannot be reached to date in tornado simulators and EF-scaling does not relate to vortex structures in tornado simulators. Therefore, although the physical simulations in Refan et al. (2014) show some similarities with full-scale tornadoes, it does not fully replicate a real tornado. Nevertheless, further investigation of the tornado-like generated flow field using PIV showed that the mini WindEEE dome was also capable of generating tornado-like vortices with one-cell and two-cell structures (Refan and Hangan, 2016). The evolution of the vortex structures while varying the swirl ratio also shows strong agreements with the description given by Davies-Jones (1973). Recently, physical simulations have been carried out in the large-scale WindEEE dome and investigated using PIV (Refan and Hangan, 2018). As discovered in previous studies (e.g. Zhang and Sarkar, 2012, Refan et al., 2014),

it was also established that the lower the swirl ratio, the higher the vortex wandering. Finally, by combining data from the MWD, the range of radial Reynolds numbers (i.e. $1.6 \times 10^4 < Re_r < 2 \times 10^6$) tested was substantial enough to show that average pressure measurements are Reynolds independent for $Re_r > 4.5 \times 10^4$.

2.3.2 Can tornadoes be modelled analytically?

Tornadoes can be simulated using vortex models to simplify all the complexities observed in tornado flow fields. These models are, for different assumptions taken that are detailed below, a solution of the Navier-Stokes equations in cylindrical coordinates. The coordinate system is defined as:

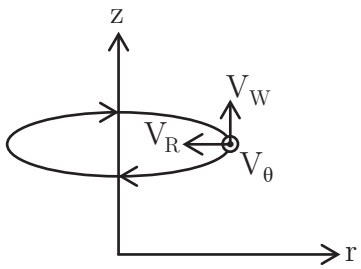


Figure 2.14: Cylindrical coordinate system and velocity vectors denotations.

where V_R denotes the radial velocity, V_θ the tangential velocity and V_W the vertical velocity.

Wind loads during transient events such as tornadoes differ from uni-directional wind events, as discussed in the previous section. Therefore, modelling tornado winds is important to establish wind load designs and recourse to analytical vortex models can help establish these guidelines. Figure 2.16 shows the radial profiles for the analytical vortex models presented in this section (i.e. Rankine, Burgers-Rott, Sullivan and Baker and Sterling vortex models). An extensive list of current

analytical vortex models can be found in Kim and Matsui (2017) and a thorough analysis of the models discussed after is given in Gillmeier et al. (2018).

Rankine model

The simplest way to express vortex behaviour has been proposed by Rankine (1882) using the following assumptions:

- One-dimensional flow field, i.e. tangential velocity only
- Steady flow
- Inviscid

The combined Rankine vortex model is then expressed as:

$$\begin{cases} V_\theta = \dfrac{V_{\theta\,\max} r}{r_c}, (r < r_c) & \text{(2.3a)} \\ V_\theta = \dfrac{V_{\theta\,\max} r_c}{r}, (r \geq r_c) & \text{(2.3b)} \end{cases}$$

and consists of a solid body rotation between the centre of the vortex and the core radius r_c, where the vortex reaches its maximum velocity $V_{\theta,max}$, and a free flow outside the core radius ($r > r_c$) where the tangential velocity decreases with the radius. The modified Rankine vortex is defined as:

$$V_\theta = \frac{r\Gamma_{max}}{\pi\left(r^2 + r_c^2\right)} \tag{2.4}$$

where $\Gamma_{max} = 2\pi r_c V_{\theta,max}$ is the maximum circulation at the core radius. The

pressure distribution for the Rankine model is given by:

$$\begin{cases} P = P_0 + \frac{1}{2}\rho_a V_{\theta,max}^2 \left(\frac{r}{r_c}\right), (r < r_c) & (2.5a) \\ P = P_\infty + \frac{1}{2}\rho_a V_{\theta,max}^2 \left(\frac{r_c}{r}\right), (r \geq r_c) & (2.5b) \end{cases}$$

where P is the static pressure, P_0 the static pressure at the centre of the vortex, P_∞ the atmospheric static pressure. The pressure distribution for the modified Rankine model is given by:

$$P = P_\infty + \frac{-\rho\Gamma_{max}^2}{2\pi^2\left(r^2 + r_C^2\right)} \tag{2.6}$$

Rankine (1882) formulated the first and simplest vortex model, consisting of a forced vortex between the centre and the core radius (r_c) and surrounded by a free vortex. The sharp discontinuity at the core radius makes the Rankine vortex model unrealistic to model atmospheric vortices. However, it is often used to numerically simulate and physically compare tornado-like flow fields (e.g. Church et al., 1979, Selvam and Millett, 2003, Gorecki and Selvam, 2015, Mishra et al., 2008*a*, Wood and Brown, 2011, Refan and Hangan, 2016, Tang et al., 2018). The modified Rankine vortex model addresses the limitation of the Rankine model with a better transition between the inner and outer vortex core. The main limitation of either the Rankine or the modified Rankine vortex model is to only model one velocity component, which is unrealistic for experimental and full-scale tornadoes.

Burger-Rott model

Burgers (1948) and Rott (1958) expressed an exact solution of the Navier-Stokes

equations for a three-dimensional vortex with the following assumptions:

- Steady flow
- Constant viscosity
- Axisymmetric flow field
- Tangential and radial velocity solely dependent on the radial distance
- Vertical velocity dependent on the height

These solutions of the Burgers-Rott vortex model for the radial (V_R), tangential (V_θ) and vertical velocity (V_W) components are given by:

$$\begin{cases} V_R = -\tilde{a}r & \text{(2.7a)} \\ V_\theta = \dfrac{\Gamma_\infty}{2\pi r}\left[1 - e^{-\left(\dfrac{\tilde{a}r^2}{2\nu_e}\right)}\right] & \text{(2.7b)} \\ V_W = 2\tilde{a}z & \text{(2.7c)} \end{cases}$$

where $\tilde{a}$ is the suction strength, Γ_∞ the circulation at infinity and ν_e the eddy viscosity. Compared to the Rankine model, the Burgers-Rott model incorporates a radial and vertical component modelling a single-cell vortex structure. The radial and vertical components are proportional to the suction strength $\tilde{a}$ and are functions of the radial distance r and the height z, respectively. The tangential velocity, similar to the modified Rankine model, increases from the centre to the core radius and reaches a maximum at r_c before decreasing with increasing radial distances.

Sullivan model

Sullivan (1959) also expressed an exact solution of the Navier-Stokes equations but for a three-dimensional two-cell vortex with the following assumptions:

- Steady flow
- Constant viscosity
- Axisymmetric flow field
- Tangential and radial velocity solely dependent on the radial distance
- Vertical velocity dependent on the radial distance and the height

The solution is given by:

$$\begin{cases} V_R = -\tilde{a}r - 6\left(\dfrac{\nu_e}{r}\right)\left[1 - e^{-\left(\frac{\tilde{a}r^2}{2\nu_e}\right)}\right] & \text{(2.8a)} \\ V_\theta = \dfrac{\Gamma}{2\pi r}\left[\dfrac{H\left(\frac{\tilde{a}r^2}{2\nu_e}\right)}{H(\infty)}\right] & \text{(2.8b)} \\ V_W = 2\tilde{a}z\left[1 - 3e^{-\left(\frac{\tilde{a}r^2}{2\nu_e}\right)}\right] & \text{(2.8c)} \end{cases}$$

with $H(\infty) = 37.9$ and the function H defined as:

$$H(x) = \int_0^x \exp\left\{-t + 3\int_0^t \left(\frac{1 - e^{-\tau}}{\tau}\right) d\tau\right\} dt \tag{2.9}$$

The Sullivan model describes a two-cell vortex structure, i.e. a region of positive radial velocity associated with a region of negative vertical velocity corresponding to a central downdraft inside the core vortex. Because the tangential velocity mathematical definition is complicated, Wood and Brown (2011) fitted a parametric equation to the tangential velocity profile and found that it can be expressed as:

$$\overline{V_\theta} = \left(\frac{r_c}{r}\right)^{2.4} \left(0.3 + 0.7\left(\frac{r_c}{r}\right)^{7.89}\right)^{-0.435} \tag{2.10}$$

where $\overline{V_\theta}$ is the tangential velocity normalised by $V_{\theta,max}$. The Burgers-Rott vortex model (Burgers, 1948, Rott, 1958) and the Sullivan vortex model (Sullivan, 1959) are an exact solution of the Navier-Stokes equations, and therefore the three velocity components are expressed for one-cell and two-cell vortices, respectively. Both models have a dependence on the radial distance for the radial and tangential velocity component as well as a dependence on the height for the vertical velocity component. Consequently, all velocities go to infinity as radial distance and height tend towards infinity. Furthermore, the lack of a boundary layer representation makes the Burgers-Rott and Sullivan unrealistic to reproduce atmospheric vortices. However, similar to the Rankine vortex model, these models can be adequate to simulate vortex signatures (Davies-Jones and Wood, 2006) or to compare with full-scale data. Wurman et al. (2013) found that the tornado scanned with a Doppler-on-Wheels radar was consistent with the Burgers-Rott vortex and determined the suction strength and eddy viscosity to be $\tilde{a} = 0.45\ s^{-1}$ and $\nu_e = 1800\ m^2.s^{-1}$, respectively. Davies-Jones and Wood (2006) used $\tilde{a} = 0.005\ s^{-1}$ and $\nu_e = 10\ m^2.s^{-1}$ to model a full-scale tornado, which is significantly different from those used in Wurman et al. (2013). These two parameters clearly lack

a physical sense. Gillmeier et al. (2018) looked at the influence of the viscosity parameter on the simulated velocity profiles. They showed that the radial and vertical velocity profiles tend to flatten as the viscosity parameter decreases. However, the authors did not look at the viscosity effect on the tangential velocities. They also concluded that if the viscosity is assumed to be the kinematic viscosity of air, the velocity components for both the Burgers-Rott and Sullivan models are small. Therefore, these parameters tend to be used as a shape parameter to fit specific velocities profiles.

By normalising the Burgers-Rott and Sullivan models, the dependency of the suction strength $\tilde{a}$ and eddy viscosity ν_e can be discarded. It is then possible to express the Burgers-Rott and the Sullivan vortex model in a non-dimensional form. In order to do so, the ratio of the Burgers-Rott vortex model as a function of the radial distance r and the core radius r_c is expressed as follows:

$$\overline{V_\theta} = \frac{V_\theta(r)}{V_\theta(r_c)} = \frac{r_c}{r}\left(\frac{1-\exp\left(-\frac{\tilde{a}r^2}{2\nu_e}\right)}{1-\exp\left(-\frac{\tilde{a}r_c^2}{2\nu_e}\right)}\right) \tag{2.11}$$

Equation 2.11 was studied numerically to express r_c as a function of $\tilde{a}/2\nu_e$. By varying $\tilde{a}/2\nu_e$ for a range of r_c values, it was found that $\tilde{a}/2\nu_e$ is a function of K_M/r_c^2 with K_M a constant (Figure 2.15). By replacing $\tilde{a}/2\nu_e$ by K_M/r_c^2 in Equation 2.11, the following expression of the tangential velocity component of the

Burgers-Rott model is obtained:

$$\begin{aligned}\overline{V_\theta} &= \frac{1}{1-\exp(-K_M)}\left(\frac{r}{r_c}\right)^{-1}\left(1-\exp\left(-\frac{K_M r^2}{r_c^2}\right)\right)\\ &\approx 1.4\left(\frac{r}{r_c}\right)^{-1}\left(1-\exp\left(-K_M\left(\frac{r}{r_c}\right)^2\right)\right)\end{aligned} \tag{2.12}$$

That expression can be found in the literature as the parametric equation of the Burgers-Rott vortex model (Wood and White, 2011). However, discrepancies were noticed for the values of K_M. It was found that Wood and White (2011) assumed $a/2\nu_e = function(r_c^2)$ with a power function $a/2\nu_e = K_M r_c^{2\gamma}$ and found that $K_M = 1.2564$ and $\gamma = 1.996$ and rounded γ to 2. Kim and Matsui (2017) give K_M to be equal to 1.26. However, by fitting $a/2\nu_e = function(r_c^2)$ with a power function $a/2\nu_e = K_M r_c^{2^2}$, it was found that $K_M = 1.253$. In this case, it was also found that the normalised tangential velocity is exactly equal to 1 at the core radius r_c, whereas it is not the case for the different values of K_M mentioned before.

By normalising with $2\tilde{a}r_c$ and replacing $\tilde{a}/2\nu_e$ by K_M/r_c^2 in Burgers-Rott and Sullivan radial and vertical velocity components, dimensionless models were obtained solely dependent on r, r_c and z, with the Burgers-Rott model expressed as following:

$$\begin{cases}\overline{V_R} = -\dfrac{r}{2r_c} & \text{(2.13a)}\\[2ex] \overline{V_\theta} = 1.4\dfrac{r_c}{r}\left(1-\exp\left(-K_M\left(\dfrac{r}{r_c}\right)^2\right)\right) & \text{(2.13b)}\\[2ex] \overline{V_W} = \dfrac{z}{r_c} & \text{(2.13c)}\end{cases}$$

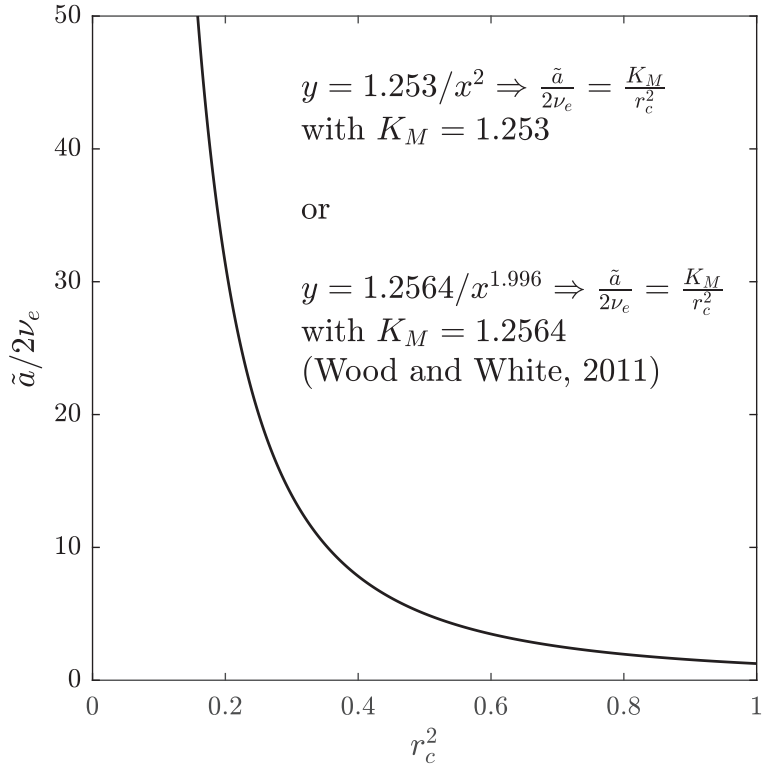


Figure 2.15: Variation of the ratio of suction strength and eddy viscosity as a function of the square of the core radius to determine the constant K_M as defined in Wood and White (2011).

and the Sullivan model expressed as following:

$$\begin{cases} \overline{V_R} = -\dfrac{r}{2r_c} + \dfrac{3r_c}{2K_M r}\left(1 - \exp\left(-K\left(\dfrac{r}{r_c}\right)^2\right)\right) & \text{(2.14a)} \\ \overline{V_\theta} = \left(\dfrac{r_c}{r}\right)^{2.4}\left(0.3 + 0.7\left(\dfrac{r_c}{r}\right)^{7.89}\right)^{-0.435} & \text{(2.14b)} \\ \overline{V_W} = \dfrac{z}{r_c}\left(1 - 3\exp\left(-K_M\left(\dfrac{r}{r_c}\right)^2\right)\right) & \text{(2.14c)} \end{cases}$$

Baker and Sterling model

Recently, Baker and Sterling (2017) developed a new wind field model to describe tornado-like vortices with a one and two-cell structure and it was derived from the following assumptions:

- Steady-state
- Inviscid
- Radial and vertical velocity dependent on the radial distance and the height
- Vertical velocity dependent on the height

The one-cell vortex dimensionless expression of the Baker and Sterling model is given by:

$$\begin{cases} \overline{V_R} = \dfrac{-4\overline{r}\overline{z}}{\left(1+\bar{r}^2\right)\left(1+\bar{z}^2\right)} & \text{(2.15a)} \\ \overline{V_\theta} = \dfrac{K\bar{r}\left[\ln\left(1+\bar{z}^2\right)\right]}{\left(1+\bar{r}^2\right)} & \text{(2.15b)} \\ \overline{V_W} = \dfrac{4\delta\ln\left(1+\bar{z}^2\right)}{\left(1+\bar{r}^2\right)^2} & \text{(2.15c)} \end{cases}$$

where $\overline{V_R} = V_R/V_{\theta,max}$, $\overline{V_\theta} = V_\theta/V_{\theta,max}$, $\overline{V_W} = V_W/V_{\theta,max}$, $\overline{r} = r/r_c$, $\overline{z} = z/z_{max}$, $\delta = z_{max}/r_c$, $K = S/0.347$. $V_{\theta,max}$ denotes the maximum tangential velocity, z_{max} the height where the maximum tangential velocity occurs, and S the swirl ratio. Unlike the different models detailed above, Baker and Sterling's model is a solution of the Euler equations. In the case of the Euler equations, the fluid is considered inviscid, and Runstedtler (2013) showed that for high Reynolds numbers, a viscous flow can be arranged in a way that viscous forces vanish and the flow behaves as

inviscid. Runstedtler (2013) also showed that inviscid arrangements are vortex-like and applicable to hurricanes or tornadoes. Baker and Sterling's model also uses dimensionless parameters to represent a single-cell structure with a height dependency for each velocity component. Only the vertical component of the Sullivan model is actually accounting for a dependency on both radial position and height.

The dimensionless pressure is obtained from the simplified Euler equations using the assumptions given above and the Equations 2.15, and is expressed as follows:

$$\overline{P} = -\frac{8\overline{r}^2\overline{z}}{\left(1+\overline{r}^2\right)^2\left(1+\overline{z}^2\right)^2} - \frac{4\cdot 15S^2\left[\ln\left(1+\overline{z}^2\right)\right]^2}{\left(1+\overline{r}^2\right)} - \frac{4\left[\ln\left(1+\overline{z}^2\right)\left(1-\overline{z}^2\right)\right]}{\left(1+\overline{r}^2\right)^2\left(1+\overline{z}^2\right)^2} \quad (2.16)$$

The main difference between the models discussed above is that each velocity component is a function of the radial distance and height. As a result, unlike the aforementioned models, the Baker and Sterling model includes a boundary layer. Since boundary layer wind data in full-scale tornadoes are still quite limited; it is difficult to assess the real benefit of expressing the boundary layer in analytical vortex models. However, including some representation of a boundary layer in the models is necessary to assess the viscous effects near the ground. Since tornadoes are rotational flows, it is unclear if the boundary layer depends on the location and wind direction and if the thickness varies from the tornado centre. The variation of the boundary layer thickness in tornadoes would then induce different wind loads on buildings. Baker and Sterling (2018) calculated the wind loading at the top of the boundary layer, but it is uncertain what the loading would be if considered lower or higher. Nevertheless, radial and tangential velocities in Baker and Sterling's model seem to better fit experimental data than the other models,

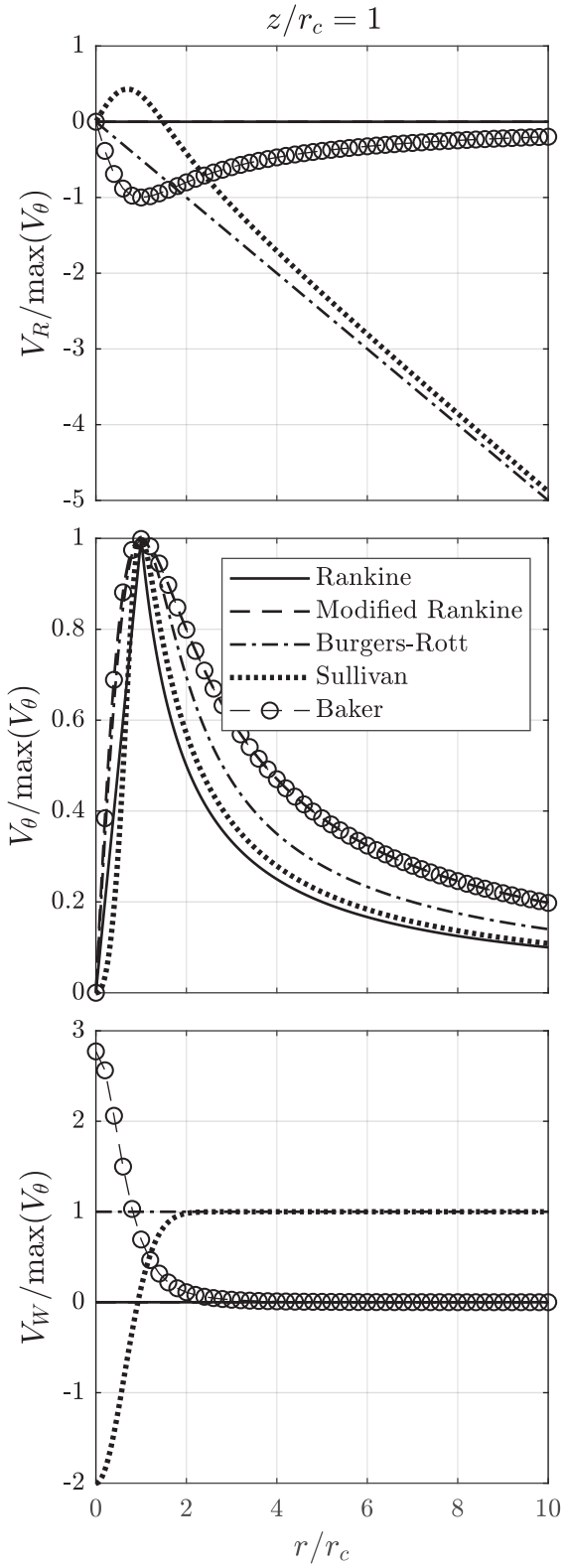


Figure 2.16: Radial profile of radial, tangential and vertical velocities at $z/r_c = 1$ for Rankine, modified Rankine, Burgers-Rott, Sullivan and Baker and Sterling analytical vortex models.

at least near the ground (Gillmeier et al., 2018) . The fact that the tangential and vertical velocities increase with height is a limitation of Baker and Sterling's model, knowing that maximal tangential velocities are typically found in the corner region.

2.3.3 Debris in tornadoes

Particle Tracking Velocimetry

Particle tracking velocity (PTV) is a discrete Lagrangian flow measurement technique which uses tracer particles to obtain an insight into the flow. The positions of the particles on an image can then be determined after careful calibration using intrinsic and extrinsic parameters of the cameras and the principle of triangulation. Recording consecutive images will determine the particle positions over time, with displacements determined by reconstructing the trajectory of individual particles. The particle velocities are then determined by deriving the particle displacements. Using stereoscopic imaging, it is possible to follow tracer particles in three dimensions over time and therefore quantify velocities in a specific volume of fluid.

Particle tracking was first developed in the 1950s with the examination of a low-speed turbulent jet using a stereoscopic imaging system with two cameras (Chiu and Rib, 1956). Turbulence research in a wind tunnel using particle tracking was first carried out by Snyder and Lumley (1971) using a single camera. Image digitisation has had a significant impact on the development of particle tracking methods. Manual measurements were not required anymore, and the development

of particle recognition and tracking algorithms has been supported by the digitisation. The first digitised images and image processing techniques were performed by Chang et al. (1985) to determine particle positions in three-dimensional flow fields. Since then, efforts have been made to track more simultaneous particles (Adamczyk and Rimai, 1988, Racca and Dewey, 1988, Nishino et al., 1989) but it was in the 90s that particle tracking methods radically changed with a completely new approach developed by the Institute of Geodesy and Photogrammetry at ETH Zurich (Papantoniou and Dracos, 1990, Maas et al., 1993, Malik et al., 1993). The mathematical model of photogrammetric 3D coordinate determination developed by Maas et al. (1993) included the different refractive indices in the optical path, which as a result significantly increased the accuracy of the 3D coordinate determination. Maas et al. (1993) also introduced the epipolar geometry to determine the particle coordinates for each camera. The principle of epipolar geometry is shown in Figure 2.17. A point M is seen by a stereoscopic system consisting of two cameras of projection planes π_1 and π_2 and projection centres O_1 and O_2. m_1 and m_2 are the projections of M onto the projection planes π_1 and π_2, respectively. The line (O_1O_2) defines the baseline of the epipolar plane. The projection of the points M and m_1 onto the projection plane π_2 defines the epipolar line e_2, and vice-versa for the epipolar line e_1. By overlaying the projection plane π_1 and π_2 and by knowing the intrinsic and extrinsic parameters of the cameras, it is possible to determine the 3D coordinates of the point M at the intersection of the epipolar lines e_1 and e_2.

The stereoscopic system can also be extended to more than just two cameras, increasing the accuracy and reducing the ambiguity of the intersecting epipolar

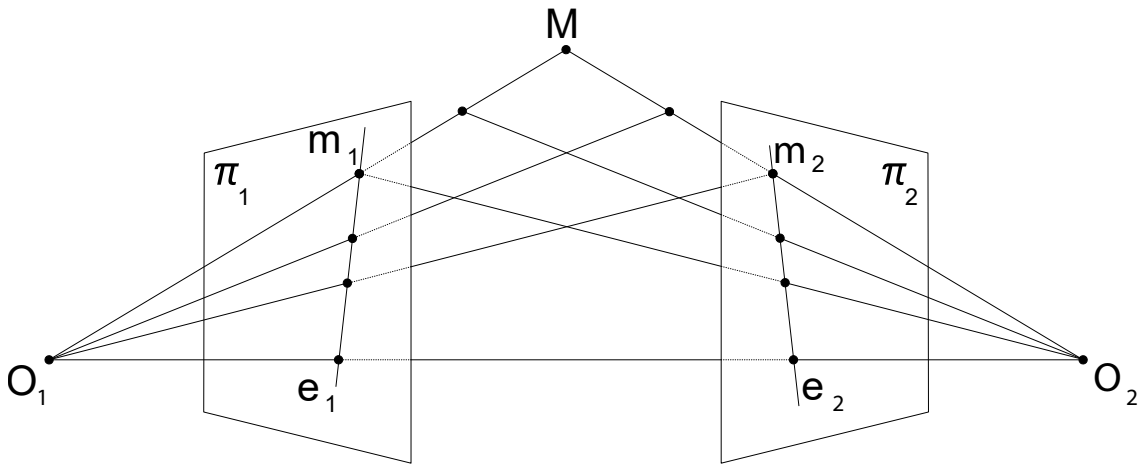


Figure 2.17: Stereoscopic system and epipolar lines.

lines. Maas et al. (1993) examined the influence of the number of cameras and their respective locations on the accuracy of the epipolar correspondences. Malik et al. (1993) then developed the fully automated tracking algorithm to determine the sequence of velocity vectors over time in a three-dimensional flow field. Therefore, the particle tracking method developed by the research group at ETH Zurich has shown to be a robust and accurate technique to characterise the observation volume of fluid flow. Since then, the technique has been used on numerous occasions to study turbulent flow (e.g. Luthi et al., 2005), vortex-like flow field (e.g. Shnapp and Liberzon, 2015) or flow structure in water channels (e.g. Akutina et al., 2018).

Compared to common measurement techniques, such as hot-wire anemometry, multi-hole probes or sonic sensors, PTV has the advantage of being non-intrusive and therefore does not disturb the flow. It also allows measuring at different scales, from silicon microchannels (Kolaas et al., 2013) to large-scale indoor flow (Biwole et al., 2009). Instantaneous and averaged velocities over large-scale flow fields can be determined with relatively good accuracy and spatial resolution. The

Lagrangian approach also gives a better estimation of the 3D velocity vectors compared to particle image velocimetry (Bown et al., 2006). Nonetheless, 3D-PTV also has limitations. The density of tracer particles in the flow has a significant influence on the quality of tracking, with high density leading to correspondence issues due to overlapping particles. Therefore, the tracer particles size matters as well as the density and ideally, the tracer particles would have neutral buoyancy. For large-scale indoor flow, helium-filled soap bubbles (HFSBs) are typically used as neutral buoyancy tracers (Kerho and Bragg, 1994, Bosbach et al., 2009). However, since HFSBs are empty, extensive lights must be used to ensure tracer visibility (Fu et al., 2015). High-speed cameras are also required for high velocity and/or turbulent flow to ensure good flow field characterisation. The limitation with cameras is if the frame rate is not high enough, the tracers will be seen as streaks and will lead to particle identification and correspondence issues. However, by adapting the particle tracking algorithm, it is possible to retrieve 3D motion from streaks, commonly known as Particle Streak Velocimetry (Wang et al., 2017). Finally, it is worth noting that PTV has to date frequently been used to determine flow characteristics but has not really been used to investigate the motion of individual particles.

Debris

In the 1970s, assessing the risk of flying debris on nuclear power plants embedded in tornadoes motivated the modelling of debris' behaviour. Debris flight models were then at that time extremely simplified and only considered the drag forces (McDonald et al., 1974) or drag and lift forces (Lee, 1974). Subsequently, an effort has been made by researchers to understand the forces involved during the flight of

debris. Tachikawa (1983) extensively studied the flight of square and rectangular flat plates in a wind tunnel and compared the trajectories with trajectories from integrated equations of motion. Tachikawa expressed the equation of motions in a dimensionless way which features an important parameter for the flight of debris:

$$K = \frac{\rho_a U^2 A}{2mg} \tag{2.17}$$

with ρ_a the air density, U^2 the wind speed, A the frontal area of the debris, m the mass of the debris and g the gravity acceleration. The parameter K, which represents the ratio of aerodynamics forces to the gravity forces, has subsequently been named Tachikawa number (Holmes et al., 2006). A small K describes heavy/small debris when a large K describes light/large debris. Tachikawa (1988) then developed a methodology to estimate the range of debris trajectories. Using photogrammetry, Tachikawa collected the distribution of trajectories for different debris type over a range of Tachikawa numbers and identified the debris and wind characteristics influencing the trajectories, using the probability density function of the lift coefficient. McDonald (1990) identified 2 x 4 inches timber planks and 3 inches diameter steel pipes to be the most common type of debris found in tornado paths in the U.S.A. Impact tests concluded that for tornado winds higher than 80km/h, conventional house walls in the U.S., excluding brick veneer walls, cannot resist timber planks and steel rods. Wills et al. (2002) classified windborne debris types into three categories based on their shapes and aerodynamic properties: compact, rod and plate debris. Compact debris consists of three-dimensional debris with similar length for all dimensions, while rod and plate debris have one dimension larger and smaller than the others, respectively (Figure 2.18).

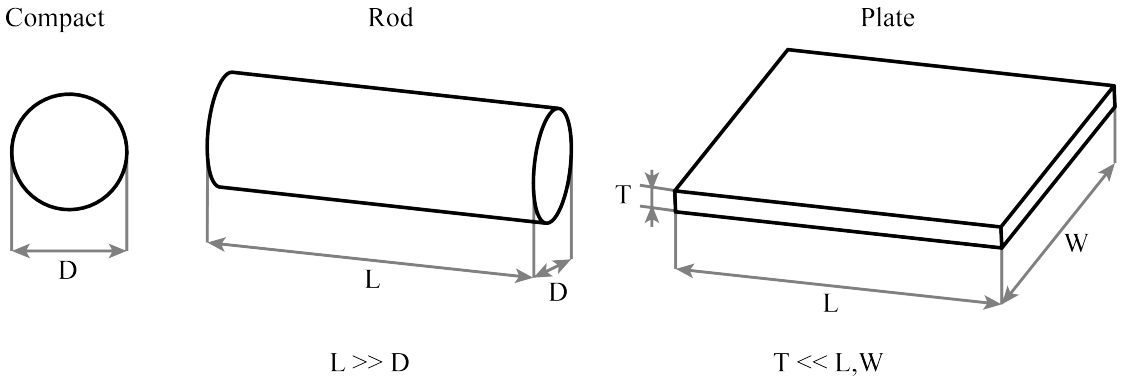


Figure 2.18: Debris classification (Wills et al., 2002).

Compact debris in horizontal winds have been investigated numerically by Holmes (2004) and including the vertical air resistance led to the following equations for the horizontal and vertical acceleration of the debris:

$$\begin{cases} \dfrac{\mathrm{d}V_{U,d}}{\mathrm{d}t} = k\sqrt{\left(V_U - V_{U,d}\right)^2 + V_{W,d}^2}\left(V_U - V_{U,d}\right) & \text{(2.18a)} \\ \dfrac{\mathrm{d}V_{W,d}}{\mathrm{d}t} = k\sqrt{\left(V_U - V_{U,d}\right)^2 + V_{W,d}^2}\left(-V_{W,d}\right) - g & \text{(2.18b)} \end{cases}$$

where $k = \rho_a C_D / 2\rho_d l$ is the buoyancy parameter, ρ_a and ρ_d the air and debris densities, respectively, V_U the horizontal wind speed, $V_{U,d}$ and $V_{W,d}$ the horizontal and vertical debris velocities, respectively, C_D the drag coefficient, l the debris characteristic length. Holmes also introduces turbulence to the flight equations to add up variability to the trajectories. It was found that adding vertical air resistance has a significant impact on the flight characteristics. However, adding turbulence modifies the flight trajectories, even though it does not considerably affect the overall trajectories. A new approach to debris flight equations has been undertaken by Baker (2007) to study both compact and plate debris. Baker expressed the dimensionless debris flight equations that feature three dimensionless

parameters that characterise the debris flight:

$$\begin{cases} \Omega = \dfrac{mg}{0.5\rho_a A U^2} & \text{(2.19a)} \\ \Delta = ml^2/I & \text{(2.19b)} \\ \Phi = \dfrac{0.5\rho_a A l}{m} & \text{(2.19c)} \end{cases}$$

where m is the debris mass, g the gravity acceleration, ρ_a the air density, A the debris surface area, U the reference wind velocity, l the debris characteristic length and I the moment of inertia. The parameter Ω is the reciprocal of the Tachikawa number (K) and Δ is considered constant for a square or rectangular plate (Tachikawa, 1983). The parameter Φ acts similarly to the buoyancy parameter in Holmes' equations and was mainly found to be governing the flight of compact debris. Results from Baker's flight equations also compare well with experimental and numerical works undertaken by Wills et al. (2002) and Holmes (2004), respectively. It only showed little underestimation (12%) from Wills et al. calculations due to the absence of vertical air resistance in the equations. Another parameter to consider with windborne debris is the Froude number. The Froude number is the ratio of inertial and gravitational forces, and is defined as:

$$Fr = \frac{U}{\sqrt{g d_{debris}}} \tag{2.20}$$

where U is the reference wind velocity, g is the gravity acceleration and d_{debris} the debris diameter. Karimpour and Kaye (2012*b*) showed that the Froude number is an important parameter during the motion initiation of loose-laid debris.

Additional work has been undertaken to investigate the flight of windborne debris from different perspectives, with numerical and experimental investigations of the 3D motion of plate type debris (Richards et al., 2008, Kordi and Kopp, 2011, Richards, 2012) and Monte Carlo simulations to study the stochastic nature of windborne debris (Karimpour and Kaye, 2012*a*). However, all these researches were concerned with windborne debris subjected to uni-directional winds. To date, very little research has been undertaken on windborne debris in rotational flow, such as tornadoes or even dust devils. In the late 1970s, Twisdale et al. (1979) and Dunn and Twisdale (1979) developed a wind field model and performed an analysis of tornado missile transport using a 'random orientation 6-degree of freedom' 3D model including drag, lift and side forces. Comparison with a '3-degree of freedom missile transport' model (Simiu and Cordes, 1976) suggested that simpler models are possibly not conservative in predicting the impact of debris ranges and velocities.

After a quiet period, interest in the study of windborne debris in tornadoes increased with Sassa et al. (2009) who examined the motion of debris in a travelling tornado. Using a translating tornado simulator, Sassa et al. recreated the spiral pattern, which is usually observed with deposited debris in full-scale tornadoes. However, the simplicity of the tornado simulator does not allow any kind of full-scale comparison or any understanding of the debris motion. Maruyama (2011) conducted numerical, large-eddy simulations (LES) of a tornado-like vortex and calculated the three-dimensional motion of two different compact debris types. Although two-way interactions between wind and debris are not considered in the transport model, debris trajectories show larger deviations when released from the

core vortex location. However, the simulated vortex flow field is considered stationary, but a translation velocity is added into the flight equations. It is difficult to evaluate the real effect of this translation velocity as the translation disturbs the tornado flow field symmetry and shear stress generated due to roughness interaction increases the turbulence (Liu and Ishihara, 2016). Noda et al. (2013) also conducted LES simulations and debris flight analysis but focused on 6 DOF motion simulations of plate type debris for different scales, swirl ratios and wind speeds. The falling distance was found to be dependent on the Tachikawa number, the Froude number and the swirl ratio but also debris cloud inevitably forms due to the equilibrium of all forces acting on the debris.

Baker and Sterling (2017), based on the work of Baker (2007), developed the debris flight equations for tornado application. Compared to other flight equations, Baker and Sterling's equations include a centrifugal force term in the radial acceleration equation, but also feature two dimensionless parameters governing the debris flight:

$$\Phi_T = \frac{0.5\rho_a A r_m}{m} C_D \tag{2.21}$$

$$\Psi_T = \frac{g r_m}{u_m^2} \tag{2.22}$$

where r_m is the core radius and u_m the maximum tangential velocity. The parameter Φ_T is similar to the buoyancy parameter found in Holmes (2004) and Baker (2007). Baker and Sterling (2017) show that the parameter Φ_T is a function of the swirl ratio and defines whether a debris flies or falls (Figure 2.19). For small Φ_T, the debris flies up and then down (Figure 2.19 (b)) while for large Φ_T, the debris flies up and reaches an equilibrium height (Figure 2.19 (a)). Additionally,

the parameter Ψ_T is the inverse Froude number, and the ratio Φ_T/Ψ_T gives the Tachikawa number.

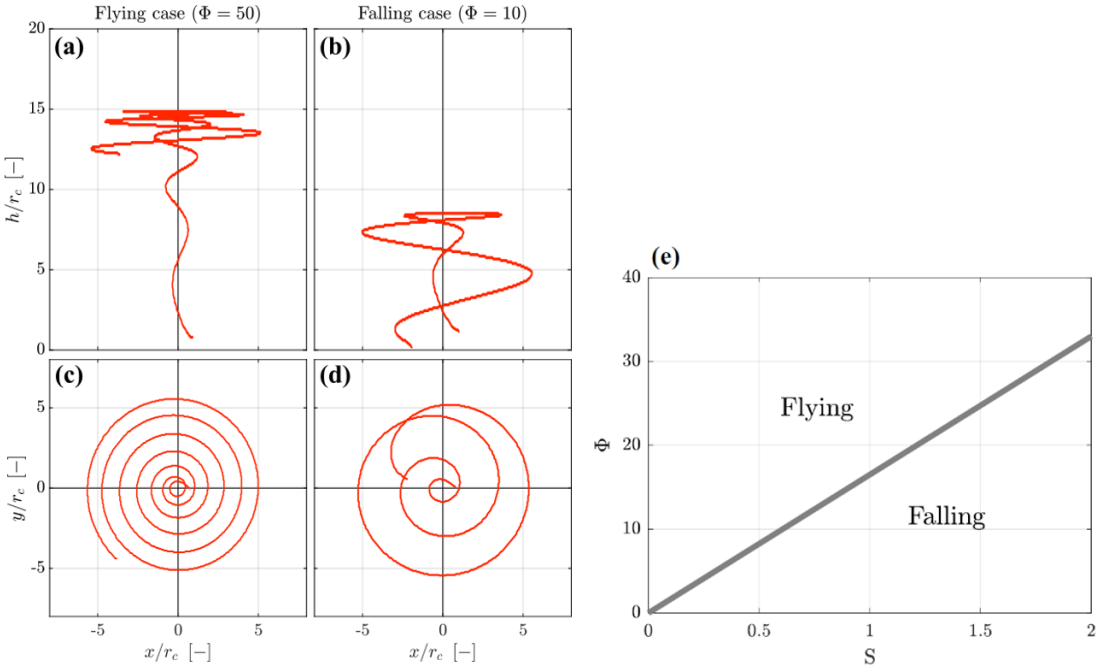


Figure 2.19: Debris flight trajectories using Baker and Sterling's model for (a&c) flying and (b&d) falling debris, (e) Flying and falling Φ_T parameter as a function of the swirl ratio S (adapted from Baker and Sterling (2017).

Finally, Baker and Sterling (2018) used their tornado wind field (Equations 2.15) to develop a conceptual design framework for wind and debris impact loading from a moving tornado. Although the model could be used for structural designs to estimate loading under different types of tornado winds, the model requires better experimental and full-scale tornado knowledge to be applied to substantial structural analysis.

Scaling issues

Davies-Jones (1973) introduced with his dimensionless analysis the aspect ratio, swirl ratio and radial Reynolds number to be the main parameters governing the physical simulation of tornado-like vortices in laboratories. However, scaling these parameters up to a full-scale tornado has been one of the biggest challenges for the modelling of tornadoes. Also, although tornado simulators have essentially been used to better understand the tornado winds, they also have been used to study wind loads on buildings at model scales. In wind tunnel studies, a scaling factor is usually based on the simulated boundary-layer (Schlichting and Gersten, 2000) but in tornado simulators, geometric, kinematic and dynamic similarities would ideally have to be achieved to determine a proper scaling ratio. Baker and Sterling (2019) showed that to date none of the current tornado simulators are capable of generating tornado-like vortices with good full-scale similarities. The authors defined parameters for geometric, kinematic and dynamic groups as well as small, medium and large arbitrary tornado sizes and maximum tangential velocity to establish the similarities. The WindEEE dome (Refan and Hangan, 2018) is the only simulator showing scaling can be achieved in all three groups with a small full-scale tornado. Nevertheless, most of the tornado simulators can reproduce geometric scaling for small and medium tornadoes but mostly fail to reproduce kinematic and geometric scaling for any tornado types. Moreover, even though geometric scaling can be achieved, Gillmeier et al. (2018) showed that the physical size of the simulator matters. By comparing a small and medium scale simulator with similar aspect ratio and swirl ratios, Gillmeier et al. (2018) showed that the flow fields were influenced by the size and significantly different. Therefore,

two similar tornado simulators with geometric similarities could show disparities between their respective flow fields.

Nevertheless, tornado-like flow fields, either experimental, numerical or analytical, are commonly normalised by the size of the core radius, r_c (e.g. Haan et al., 2008, Mishra et al., 2008*a*, Wood and White, 2011, Noda et al., 2013, Ishihara and Liu, 2014, Baker and Sterling, 2017, Gillmeier et al., 2018, Refan and Hangan, 2018). Normalising using the core radius allow defining a scaling factor, although it is usually defined against a specific full-scale tornado. For instance, Mishra et al. (2008*a*,*b*) compared experimental data with the Manchester tornado (Lee and Samaras, 2004) and obtained a scaling factor of 1:3500. In the United States, average house size is about 201 m^2; assuming a two-story house with 3m height ceilings, the full-scale house size would be $10 \times 10 \times 6$m while the model size would be about $3 \times 3 \times 2$mm. At that scale, no physical measurements can be undertaken. A more reasonable scaling factor can be achieved by building larger tornado simulators, such as the WindEEE dome, with simulated tornado-like vortices with geometric scaling factors from 1:10 to 1:100 (Refan and Hangan, 2018).

When examining the flight of debris, it is important that the geometric scale, as well as the mass scale, is considered. The Tachikawa number (Holmes et al., 2006), which represents the ratio of aerodynamic to gravity forces, can be used to define a Tachikawa scale factor λ_K (Crawford, 2012) such as:

$$\lambda_K = \frac{K_{exp}}{K_{FS}} = \frac{V_{\theta,exp}^2}{V_{\theta,FS}^2}\frac{A_{exp}}{A_{FS}}\frac{m_{FS}}{m_{exp}} = \lambda_V^2\lambda_L^2\frac{1}{\lambda_M} \tag{2.23}$$

where λ_V and λ_L is the dynamic and geometric scaling factors, respectively. Assuming similarity between experimental and full-scale, i.e. $\lambda_K = 1$, a mass scale factor can be expressed as:

$$\lambda_M = \lambda_V^2 \lambda_L^2 \tag{2.24}$$

Tachikawa scaling is used in section 4.4 to estimate the equivalent full-scale debris size for debris used in the tornado simulator.

2.4 Research gap

Due to their unpredictability and their danger, full-scale tornadoes are difficult to study, and it is particularly complex to obtain full-scale data. Therefore, recourse to physical, numerical or analytical models is often made in order to elucidate the complex flow field of tornado-like vortices. However, to date, little attention has been given to the flight of windborne debris in tornado-like flow fields. It is therefore not surprising that only a little can be found in the literature focusing on windborne debris and tornadoes. Experimental studies are extremely limited (e.g. Sassa et al., 2009), and most of the studies were carried out numerically (Maruyama, 2011, Noda et al., 2013) or analytically (Baker and Sterling, 2017, 2018).

This research work aims to provide some insight into the flying behaviour of debris in tornado-like flow fields. To that extent, physical and numerical modelling have been carried out to explore the flight of debris. Wind measurements and debris flight trajectories were obtained experimentally in the tornado simulator, and debris trajectories were calculated numerically using experimental and analytical tornado-like flow fields. The different methodology developed in this research work will benefit the tornado research community to investigate windborne debris in tornadoes further, and the results assess some aspects of flying behaviour of debris in tornadoes.

Chapter 3

Physical simulation of tornado-like vortices at the University of Birmingham

3.1 Introduction

In this chapter, the University of Birmingham Tornado-like Vortex Generator was used to physically simulate and characterise the flow field of different tornado-like vortices. This chapter aims to give a global picture of the tornado simulator and its flow properties in order to better understand in the next chapters the type of flow fields that debris are subjected to. Thus, a general overview of the simulator is given in section 3.2. Section 3.3 presents and discusses the flow visualisation experiments which were undertaken for different swirl ratios. The methodology and techniques to characterise the wind field using a traverse system and a Cobra probe are described in section 3.4. Section 3.5 and 3.6 present the results of the flow mappings for different swirl ratios. The flow mappings show significantly more complex flow structures than initially expected. Horizontal velocity profiles are presented and compared with analytical vortex models in section 3.7. Vertical profiles at different radial locations inside the simulator are presented in section

4.8. Finally, concluding remarks about the physical simulation of tornado-like vortices in the University of Birmingham Tornado-like Vortex Generator are given in section 3.9.

3.2 University of Birmingham Tornado-like Vortex Generator (UoB-TVG)

The University of Birmingham Tornado Vortex Generator (UoB-TVG) is a medium-scale Ward-type simulator (Ward, 1972) built in the Civil Engineering Laboratories (Figure 3.1). It consists of two chambers, a trapezoidal duct and a series of identical fans. Flow rotation is introduced by means of guiding vanes, located in the convergence chamber in the lower part of the simulator. The convergence chamber is 1m high, 3.6m wide and 30 guide vanes are equally spaced around the chamber. Each guide vane angle (θ) (Figure 3.2) is set individually using a protractor from

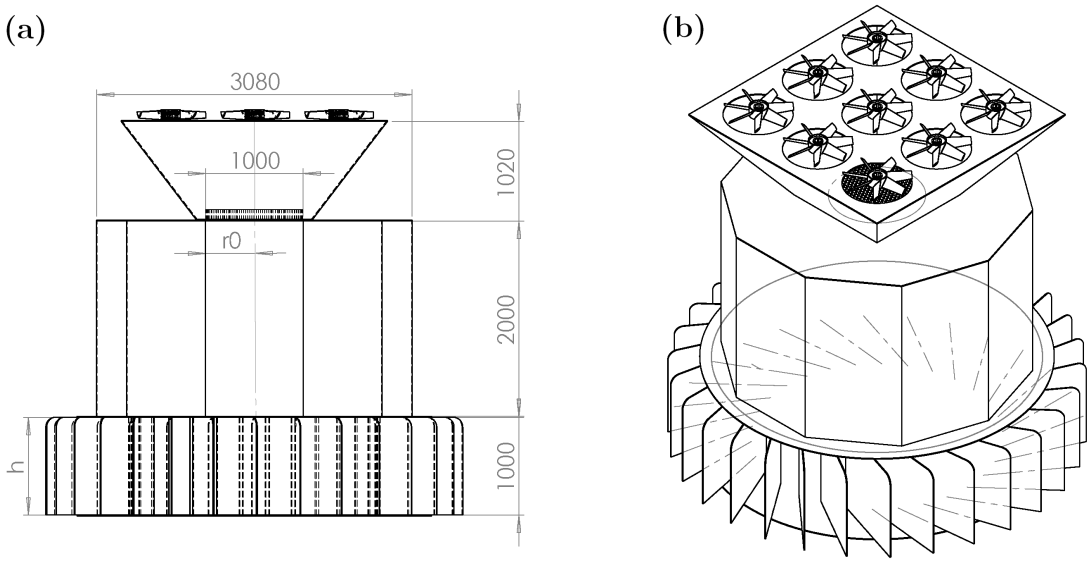


Figure 3.1: (a) Vertical-cross section and (b) iso-view of the University of Birmingham Tornado-like Vortex Generator (UoB-TVG)

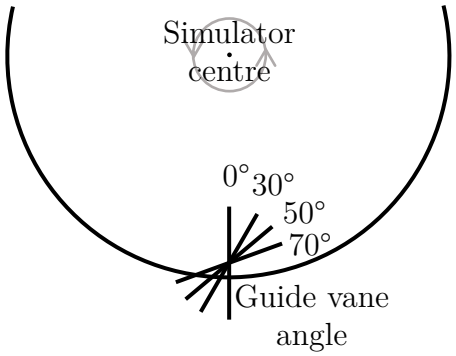


Figure 3.2: Guide vane angle θ

0 to 70 degrees. The convection chamber sits on top of the convergence chamber and is 2m high, 3.1m diameter and has an octagonal shape. The updraft hole is located on top of the convection chamber. The updraft hole has a radius (r_0) of 0.5m and is connected to the trapezoidal duct via a 0.1m thick honeycomb section. The honeycomb is placed in order to help remove fan induced rotation in the flow (Ward, 1972). For an inflow height (h_0) of 1m and an updraft hole radius (r_0) of 0.5m, the aspect ratio a ($= h_0/r_0$) is equal to 2. For the scope of this thesis, three vane angles, 30°, 50° and 70° were chosen to simulate tornado-like vortices in the UoB-TVG. The vanes angles and corresponding swirl ratios (Equation 2.1) are given in Table 3.1. The higher the swirl ratio, the more angular momentum is introduced, therefore the highest rotational wind speeds are to be expected.

Nine axis flow fans (Ziehl-Abegg, 2010) (Figure 3.1) sit on top of the trapezoidal duct into a three by three fan arrangement. Each fan has a theoretical flow rate of 3.67×10^2 m^3/s giving a theoretical flow rate through the updraft hole of 3.30×10^3 m^3/s. Therefore, assuming no loss and uniformity through the honeycomb, a maximum updraft of around 17 m/s would be expected. In order to control the fans, bespoke software was used to control the fans speed via RS232

Table 3.1: Vane angles and corresponding swirl ratios used to simulate tornado-like vortices in the UoB-TVG.

Vane angle θ (°)	Swirl ratio ($= \tan\theta/2a$)
30	0.13
50	0.30
70	0.70

communication. The software requires the total fans power as an input; therefore, point measurements are necessary to determine the required wind speed.

3.3 Flow visualisation

In order to help picture the simulated vortices in the UoB-TVG, a series of flow visualisations using smoke were undertaken. The smoke was generated using a water-based smoke machine, and different approaches were employed to obtain qualitative flow field information. The first approach was to place the smoke machine directly inside the simulator and release the smoke near the surface. This approach was not considered satisfactory since the smoke machine was positioned far away from the core vortex to avoid any disturbance. Thus, the smoke tended to quickly dissipate, and no vortices were visualised for any low swirl ratio. Therefore, an alternative approach was adopted, which consisted of releasing smoke inside the core vortex with the smoke generator connected to the simulator's surface via a length of tubing. Different locations were tried, and the only location where the smoke did not dissipate quickly was the centre of the simulator. Therefore, Figure 3.3 shows the flow visualisations obtained from the video footage recorded with a

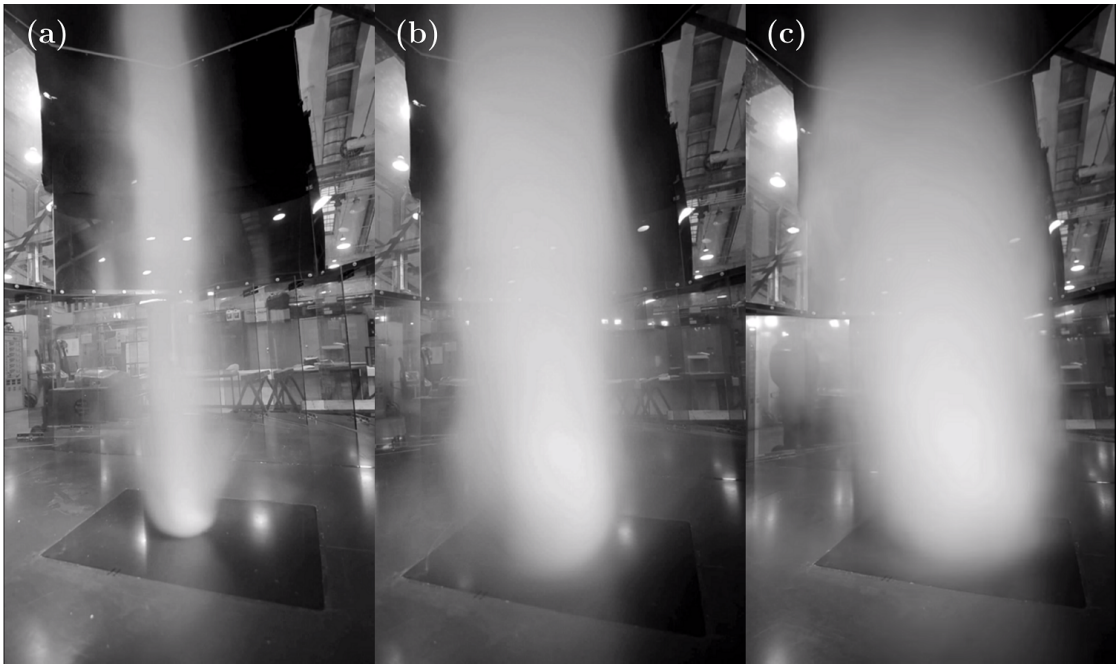


Figure 3.3: Flow visualisation for different swirl ratio (a) $\theta = 30°$ - $S = 0.13$ (b) $\theta = 50°$ - $S = 0.30$ (c) $\theta = 70°$ - $S = 0.70$

camera placed inside the simulator and for three different swirl ratios ($S = 0.13$, 0.3 and 0.7). As noted in the previous section, the higher the vane angle, the greater the swirl ratio and thus the stronger the vortex. For $S = 0.13$, the visualisation shows an increase in the vortex size close to the ground and a relatively constant size upwards (Figure 3.3 (a)). The time-evolving nature of the visualisations helped to show the large vortex wandering for this swirl ratio (not shown in the still images of Figure 3.3 (a)). A small wandering of the vortex can be described as a low displacement of the vortex centre while a large wandering shows the significant visual displacement of the vortex centre around the simulator's central position. For $S = 0.3$, the core vortex increases in size and appears almost twice as large as for $S = 0.13$ but less defined (see Figure 3.3 (a)). The flow also became more turbulent near the surface but seems to wander less with the vortex's central

position moving slightly around the simulator's central position. For $S = 0.7$, the core vortex broadened with the result that no discernible flow structure was able to be identified (3.3 (c)). High-speed recordings of the smoke from the end of the tube showed that near the ground and inside the vortex, the smoke was initially drawn towards the centre and then flowed vertically downwards and away from the core. At this stage, this was the first indication of a possible presence of a turbulent core associated with a downdraft. The downdraft was slightly visualised for high swirl ratios when the smoke was introduced inside the core vortex at different heights. However, the phenomenon was transient and therefore obtaining a clear picture was difficult.

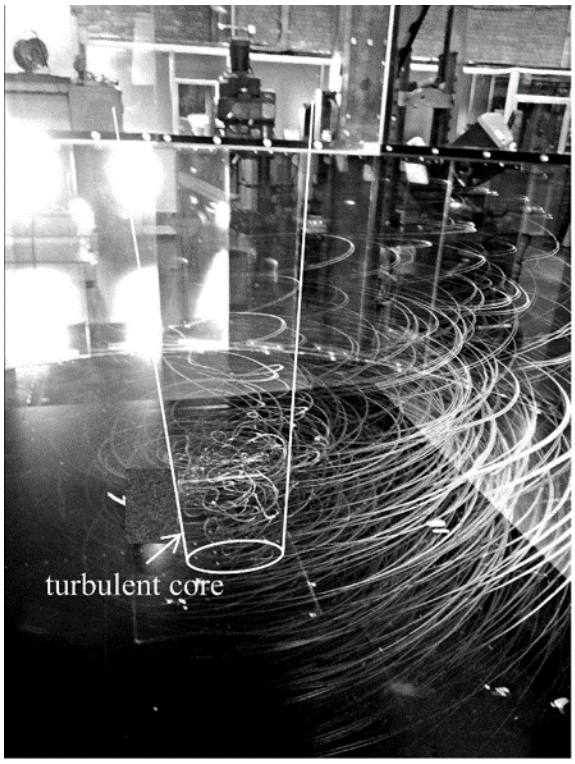


Figure 3.4: Flow visualisation using soap bubbles depicting the turbulent core for $S = 0.70$.

Overall, the use of flow visualisation in the present case was not ideal in terms of identifying flow structures, unlike that observed by others (Ward, 1972, Church et al., 1977, Refan and Hangan, 2018). However, the use of flow visualisation showed the potential presence of a downdraft, which was later identified via velocity measurements and is discussed in section 3.6. The use of helium-filled soap bubbles, as introduced in section 3.3, may have helped to identify the possible evolution of the vortex structure with the increase of the swirl ratio. Since a helium-filled soap bubble machine was not available, flow visualisation using normal soap bubbles was carried out using a simple bubble generator. A long-exposure picture was taken for $S = 0.7$ to show the motion of the soap bubbles (Figure 3.4). The picture clearly depicts the turbulent characteristics of the core vortex, while outside the core vortex the soap bubbles appears to be mainly moving tangentially.

3.4 Mapping methodology

3.4.1 Cobra probe

Mean flow velocities were measured inside the UoB-TVG using a Turbulent Flow Instrumentation (TFI) Series 100 Cobra probe (TFI, 2011). The Cobra probe is a 4-hole pressure probe measuring the 3D velocity components and local static pressure (Figure 3.5). The probe can measure data with a magnitude of velocity vector greater than 2 m/s within a cone of influence of $\pm$ 45°. Data obtained with the probe are given with a velocity, direction and static pressure accuracy within 0.5 m/s, 1° and 5 hPa, respectively. For the current work, the velocity uncertainties are taken to be $\pm$ 0.5m/s for the tangential velocity and $\pm$ 0.2m/s for the radial and vertical velocity (Gillmeier et al., 2018). The Cobra probe is provided from TFI

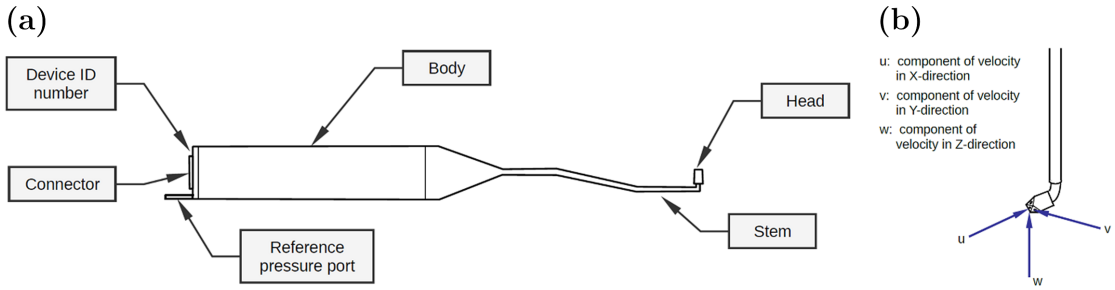


Figure 3.5: (a) Schematic and description of a TFI Cobra probe – (b) Wind velocity coordinates with a TFI Cobra probe (TFI, 2011).

fully calibrated for its own specific velocity and frequency range but still requires a zero-wind calibration to correct any temperature fluctuation and/or possible electrical noise. This 'zero' is by default required every two hours by the TFI Device Control software but could be performed between each point measurement if necessary. A TFI interface unit is used to power the Cobra probe and log data onto a computer via a USB connection. 3D velocities are calculated by the TFI Device Control software using pressure measured on the probe head. Therefore, a reference pressure is required to ensure the correct pressure measurement. For the present work, a 0.0015m nylon tube is connected to the Cobra probe reference port and is measuring atmospheric pressure outside the simulator.

The data were recorded using a TFI Data Acquisition (DAQ) box at a sampling rate of 100 Hz for 80s. Gillmeier (2019) performed a convergence analysis and showed that in the UoB-TVG, a sampling rate of 80s at 100 Hz was sufficient to ensure that the time averaged velocity has converged towards a stationary value.

3.4.2 Traverse system

The Cobra probe was mounted on an in-house built bidirectional traverse system, specifically designed to be used in the simulator (Figure 3.6). The traverse system

consists of two vertical aluminium supports and a 2m aluminium horizontal linear rail which a carriage, supporting the probe, slides along. A nut/lead screw system is mounted on the carriage allowing the carriage to slide along the linear rail when the lead screw is rotated. Finally, a stepper motor is attached to the lead screw to accurately move the probe to the individual positions in the simulator. A stepper motor is a brushless electric motor which rotates accordingly to the electrical pulses applied to its coils. The minimum angle of rotation is called a step and is given by applying electrical pulses to the different coils inside the motor. Common stepper motors have 48, 100 or 200 steps per revolution.

The stepper motor is controlled using an Arduino Uno micro-controller board and an Arduino Motor Shield. Arduino is an open-source hardware and software project (Arduino, 2011), developed to easily interface external components and prototype interactive objects. Supplied with its own compiler, libraries and code examples, self-programming codes can very easily be developed using C/C++ programming language. The Arduino Uno is connected to the host computer via a USB cable and can be either supplied via USB or with an external power supply when more power is required. For the present work, an external 9V power supply was required to drive the stepper motor. The motor speed, motor step and direction are specified by the user before compilation. After compilation, the code is uploaded onto the Arduino flash memory and automatically starts once the board is powered on.

The stepper motor used here makes a full rotation with 200 steps and therefore rotates 1.8° per step. The lead screw used with the traverse system has a lead of 0.002m, giving a horizontal displacement per pulse of:

$$dx = \frac{\text{step angle}}{360^{\circ}} \times \text{ screw lead } = \frac{1.8}{360} \times 0.002 = 0.0001\text{m/step} \qquad (3.1)$$

Thus, for every pulse sent by the motor shield, the carriage is theoretically moving along the rail by 0.0001m, i.e. 0.1mm, giving an extreme precision to the traverse system. However, the drawback to a stepper motor is the lack of feedback to ensure the motor rotated accordingly. If the torque required to move the carriage is too high, the motor will most likely miss steps leading to positioning errors. Nevertheless, after repetitive forward/backward movements, the traverse system has shown accuracy of less than 1mm for short and long distances, which is consistent with previous studies of tornado-like vortex flow fields using a traverse system (Mishra et al., 2008*a*). Finally, the motor speed was set up at 150 pulse/s, which translates into a linear speed of 1.5 mm/s.

Once the code is uploaded onto the flash memory, the traverse system can be controlled by entering the distance required to move, either via the Arduino Software using the Serial Monitor or by setting up a serial port communication. However, this method was laborious when mapping a significant portion of the flow field in the UoB-TVG. Therefore, a LabVIEW (NI, 1986) program was developed to facilitate the velocity measurements in the simulator using the traverse system. The program automatically performs the horizontal mapping at a specific height by acquiring and saving the data and moving the probe to the specified next position. The program merges the manual data acquisition using the TFI software and the manual control of the traverse system using the Arduino software. The libraries were supplied by TFI and can be used to configure the sampling as well as acquire and process the data on LabVIEW, C/C++ or MATLAB.

3.5 Flow rate and radial Reynolds number

To estimate the flow rate (Q) through the simulator and therefore the radial Reynolds number, it is necessary to measure the outflow velocities at the updraft hole. As noted in section 3.3, the updraft hole connects the convection chamber and the trapezoidal duct via a 1m diameter honeycomb. The traverse system was used and placed inside the convection to measure the outflow, as shown in Figure 3.6. For practical reasons and assuming all the fans have a similar and constant mass flow rate, a single profile along the updraft hole was performed to estimate the mass flow rate. Measurement points were carried out every 0.05m for a sampling duration of 180s and at a sampling rate of 100 Hz. The mean outflow velocities profiles for $\theta = 0°, 30°, 50°$ and $70°$ (i.e. $S = 0$, 0.14, 0.3 and 0.7) are plotted in Figure 3.7.

For $\theta = 0°$, i.e. $S = 0$ and no swirling flow, the flow is reasonably constant along the updraft hole with velocities at around 11 m/s but with a low asymmetry on the left side and a difference of about 1 m/s between each end. For $\theta = 30°$, the profile shows strong similarities with the profile obtained for $\theta = 0°$. However, a reduction in velocity is developing in the centre of the updraft hole where data quality (i.e. the ratio of the number of good and total samples) is dropping under 75%, and a slightly higher asymmetry is emphasised. As the vane angle increases, the velocities reduce further, even more in the centre. The velocity reductions observed in Figure 3.7 are more likely to be associated with the development of a downdraft at the centre of the simulator.

To ensure an accurate estimation of the flow rate through the simulator, only the case $\theta = 0°$ was considered. For higher vane angles, the velocities and data quality

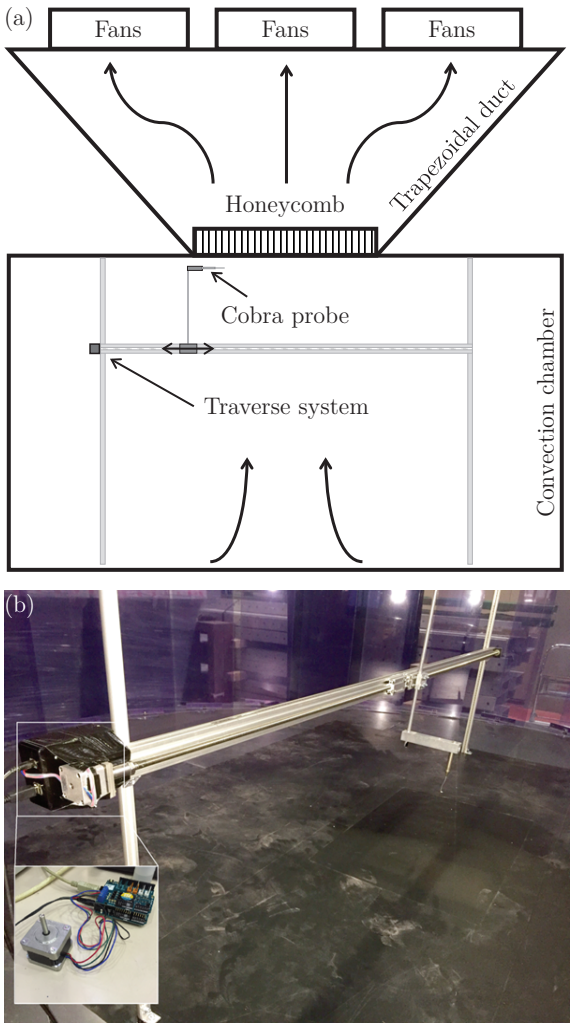


Figure 3.6: (a) Sketch of the simulator's upper half with the traverse system mounted to measure the outflow - (b) Traverse system inside the simulator while at prototype stage.

drop in the centre of the tornado, which could lead to an underestimation of the flow rate and consequently also the radial Reynolds number. The flow rate through the simulator is expressed as follows:

$$Q = \pi r_0^2 \left(\frac{1}{N} \sum_{p=1}^{N} V_p \right) = \pi r_0^2 \tilde{V} \tag{3.2}$$

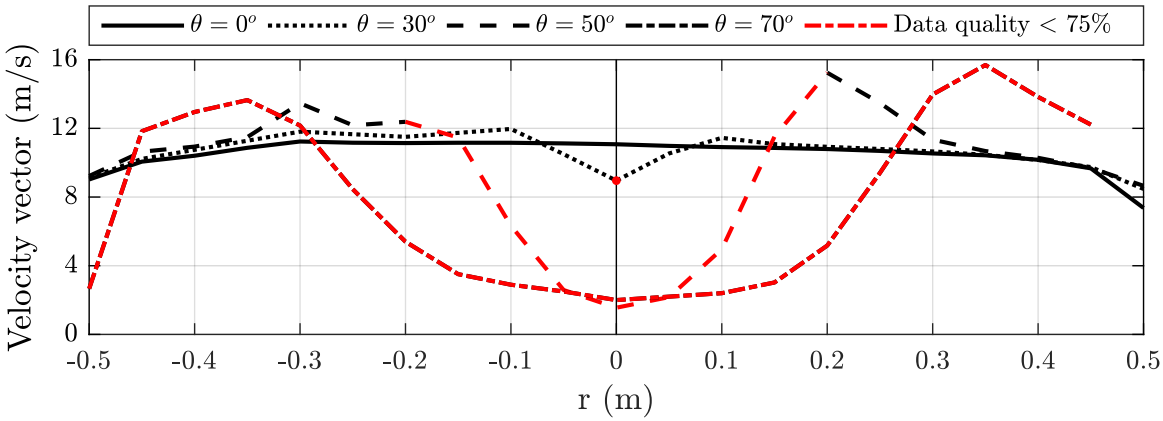


Figure 3.7: Outflow velocities profiles at the top of the convection chamber for $\theta = 0°$ (plain), 30° (dotted), 50° (dashed) and 70° (dash-dotted). The red colour outlines when the data quality is lower than 75%.

where $\tilde{V}$ is the spatially averaged velocity of the point measurements. Given an averaged velocity of 10.5m/s at the updraft hole, the flow rate through the simulator was estimated to be $4.93 \times 10^2 \mathrm{m}^3/\mathrm{s}$. The updraft velocity and flow rate are approximately 60% and 15%, respectively, of the theoretical values estimated in section 3.2. Therefore, losses inside the trapezoidal duct, losses due to the honeycomb or high fan static pressure significantly reduce the overall performance of the simulator.

The radial Reynolds number ($Re_r = Q'/2\pi\nu$) was expressed for Ward-type simulators as a function of the flow rate in Equation 2.2 (section 2.3.1). For a flow rate of $4.93 \times 10^2 \mathrm{m}^3/\mathrm{s}$ through the simulator, the radial Reynolds number is therefore estimated to 8.7×10^4.

3.6 Tornado-like vortex flow field and structure

Using the traverse system, flow velocities were recorded in order to map the flow field in the simulator for different swirl ratios. Figure 3.8 shows the 3D velocity

flow fields in the UoB-TVG for a swirl ratio of 0.13, 0.30 and 0.70. Heights are normalised by the inflow height h_0, radial positions are normalised by the core radius r_c, located at $r/r_c = 1$, and velocities are normalised by the maximal tangential velocity of the corresponding swirl ratio. Figure 3.8 shows the complexity of a tornado-like flow field, with a strong inflow in the lower level towards the core vortex region and a strong updraft at the corner region ($r/r_c = 1$) for each swirl ratio. The strongest tangential velocities are typically found in the corner region and are identified in Figure 3.8 with the red areas.

For $S = 0.13$, the flow field does not exhibit a clear vortex structure (Figure 3.8 (a)) but shows a region of strong tangential velocities between $r/rc = 0$ and 3. The region between $r/r_c = 0$ and 3 also shows an outflow which is consistent with previous observations made by Haan et al. (2008), Gillmeier et al. (2017), Tang et al. (2018). Different possible reasons could explain this behaviour, such as the vortex located off-centre the simulator's centre or due to vortex. Gillmeier et al. (2018) also identified vortex wandering in surface pressure measurements of the UoB-TVG and found that the lower the swirl ratio, the higher the wandering. Quantification of the vortex wandering will be given in section 4.8 but also draws the same conclusion. However, it is still uncertain what is precisely causing the radial outflow for $S = 0.13$, and it is therefore difficult to draw a general conclusion considering the measuring techniques employed in the present case. For $S = 0.3$, the flow structure appears to be more structured. The recirculation located at $z/h_0 = 0.1$ and $r/r_c = 1$ seems to indicate the presence of a vortex breakdown, which would indicate that for $S = 0.3$ the tornado flow field is not yet fully developed into a two-cell vortex. Therefore, for $S = 0.13$, the vortex could possibly

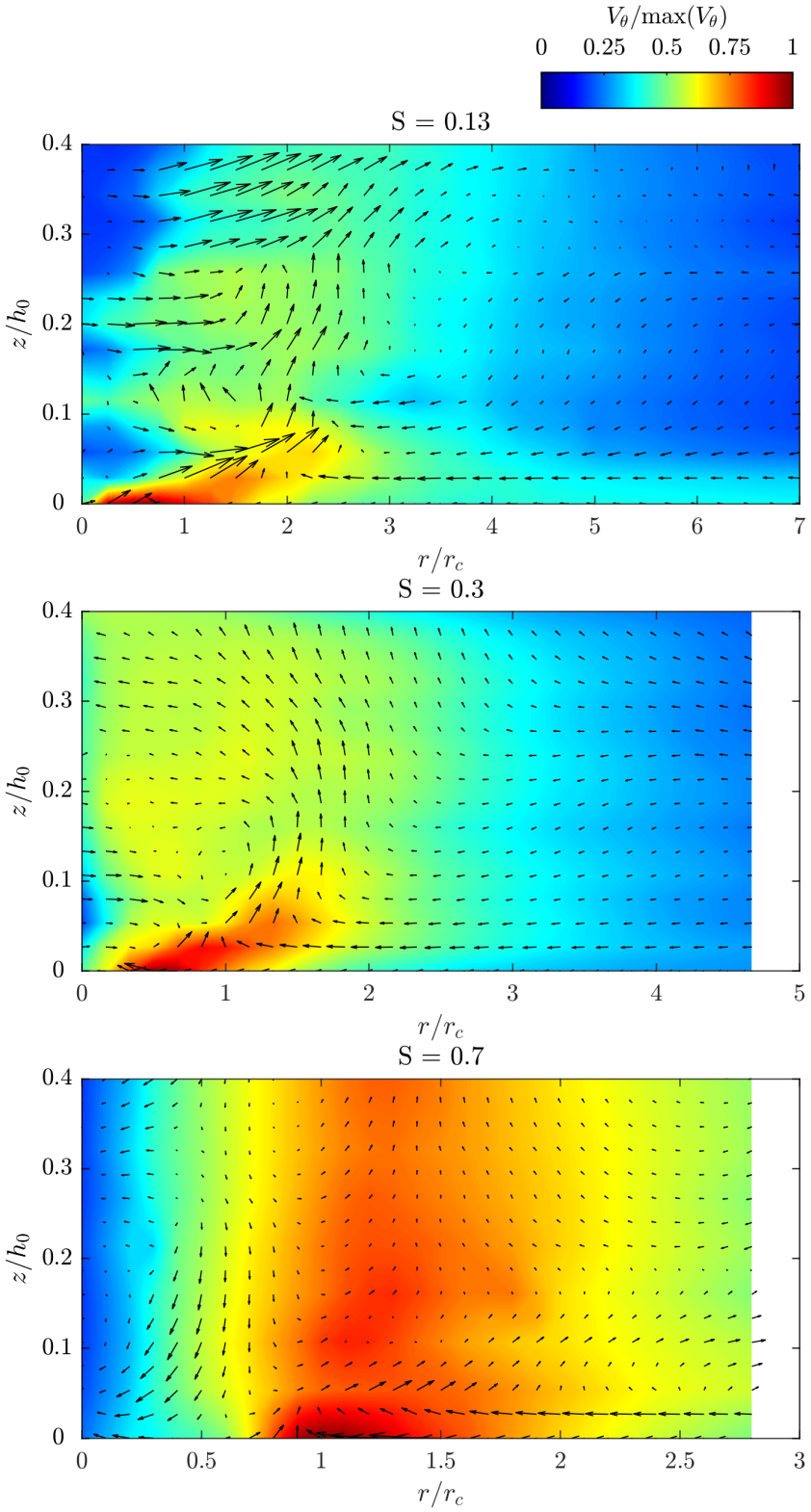


Figure 3.8: 3D velocity flow fields for (a) $S = 0.13$, (b) $S = 0.3$ and (c) $S = 0.7$. The white contour outlines the normalised tangential velocities, and the arrows show the 2D vector field of radial and vertical velocities.

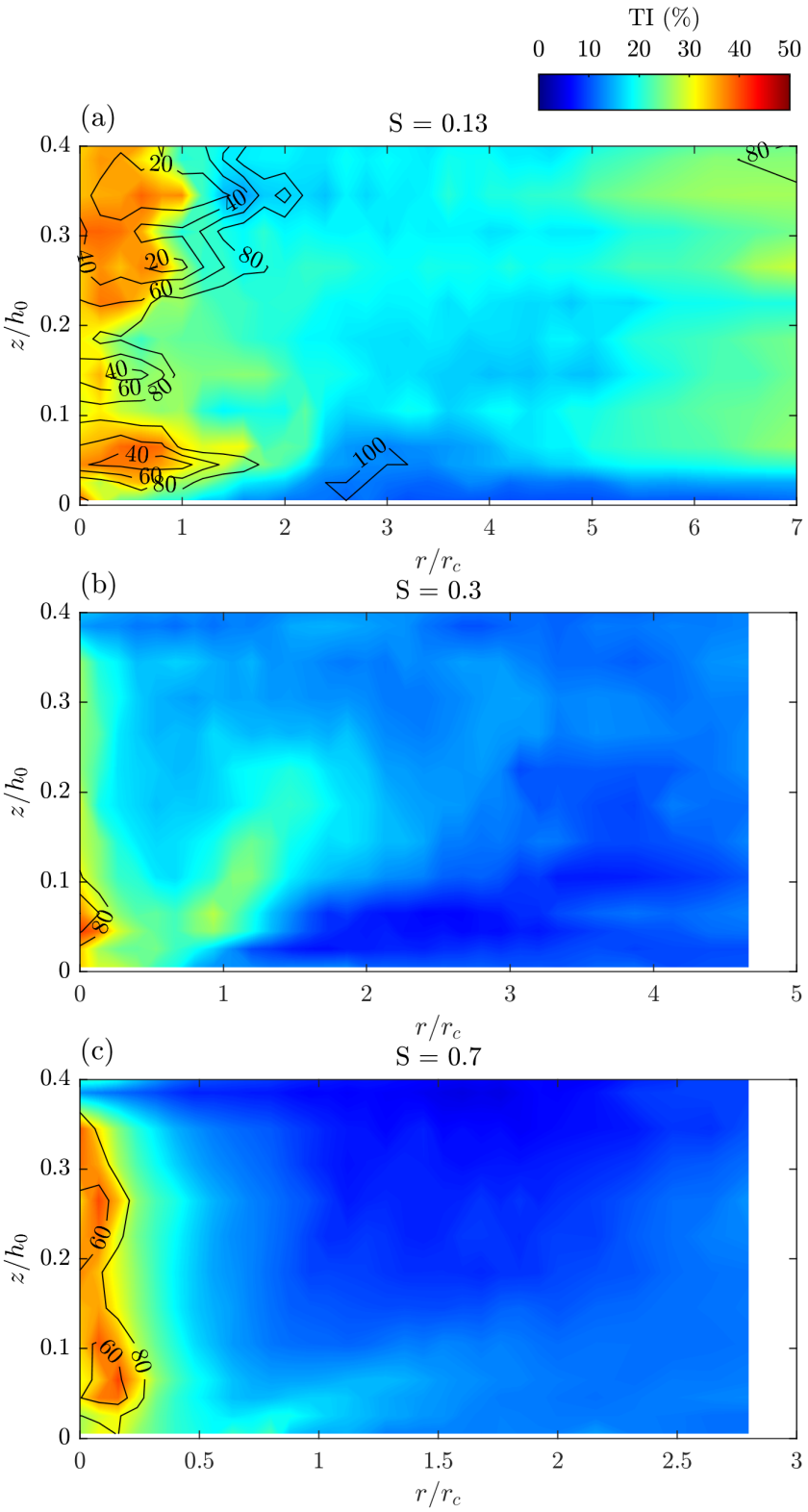


Figure 3.9: Turbulence intensity of the velocity vector for different swirl ratios of (a) $S = 0.13$, (b) $S = 0.3$ and (c) $S = 0.7$. The white contour outlines the data quality defined as the ratio of non-zero to the total number of measured points.

feature a one-cell vortex structure. Overall, the vortex structure for $S = 0.3$ shows a relatively good agreement with previous work from Gillmeier et al. (2018) and the VorTECH generator for a similar swirl ratio (Tang et al., 2018). For $S = 0.7$, the flow field exhibits a downdraft in the core vortex but shows a rather more complex structure than expected from a two-cell vortex structure. The downdraft appears to be weaker at the centre of the tornado simulator ($r/r_c = 0$) than closer to the core radius. The flow field was most likely too turbulent for the Cobra probe to capture a realistic flow pattern. Nevertheless, Figure 3.8 shows some agreement with the vortex structure and downdraft found in the previous work from Haan et al. (2008) and Gillmeier et al. (2018).

Figure 3.9 shows the turbulence intensity of the velocity vector $V \left(= \sqrt{V_\theta^2 + V_R^2 + V_W^2}\right)$ (see section 2.3.2 for the coordinate system) and data quality. For $S = 0.13$, overall high turbulence intensities are expected due to the fluctuation caused by the vortex wandering with values up to 50% (Figure 3.9 (a)). For $S = 0.3$, the turbulence intensity is lower and rather uniform outside the core region with values around 10 to 20% and higher turbulence intensity associated with the updraft (Figure 3.9 (b)). For $S = 0.7$, the turbulence intensity is mostly uniform with values around 10%, but high turbulence is observed inside the core vortex associated with the downdraft (Figure 3.9 (c)). However, it is difficult to draw any conclusion regarding the turbulence in tornado-like vortices considering the non-stationarity of current flow fields and the presence of the traverse system inside the simulator. Tang et al. (2018) obtained more uniform and structured distributions of turbulence intensity while not placing a traverse system inside their simulator and generating more stable vortices. Nevertheless, it is worth noting that the data

quality achieved during these simulations is significantly high enough for $S = 0.3$ and $S = 0.7$ to support the flow fields observed in Figure 3.8, and therefore considered the full dataset to be representative. For this reason, the threshold of 75% data quality used by Mishra et al. (2008*a*) and Gillmeier et al. (2018) was not set in the current work.

3.7 Horizontal velocity profiles

Figure 3.10, Figure 3.11 and Figure 3.12 show the horizontal profiles of each velocity component for a height of $z = 0.005,\ 0.1,\ 0.2,\ 0.3$ and 0.4m and for a swirl ratio of $S = 0.13$ (a), 0.3 (b) and 0.7 (c) respectively. Each profile was normalised with the local maximum tangential velocity and core radius, as shown in Figure 3.13. The different analytical vortex models (Rankine, modified Rankine, Burgers-Rott, Sullivan, Baker and Sterling) described in section 2.3 were fitted to the experimental data. For the sake of the current analysis, only one profile is plotted for each model using the maximum tangential velocity and the core radius of the lowest height (i.e. z = 0.005m).

Figure 3.10 shows the horizontal profiles of the normalised tangential velocities for different swirl ratios. For $S = 0.13$ (Figure 3.10 (a)), the profiles significantly vary with height, and therefore none of the models can precisely reproduce the profiles. However, the modified Rankine, Sullivan and Baker and Sterling models perform better at reproducing the profile trend. It is worth noting that the modified Rankine and Baker and Sterling tangential velocities are identical in the current analysis and therefore are overlapping. For $S = 0.3$ (Figure 3.10 (b)), the same conclusion can be drawn from the $S = 0.13$ case. Discrepancies inside

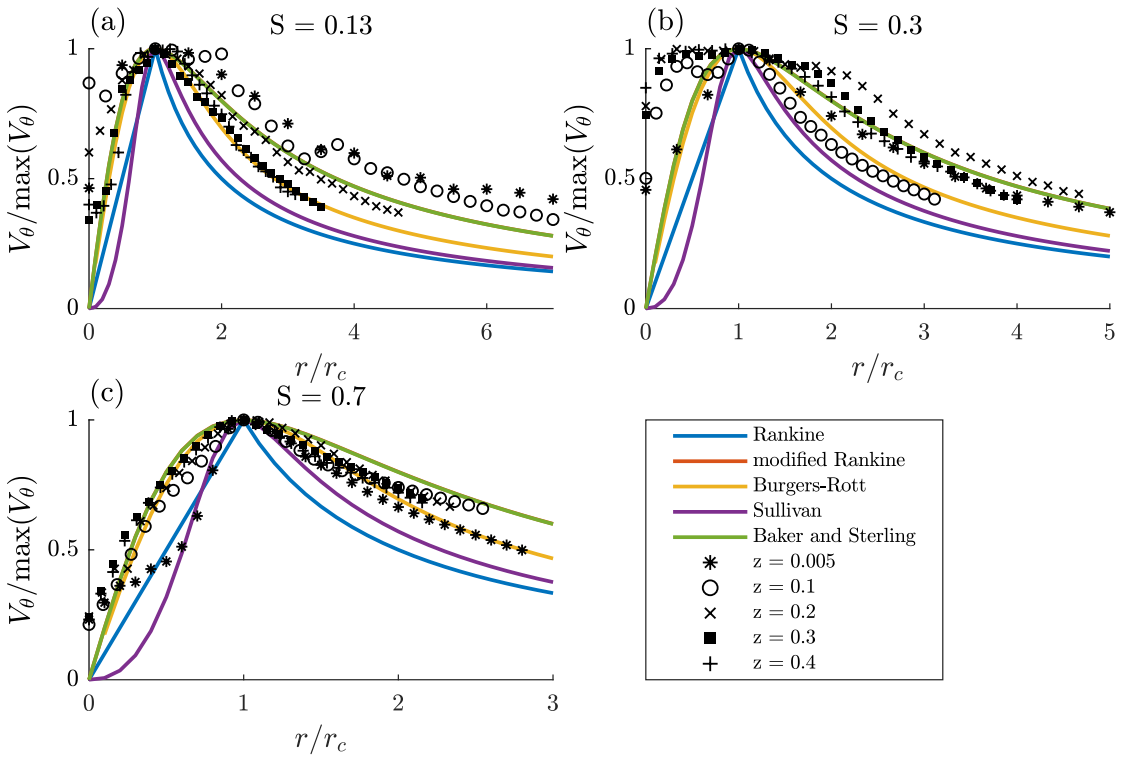


Figure 3.10: Horizontal profiles of tangential velocity for different heights, analytical vortex models and for different swirl ratios of (a) $S = 0.13$, (b) $S = 0.3$ and (c) $S = 0.7$.

the core radius ($r/r_c < 1$) can be a result of recirculation due to the potential vortex breakdown observed in Figure 3.8. For $S = 0.7$ (Figure 3.10 (c)), the flow field tends to be more uniform, and therefore each profile for each height is in good agreement except for z = 0.005m. Close to the ground, radial velocities have higher magnitude than above due to friction (Trapp, 2000). Similarly, for lower swirl ratios, all models perform well except the Rankine and Burgers-Rott models. However, inside the core vortex ($r/r_c < 1$) at the lowest height (z = 0.005m), the profile follows a similar trend to the Burgers-Rott model.

Figure 3.11 shows the horizontal profiles of the normalised radial velocities for different swirl ratios. For $S = 0.13$ (Figure 3.11 (a)), the outflow observed in

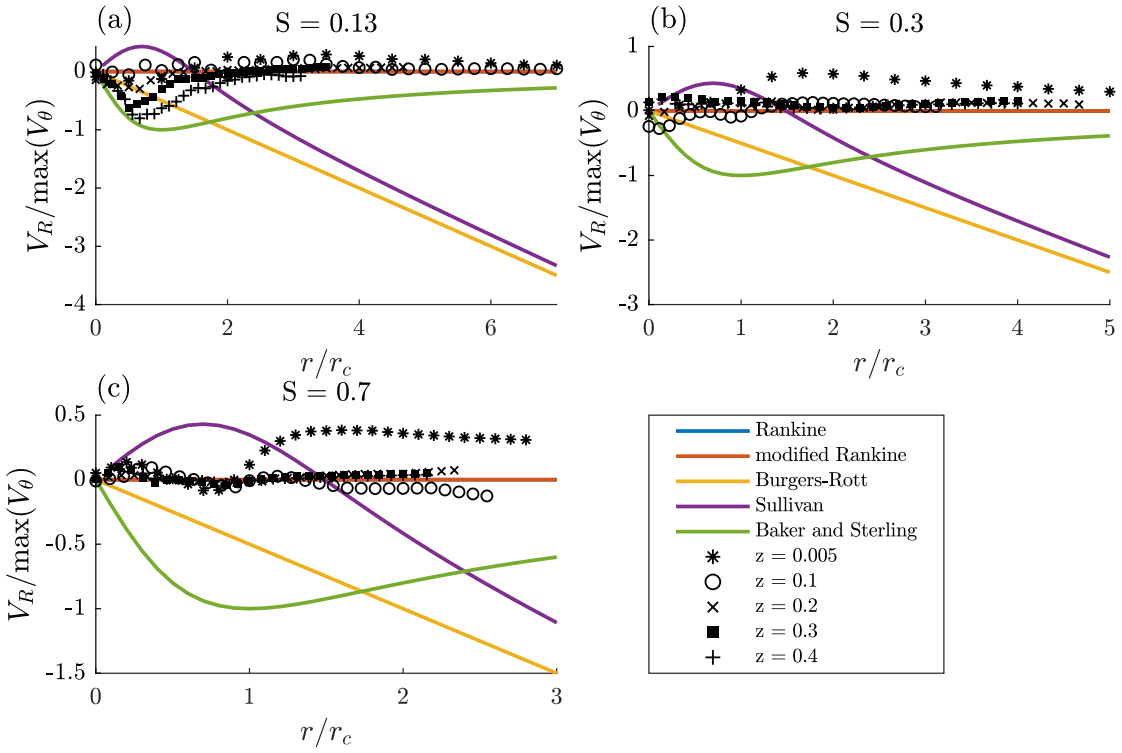


Figure 3.11: Horizontal profiles of radial velocity for different heights, analytical vortex models and for different swirl ratios of (a) $S = 0.13$, (b) $S = 0.3$ and (c) $S = 0.7$.

Figure 3.8 is characterised by negative radial velocities for $r/r_c < 1$. The outflow also tends to be more important at a higher height. That outflow has previously been observed for small swirl ratios in the simulator (Gillmeier et al., 2018) but also in simulators with different geometry and scale (Mishra et al., 2008*a*, Haan et al., 2008). Regarding the vortex models, the Baker and Sterling's model shows good agreement in reproducing the shape of the outflow, even though it does not precisely fit the experimental data. However, the parameters of Baker and Sterling models were not adjusted for each velocity component as done by Gillmeier et al. (2018). For $S = 0.3$ (Figure 3.11 (b)) and 0.7 (Figure 3.11 (c)), the flow field is too complex to be reproduced by any of the vortex models. However, it is noted that

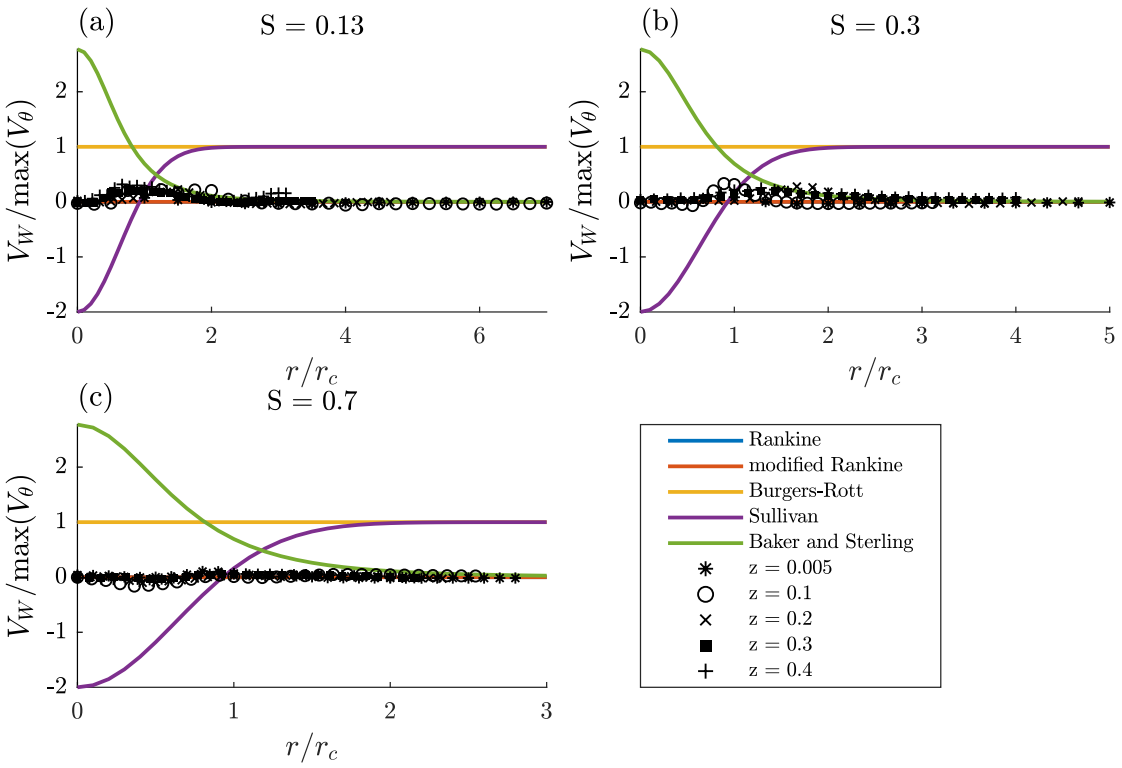


Figure 3.12: Horizontal profiles of vertical velocity for different heights, analytical vortex models and for different swirl ratios of (a) $S = 0.13$, (b) $S = 0.3$ and (c) $S = 0.7$.

the models used here are only a one-cell representation of the vortex structure, and therefore it is not too surprising that they fail to fit the experimental data.

Figure 3.12 shows the horizontal profiles of the normalised vertical velocities for different swirl ratios. Overall, the conclusions regarding the complexity of the flow field can also be drawn here. The Burger-Rott model shows unrealistic constant updraft, while the Sullivan and Baker and Sterling models show negative and positive strong updraft at the centre of the vortex.

In section 3.3, the Burgers-Rott and Sullivan vortex models were expressed in a dimensional way to discard the shape parameters and solely express them as a

function of the core radius and the maximum tangential velocity. The comparison between models and experimental data shows that the models generally failed to reproduce the complexity of the flow field but also the velocity magnitude. Figure 3.10, Figure 3.11 and Figure 3.12 show that the models tend to overestimate the velocity magnitudes. However, as reported by Gillmeier et al. (2018), with a different set of measurements in the same simulator, Baker and Sterling's model tends to fit the experimental tangential velocity data the best but still fails to reproduce the radial and vertical velocities. For a small swirl ratio ($S = 0.13$) where most of the uncertainties are observed, Baker and Sterling's model presents some similarities with the experimental data, which could indicate the presence of a one-cell, unsteady vortex. A non-intrusive measuring technique could help to investigate further and better picture the vortex structure evolution as a function of the swirl ratio without introducing disturbances due to measuring systems.

3.8 Vertical velocity profiles

Figure 3.13 (a) shows the variation with height of the local maximum tangential velocity. For all swirl ratios, the highest tangential velocity is located at the lowest height (z = 0.005m) and is given by $V_\theta / \max(V_\theta) = 1$. Figure 3.13 (a) shows that the lower the swirl ratio, the larger the decrease of maximum tangential velocity with height. For $S = 0.7$, the maximum tangential velocity appears to be rather constant with a height above $z/h_0 = 0.05$.

Figure 3.13 (b) shows the variation with height of the local core radius defined as the radial location of maximum tangential velocity for each height. For $S = 0.13$ and 0.7, the core radius increases slightly with height to be respectively $1.6r_c$ and

$1.2r_c$ at $z/h_0 = 0.4$. For $S = 0.3$, the fluctuation between $z/h_0 = 0.05$ and 0.2 are most likely associated with the recirculation identified in Figure 3.8. Above $z/h_0 = 0.2$ the core radius is about $2.3r_c$ with a size relatively close to the core radius for $S = 0.7$. However, the estimation of the core radius with height is based upon the estimation of the maximum tangential velocity. When considering the measuring techniques employed here, a tendency is observed and described, but a general conclusion cannot be drawn. Non-intrusive measurements would be required to validate the tendency observed in Figure 3.13.

Figure 3.14 shows the variation with height of the normalised tangential velocity at different core radius locations and for different swirl ratios. For all swirl ratios, non-zero tangential velocities for $r = 0r_c$ suggest that the vortex is potentially not

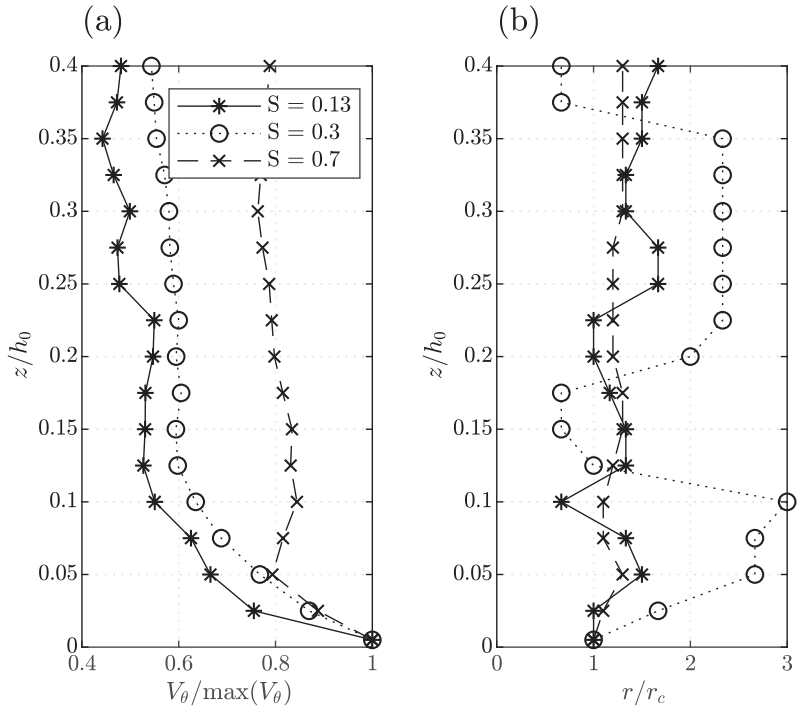


Figure 3.13: Vertical profiles of (a) normalised local maximum tangential velocity and (b) local core radius for swirl ratios of $S = 0.13$, 0.3 and 0.7

located at the centre of the simulator. This could be due to vortex wandering or the vortex centre being located off-centre. Even though the flow field for $S = 0.13$ appears to be quite unstructured, Figure 3.14 (a) shows that the vertical profiles at the different locations follow a similar trend. For $S = 0.3$ (Figure 3.14 (b)), the profiles for $r > 0.5r_c$ show good agreements when $z/h_0 > 0.05$. The variation below $z/h_0 = 0.05$ is most likely associated with the maximum tangential velocities observed in the corner region. Not surprisingly, the profile for the $r = 0r_c$ is significantly different and is certainly associated with the downdraft inside the core vortex. For $S = 0.7$, each profile shows different tangential velocities but uniform with height. The vertical profiles are also consistent with the horizontal profiles, as shown in Figure 3.10 (a) where horizontal profiles show strong similarities for

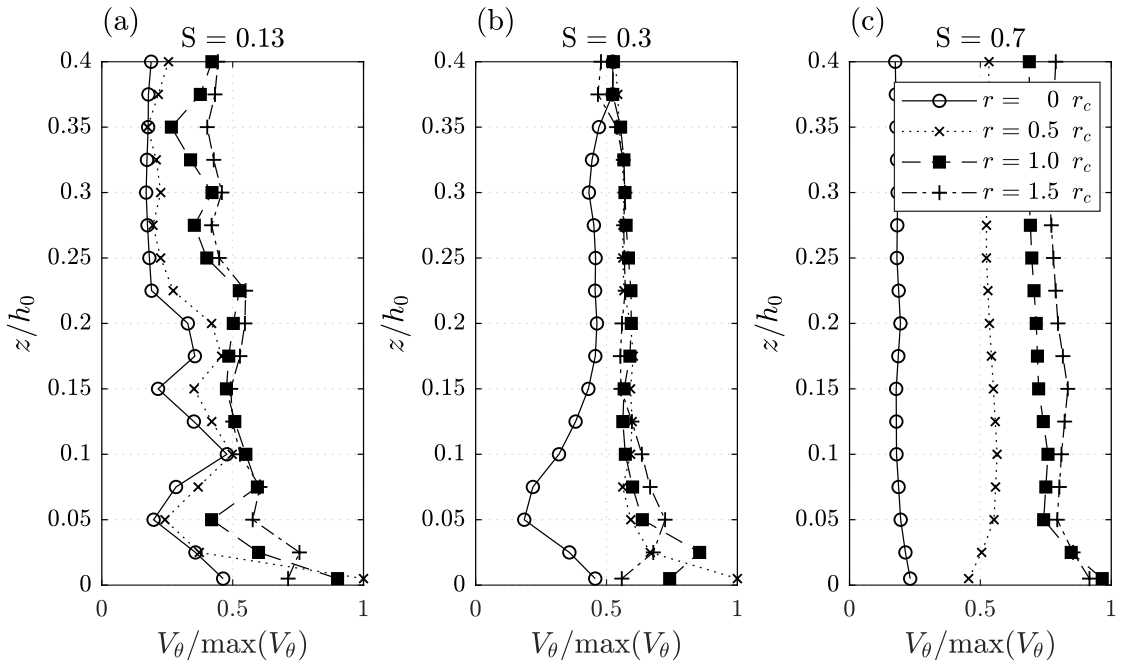


Figure 3.14: Vertical profiles of the tangential velocity components for different swirl ratios of (a) $S = 0.13$, (b) 0.3 and (c) 0.7 and at different core radius locations ($r = 0,\ 0.5,\ 1.0$ and $1.5r_c$)

each different height.

Figure 3.15 shows the variation with height of the normalised radial velocity at different core radius locations and for different swirl ratios. Similarly to Figure 3.14, the vertical profiles exhibit similar trends for the different radial locations. For $S = 0.3$ (Figure 3.15 (b)), since the recirculation is centred at $r/r_c = 1$, the profiles show a double change of sign because of the change of wind direction induced by the potential vortex breakdown. For $S = 0.7$ (Figure 3.15 (c)), radial velocities are not significantly important as the flow is primarily circumferential, except for $r = 1.5r_c$ and near the ground where a strong inflow was recorded.

Figure 3.16 shows the variation with height of the normalised vertical velocity at different core radius locations and for different swirl ratios. For $S = 0.13$ (Figure

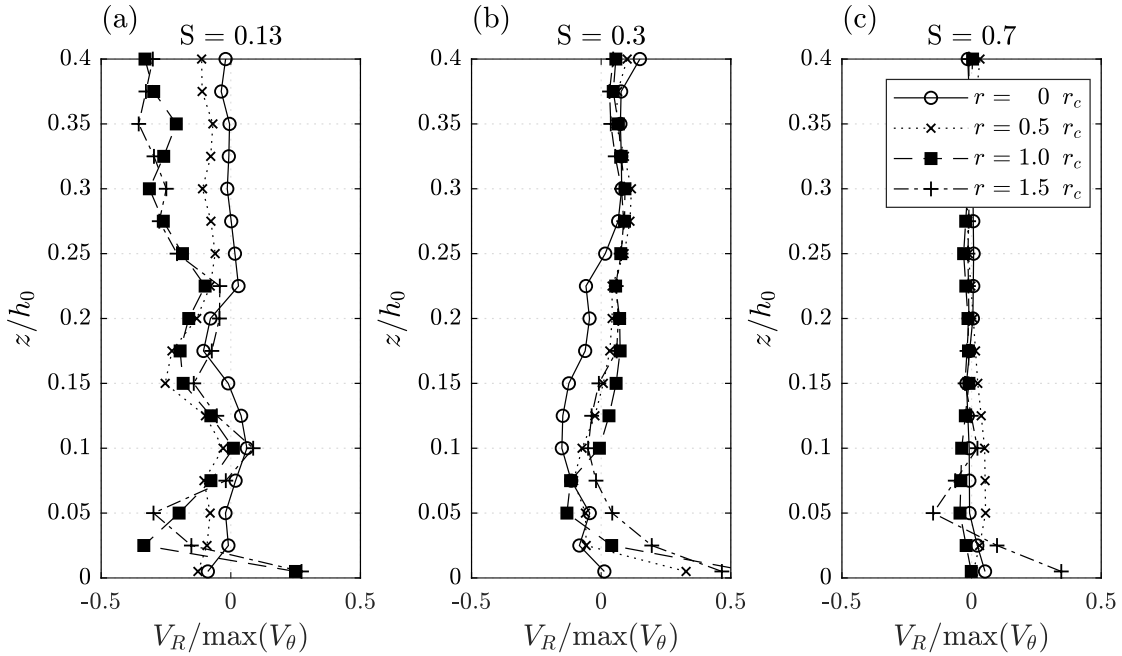


Figure 3.15: Vertical profiles of the radial velocity components for different swirl ratios of ((a) $S = 0.13$, (b) 0.3 and (c) 0.7 and at different core radius locations ($r = 0,\ 0.5,\ 1.0$ and $1.5r_c$)

3.16 (a)), the vertical velocities are predominantly positive, although the profiles do not exhibit any peaks that would suggest a strong updraft. For $S = 0.30$ (Figure 3.16 (b)), the profile at the core radius ($r = 1.0r_c$) shows a peak at $z/h_0 = 0.05$, whereas the profile outside the core radius ($r = 1.5r_c$) shows a peak at $z/h_0 = 0.125$. This corroborates the increase of the core with height as observed in Figure 3.13. For $S = 0.70$ (Figure 3.16 (c)), the vertical profiles confirms the double cell structure of the vortex, with vertical velocities predominately negative inside ($r = 0.5r_c$) and positive outside ($r = 1.5r_c$) the core vortex. The updraft at the core radius location ($r = 1.0r_c$) is the strongest at the lowest height ($z/h_0 = 0.025$) and is associated with the strongest winds in the corner region.

Overall, the vertical profiles show good similarities between the different radial

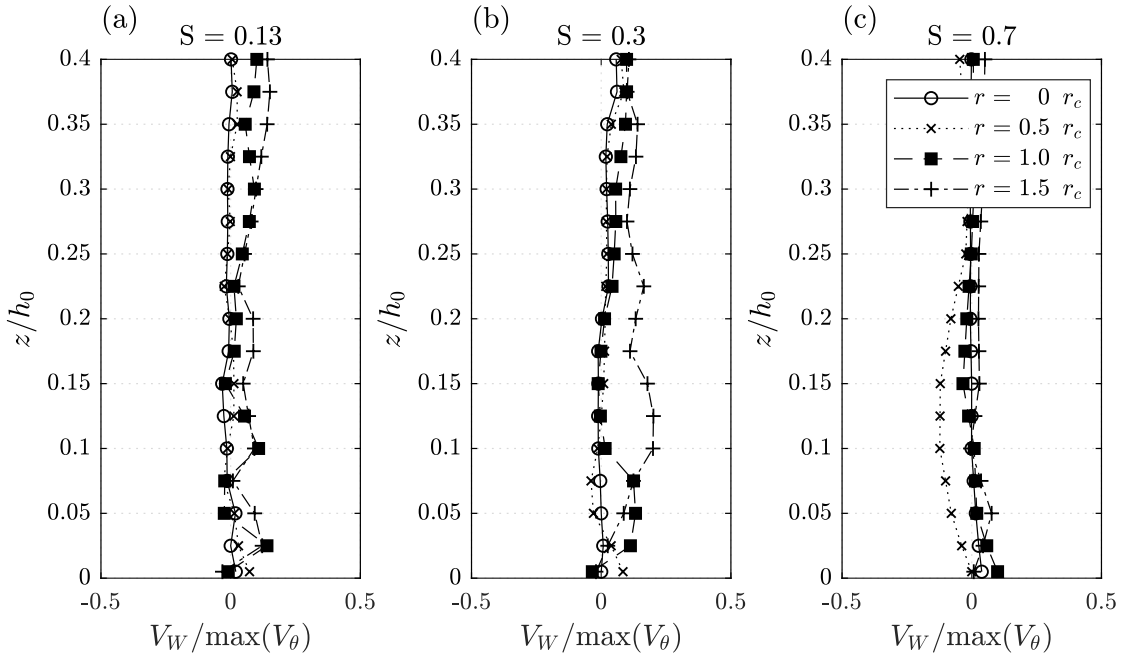


Figure 3.16: Vertical profiles of the vertical velocity components for different swirl ratios of ((a) $S = 0.13$, (b) 0.3 and (c) 0.7 and at different core radius locations ($r = 0,\ 0.5,\ 1.0$ and $1.5r_c$)

locations $r = 0$, 0.5, 1 and $1.5r_c$. However, these arbitrary radial locations might not reflect regions where the flow field could be, for instance, transitioning from radial inflow/outflow to vertical updraft. Therefore, the analysis is potentially missing some features of the flow characterisation. These locations were chosen to ensure consistency in the analysis and because the positions $r = 0$, 0.5, 1 and $1.5r_c$ were for all swirl ratios very close, if not equal, to the exact point measurement location.

3.9 Concluding remarks

The following conclusions can be drawn from the physical simulations undertaken and presented above:

1. The flow field observed and measured in the UoB-TVG is far less structured than described by conceptual views, as given by Davies-Jones (1973) or by analytical vortex models.

2. The tangential velocity is generally well modelled by the modified Rankine, Sullivan and Baker and Sterling models. However, the Rankine and Burgers-Rott models fail to replicate it.

3. Expressing the analytical vortex models solely as a function of the core radius and maximum tangential velocity showed that they fail to replicate the complexity of the flow field with higher radial and vertical velocities.

4. The core radius was found to be increasing with height for the different swirl ratios as generally observed in the different tornado simulators.

5. Vertical profiles at different arbitrary radial locations, i.e. $r = 0,\ 0.5,\ 1.0$ and $1.5r_c$, mostly look consistent with height for each velocity component and swirl ratio tested. However, the locations were not chosen at specific points of interest and therefore, could lack representativeness of the flow field complexities.

Chapter 4

Experimental investigation of the flight of debris in tornado-like vortices

4.1 Introduction

4.2 Experimental set up

Particle Tracking Velocimetry was introduced in section 2.3.3 and is a Lagrangian velocimetry technique using one or multiple cameras to track individual particles and determine their trajectories and velocities over time. The scope of particle tracking experiments is to retrieve flow field information using tracer particles and assumes that these particles follow fluid streamlines, i.e. all particles must have a Stokes number close to or lower than 1. In this case, point measurement at a specific location and time can be retrieved, but spatial and time averaging can also be computed to obtain global characteristics of the flow field. However, the current work focuses on investigating the flight of debris in tornado-like vortices, and therefore individual debris trajectories were examined. 2D-PTV only requires a single camera while 3D-PTV requires at least two cameras to retrieve three-dimensional data. Generally, high-speed cameras are used to accurately measure

the tracer particles in space and time. Thus, when investigating 3D trajectories, time synchronisation between the cameras and precise calibration of the system is necessary to obtain satisfactory qualitative and quantitative tracking data (Maas et al., 1993). Finally, Figure 4.1 shows the coordinate system used when performing 2D/3D-PTV.

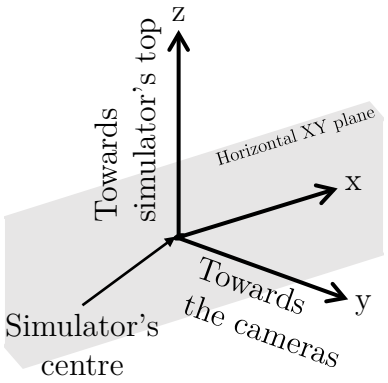


Figure 4.1: Particle tracking velocimetry coordinate system.

4.2.1 High-speed camera

The Sony FS700RH is a professional camcorder (Figure 4.2) with slow-motion capability, and up to three cameras were used as part of the particle tracking system.



Figure 4.2: Sony FS700RH camera and SELP18200 (18–200mm F3.5–6.3 OSS) 11x zoom E-Mount lens used for Particle Tracking Velocimetry.

The FS700RH has a 4K CMOS sensor capable of recording videos at a resolution up to 4096 x 2160 pixels. The cameras can record RAW (i.e. no compression) videos up to 120 frames per second (fps) at 4K resolution for approximatively 4 seconds, up to 240 fps at 2K RAW resolution (2048 x 1080 pixels) continuously. However, this requires a special memory card device to be able to record at these frame rates. For compressed videos, the camera can record up to 960 fps at full HD resolution (1920 x 1080 pixels) for 5 or 10 seconds and the footage is saved onto a memory card (SD card). For the current application, the cameras were set up to record videos at full HD resolution and at 480 fps. The camera is supplied with an 11× zoom power lens with built-in optical image stabilisation. The zoom range of the lens enables easy adaption of the field of view of the camera in order to focus on the region of interest. For the current work, the horizontal field of view for each camera was adjusted to cover around 2 × 1.2m, roughly giving a real-world pixel size of 0.001m. For an averaged maximum wind speed of 10 m/s, a particle would travel about 0.02m between two frames when recorded at a frame rate of 480 fps, which is 20 times more than the real-world pixel size. Therefore, the resolution of the camera and the adjusted field of view appears to be sufficient to identify, between two frames, the motion of any particle larger than 0.001m travelling at lower or equal to 10 m/s. Nevertheless, light luminosity and surface reflections appeared to have a significant impact on the particle detection during the particle tracking process and pre- and post-processing adjustments were required to enhance the particles detection.

In slow-motion mode, the camera integrates three different triggering modes, as described in Table 4.1. For the current work, the camera was set up either to End Trigger or End Trigger Half depending on the case study. As this mode buffers

Table 4.1: Summary of the different triggering modes available on the Sony FS700RH camera.

Triggering mode	Description
Start Trigger	Records to the SD card for 10 seconds once the RECORD button is pressed.
End Trigger	Continuously buffers for 10 seconds and starts recording the buffer onto the SD card once the RECORD button is pressed.
End Trigger Half	Continuously buffers for 5 seconds and starts recording the buffer onto the SD card once the RECORD button is pressed.

images for 5s or 10s, it allows the user to visually monitor the flow being seeded with particles and typically only starts recording when the situation is applicable (typically when particles stopped flying in the present work).

4.2.2 Camera triggering device

The camera can be externally triggered using the software and hardware communication protocol developed by Sony, called Logic Application Control Bus System (LANC). The protocol is a two-way protocol sending a command and reading the acknowledgement from the camera. To ensure the command was sent and received, the protocol sends and verifies the acknowledgement three times before processing the command. To externally trigger several cameras, a Multi-Camera LANC Controller ALE718 (Figure 4.3), developed by Applied Logic Technology, was used. The ALE718 is powered with 5V using a micro-USB cable, and the cameras are plugged in using a 2.5mm jack connector. When the Start button is pressed, the ALE718 sends the command simultaneously to trigger all cameras at



Figure 4.3: Multi-Camera LANC Controller ALE718, developed by Applied Logic Technology, used to trigger three cameras Sony FS700RH.

the same time. At normal frame rates, the controller provides a good synchronisation between cameras for stereoscopic recordings. However, at higher frame rates, it was found that random disparities between the cameras, up to 100ms, were occurring. Nevertheless, it was also found that each individual frames were recorded at the exact same time but only the starting time was randomly shifted positively or negatively in time. This behaviour could be due to different internal response times for each camera and could not be corrected or adjusted due to the lack of control on either the camera or triggering device side.

4.3 Calibration

In section 2.3.3, the particle velocimetry tracking technique was introduced and described as the principle of triangulation. The camera calibration is the central procedure of a particle tracking system and consists of determining the relation between pixels on images and corresponding real-world positions. A good calibration will result in a precise determination of the particle positions but also ensure a good connection between particles during the tracking process. In order to determine the position of a point in two or three dimensions, it is necessary to estimate

the cameras intrinsics (i.e. the inherent parameters of the camera, such as the focal length), extrinsics (i.e. the parameters used to describe the transformation between the camera and the real-world) and lens distortion (i.e. the optical aberration due to an imperfect lens) parameters. The mathematical model developed by Maas et al. (1993) requires 15 parameters describing the geometry of the camera to establish the relationship between the image and real-world coordinates.

Assuming a pinhole model for the camera, it is possible to calculate the camera projective centre coordinates from the real-world camera coordinates. To perform the calibration, a series of well-known located points, i.e. targets, ideally cover the entire camera field of views, which can be found difficult to overcome in large scale computer vision applications. The unknown parameters in Maas et al. 's model are then determined by resolving the mathematical model (not shown for the purpose of simplicity). However, the model needs to be input with physical realities such as described thereafter to reproduce as accurately as possible the real-world phenomena.

Lenses are generally not perfect, and therefore distortion is generally present and must be considered in the model. Brown (1971) described the lens distortion to be dependent on five radial and tangential parameters. Furthermore, optical media with different refractive indices cause light rays to be deflected, introducing errors in determining particles positions. Corrections can be added to the model if different optical media are used.

4.3.1 Calibration target

A calibration target is a planar or three-dimensional object, with a certain number of dots or targets, used to perform the camera calibration of a computer vision

system.

For the present work, different calibration targets have been tried. However, given the significantly large field of view, it was impractical or even impossible to consider a three-dimensional target covering the whole field of view. Therefore, a large planar target was used to perform the calibration, and a three-dimensional target was used to validate the calibration.

Figure 4.4 shows the pattern of the planar calibration target. It consists of an array of 21×15 dots, 0.003m in diameter and spaced every 0.04m for a total dimension of 1.05m $\times$ 0.75m. The target was generated using a calibration pattern generator and printed on an A0 poster. The poster was then glued onto a plastic board to ensure a flat surface. This method, although looking easy, was significantly cheaper than conventional calibration target boards but showed a submillimetre level of precision (detailed in the next chapter), which is good for a large-scale application. The three-dimensional calibration target was designed with the optics to be printed in a 3D printer available in the Civil Engineering Laboratories. Therefore, the size of the target was limited to the size of the 3D printer. Figure 4.5 shows the CAD model and the printed version of the target. The dimensions of the target are 0.2m $\times$ 0.2m $\times$ 0.1m, with 81 dots evenly spaced every 0.0225m horizontally and vertically. Each dot location was made of a shallow hole that has been filled with white paint as precisely as possible.

4.3.2 Camera arrangement

The camera arrangement also plays a critical part in the calibration process. A good arrangement will see each individual particle from a different angle of view

and will facilitate the detection and correspondence of every particle between the cameras. A bad arrangement will lead to particle mismatches and wrong correspondences and will ultimately engender disconnection or wrong connections between partial trajectories. However, the camera arrangement is generally imposed by the experiment itself and cannot be optimal. Refan et al. (2014) and Refan and Hangan (2018) carried out PIV measurements in the both the small and large WindEEE dome and placed the cameras under the simulator, looking through the glass floor. For the UoB-TVG, the cameras could not be placed under the simulator, and the convergence and convection chambers were made of blue transparent acrylic panels reducing the visibility and causing significant reflections. Therefore, the cameras were placed and mounted inside the simulator, allowing different camera arrangements.

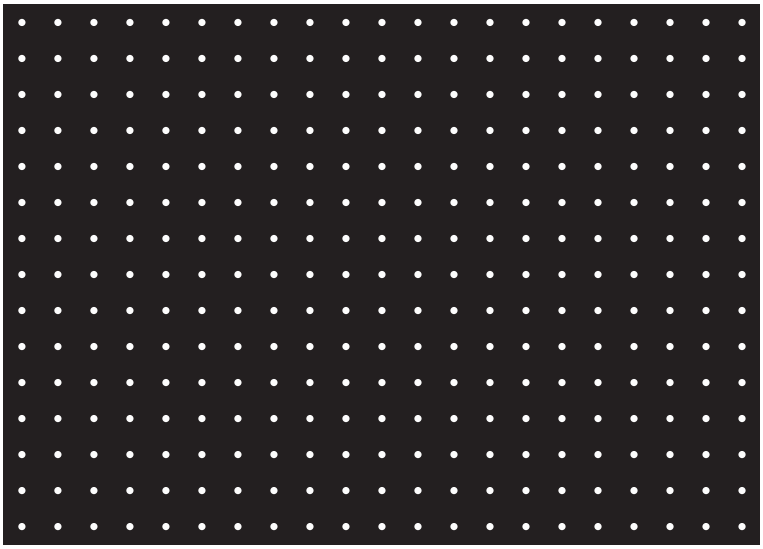


Figure 4.4: Planar calibration target. Each dot is spaced every 0.04m covering 1.05m $\times$ 0.75m.

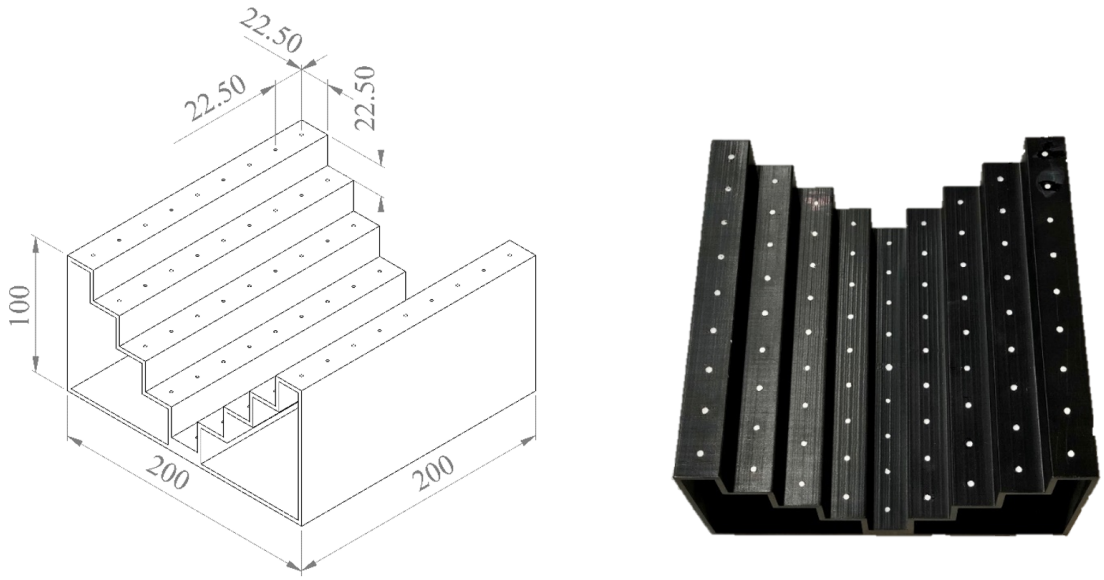


Figure 4.5: 3D calibrated target with the CAD design (left) and the 3D printed target (right).

For a one-camera arrangement, the camera was mounted on an aluminium structure and placed in the centre of the simulator in x-direction but off-centre in y-direction, pointing downward at the height of approximatively 1.5m (Figure 4.6). The zoom was then adjusted to cover a field of view of 2×1.2m. This field of view proved to be optimal, considering the size of the particles to be tracked, and for the overall distances travelled for the particles during the different experiments.

Different approaches were carried out with a two-camera arrangement. However, it quickly became apparent that given the large field of view and the size of the particles, it was difficult to successfully obtain good correspondence when particles were close together, and therefore to obtain good trajectories. Consequently, three-dimensional particle tracking was undertaken with three cameras (Figure 4.7).
For the three-camera arrangement, different approaches have also been attempted.

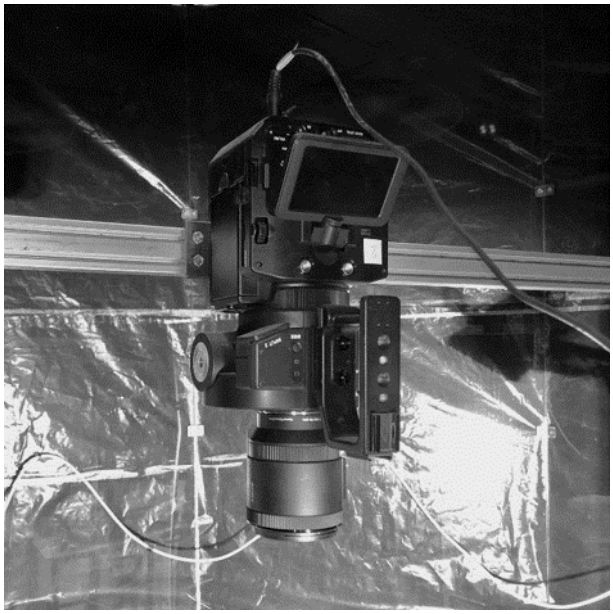


Figure 4.6: Camera used in a one-camera arrangement to perform 2D-PTV and mounted at the centre of the simulator (in x-direction but off-centre in y-direction) pointing downward.

Three main arrangements were investigated and are shown in Figure 4.8. Arrangement 3B (i.e. 3 "Bottom") has the 3 cameras placed at the same height (Figure 4.8 (a)); Arrangement 2B-1M (i.e. 2 "Bottom", 1 "Middle") has one camera slightly above the two others (Figure 4.7 and 4.8 (b)); and Arrangement 2B-1T (i.e. 2 "Bottom", 1 "Top") has one camera at the top of the convection chamber (Figure 4.8 (c)). Table 4.2 summarises the different arrangements and the respective locations of the cameras from the centre of the simulator. The zoom was adjusted for each camera and arranged to also cover a field of view of approximately 2 $\times$ 1.2m.



Figure 4.7: Example of a three-camera arrangement mounted inside the simulator and used to perform 3D-PTV.

4.3.3 Validation

Two different methods for validating the calibration have been carried out. The first method was a static validation with the 3D printed calibration target. Initially used to perform the calibration, the target was too small for the field of view and therefore was finally used as a validation target. The target was placed in the field of view of the cameras, and static images were taken to retrieve the 3D position of each individual dot (Figure 4.9).

The other method that was tried was a dynamic method, used to evaluate the performance of the tracking system to follow a moving target and retrieve the correct velocities. An individual target was placed on a motor to simulate a circular motion (Figure 4.10). The motor rotated at a known and constant angular velocity, and the target was tracked over time. The validation and performance of the cameras calibration are detailed in section 4.7 and show that the current particle

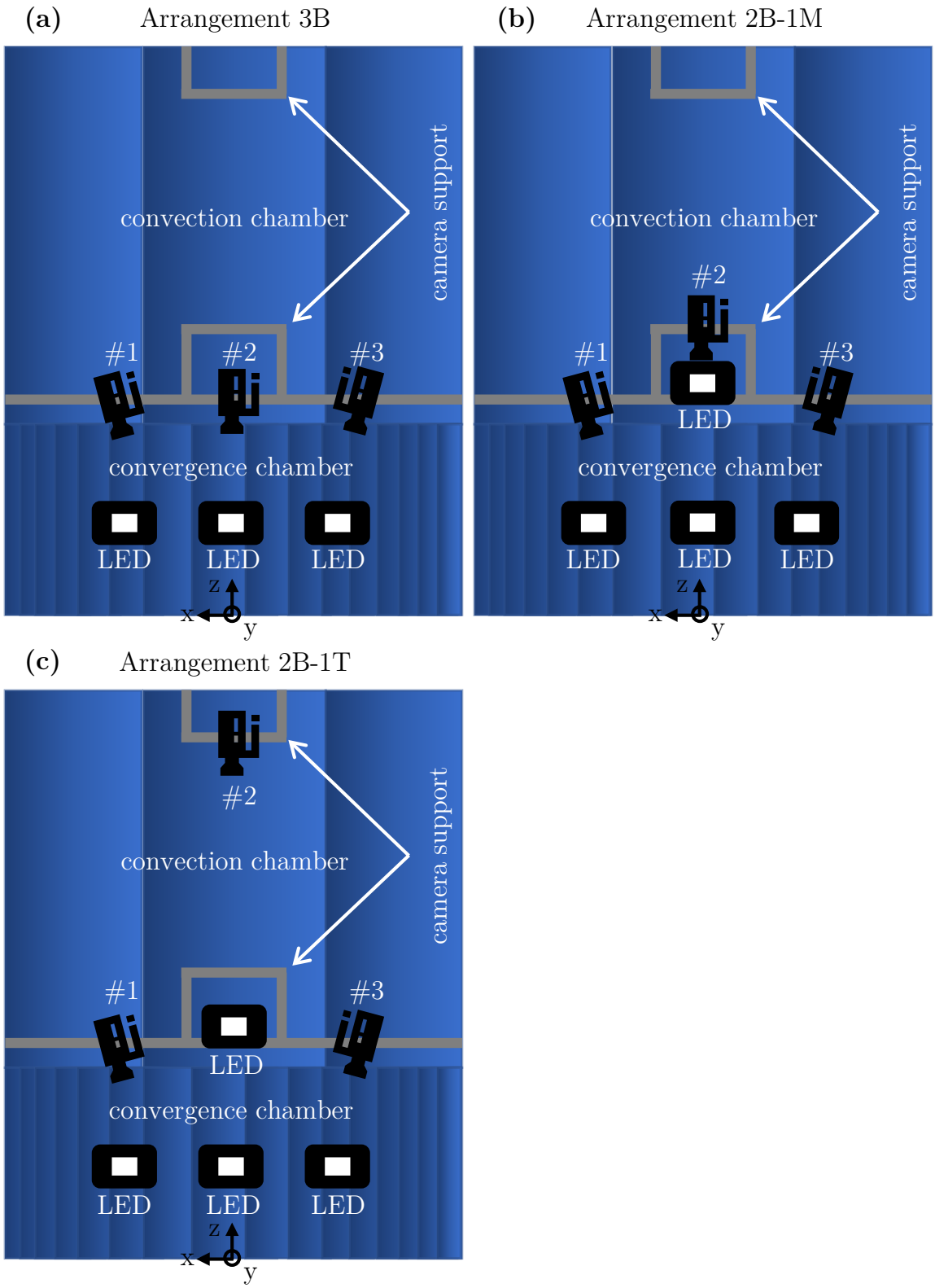


Figure 4.8: Schematic of the different arrangements used with three cameras #1, #2 and #3. (a) All three cameras #1, #2 and #3 are placed at equal Y and Z positions but are evenly spaced along X direction from the centre of the simulator. (b) Positions of camera #1 and #3 remain unchanged but camera #2 is placed slightly above. (c) Positions of camera #1 and #3 remain unchanged but camera #2 is placed at the top of the convection chamber.

Table 4.2: Summary of the three-dimensional coordinates for different arrangements of the cameras used to perform the calibration of the 3D-PTV system.

Arrangement	Camera	X [m]	Y [m]	Z [m]
3B	#1	-0.50	1.20	1.20
	#2	0.00	1.20	1.20
	#3	0.50	1.20	1.20
2B-1M	#1	-0.50	1.20	1.15
	#2	0.00	1.20	1.35
	#3	0.50	1.20	1.15
2B-1T	#1	-0.50	1.20	1.15
	#2	0.00	1.20	2.70
	#3	0.50	1.20	1.15

tracking system is accurate both statically and dynamically to have confidence in the results presented in section 4.8 and 4.9.

4.4 Debris

Many different types of materials, such as pieces of paper, wood, plastic, tissue and Styrofoam balls, were used to investigate the flight of debris in the tornado simulator. However, due to the relatively low Reynolds number and the vortex structure, it was quickly found that debris does not significantly get lifted off the ground. Therefore, recourse to debris as small and light as possible was necessary. In order to ensure repeatability and convenience, Styrofoam balls were used to

carry out the particle tracking experiments, and statistical analysis of the flight of debris was performed. Styrofoam balls were available in a range from 0.0015 to 0.006m, and particle sieving was performed in order to obtain the required size. It proved difficult to obtain a large number of spheres of an exact size; therefore, a particle size analysis was performed to obtain statistics on the size and variation of the spheres. The particle size analysis was performed using ImageJ software from a high-resolution picture, typically 16-megapixel. ImageJ software is capable of determining the number of particles, the pixel area of each particle and their roundness. After calibration with a ruler, pixel areas were converted from pixel to the SI system.

The theoretical density of Styrofoam is 28 kg/m^3 but can vary depending of the size on the spheres and the manufacturer. To precisely estimate the density of the

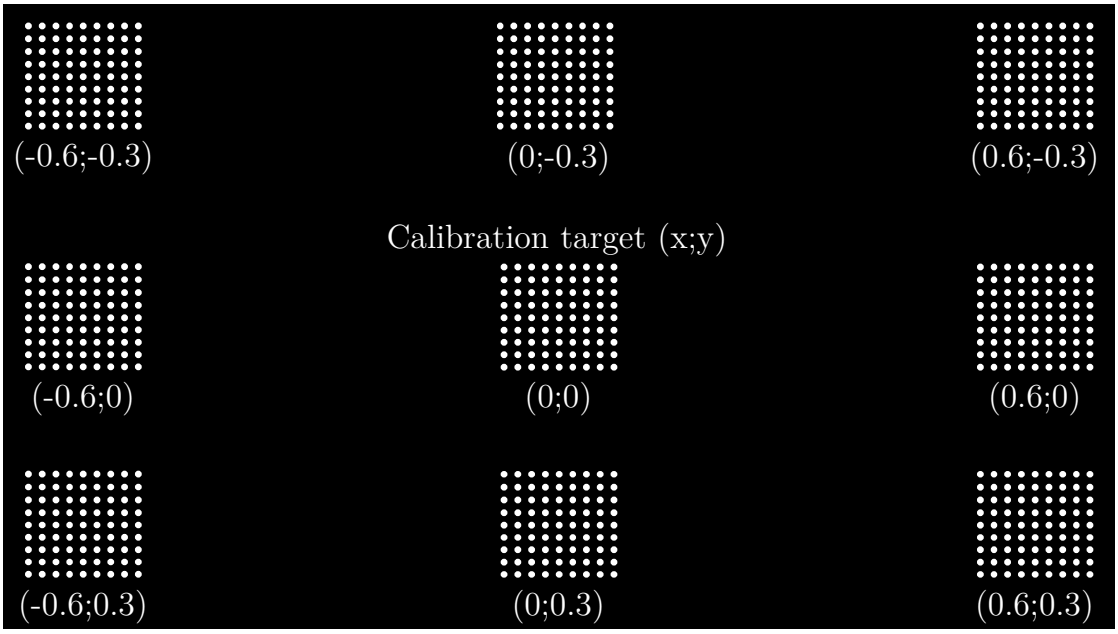


Figure 4.9: Calibration validation using the 3D calibration target placed at different locations inside the simulator.

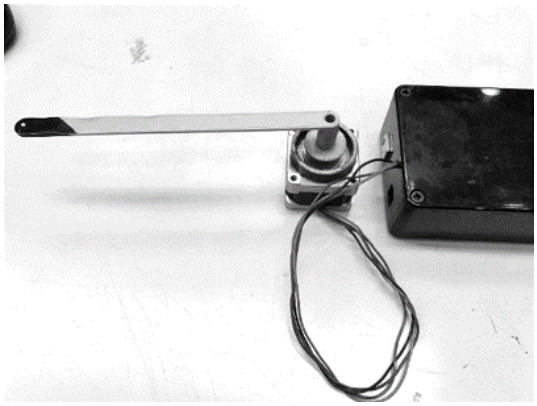


Figure 4.10: Calibration validation using a moving target mounted on a motor.

spheres used in the current work, a known volume with Styrofoam spheres inside was weighed using a precision scale, and it was found that the current spheres had a density of around 24 kg/m^3.

In an attempt to scale the debris, geometric scaling (λ_R) and Tachikawa scaling (λ_K) (detailed in section 2.3.3) were used to determine the equivalent debris size and mass at full scale. This represents a potential approach to scaling, and it is acknowledged that different approaches could have been used for scaling tornadoes (Refan and Hangan, 2018, Baker and Sterling, 2019). A geometric scaling (λ_R) is defined as the ratio between simulated ($r_{c,TVG}$) and full-scale ($r_{c,full-scale}$) core vortex radii as follows:

$$\lambda_R = \frac{r_{c,TVG}}{r_{c,full-scale}} \tag{4.1}$$

with the core radius value taken where the maximal velocities occur. The Fujita scale (Fujita, 1971) gives an estimation of the tornado wind intensity based on damage surveys but no accurate correlation or generalisation between tornado size and wind speed has been found to date. Nevertheless, Wurman et al. (2013) measured the core radius and maximum tangential velocity of 100m and 50m/s,

respectively, at one specific time during an EF2 tornado. Therefore, Table 4.3 gives a selection of "standard" full-scale tornado sizes and maximum wind speeds accounting for a small, medium and large size tornado. The tornado sizes were estimated based on the distribution of mean tornado path widths (Brooks, Doswell and Kay, 2003) with small, medium and large size tornadoes representative of EF0-EF1, EF2-EF3 and EF4-EF5 tornadoes, respectively. Since the EF2 tornado measured by Wurman et al. (2013) matches the medium tornado size in Table 4.3, the maximum wind speed for a small and large tornado was estimated based on the measured maximum tangential velocity. The comparison with different swirl ratios was solely used here to obtain full-scale equivalent based on the experimental measurements.

The full-scale equivalent debris radius was then determined using the geometric scale λ_R and introduced into the Tachikawa scaling equation (Eq. 2.23). The Tachikawa scaling was defined as the ratio of the experimental to full-scale Tachikawa number and taken to be equal to 1 in order to keep similarity. Therefore, it is possible to determine a mass scaling between experimental and full-scale (Eq. 2.24). Table 4.4 summarises the calculated full-scale equivalent debris radius and mass, as well as impact moment and energy and Tachikawa for different experimental debris sizes and swirl ratios.

Table 4.3: Swirl ratio tested and arbitrary full-scale equivalent core radius and maximum wind speed.

Swirl ratio	0.13	0.30	0.7
Full-scale equivalent core radius [m]	20	100	300
Full-scale equivalent maximum wind speed [m/s]	30	50	70

The impact momentum (p_{max}) and loading (E_{max}) were calculated for each experimental debris size and swirl ratio using the equivalent full-scale debris mass and maximum tangential velocity (Table 4.3) as follows:

$$p_{max} = mV_{\theta,max} \tag{4.2}$$

$$E_{max} = \frac{1}{2}mV_{\theta,max}^2 \tag{4.3}$$

where m is the mass of the debris and $V_{\theta,max}$ the maximal tangential velocity. During strong wind events, the most common and most likely structural part of a building to be damaged is the windows, and depending on the glass properties and thicknesses, windows may or may not resist debris impacts. Vickery et al. (2006) showed that the impact resistance of the glass is critical and must be larger than the impact momentum of the debris to avoid failure by impact. Behr and Minor (1994) estimated average impact resistance of 0.1 kg.m/s for 6mm thick window glass. However, this value is likely to significantly vary upon the dimensions, thickness, physical properties and mounting of the glass panel. Impact cladding, with impact velocities between 9 and 34 m/s on 0.48mm Base Metal Thickness corrugated metal cladding (Frye et al., 2009), generally showed that for impact momentum and energy lower than 100 kg.m/s and 1300 J, respectively, the cladding only gets deformed, whereas for higher momentum and energy, the cladding is penetrated by the missile. Impact test requirements for tornado shelters require the safe room to resist impact momentum and energy of respectively 245 kg.m/s and 4350J (FEMA-361, 2015).

Based on Tachikawa scaling calculations, it is found that for the range of debris

sizes and swirl ratios tested in the simulator, the range of equivalent full-scale debris size and mass goes from 0.028 to 0.173m and from 0.006 to 0.513kg for the debris radius and mass, respectively. This gives a range of impact momentum and energy from 0.17 to 35kg.m/s and from 2.6 to 1260J, respectively. This means that the debris tested would most likely cause damage to the building envelope during a full-scale event if the debris reaches and impacts a building at the maximal wind velocities of the tornado stated in Table 4.3. However, debris commonly does not reach the maximum wind speed. During strong wind events with wind gusts exceeding 50 m/s, the debris would generally reach speeds of between 15 and 30 m/s (Song and Ou, 2010).

Finally, the Tachikawa number range, equal for model and full scale, goes from 3 to 43.8, which is consistent with previous work in tornado-like flow fields. Noda et al. (2013) simulated the flight of debris in tornado winds with a range of Tachikawa numbers from 1 to 100, while Maruyama (2011) simulated heavy debris with Tachikawa numbers between 0.71 and 5.69.

Table 4.4: Calculated full-scale equivalent debris characteristics from different swirl ratios and debris sizes tested in the simulator.

	$S = 0.13$				$S = 0.30$				$S = 0.7$			
	experimental debris radius [m]				experimental debris radius [m]				experimental debris radius [m]			
	0.002	0.003	0.004	0.005	0.002	0.003	0.004	0.005	0.002	0.003	0.004	0.005
full-scale equivalent debris radius [m]	0.028	0.042	0.057	0.071	0.052	0.077	0.103	0.129	0.069	0.104	0.139	0.173
full-scale equivalent debris mass [kg]	0.006	0.02	0.046	0.09	0.017	0.056	0.132	0.259	0.033	0.111	0.263	0.513
full-scale equivalent impact momentum [kg.m/s]	0.17	0.59	1.39	2.71	0.83	2.79	6.62	12.93	2.3	7.76	18.39	35.92
full-scale equivalent impact energy [J]	2.6	8.8	20.8	40.7	20.7	69.8	165.5	323.2	80.5	271.5	643.7	1257.2
Tachikawa number	7.6	5.1	3.8	3	24.6	16.4	12.3	9.9	43.8	29.2	21.9	17.5

In order to release the debris inside the simulator, a seeding system has been designed and manufactured in the Civil Engineering Laboratories (Figure 4.11). It consists of a disc with 100 equidistant holes of 0.002m diameter connected to a stepper motor. The disc was enclosed in a chamber and attached to a motor rotating at a constant speed. A vent passing through and aligned with the holes on the wheel, which were then filled with 0.002m Styrofoam spheres. The seeding system was then closed and attached to the floor under the simulator connecting the vent to the surface pressure taps. The seeding system was placed at either 0, 0.5, 1 or $2r_c$. In order to release the spheres inside the simulator, the motor rotated the disc which aligned the vent with each individual particle at a time. The pressure difference between inside and under the simulator naturally sucked the spheres in. Different motor speeds were tried out to evaluate the shortest but most efficient time to release the spheres as fast as possible while still being

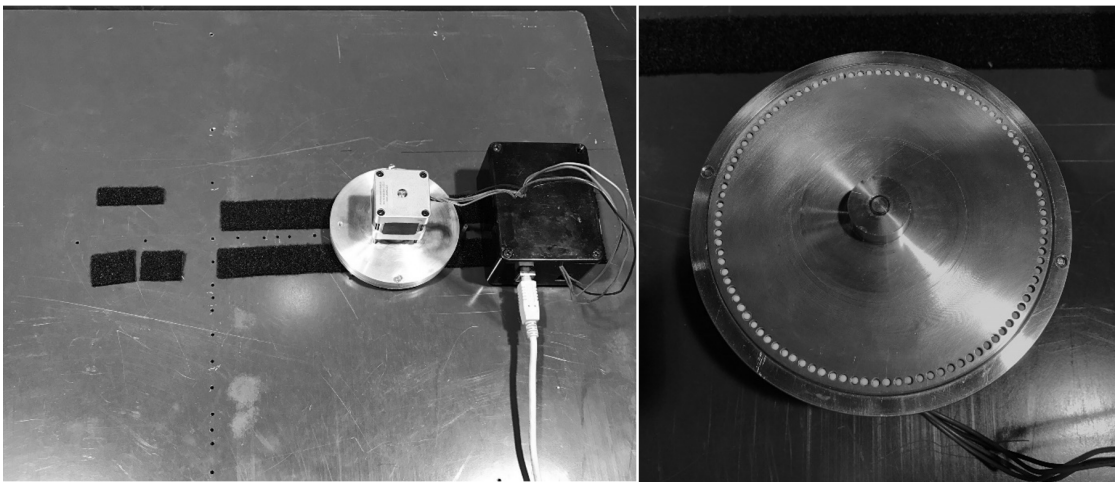


Figure 4.11: Device used to release Styrofoam spheres inside the simulator. The device is mounted under the simulator and can be placed at different positions (left) and consists of a perforated wheel loaded with Styrofoam spheres (right).

able to distinguish them during the particle tracking process. It was found that a motor speed of 30 rotations per minute, releasing 100 spheres in about 2 seconds, was optimal. Finally, the fact that this device could only seed 0.002m Styrofoam spheres was a drawback but this limitation was only caused by the use of the pressure taps to seed the flow.

A low-rise building model (20mm sides length $\times$ 20mm height, Figure 4) was 3D printed and also used to initiate debris flight from the building's roof. The building model has a geometric scale of 1/8 with regards to the size of the experimental core radius. Based on Wurman et al. (2013)'s full-scale tornado measurements, the building model would be equivalent to a building of around 13 $\times$ 13 $\times$ 13m at full-scale. The building model was placed at different locations and one hundred spheres (compact debris) were injected into the flow field from the top of it.

4.5 Data pre-processing

The pre-processing of the video footage and images before being used in the particle tracking software plays an important role in the rendering of the particle trajectories. The particle tracking software used in the current work requires the images to be processed with a specific format. Therefore, careful preparation of the images was necessary to quickly and easily obtain particle tracking datasets.

The cameras record videos in an MTS format, which is a "Advanced Video Coding High Definition" video format. However, the PTV software requires input with TIFF 8-bit grayscale images sequentially named. Therefore, to extract each individual frame from the recordings, a script was developed using the FFmpeg software (FFmpeg, 2000) and was coded in either a Unix or Windows version.

FFmpeg is a free software containing all the video codecs and libraries to handle multimedia media. The first step was to extract images from the recordings. Extracting each frame sequentially can easily be done by a command prompt of the form:

```
1: ffmpeg -i example_video.mts frame_%4d.tif
```

where '`-i`' specifies the input data, `example_video.mts` is the name of the file and '`%4d`' a 4-digit output number. However, each TIFF image sizes 3MB in memory, which means each second recorded at 480fps takes around 1.5GB of hard drive space per camera.

To be able to reduce the size of the files, more pre-processing was carried out. The image processing was performed using the open-source ImageMagick software suite (ImageMagick, 1990). ImageMagick is a software suite capable of editing, processing, and displaying images. The following methods were used to process the images, enhance the visibility and reduce the file sizes:

- *Baseline image subtraction.* Subtracting a baseline image is a common technique in image processing to isolate a moving object from a fixed background. In the present case, it helps to isolate white particles on a black background, which improves the detection and tracking of the particles by increasing their contrasts. On ImageJ, the operation is performed by adding the command option "`-compose minus`".

- *Threshold.* To reduce the size of the images, a threshold is applied to create a binary image. By doing that, each pixel value above the brightness threshold is given the value '1' while a pixel value below is given the value '0'. It reduces

the size of the output file to around 35KB, i.e. 85 times smaller than the original file. Consequently, each second of post-processed images takes 16MB of hard drive space per camera. On ImageJ, the operation is performed by adding the command option '`-auto-threshold`'.

- *Conversion.* The conversion converts the original TIFF file into an 8-bit grayscale TIFF scale. Whereas the previous steps are not mandatory to use the OpenPTV software, the conversion into the right image type is vital to make sure the software reads the images. On ImageJ, the operation is performed by adding the command option '`-depth 8`' and '`-type grayscale`'.

- *Renaming.* The OpenPTV software requires the file names to be sequentially named from `cam1.10001`. Therefore, the original TIFF files have to be renamed to remove the extension '.TIFF'.

The image processing was performed in a single command line using ImageMagick as follows:

```
1: convert ${files[$i+1]} ${files[$i]} -compose minus -composite -auto
2: -level -depth 8 -type grayscale -auto-threshold ${files[$i]
```

The images were then renamed to match the required input filename:

```
1: for f in *.tiff; do mv $f ${f%.tiff}; done
```

4.6 Data post-processing

4.6.1 OpenPTV software

Once the images were extracted from the videos, it was necessary to post-process the images to determine the particle coordinates in each camera reference, perform

the correspondence between the cameras and determine the 3D positions of each camera. The open-source OpenPTV software, initially developed at ETH Zurich (Willneff, 2003), and recently available in an open-source package (OpenPTV, 2012), was used to perform the camera calibration, post-process the images and perform the tracking. However, some background on the main procedure steps is given thereafter.

Either on the calibration or the tracking side, particle detection is based on a high-pass filter and grey value threshold. Using this method, it is possible to tune the particle recognition based on the particle brightness and therefore reduce the detection of background noise. The particle detection identifies each particle as a sum of pixel brightness values above the grey value threshold. Once the particles are detected, it is either possible to determine the particles 3D positions on a specific image or run the particle recognition sequence over a set of images. Working on a specific image and determining 3D positions helps to evaluate the calibration performance. In section 2.3.3, epipolar lines were introduced and described as virtual lines related to a stereoscopic system. Once the calibration is done, the corresponding epipolar lines for each particle detected can be displayed on the software for each camera image. Therefore, when using two cameras or more, it is possible to display the intersection of the epipolar lines for each camera (see Figure 4.12). The closer the intersections to the particle centroid, the better the calibration. In order to obtain a good correspondence between the cameras, correspondence criteria based on the distance of the particle centroid to the epipolar lines are used to determine the quality of the correspondence. Once correspondences are established for the particles, each particle is attributed to an

asset number and will be identified by this number during the tracking process. If at some point during the tracking process a correspondence cannot be established, the particle is seen as a new particle, and a new trajectory is created.

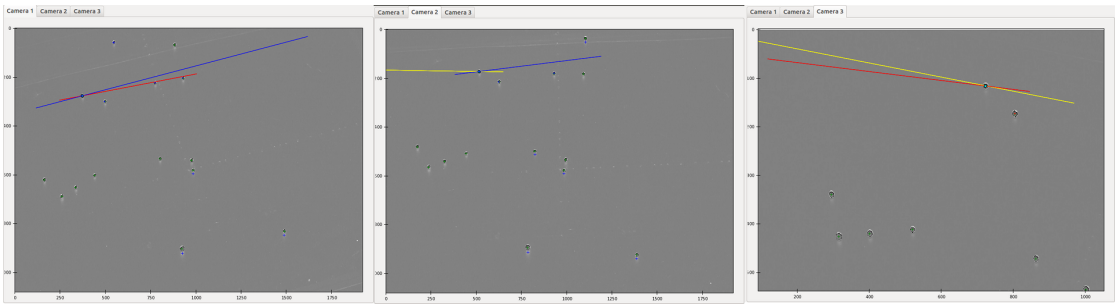


Figure 4.12: Example of epipolar lines displayed for each camera for a specific particle on OpenPTV software. The closer the intersection from the particle centroid, the better the calibration.

The tracking process consists of finding the closest particle and connecting each individual one over time to construct a trajectory. However, when a significant number of particles are present, it can be difficult to determine the closest neighbour. In order to reduce any ambiguities, the particle position for the next timestep is predicted from the previous timesteps, and the predictions are transferred and compared between cameras to find the corresponding area where the particle is expected (Willneff, 2003). The calibration is, therefore, not only important for finding correspondences between the cameras but also plays a crucial role in obtaining good quality trajectories.

Since the software itself only provides the raw particle tracking data and does not perform any statistical analysis, compared to commercial software available on the market such as Shake-the-Box (Schanz et al., 2013); therefore, significant post-processing of the data was necessary to analyse the trajectory data obtained with OpenPTV.

4.6.2 Particle trajectories

Trajectory reconnection

The present work focuses on tracking individual debris trajectories over time. Therefore, it is important that each trajectory can easily be identified from its starting and stopping point and only counts a single trajectory, i.e. no disconnection. A significant effort was made in the pre- and post-processing of the data images to ensure long fully tracked trajectories. However, sometimes correspondences could not be established, and partial trajectories were obtained. As a result, an algorithm was developed, with a similar approach to the particle tracking algorithm, to link partial trajectories by seeking neighbour trajectories. In the present work, the fact that each particle describes a circular motion, due to the tornado-like vortex flow field, makes the linking easier. As the particle leaves the release point, its radial distance typically increases with time. Therefore, by predicting the next potential radial distance and searching for trajectories starting in a specific area, it was possible to reconnect partial trajectories and obtain a set of fully tracked trajectories.

Filtered positions, velocities and accelerations

As previously mentioned, the quality of the calibration as well as the illumination influences the correspondences and trajectories and can result in noisy trajectories. To be able to reduce the noise and obtain smooth trajectories, 3D coordinates were smoothed out using a polynomial fitting, as used by Luthi et al. (2005) for post-processing particle tracking data. The fitting is based on a moving cubic spline data interpolation acting as a low-pass filter (Luthi et al., 2005) and is expressed

as:

$$\hat{x}_i^t = c_{i,0} + c_{i,1}t + c_{i,2}t^2 + c_{i,3}t^3 \tag{4.4}$$

where $i = 1, 2, 3$ corresponds to the x, y and z direction and $\hat{}$ the filtered expression. 21 points centred on x_i^t are fitted using a spline to determine the coefficients $c_{i,j}$. Determining the velocities from the filtered positions using central differences is only first order, therefore velocities are particularly sensitive to the position errors. However, taking the first and second derivative of Equation 4.4 gives, respectively, the filtered velocity and acceleration, which are defined as:

$$\hat{u}_i^t = c_{i,1} + 2c_{i,2}t + 3c_{i,3}t^2 \tag{4.5}$$

and

$$\hat{a}_i^t = 2c_{i,2} + 6c_{i,3}t \tag{4.6}$$

4.6.3 Vortex wandering

In order to quantify the fluctuations in the vortex centre's position over time, a single camera and multiple debris were used to determine the motion of the vortex centre. It was suggested in section 3.6 that the physically simulated vortices tend to only have a two-cell structure, or at least transitional. Therefore, it was found during preliminary tests that debris never reached the vortex centre and described a circular 'free-of-debris' region. Debris positions were recorded using PTV technique and post-processed to calculate the size and position of the circular region over time by fitting a circle to it.

Different statistical methods based on the least-squares method exist to fit a circle

to scattered data (Umbach and Jones, 2003) but mainly differ for a low number of scattered points and partial circle shapes. In the present work, a large number of scattered points ($>$ 100 points) describing a full circle were used; therefore, only low divergence between the methods would be noticed. The direct least-squares fitting method developed by Pratt (1987) and coded by Chernov (2009) was used to estimate the vortex centre's position and radius over time. The algorithm was initiated by a rough estimation of the vortex centre's position to search for neighbour points within a boundary limit (dot-dashed line in Figure 4.13), and determine the best circle fit in the central region at $t = 0$s. Then, for each timestep, a circle was fitted to the set of points located within the boundary threshold around

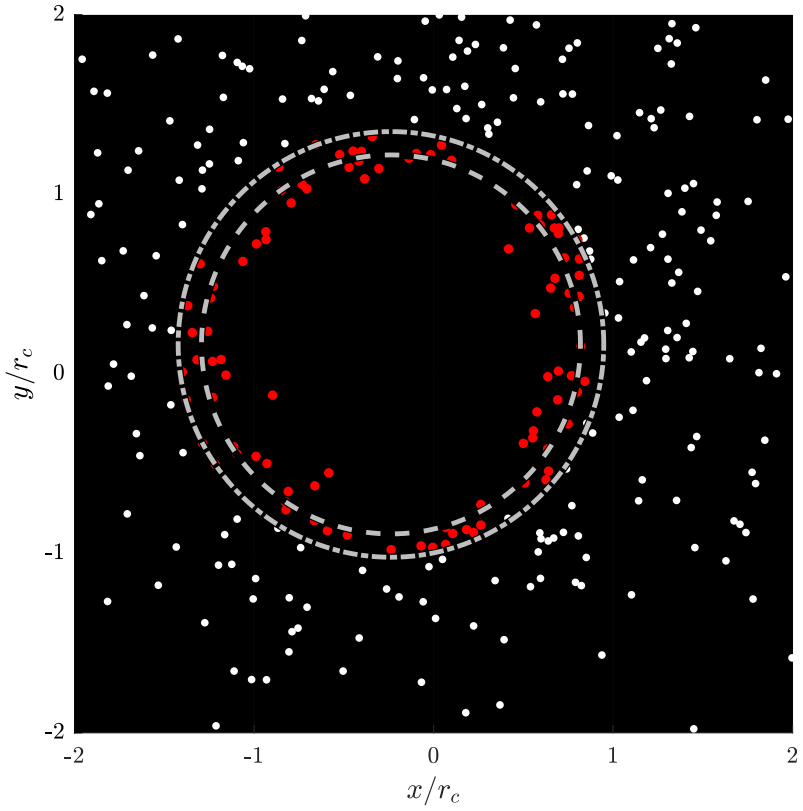


Figure 4.13: Circle fitting in scattered data.

the previous circle fit. As the vortex centre is not significantly moving between two timesteps, searching for neighbour points to the previous circle fit helped to reduce the calculation time and improve robustness.

This technique revealed to be very accurate and easy to implement. Results are discussed in section 4.8.2. This technique also has good potential for accurately evaluating the vortex wandering in other tornado simulators. Vortex wandering is to date generally estimated using Particle Image Velocimetry (PIV) (Zhang and Sarkar, 2012) or surface pressure analysis (Gillmeier et al., 2017, Refan and Hangan, 2018) . PIV gives accurate results but requires using a laser and post-processing to estimate the vortex wandering (Pelc, 2014, Zhang and Sarkar, 2012), whereas a considerable number of pressure taps would be required to accurately estimate the vortex wandering from surface pressure data. The technique used here only requires a single camera, debris and little efforts to detect particle positions and fit a circle to each image.

4.6.4 Debris path

When seeding a large number of particles to the flow over time, each particle trajectory was found to have different initial directions due to the non-stationarity of the flow field. As a result, particles trajectories between initial and final flight times describe a path. In full-scale, the path would be the region where potential damage can be caused to engineering and non-engineering structures. Therefore, knowing the evolution of the debris path over time gives an idea of the potential risk associated with windborne debris in close or far vicinity of a tornado. In order to study the debris path from experimental data, a method was developed to estimate the debris path width over time using data obtained with PTV. The method

consists of finding over time the positions of all particles located perpendicularly to the mean trajectory and estimating the path width based on these positions. The method was performed through different steps described thereafter and is also summarised in Figure 4.14:

1. Calculating the radial positions and flight distances for each particle n and for each timestep t (Step 1 - Figure 4.14). As particles were seeded overtime and described a 3D trajectory, working with radial position r and flight distance reduces a 4-variable system to only two variables. The radial positions were calculated as follows:

$$r_n^t = \sqrt{(x_n^t)^2 + (y_n^t)^2 + (z_n^t)^2} \tag{4.7}$$

   where x_n^t, y_n^t and z_n^t are the 3D positions for each particle at each timestep.

   The flight distances were computed using the cumulative trapezoidal numerical integration of the mean debris velocities, which gives the evolution of the distance travelled by a particle over time.

   From this point, all the calculations were done using the radial distance (r) and the flight distance (FD) (Step 2 - Figure 4.14).

2. Calculating the mean trajectory over 100 samples.

3. For each radial position and particle, computing the local slope A and intercepting B coefficients of the mean trajectory and the line perpendicular to it (Step 3 - Figure 4.14). This is done to ensure the time-dependency between

each particle. The coefficients are determined as follows:

$$\left\{ A^t_{\text{mean}} = \frac{r^{t+1}_{\text{mean}} - r^t_{\text{mean}}}{FD^{t+1}_{\text{mean}} - FD^t_{\text{mean}}} \; ; \; B^t_{\text{mean}} = r^t_{\text{mean}} - A^t_{\text{mean}} \cdot FD^t_{\text{mean}} \right\} \tag{4.8}$$

and

$$\left\{ A^t_{\perp,\text{mean}} = -\frac{1}{A^t_{\text{mean}}} \; ; \; B^t_{\perp,\text{mean}} = r^t_{\text{mean}} - A^t_{\perp,\text{mean}} \cdot FD^t_{\text{mean}} \right\} \tag{4.9}$$

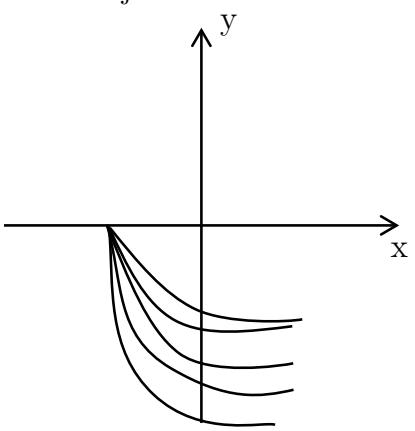
where for each particle and timestep A^t_{mean} is the local slope, B^t_{mean} the local intercept and FD^t_{mean} the flight distance, $A^t_{\perp,\text{mean}}$ is the local perpendicular slope to the mean trajectory, $B^t_{\perp,\text{mean}}$ the local perpendicular intercept to the main trajectory.

4. For each radial position and particle, finding the closest points to the perpendicular direction of the main trajectory (Step 4 - Figure 4.14).

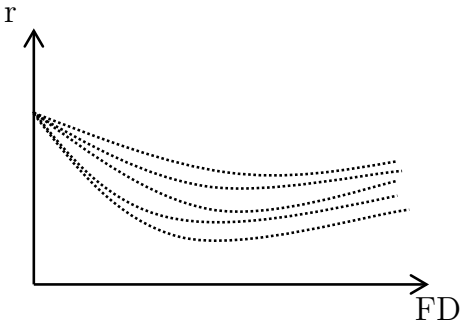
$$d^t_n = \min \left(\frac{\left| B^t_{\perp,\text{mean}} + A^t_{\perp,\text{mean}} \cdot FD^t_n - r^t_n \right|}{\sqrt{1 + \left(A^t_{\perp,\text{ mean}} \right)^2}} \right) \tag{4.10}$$

5. For each radial position, calculating the probability density function (PDF) of the closest points found in Step 4, and determining the path width as 90% probability (2σ) (Step 5 - Figure 4.14).

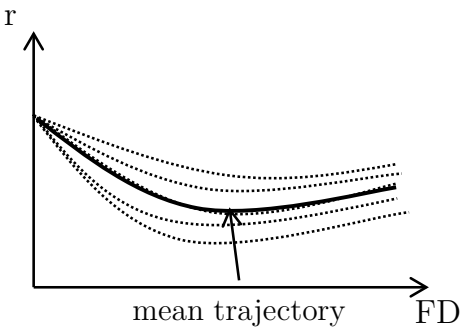
0. Obtain trajectories



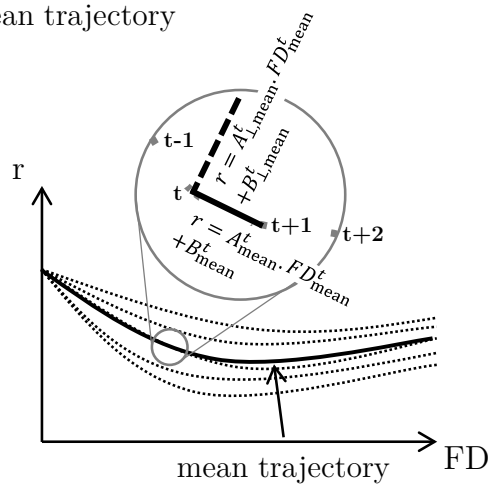
1. Calculate radial position and flight distance



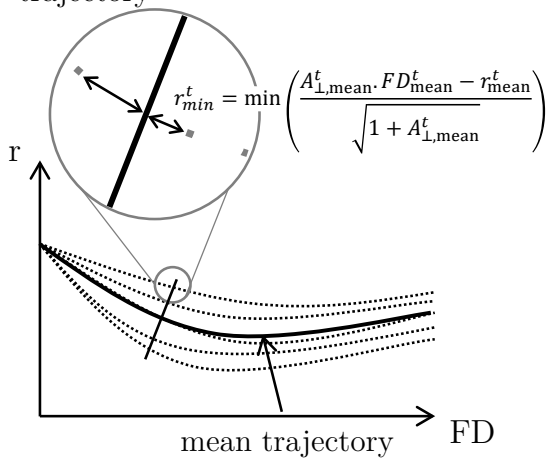
2. Calculate mean trajectory over 100 samples.



3. Calculate perpendicular direction to mean trajectory



4. Calculate closest distance to mean trajectory



5. Obtain path width from PDF of minimal distances

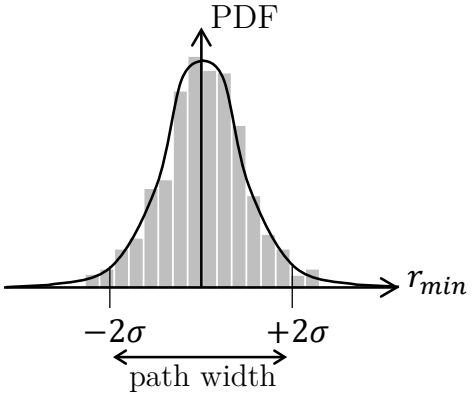


Figure 4.14: Step by step procedure to calculate the debris path width from trajectory data.

4.7 Camera validation

The camera calibration methodology was described in section 4.3 which dictates the accuracy of a particle tracking system. Therefore, it is necessary to validate the calibration to ensure accurate position and velocity tracking data.

Figure 4.15 and Figure 4.16 show examples of the reconstructed 3D positions of the calibration targets. The circles with a cross refer to the reconstructed centroid. When the cross overlaps the target position, the reconstructed centroid is located above it; when the cross is not visible, the reconstructed centroid is located under it. After calibration, the images were processed using the tracking software to

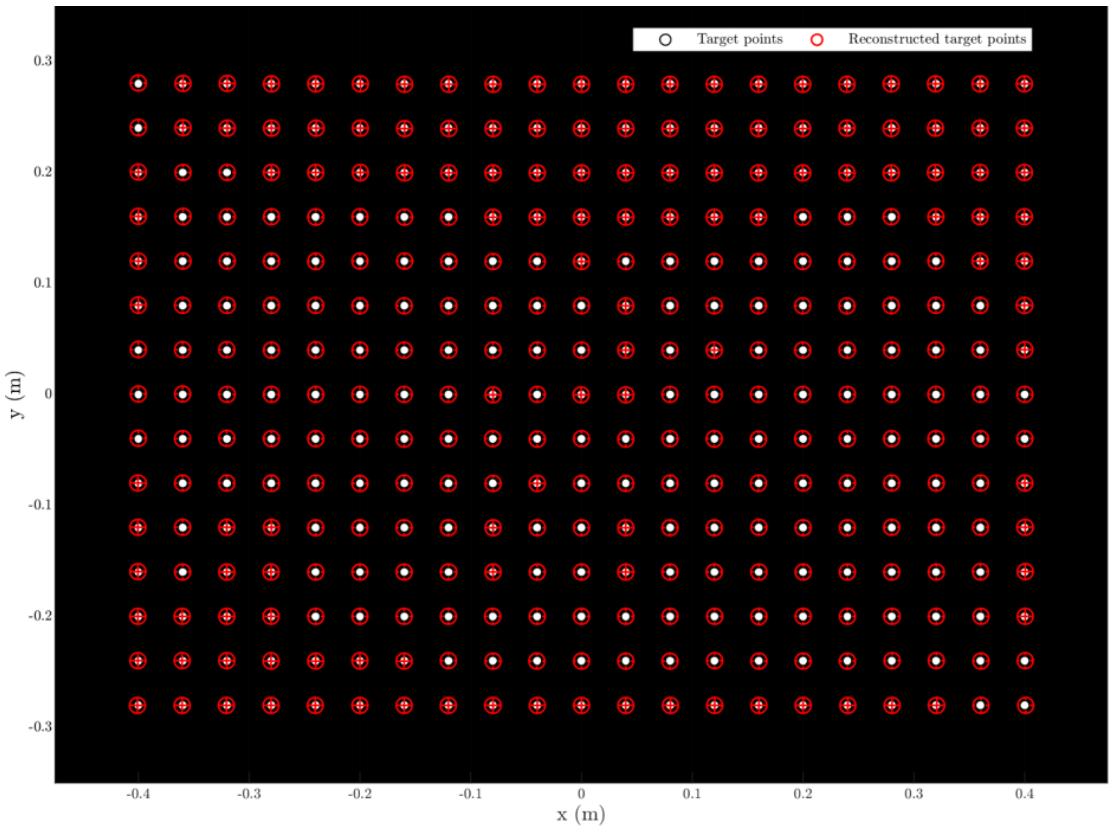


Figure 4.15: Real and reconstructed target points using the planar calibration target.

evaluate the calibration performance. For any of the arrangements mentioned in section 4.3.2, the reconstructed 3D positions generally matched reasonably well to the calibration target positions with errors up to about 3mm (Table 4.5, Table 4.6, Table 4.7). However, as the calibration targets did not cover the entire field of view, and extrapolation outside the calibrated region can result in large deviations, it was important to validate and evaluate the calibration at different locations in the field of view. Figure 4.9 showed the different locations where the 3D calibration target was placed to perform the calibration validation. For each location, the 3D positions of the calibration were reconstructed, and the root mean square (RMS) error was calculated to evaluate the accuracy of the calibration and expressed as

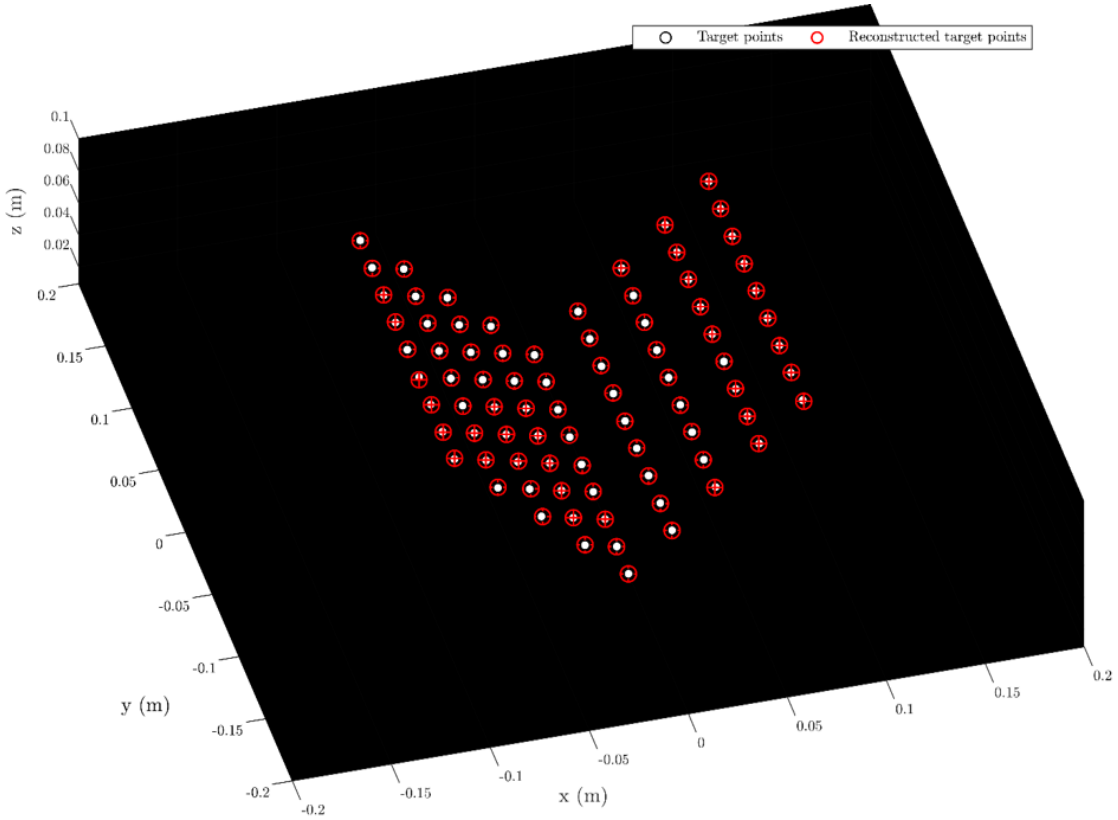


Figure 4.16: Real and reconstructed target points using the 3D calibration target.

follows:

$$RMS_i = \sqrt{\frac{\sum_0^N (\hat{y}_i - y_i)^2}{N}} \tag{4.11}$$

where $i = 1, 2, 3$ corresponds to the x, y and z direction, $\hat{y}_i$ the positions on the calibration target, y_i the reconstructed positions of the calibration target and N the number of calibrated points.

4.7.1 Static validation and positioning errors

Table 4.5 and Table 4.6 summarise the RMS errors in the $x-$, $y-$ and $z-$direction for each target location and each camera arrangement using the 3D and planar calibration target, respectively. For the 3D calibration target (Table 4.5) and the camera arrangement 3B, where all cameras were located at the same height, the RMS errors for all targets outside the calibrated region (i.e. $\pm$ x/y $>$ 100mm) show significant errors up to about 3mm, which is bigger than the debris size mainly used. Within the calibrated region, the RMS errors in the $x-$ and $y-$ direction are relatively marginal, albeit the RMS error in the $z-$direction is about ten times higher. The further away from the target was from the cameras, the bigger the errors. This is most likely due to the orientation of the cameras with target centroids more identifiable closer to the cameras. For arrangements (b) and (c), one of the cameras was placed higher than the others. The arrangement 2B-1M gave similar errors to the arrangement 3B. However, arrangement 2B-1T significantly reduced the errors in the $x-$ and $y-$ direction, although a lower amelioration is shown in the z direction.

For the planar calibration target, the RMS errors for each target location are significantly lower than when using the 3D calibration target (Table 4.6). The

planar target covers approximatively 20 times more horizontal field of view than the 3D target, resulting in a more precise calibration. Similarly to the 3D target, the arrangements 3B and 2B-1M gives large errors in the z direction, most likely due to the orientation of the camera. However, the errors for the arrangement 2B-1T reasonably reduce in the $x-$, $y-$ and $z-$direction, compared to the previous arrangements, and therefore give an overall error lower than the real-world pixel size.

Table 4.7 shows the evaluation of the calibration between the different arrangements and calibration targets. Since the calibration is usually performed with a 3D target for a stereo system, the average RMS errors in the $x-$, $y-$ and $z-$direction were calculated and compared to the errors of arrangement 3B with the 3D target. Table 4.7 reveals that placing the camera marginally higher improves the accuracy of the calibration when using either the planar or 3D target. However, placing the camera higher with the arrangement 2B-1T shows significant improvement in the calibration. Finally, the results show that when using a large planar target 3D positions are more accurately measured by the PTV system than when using a small 3D target.

Table 4.5: 3D position RMS errors (RMS_x;RMS_y;RMS_z) of the calibration target using the 3D calibration for the three different camera arrangements.

		x ($\times 10^{-3}$ m)		
	3B	-0.6	0	0.6
y ($\times 10^{-3}$ m)	-0.3	(3.62;2.88;4.31)	(3.15;3.63;4.05)	(2.97;3.11;3.89)
	0	(2.39;1.94;3.77)	(0.24;0.28;2.16)	(1.56;0.98;3.12)
	0.3	(1.98;2.32;3.19)	(1.73;1.50;2.63)	(1.44;1.37;3.09)

	2B-1M	-0.6	0	0.6
y ($\times 10^{-3}$ m)	-0.3	(3.42;2.88;4.16)	(3.14;3.51;3.94)	(2.71;2.92;3.82)
	0	(2.35;1.81;3.59)	(0.35;0.27;1.99)	(1.42;0.95;3.06)
	0.3	(1.87;2.20;3.08)	(1.71;1.45;2.42)	(1.34;1.36;2.83)

	2B-1T	-0.6	0	0.6
y ($\times 10^{-3}$ m)	-0.3	(1.30;1.18;3.97)	(1.39;0.88;3.54)	(1.04;1.05;3.56)
	0	(1.05;0.84;2.92)	(0.21;0.16;1.54)	(1.15;0.87;2.48)
	0.3	(1.12;1.29;2.71)	(1.39;1.11;2.19)	(1.07;0.99;1.51)

Table 4.6: 3D position RMS errors (RMS_x;RMS_y;RMS_z) of the calibration target using the planar calibration for the three different camera arrangements.

		x ($\times 10^{-3}$ m)		
	3B	-0.6	0	0.6
y ($\times 10^{-3}$ m)	-0.3	(0.38;0.35;1.19)	(0.36;0.37;1.22)	(0.36;0.35;1.19)
	0	(0.37;0.39;1.21)	(0.35;0.37;1.20)	(0.35;0.40;1.18)
	0.3	(0.36;0.39;1.18)	(0.36;0.33;1.15)	(0.37;0.40;1.15)

	2B-1M	-0.6	0	0.6
y ($\times 10^{-3}$ m)	-0.3	(0.36;0.37;0.98)	(0.40;0.36;1.22)	(0.49;0.27;0.99)
	0	(0.37;0.38;1.05)	(0.38;0.30;1.02)	(0.40;0.36;0.97)
	0.3	(0.36;0.39;1.00)	(0.36;0.38;0.99)	(0.38;0.41;1.08)

	2B-1T	-0.6	0	0.6
y ($\times 10^{-3}$ m)	-0.3	(0.18;0.16;0.72)	(0.19;0.18;0.73)	(0.17;0.18;0.66)
	0	(0.20;0.16;0.70)	(0.18;0.17;0.76)	(0.15;0.16;0.66)
	0.3	(0.18;0.17;0.74)	(0.20;0.17;0.71)	(0.21;0.18;0.72)

Table 4.7: Percentage of calibration precision increase between the different camera arrangements and calibration targets, relative to planar and 3D targets with arrangement 3B.

Target		planar	3D
	Arrangement	3B	3B
3D	3B	-	0.00%
3D	2B-1M	-	4.76%
3D	2B-1T	-	35.60%
planar	3B	0.00%	63.30%
planar	2B-1M	5.40%	65.00%
planar	2B-1T	48.70%	81.00%

4.7.2 Dynamic validation and velocity errors

The static validation showed a satisfactory level of spatial accuracy but did not account for the position and velocity accuracy dependent on the synchronisation between the cameras. A slight delay from a camera will incur a slightly erroneous position which will ultimately result in a wrong velocity. Variability of the particle centroid recognition due to illumination variations also influences the accuracy of the particle position, which also gives erroneous velocities. Therefore, a dynamic validation doing a circular motion was performed to evaluate the position and velocity error using a target rotating at a known constant velocity. The arrangement 2B-1T was used with the planar calibration as it showed the highest level of accuracy. Figure 4.17 shows four different views of the reconstructed motion of the moving target. Overall, the moving target was correctly tracked and described a circle as expected. Slight offset from the expected trajectory could be due to a small fluctuation of the target during the motion, calibration errors or errors in determining the particle centroid. The average RMS error, evaluated from each RMS error of each position over time, was 1.14mm, 1.36mm and 1.98mm in the $x-$, $y-$ and $z-$direction, respectively. This indicates that the accuracy of the system is decreasing due to the different factors mentioned before, although the error increase could be attributed to synchronisation disparities between the cameras. Table 4.8 summarises the average radial position and height of the moving target and its average velocity. It shows that overall, the tracking system is, in addition to the static accuracy, also accurate dynamically. The position errors are considered below 2% while the velocity error around 1%. Given the level of position and velocity accuracy, the arrangement 2B-1T was therefore used in the

following section to investigate the flight of debris subjected to a tornado-like flow field.

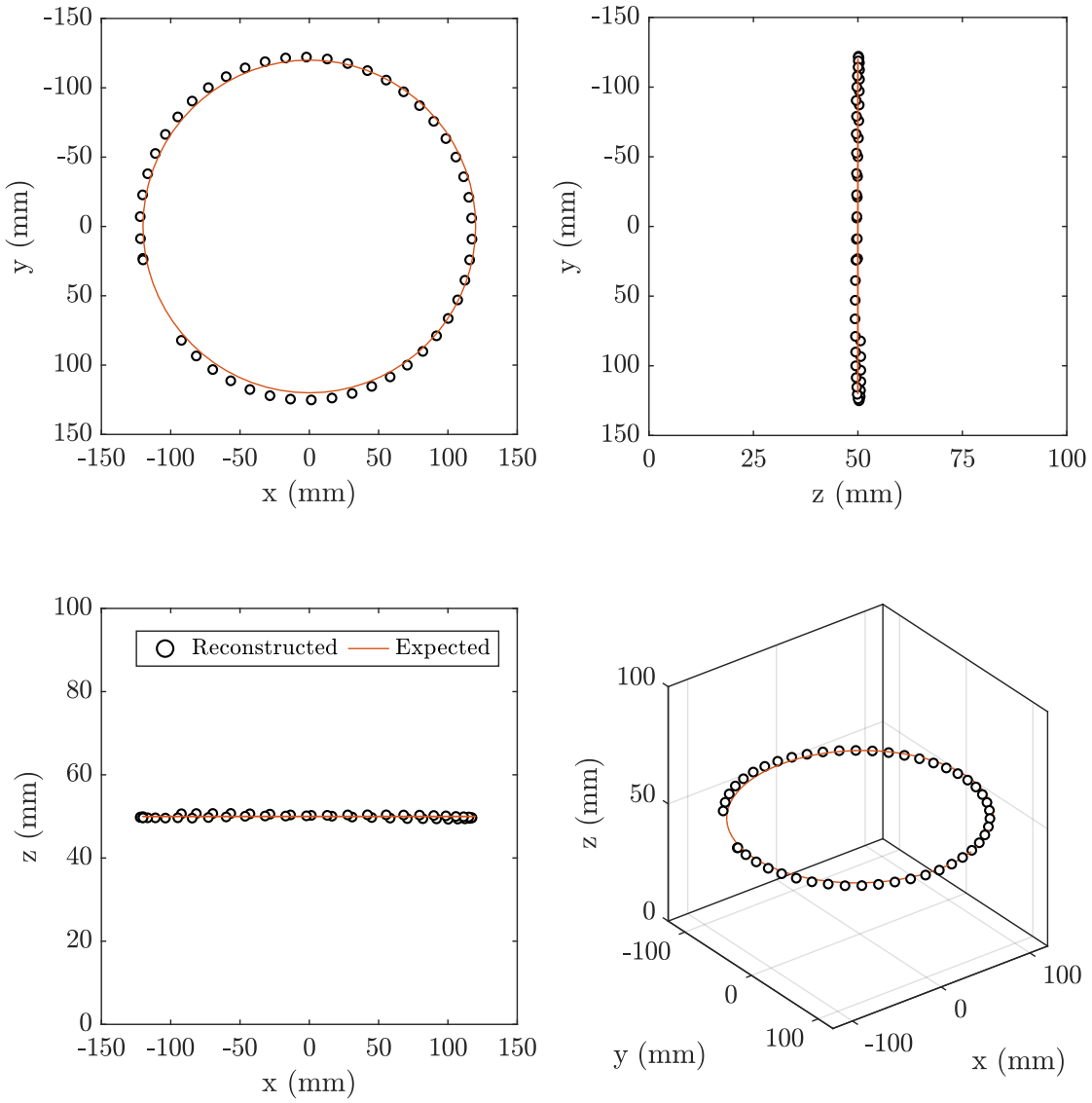


Figure 4.17: Top (a) – Side (b & c) and isometric view of the reconstructed moving target used during dynamic calibration validation.

Table 4.8: Real and reconstructed radial position, height and velocity of a circular moving target.

	Radial position ($\times 10^{-3}$m)	Height ($\times 10^{-3}$m)	Velocity (m/s)
Expected	120	50	10
Reconstructed	120.79	50.93	10.11
Error	0.65%	1.82%	1.10%

4.8 2D-PTV

In this section, the results looking at the flight of a single particle, as well as the vortex wandering for different swirl ratios using a single camera, are presented. The debris was simply introduced into the flow field manually and the recording started once the debris was swirling around the vortex. The use of a single camera in the present case was judged appropriate as it was visually observed that debris were not lifted up when freely flying in the simulator, i.e. as opposed to mechanically released.

4.8.1 Single debris

Figure 4.18 shows the results obtained using 2D-PTV of a single item of debris subjected to a tornado-like flow field. Debris were found to be swirling around the vortex core without flying up but were lifted enough to be bouncing while swirling. Different sizes of debris, i.e. 0.002, 0.003, 0.004 and 0.005m in diameter, and different swirl ratios, i.e. $S = 0.13$, 0.3 and 0.7, were used to investigate the flight of a single debris. At full-scale, this scenario would represent a nearly stationary tornado in a landscaped environment (i.e. no surrounding buildings or vegetations) with a single item of flying debris.

For $S = 0.13$, Figure 4.18 (a), (d), (g) and (j) show that the debris tends to mainly swirl close to the core radius while being occasionally ejected. The ejections could either be due to a local and transient flow field at the core radius, changing in velocity and/or direction associated with wind fluctuation or due to vortex wandering. Interaction with the simulator's surface (e.g. pressure taps, surface imperfections, etc.), lifting the debris to higher velocity regions, could possibly

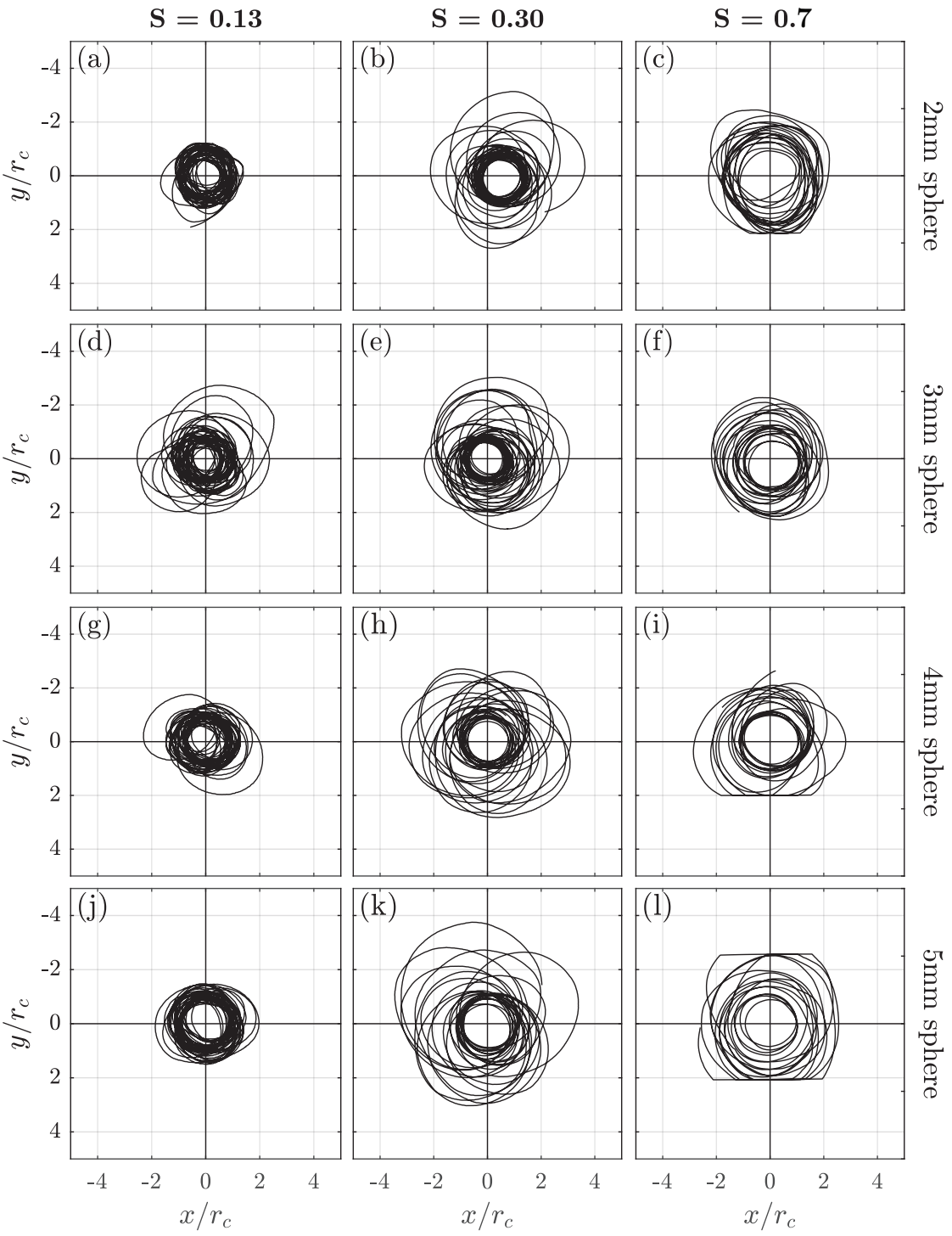


Figure 4.18: Single debris trajectories subjected to tornado-like winds for different swirl ratios (columns) and debris sizes (rows).

be another justification. For $S = 0.13$, the ratio between radial and tangential velocity right outside the core radius is about 50-60 %, which prevents the debris from being ejected by forcing it back to the equilibrium between centrifugal and pressure forces. The different debris path for each revolution also suggests that the vortex inside the simulator wanders. However, turbulent velocity fluctuations may also have an effect on each debris path but separating effects due to vortex wandering or wind field fluctuations seems difficult. For each debris size, it seems that the debris wanders for each revolution between $r = 0.5$ and 1.5, suggesting the vortex to wander up to one core radius size. Zhang and Sarkar (2012) drew a similar conclusion for a lower swirl ratio ($S = 0.03$) in the mini ISU tornado simulator. A description of the vortex wandering for each swirl ratio will be given in the following subsection.

For $S = 0.30$, the debris trajectories tend to be more ejected than for $S = 0.13$ (Figure 4.18 (b), (e), (h), (k)). For this swirl ratio, the tangential velocity is about 30% higher than for $S = 0.13$, which lowers the ratio with the radial velocity up to 40%. As a result, the debris gets potentially ejected more easily and reaches distances up to three times the core radius, before flying again towards the core radius. This behaviour has been observed and recorded at full-scale from a drone with individual debris being ejected before flying back towards the tornado (LiveStormMedia, 2019). Figure 4.18 (b), (e), (h), (k) also shows that the smaller the debris, the closer and longer it swirls around the core vortex, with outer regions repeatedly reaching for larger debris (Figure 4.18 (k)). Therefore, it would suggest the risks at close vicinity to a medium-sized tornado, e.g. EF2-EF3 tornado, varies significantly. The variation of debris size affects not only the momentum but also the flying trajectory. Noda et al. (2013) showed that for a low Tachikawa number

debris tends to fly further when released from the core radius than high Tachikawa, i.e. for heavier and large debris.

For $S = 0.7$, the debris are transitioning towards a similar behaviour than observed for $S = 0.13$, where debris are mainly swirling around the core radius without being significantly ejected outward. An exception is made for Figure 4.18 (i) where the debris was ejected much further than in any other cases. To date, nothing points towards a clear reason why this specific case showed a different behaviour. Repeating the test may have ruled out any potential explanation. Nevertheless, debris trajectories typically fluctuate between $r/r_c = 1$ and $r/r_c = 2$, with the central downdraft preventing the debris from flying inside the core vortex, i.e. for $r/r_c < 1$.

In 2009, Wurman et al. (2013) observed an EF-2 tornado using a fine-resolution DOW and showed that the debris cloud, formed from airborne debris, was approximately twice the size of the tornado itself. Figure 4.18 shows that single debris generally tends to revolve around the core vortex at a radial distance up to $2r_c$. Although the current vortex simulations used here are not in any way a scaled representation of full-scale events, it is interesting to notice that for different swirl ratios and debris sizes a single debris is also generally contained within or close to $2r_c$. Nevertheless, more full-scale observations or measurements would be necessary to assess whether the size of the debris cloud could somewhat be directly related to the tornado size itself. To date, tornadic debris signature (Ryzhkov et al., 2005) can be identified on weather radar images when a tornadic is rich in airborne debris. High debris loading causes high reflectivity on weather radar which most likely indicates a severe tornado. However, the resolution of a weather

radar varies with distances which limits the possibility of a real-time and accurate measurement of the tornado sizes.

Table 4.9 shows the average and maximum total velocity magnitude of the debris normalised by the maximum tangential velocity for each swirl ratio and debris size. For each swirl ratio, average velocities appear to be approximatively constant for any debris size, although variations up to 20% can be observed in somes cases, and consistently lower than half the maximum tangential wind velocity for the specific swirl ratio. However, the maximum wind speed appears to reduce as the debris size increases, with maximum speed up to 80% of the maximum tangential wind velocity. Therefore, the debris is either not reaching the region of maximum tangential velocities or not accelerating fast enough to reach such velocities. This seems to corroborate the conclusions from Song and Ou (2010) that indicate debris are not reaching the maximal wind velocities during strong wind events.

Finally, it is worth noting that in the current work, debris were not being kept in position and then mechanically released, and appeared to not fly up. The main supposition to this behaviour is probably due to the vortex structure, with a central downdraft when the debris is moving towards the core radius, the nature of the

Table 4.9: Normalised average and maximal velocity magnitude of single debris for different swirl ratios and debris sizes.

	$S = 0.13$	$S = 0.30$	$S = 0.7$
2mm sphere	0.297 / 0.753	0.430 / 0.784	0.477 / 0.807
3mm sphere	0.351 / 0.626	0.479 / 0.705	0.451 / 0.772
4mm sphere	0.315 / 0.477	0.400 / 0.611	0.439 / 0.681
5mm sphere	0.316 / 0.454	0.382 / 0.583	0.391 / 0.650

corner region keeps the debris from being lifted.

4.8.2 Vortex wandering

Flow visualisation presented in section 3.3, velocity fluctuations during the velocity mapping in section 3.6, or single debris tracked in the previous section all suggested that the simulated vortices in the simulator wander but could not be clearly quantified. Gillmeier et al. (2017) performed Proper Orthogonal Decomposition on the surface pressure data in the UoB-TVG and identified the vortex wandering in the simulator to be related to an intensifying/weakening of the vortex centre as well as a circular motion around it. However, the number of pressure taps used in this study did not allow the authors to precisely quantify the fluctuation in the vortex centre's position, but only the speed at which it revolves around its centre.

Figure 4.19 shows the distribution of the vortex centre's position over a period of 10s in the simulator. Knowing particles are not reaching the vortex core due to the downdraft in the centre, and by seeding the simulator with a large number of

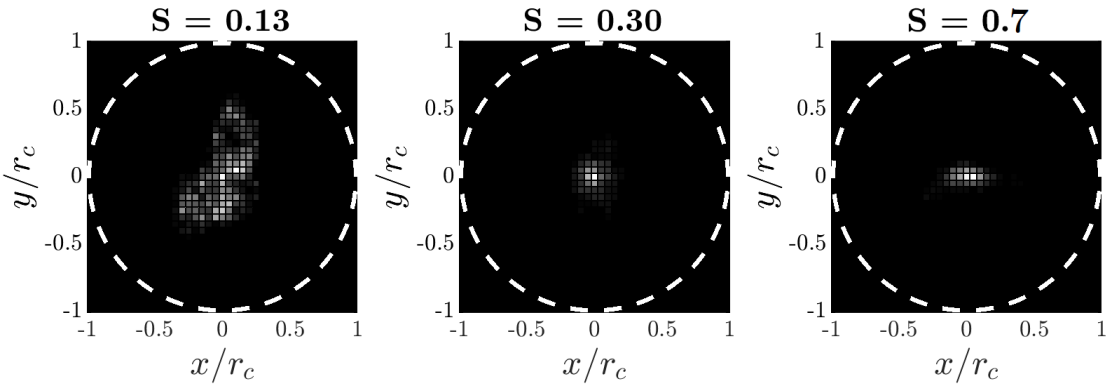


Figure 4.19: Distribution of the vortex centre picturing the vortex wandering for (a) $S = 0.13$, (b) $S = 0.30$ and (c) $S = 0.7$. The dashed line outlines the size of the normalised core radius determined from the wind velocity mappings.

debris, it was possible to track the centre of the core vortex as detailed in section 4.6.2. Figure 4.19 (a) shows the distribution of the vortex centre for $S = 0.13$, which clearly illustrates a large vortex wandering with the vortex centre moving up to $0.5r_c$. The lack of clear structure in the core vortex regions identified in the velocity mapping for $S = 0.13$ can be explained by the large fluctuation in the vortex position observed in Figure 4.19 (a). Zhang and Sarkar (2012) estimated that vortex wandering leads to an underestimation of the maximum tangential velocity by 15% and 4%, and an overestimation of the core radius by $18-29\%$ and 4%, for small and medium swirl ratios, respectively. For $S = 0.30$ and $S = 0.7$, the vortex wandering is clearly lower than for $S = 0.13$ and appears to be confined between $r/r_c = 0$ and 0.25. In addition, in order to determine the travelling of the vortex around the simulator's centre, the technique employed allows the estimation of the size of the core vortex. The ratio between the core radius estimated from the velocity mappings and the methodology here and the relative errors are shown in Table 4.10. Considering the methodology used here to estimate the core radius is being more accurate, it clearly demonstrates the underestimation of the core radius size when performing the velocity mappings for low and medium swirl ratios. However, it is worth noting that the current method is affected by the size of the debris used. Larger/heavier debris would give a larger estimation of vortex

Table 4.10: Estimated error between core radius sizes estimated from wind measurement and particle tracking.

	$S = 0.13$	$S = 0.30$	$S = 0.7$
$r_{c,wind}/r_{c,tracking}$	0.625	0.556	0.824
Error	37%	44%	17%

core, as showed in Figure 4.18, whereas smaller/lighter debris would potentially fly up and compromise the calculation of the vortex core's size. By introducing fluctuations into analytical vortex models, Snow and Lund (1997) estimated errors in core radius size were up to 46%, which agrees with the errors found in Table 4.10. For $S = 0.7$, a low vortex wandering only incurs a 17% difference between the two methods.

4.9 3D-PTV

In this section, 3D trajectories obtained using three cameras are presented. 100 debris were released using the seeding system described in section 4.4 either from the floor, simulating a large number of debris flying in a landscaped environment, or from a building model, simulating the flight of debris consecutive to a building failure. Each test and analysis was carried out using one set of 100 debris.

4.9.1 Floor seeding

Figure 4.20 (a) shows the typical kind of 100 debris trajectories when the debris are seeded into the tornado-like flow field. The debris are lifted aloft, reach their maximum velocities then fall and impact the ground. In order to simplify the visualisation and analysis of the debris trajectories, trajectories are only shown and analysed from their initiation into the flow field until they fall to the ground. However, it is worth noting that the debris tends to bounce on the ground and keeps flying in a similar manner, as shown in Figure 4.18. Figure 4.21 shows the effect of varying the swirl ratios and the release locations on the debris flight behaviour. For all positions and swirl ratios, debris are always ejected outwards from the core vortex before falling down to the ground following the specific vortex flow fields. However, differences in initial direction are noticed when released at the centre of the vortex ($0r_c$), leading to significantly different impacting regions. The variations in the initial directions could be attributed to the variation of the debris shape, the wandering of the vortex or fluctuation of the local flow field around the release position. The former is relatively difficult to validate considering the size of the debris used in this study, although the debris analysis showed an

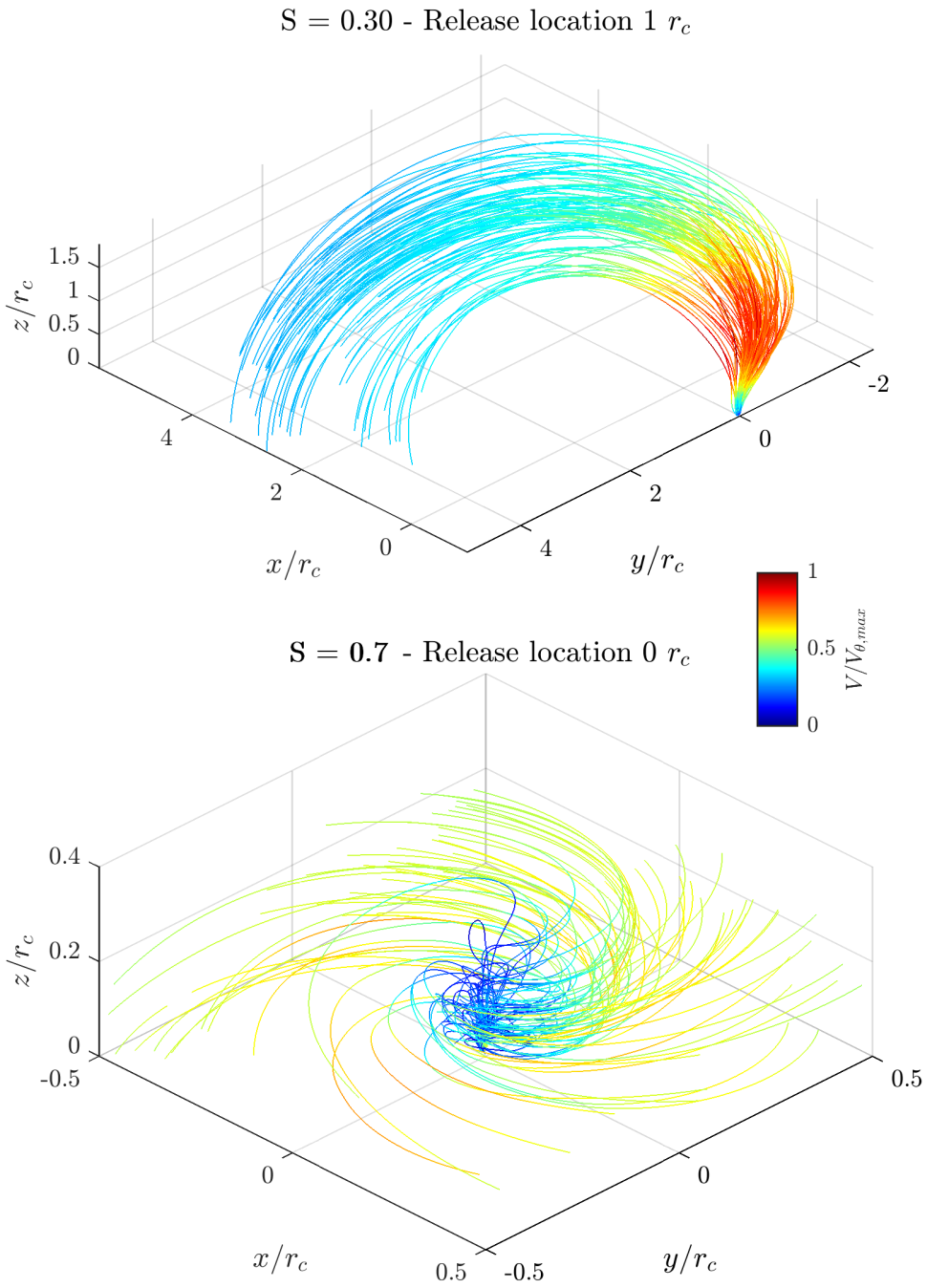


Figure 4.20: 3D representation of debris trajectories when released from (a) the core radius for $S = 0.30$ and (b) the vortex centre for $S = 0.7$. The colours depict the normalised velocities of the debris.

average circularity of 0.93. The latter though can be somewhat correlated to the flow field fluctuation. Figure 4.22 shows the horizontal velocity vectors, taken from the point measurements described in section 3.6, overlapping the early stage debris trajectories for $S = 0.30$ and different release positions. It is relatively clear that early-stage trajectories follow the fluctuation tendency of the flow field around the release position. Therefore, variation in the debris trajectory directions can be attributed to local flow field fluctuation, although it is acknowledged that variations in debris shape may also influence the debris behaviour but could not be validated at this stage. For $S = 0.13$ and $S = 0.30$, this behaviour could be attributed to the vortex wandering with the centre of the vortex not located at the centre of the simulator. For $S = 0.7$, the debris are released inside the turbulent core vortex, as identified during flow visualisations in section 3.3, which results in debris being ejected outside the core in all directions. The 3D plot of this case shows that debris are lifted aloft inside the core vortex until a level of stagnation where the debris vertical motion is slowed down before being ejected outside (Figure 4.20 (b)). This situation reveals that the vortex breakdown has most likely not fully reached the surface yet and that for $S = 0.7$, the flow field has not evolved into a fully developed two-cell vortex structure.

For $S = 0.13$, debris trajectories show similar behaviour when released from the centre ($0r_c$), inside the core vortex ($0.5r_c$) and from the core radius ($1r_c$). When released far from the core radius ($2r_c$), the vertical velocity of the flow field appears to be too low to lift the debris up enough, and the debris tend to generally fall at the proximity of the core radius. The large vortex wandering for this swirl ratio makes it difficult to realistically analyse the debris behaviour. For $S = 0.30$, debris

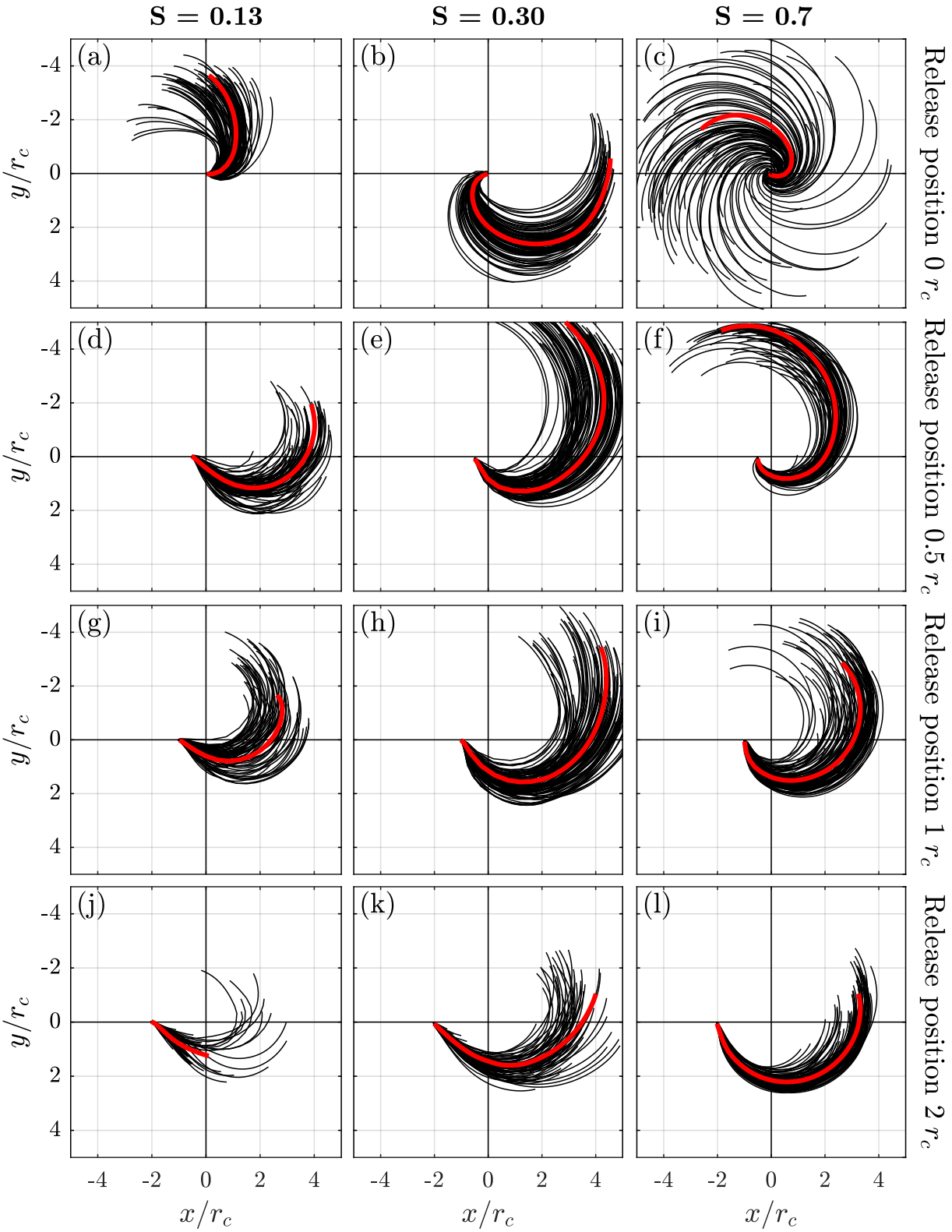


Figure 4.21: Horizontal view of debris trajectories released from different distances from the origin (row) in tornado-like flow with different swirl ratios (column). The red line denotes the mean debris trajectory.

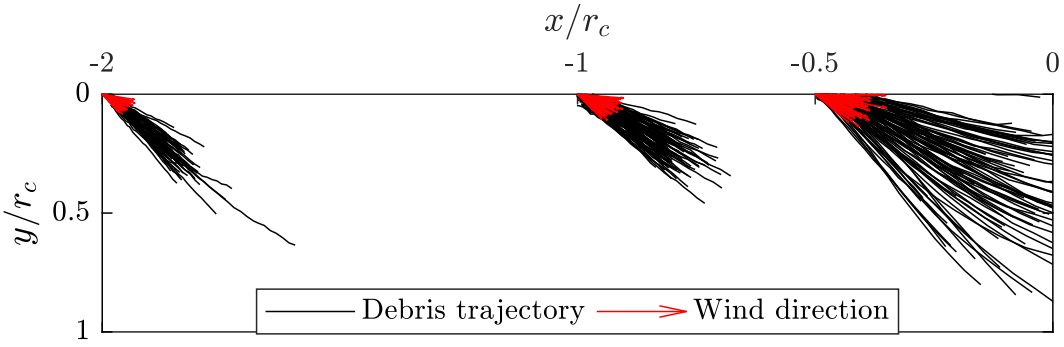


Figure 4.22: Early flight trajectories and wind velocity vectors for S = 0.3.

are flying further than for $S = 0.13$ but still shows a large variation in their initial directions. Disregarding the release position $0r_c$, the closer the release position to the core, the further the debris are flying. Similar behaviour is observed from $S = 0.7$ where the debris are flying longer distances due to higher wind velocities.

Although Figure 4.21 gives a general overview of the flying behaviour of debris released for different locations and swirl ratios, it does not reflect the regions affected by the debris, as trajectories overlap on the figure. Therefore, the impact locations of the debris are first looked at. Table 4.11 gives the mean radial and flying distances at impact, normalised by the core radius r_c; the area, normalised by the core vortex area ($=\pi r_c^2$), covered by the impacting debris; and the mean normalised maximal total velocity magnitude. Table 4.11 (a) reveals that the mean radial distance of impacting debris is relatively similar when released from 0, 0.5 and $1r_c$ and for each swirl ratio. As pointed out before, the low vertical velocities at $2r_c$ tend to reduce the overall flying distance of the debris, and therefore the mean radial distances are roughly 30% lower than for 'closer-to-vortex' released locations. Overall, the debris appears to be impacting at a distance of between 3 and 5 times the size of the core radius, which for full-scale tornadoes would

Table 4.11: Debris flight analysis of (a) mean normalised radial distance at impact, (b) mean normalised flight distance at impact, (c) normalised impacting debris area and (d) mean normalised maximal velocity magnitude for different swirl ratios and release locations.

(a)	$S = 0.13$	$S = 0.3$	$S = 0.7$
$0r_c$	3.47	5.84	3.67
$0.5r_c$	3.49	5.66	3.93
$1r_c$	3.55	4.88	3.63
$2r_c$	2.55	2.99	3.14

(b)	$S = 0.13$	$S = 0.30$	$S = 0.7$
$0r_c$	4.5	10.18	7
$0.5r_c$	5.32	9.99	8.21
$1r_c$	5.75	8.75	7.91
$2r_c$	3.79	5.84	7.79

(c)	$S = 0.13$	$S = 0.30$	$S = 0.7$
$0r_c$	3.01	2.43	22.66
$0.5r_c$	3.37	2.41	4.46
$1r_c$	2.82	3.13	4.25
$2r_c$	3.7	4.09	1.16

(d)	$S = 0.13$	$S = 0.30$	$S = 0.7$
$0r_c$	0.61	0.46	0.52
$0.5r_c$	0.51	0.51	0.53
$1r_c$	0.67	0.57	0.54
$2r_c$	0.55	0.54	0.55

represent distances of several kilometres. Knox et al. (2013) found that during the 27 April 2011 tornado outbreak in Alabama (U.S.A.), light debris, classified as lighter than 0.45 kg, were transported by EF4-EF5 tornadoes for distances up to 150km with most debris travelling 2.5km. Brooks, Doswell and Kay (2003) has estimated that EF4 tornadoes are around 480m wide, which multiplied by the averaged mean radial distances of 3 and 5, gives a scaled-up transported distance of between 1.44 and 2.4km. This seems consistent with Knox et al.'s conclusions, although they cannot be generalised to all tornadoes and debris.

Table 4.11 (b) again shows consistency in how far debris travel when released between the core centre ($0r_c$) and core radius ($1r_c$) between the different swirl ratios. For $S = 0.13$, travelled distances are about 40% higher than the impacting

radial distances, which means the debris tend to follow low curve trajectories. Since for this swirl ratio the core vortex is relatively small, it suggests that the debris are initially affected by the local flow around the release location, and as it gets ejected, it only gets affected by a weaker surrounding flow field. For $S = 0.30$ and 0.7, the travelled distances are about twice as large as for the impacting radial distances. This indicates that for medium and large vortices debris are flying around the core vortex longer distances before reaching the floor than for small vortices when being transported at close vicinity of a tornado. The longer the debris travels, the more likely the debris is to impact engineering and non-engineering structures, which can possibly generate even more debris.

Table 4.11 (c) gives the proportion of the affected regions of impacting debris in relation to the size of the vortex. This gives an estimation of the size of the region (calculated from the scattered impact positions of the debris) where debris are likely to fall and produce damage to surrounding structure. For $S = 0.13$, the affected regions are around three times the size of the vortex itself and does not seem to be dependent on the release location. However, the debris released far from the centre ($2r_c$) are mostly impacting the ground after being released and therefore possibly do not reflect the real affected region. For $S = 0.30$, the sizes of the affected regions are consistent for the different release locations, but again releasing debris far from the centre increases the area due to in this case debris flying in straight trajectories (Figure 4.21 (k)). For $S = 0.7$, releasing the debris at the core centre ($0r_c$) unsurprisingly shows a significant affected area 22 times bigger than the core vortex. Debris are scattered in all directions due to the turbulent core vortex, which would mean during a full-scale event any structures

located within $4r_c$ would potentially be damaged.

Table 4.11 (d) gives the mean normalised maximal velocity the debris reached for each release location and swirl ratio. Interestingly, each case shows that the debris reached on average only 50% the maximal tangential velocity for each respective vortex. In comparison with a single debris flight (Figure 4.18; Table 4.9), single debris revolving around the core vortex appeared to reach up to 80% of the maximal tangential velocity. This shows debris already airborne reaches higher velocities when swirling around the vortex and therefore it would suggest that the maximum damage associated with a tornado would be caused by airborne debris in the debris cloud rather than debris becoming windborne due to a building failure. Nevertheless, debris reaching half the maximal velocity of a full-scale tornado would still cause significant damage to engineering structures.

Although Figure 4.21 gives a good idea of how initial conditions affect the debris trajectories and impact locations, it was necessary to analyse how this compares between each case. To do that, the debris path width, where the methodology was detailed in section 4.6.2, was calculated along with the travelling distance of the mean trajectory. This gives an idea of how the probability of debris to hit a structure on its path varies as it is travelling. Figure 4.23 shows the evolution of the debris path width with travelling distance for different release locations and swirl ratios. Although the visual representation on Figure 4.21 seems to indicate that the debris path simply increases for each release case, Figure 4.23 shows that the statistical path width varies between each case. When released from the centre, i.e. $0r_c$, no particular similarities are picked up by the analysis between the different swirl ratios. It is somewhat not surprising considering the

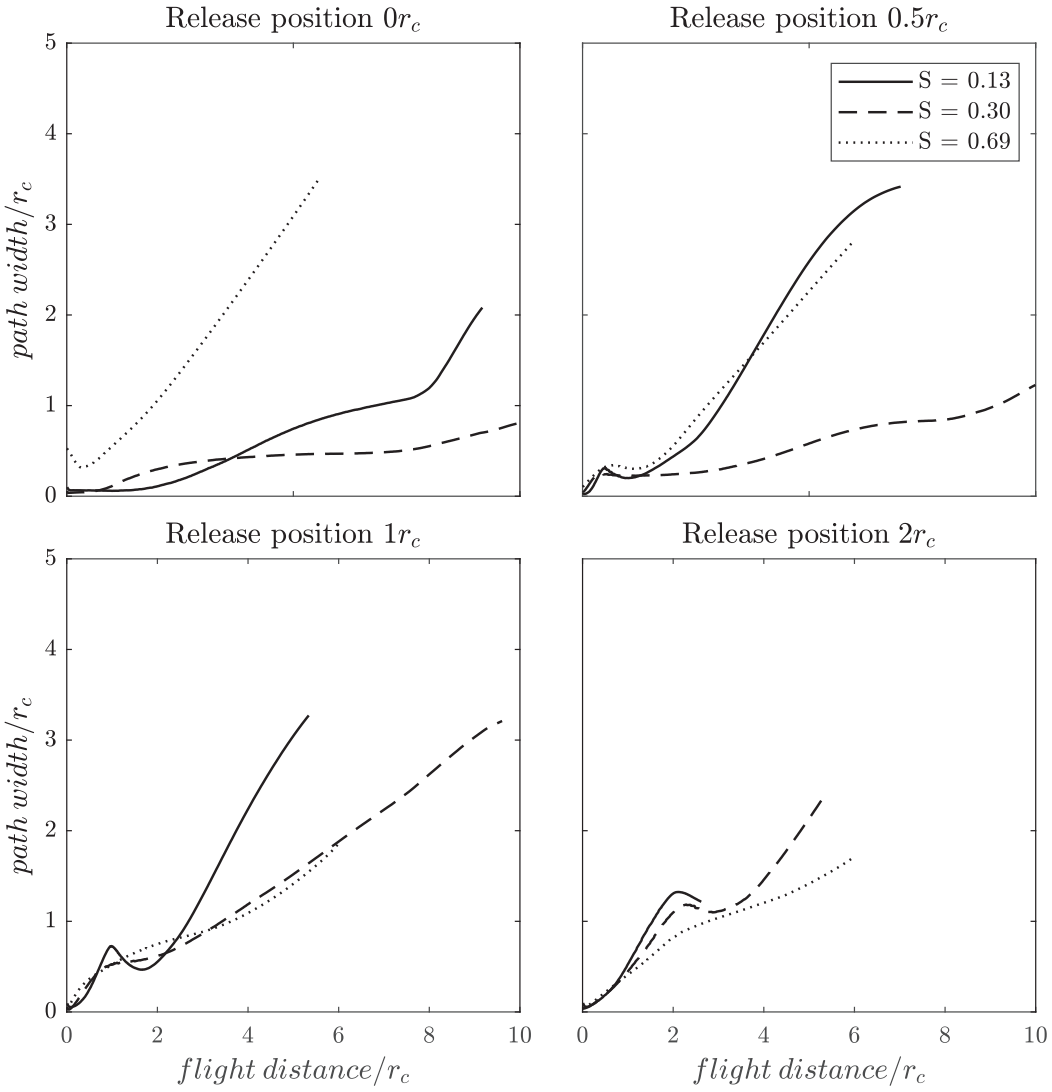


Figure 4.23: Evolution of the debris path width with flight distance for different swirl ratios.

previous analysis and behaviours observed when releasing debris "inside" the core vortex. Debris are scattered in all directions and defining a path based on a mean trajectory seems rather challenging. At $0.5r_c$, good similarities between $S = 0.13$ and 0.7 are observed, with a debris path reaching up to 3 times the core radius size at the average impact position. The debris path for $S = 0.3$ increases at a

slower rate to present a much narrower path at the impact location. At $1r_c$, good similarities are now observed between $S = 0.3$ and 0.7, whereas for $S = 0.13$ the debris path increases at a much faster pace. At $2r_c$, the debris path increases similarly for each swirl ratio up to about $1r_c$ flight distance, from where the smaller the swirl ratio, the larger the debris path increases. However, it is interesting to note that each swirl ratio tends to show a similar tendency. The analysis of the debris path seems to indicate some similarities between the swirl ratio and the release position. Figure 4.23 also seems to illustrate that the debris path increases faster when debris are released closer to the core vortex. Therefore, there may exist a relationship between the different vortex sizes regarding the initiation of debris flight. However, at this stage, it is difficult to draw such a conclusion, thus simulating more stable vortices would be required to confirm this assumption.

Finally, vortex wandering and fluctuation of the local flow field around the release location may significantly influence the initial direction of the debris and thus the whole trajectory and the final location where it impacts the ground. Therefore, to validate the results and ensure the repeatability, debris released at the core radius position ($1r_c$) were repeated five times (i.e. five times 100 debris) for each swirl ratio. For each, the mean radial and travelling distance were calculated,

Table 4.12: Relative standard deviation of the repeated mean radial distance and travelling distance of debris released from the core radius location for $S = 0.13$, 0.30 and 0.70.

	$S = 0.13$	$S = 0.30$	$S = 0.7$
RSD(mean radial distance) [%]	27.2	2.2	7.11
RSD(mean travelling distance) [%]	24.5	1.39	8.48

and the relative standard deviation (=standard deviation/mean *100) was calculated to evaluate the dispersion between each repeated case. For $S = 0.13$, as could be expected, significant variations are shown in Table 4.12 with 27.2% and 24.5% difference compared to the average value for the mean radial and travelling distance, respectively. For $S = 0.30$ and 0.7, the fluctuations significantly drop, which confirms a lower vortex wandering as the swirl ratio increases, with very small dispersion at medium swirl ratio ($S = 0.30$).

4.9.2 Building model seeding

To simulate the flight of debris resulting from a building failure, whether due to high wind loading or debris impact, a low-rise building model was placed in the simulator and debris were released from its top using the seeding device (Figure 4.11). As discussed previously, Wurman et al. (2013) measured winds using a DOW during an F2 tornado and were able to determine the size of the tornado and debris cloud around it, as well as the maximum wind speed. For this reason, this specific tornado was already chosen for scaling debris using Tachikawa scaling (see section 2.3.1). In order to investigate the effect of a low-building, a swirl ratio of 0.3 was chosen due to the "similarities" with an F2 tornado, i.e. medium size simulated vortex versus medium size tornado, and the fact Tachikawa scaling gives reasonably good full-scale debris characteristics for this swirl ratio. The debris used here are the same as for the floor seeding study, i.e. 0.002m Styrofoam spheres with a Tachikawa number of around 25, full-scale equivalent size and mass of 0.057m and 0.017kg. The building model measures $0.02 \times 0.02 \times 0.02$m equivalent at full-scale to a building of around $13 \times 13 \times 13$m.

To be able to characterise the effects of the low-rise building model on the vortex

flow field, vertical profiles close to the simulator's ground, i.e. within the first 0.03m, were taken at the core radius location ($r = r_c$). Figure 4.24 shows the vertical profiles of velocities close to the ground at the core radius location with and without building model included. To measure the vertical profile on top of the model, the Cobra probe's head was placed tangential to the core vortex and at the model's corner between the top and leeward side. With no building model, the tangential velocity (Figure 4.24 (a)) at this location is similar in many respects to a typical boundary-layer profile. The radial velocity (Figure 4.24 (b)) is predominantly negative over the height and accounts for the radial inflow, as found in Figure 3.8. The vertical velocity (Figure 4.24 (c)) shows a change of sign

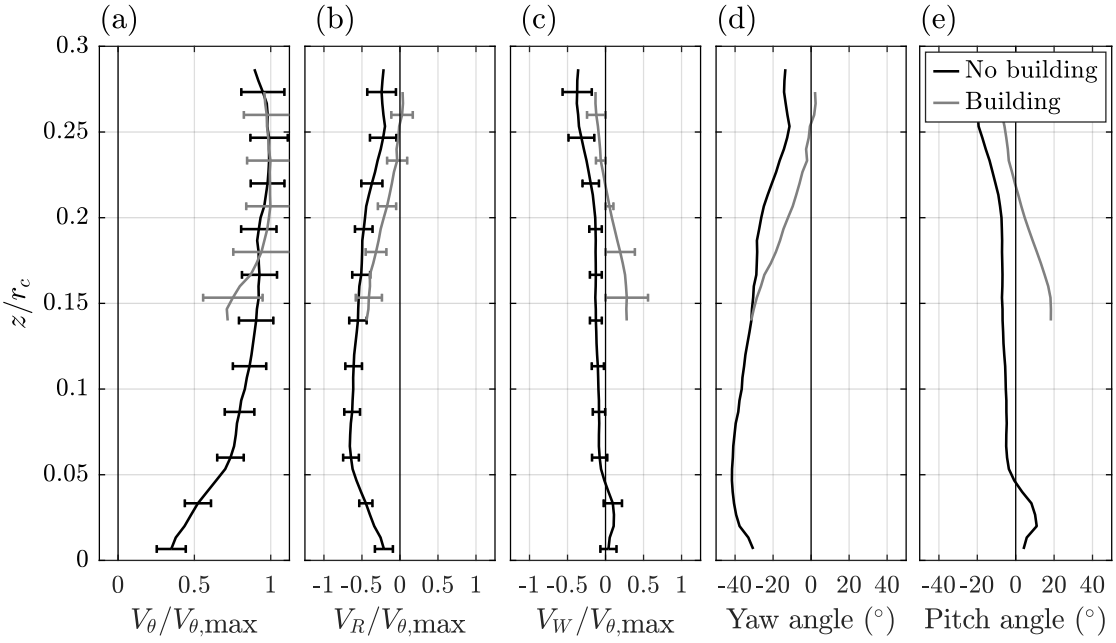


Figure 4.24: Vertical velocity profiles at the core radius location ($r = r_c$) of normalised – (a) tangential, (b) radial, (c) vertical velocity, (d) yaw angle and (e) pitch angle. The black line denotes when the building model is not included in the flow field, and the grey line when it is included. The horizontal capped lines denote the measurement uncertainties.

at around $z/r_c = 0.05$ which is difficult to interpret since the velocity remains relatively close to zero and the measurement is taken in a turbulent region. When the building model was included, the profile was measured from the top of the leeward side, to be as close as possible to the debris released position. It shows that the tangential velocity is typically not affected with height by the building model (Figure 4.24 (a)) and that the radial and vertical velocities are reduced in magnitude but still display a similar profile with height (Figure 4.24 (b) and (c)). The largest discrepancies observed around $z/r_c = 0.15$ are associated with a potential flow separation occurring on top of the building model. Numerical simulations of a low-rise building in a tornado-like flow field with a similar swirl ratio ($S = 0.4$) showed that recirculation is generated on the lee-ward side of the building (Nasir, 2017). That recirculation produces a downward flow in the wake of the building, which most likely explains the debris behaviour described thereafter where debris tends to fly upward and downward when ejected from the building model. The yaw angle (Figure 4.24 (d)) refers to the horizontal wind direction facing the probe while the pitch angle (Figure 4.24 (e)) refers to the vertical wind direction. Figure 4.24 (d) and (e) indicates a change of wind direction on top of the building model. It emerged from Figure 4.25 and Table 4.13 that this change of direction has a significant effect on the debris flight initiated from the model.

Comparing mean trajectories for debris released from 0, 0.5, 1 and $2r_c$ for $S = 0.30$ Figure 4.25 clearly highlights the effect of the changes in wind direction identified in Figure 4.24. Debris tend to be initiated with a slightly higher relative angle when initiated from the building model.

Figure 4.26 illustrates the flight of the debris released from the top of the building

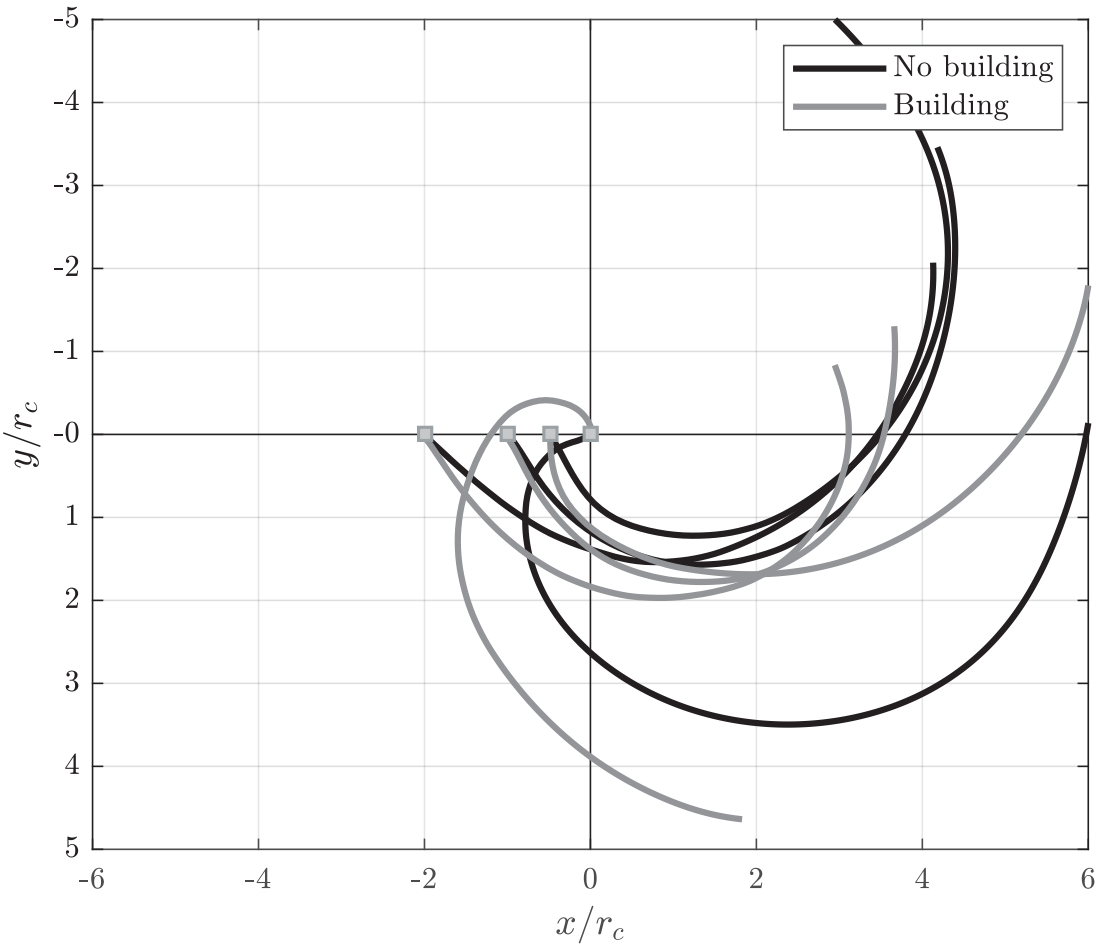


Figure 4.25: Mean debris trajectories for $S = 0.30$ initiated with and without a building model.

model. Strong similarities are shown with the case without the building model (see Figure 4.20 (a)) with debris initiated with different horizontal and vertical directions resulting in a large spread of the impacting locations. Similarly to the analysis carried out when seeding debris from the floor, Table 4.13 (a) shows the different parameters characterising the flying debris. Debris are impacting the floor at radial distances up to $5r_c$ when the building model is placed within and at the core radius position (i.e. $r/r_c \leq 1$), and travel distances up to $10r_c$. Table 4.13

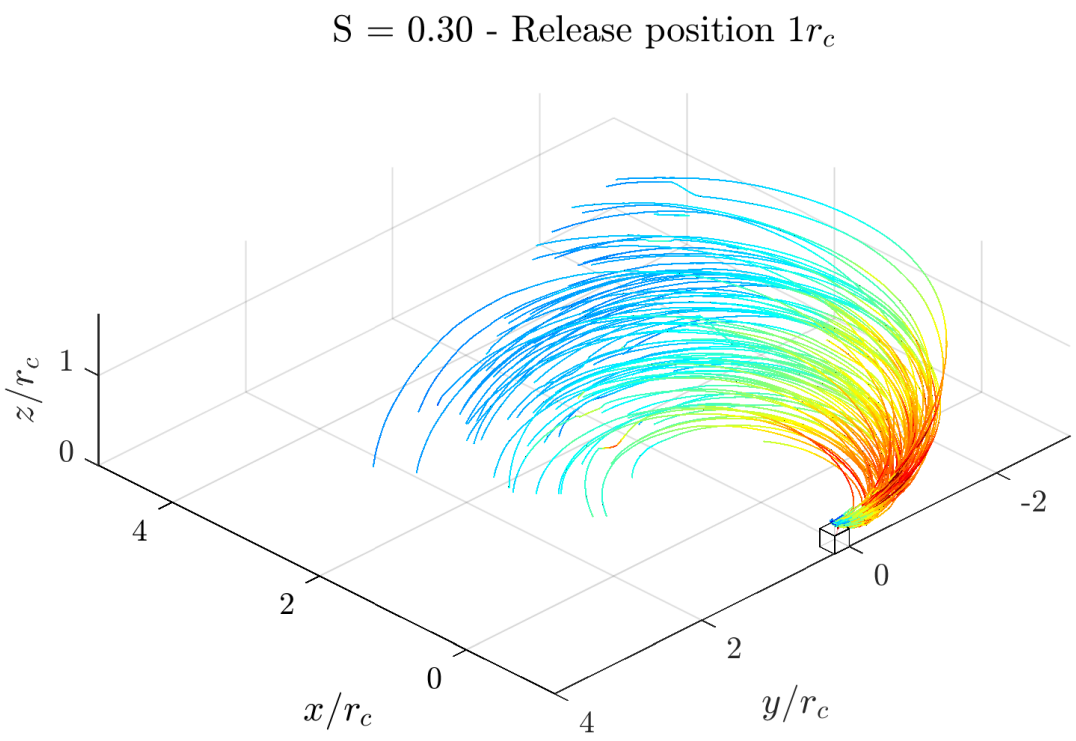


Figure 4.26: (a) 3D representation of the flight of debris from a low-rise building at the core radius (r_c) location. The dashed line denotes the size of the core radius, the arrows denote the idealised flow-field the building is subjected to.

(b) shows the difference in characteristic flight parameters for the building model and the difference without the building model. For the mean radial and travelling distances, including the building model makes little difference with maximal difference up to about 10%. However, the impact patch, which is defined from the contour area of the debris impacting positions, shows extremely large difference between with and without the building model. As the model is moved away from the vortex centre, the impact patch area reduces from 94 times the size of the impact patch area without the model to 7 times. This shows how debris initiated

Table 4.13: (a) Debris flight analysis for the building model and (b) the difference without the building model for $S = 0.30$.

(a)	mean radial distance	mean flight distance	mean debris patch	mean maximum velocity
$0r_c$	5.78	10.08	34.29	0.64
$0.5r_c$	5.92	10.48	19.4	0.66
$1r_c$	4.46	7.7	5.3	0.56
$2r_c$	3.21	5.16	4.94	0.53

(b)	mean radial distance	mean flight distance	mean debris patch	mean maximum velocity
$0r_c$	-1.03%	-0.96%	9317.02%	40.31%
$0.5r_c$	4.56%	4.91%	5267.05%	30.94%
$1r_c$	-8.74%	-11.93%	1031.59%	-1.43%
$2r_c$	7.35%	-11.54%	705.04%	-1.73%

from an engineering structure significantly increases the risk of a surrounding engineering and non-engineering structure to be impacted by windborne debris and maintain the debris chain. Maximum velocities reached by the debris show large discrepancies for $0r_c$ and $0.5r_c$ but little discrepancies for $1r_c$ and $2r_c$. Considering the impact patch area and maximum velocities for $0r_c$ and $0.5r_c$, it is unclear how the flow field was affected by the building model at these positions. However, a significant difference in initial debris directions was already observed without the model (Figure 4.21). Therefore, it is suggested that a different local flow field around the building affected the initial flying conditions of the debris at the time of the tests.

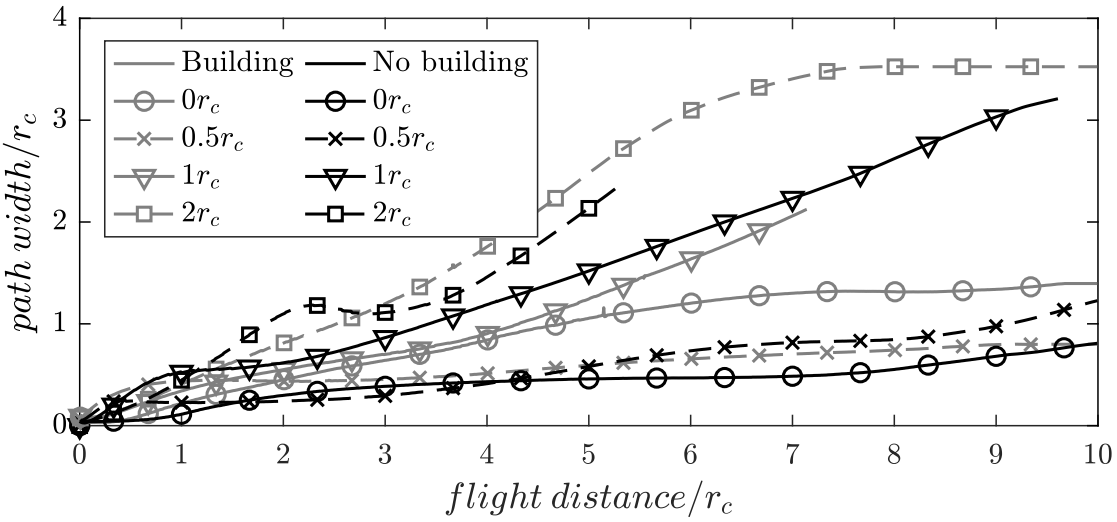


Figure 4.27: Comparison of the debris path width evolution with and without the building model for $S = 0.30$.

Figure 4.27 shows the evolution of the debris path width with travelling distance, with and without the building model for $S = 0.30$. Disregarding when the debris are released from the centre position ($0r_c$), the debris path for each release position seems to increase more as the debris are released further away the vortex centre. The path width seems to be approximatively multiplied by a factor 2 as the release position is also increased by a factor 2. Figure 4.27 also reveals very similar trends, whether a building model is included or not. For each release position, the evolution of the debris path is generally in good agreement with including the model or not but is also lower than for the next release position. This again seems to indicate that the model had little effect on the overall flow field generated in the simulator.

4.10 Concluding remarks

The following conclusions can be drawn from the simulation and analysis of the flight of windborne debris in the simulator undertaken and presented above:

1. The Particle Tracking Velocity appeared to be a good tool to investigate the flight of debris in tornado-like flow fields. The level of accuracy (submillimetre) reached after calibration allowed the quantification of the flight of debris for different situations. However, the way the cameras are arranged appeared to have a significant effect on the calibration performance,

2. Tracking single debris flying freely in the simulator revealed the debris generally revolved around the core vortex before being ejected outward. The debris appeared to be ejected up to a distance twice the size of the core radius, which seems in good agreement with Wurman et al. (2013) full-scale observations,

3. Characterisation of the vortex wandering showed that the lower the swirl ratio, the higher the wander. It also appeared that the size of the core radius, estimated using the circle fitting technique, was generally much smaller than when determined using wind profiles,

4. In order to statistically investigate the flight of debris, 100 debris were seeded into the simulator flow field, either from the floor or a building model. This showed that variability in the initial debris directions infers large variability of the impacting locations. This initial variability appears to be wind-related, rather than aerodynamically related due to the variation in debris sizes,

5. Investigating the flight of debris initiated from a building model revealed good similarities in the analysed flight parameters when including and not including the model. Therefore, it is considered that the overall flow field is not affected by the building model, but only the local flow field around it influences the initial condition of the debris. It also showed that this change in direction does not affect the distances travelled by the debris but has a significant effect on the size of the region where debris are falling.

Chapter 5

Comparison between physical and numerical approaches to debris flight in tornado-like winds

Some of the material presented in this chapter has previously been published in the proceedings of the ICWE15 (Bourriez et al., 2019), and has also been accepted for publication to the Journal of Wind Engineering and Industrial Aerodynamics, and is reproduced with the permission of the co-authors.

5.1 Introduction

In this chapter, a comparison between experimental and numerically calculated trajectories is presented. Section 5.2 details the numerical methodology developed to compute the motion of debris by incorporating experimental data. Section 5.3 describes the results obtained experimentally and numerically. Finally, section 5.4 completes this chapter with concluding remarks.

5.2 Numerical methodology

5.2.1 Debris equations

The 3D motion of Styrofoam beads in a tornado-like vortex was computed to numerically determine 3D trajectories, following a similar approach from Sassa et al. (2009). A compact debris with only drag forces acting and no rotation is assumed. The accelerations of the compact debris are defined as:

$$\begin{cases} \dfrac{\mathrm{d}V_{\theta,d}}{\mathrm{d}t} = k\boldsymbol{V}\left(V_\theta - V_{\theta,d}\right) & \text{(5.1a)} \\ \dfrac{\mathrm{d}V_{R,d}}{\mathrm{d}t} = k\boldsymbol{V}\left(V_R - V_{R,d}\right) & \text{(5.1b)} \\ \dfrac{\mathrm{d}V_{W,d}}{\mathrm{d}t} = k\boldsymbol{V}\left(V_W - V_{W,d}\right) - g & \text{(5.1c)} \end{cases}$$

where V_θ and $V_{\theta,d}$,d are the local circumferential wind and debris velocities respectively, k is a buoyancy parameter (Eq. 5.3), t represents the time, V_R and $V_{R,d}$ are the local radial wind and debris velocities respectively, V_W and $V_{W,d}$ are the local vertical wind and debris velocities respectively, and $\boldsymbol{V}$ is the vector of the relative velocity between the wind and debris defined as:

$$\boldsymbol{V} = \sqrt{\left(V_\theta - V_{\theta,d}\right)^2 + \left(V_R - V_{R,d}\right)^2 + \left(V_W - V_{W,d}\right)^2} \tag{5.2}$$

The buoyancy parameter (Holmes, 2004) is defined as:

$$k = \frac{\rho_a C_D}{2\rho_d l} \tag{5.3}$$

where ρ_a and ρ_a are the air and debris densities, respectively C_D the drag coefficient

and l the debris characteristic length. The parameters were set to $\rho_a = 1.2\,kg/m^3$, $C_D = 0.5$, $\rho_d = 24\,kg/m^3$ and $l = 2d_{\text{debris}}/3$, with d_{debris} the debris diameter.

5.2.2 Equations discretisation

The velocity and position components, denoted hereafter with $\bullet$, were computed numerically using a linear method as:

$$\begin{cases} V_\bullet^{t+1} = V_\bullet^t + A_\bullet^t \Delta t & \text{(5.4a)} \\ X_\bullet^{t+1} = X_\bullet^t + V_\bullet^t \Delta t & \text{(5.4b)} \end{cases}$$

with Δt the timestep and $A_\bullet^t$ the acceleration component. The Courant–Friedrichs–Lewy or CFL condition (Courant et al., 1928), which determines the stability of numerical methods, is defined for a one-dimensional case by:

$$C = \frac{V_{\theta,\max}\Delta t}{\Delta x} \tag{5.5}$$

where $V_{\theta,max}$ is the maximum tangential velocity and Δx the grid spacing used experimentally to characterise the flow field. C is typically known as the Courant number, and it is generally assumed that $C \leq 1$ is needed to insure numerical stability in explicit schemes. A timestep of $0.001s$ was chosen, which gives $C = 0.5$ and therefore offers a good ratio stability/time efficiency considering the maximal wind velocities of the flow field used in the present work. However, as described in the next section, bilinear interpolation is used to determine sub-grid velocities that are to be incorporated into the equations and then calculate the next velocity and position components. Therefore, the notion of grid spacing is somewhat eliminated,

which increases the robustness of the model.

5.2.3 Data incorporation

Experimental data were included in the calculations, by incorporating the experimental wind and tracked debris data into the calculated accelerations (Equations 5.1 and 5.2). Wind data were incorporated by means of the terms V_θ, V_R and V_W (i.e. from Figure 3.8) into the Equations 5.1 and 5.2, and therefore, the flow field is assumed steady and axisymmetric. The initial debris positions and velocities obtained experimentally with 3D-PTV were incorporated by means of the terms $V_{\theta,d}$, $V_{R,d}$ and $V_{W,d}$ into the Equations 5.1 and 5.2, and by means of the terms $X^t_\bullet$ and $V^t_\bullet$ in Equations 5.4. Therefore, for $t = 0s$, the initial conditions ($V^0_\bullet$ and $X^0_\bullet$)

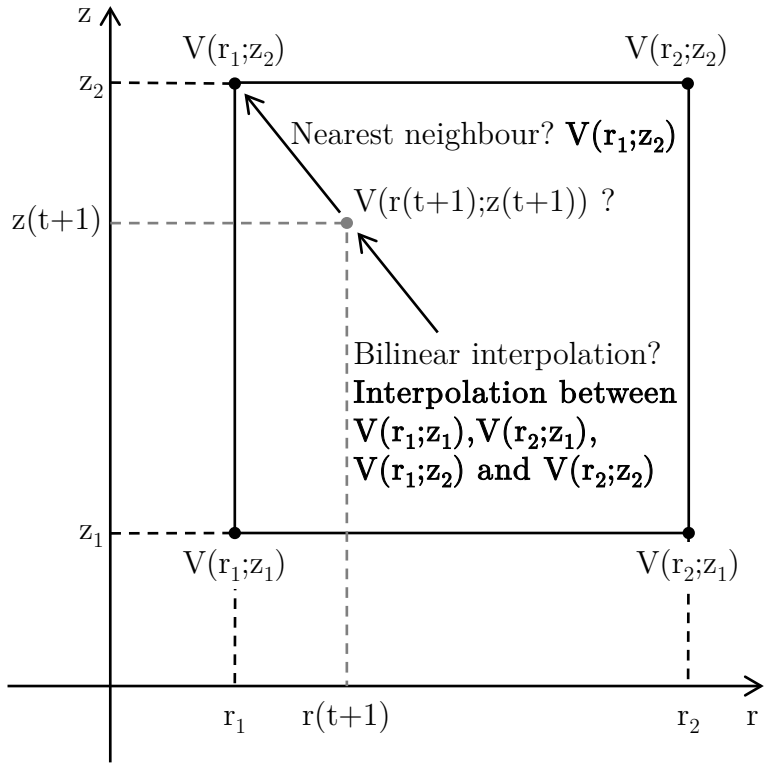


Figure 5.1: Sub-grid wind determination using bilinear interpolation.

were set to the first velocity and position data obtained from the particle tracking experiment. To determine at each timestep t the wind velocities to be incorporated into the calculations, bilinear interpolation was used to interpolate sub-grid velocities from the positions (Figure 5.1). Since the measurement grid was coarse (0.025m grid spacing), this technique improves the accuracy and robustness of the calculations by interpolation wind velocities rather than finding the nearest measured point.

To reproduce the effect of vortex wandering of the debris trajectories, experimental vortex wandering data (obtained in section 4.8.2, Figure 4.19) were incorporated into the calculations by adding the vortex centre displacements into Equation 5.4 (b).

5.2.4 Elastic collision

As mentioned in section 4.9.1, debris inside the simulator tend to bounce on the floor after being lifted aloft. A simple elastic collision condition was added to the model to reproduce some sort of bouncing behaviour. Given the fact small size Styrofoam spheres were used as debris in the physical simulation, it was impossible

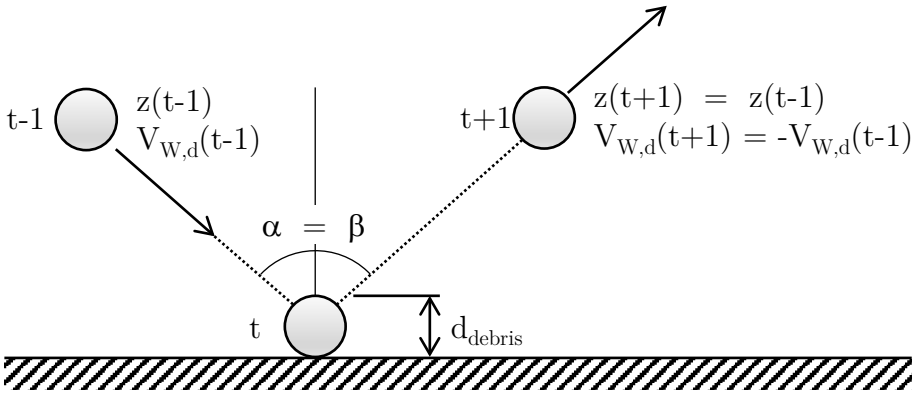


Figure 5.2: Perfect elastic collision model.

to determine their mechanical properties in impact. Therefore, a perfectly elastic collision with no kinetic energy dissipated was considered in the model, i.e. the speed after impact is the same as the speed before impact (Figure 5.2). In the model, when the next vertical position were lower than the debris radii, i.e. $z(t+1) < d_{\text{debris}}/2$, the vertical position and velocity was replaced with the position and velocity at $t = t-1$. This was shown to be a simple and efficient way to introduce bouncing to the computed debris trajectories. On the other hand, if bouncing does not need to be considered in the model, such as for the trajectories in section 5.3.2 and 5.3.3, the model was simply stopped for each individual trajectory when the condition $z(t+1) < d_{\text{debris}}/2$.

5.2.5 Validation

In order to validate the numerical methodology, a simple experiment was set up using the University of Birmingham Mobile Wind Tunnel (Figure 5.3). Frequently utilised for educational purposes, it was used for the present purpose considering the low turbulence intensity and relatively constant wind velocities across the test section showed during wind measurements, as well as the ease to undertake the experiment. The UoB Mobile Wind Tunnel consists of three independent fans connected to a contraction section with a test section of about $0.2 \times 0.2 \times 1m$ ($w \times h \times l$). A coarse ($0.01m$) and fine ($0.0025m$) honeycomb mesh were placed at the end of the contraction section to straighten the flow and reduce turbulence. Debris were held in place via a fine tube connected to a vacuum pump in the test section far enough from the walls to avoid boundary layer effects. Once released, the motion of the debris was recorded using one high-speed camera and data reduction was performed on OpenPTV software (OpenPTV, 2012). The 2D motion of

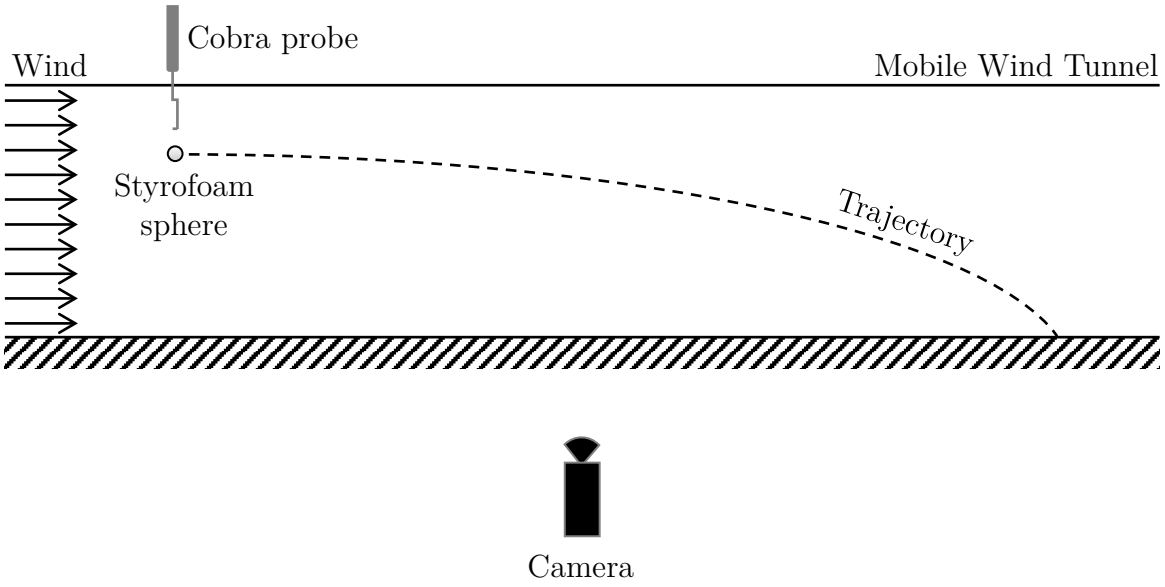


Figure 5.3: PTV set up for single debris tracking in the wind tunnel.

debris was numerically calculated by following the same method described above. Holmes' equations (Holmes, 2004) were used and when considering horizontal drag only, horizontal and vertical positions were calculated over time, $x_d(t)$ and $z_d(t)$, respectively, as follows:

$$\begin{cases} x_d(t) = V_{U,wt}\left[t - \left(\dfrac{1}{kV_{U,wt}}\right)\log\left(1 + kV_{U,wt}t\right)\right] & \text{(5.6a)} \\ z_d(t) = -\left(\dfrac{1}{2}\right)gt^2 & \text{(5.6b)} \end{cases}$$

whereas when considering horizontal and vertical drag with and without incorporating experimental data, the following horizontal and vertical accelerations were

resolved numerically:

$$\begin{cases} \dfrac{\mathrm{d}V_{U,d}}{\mathrm{d}t} = k\boldsymbol{V}_{wt}\left(V_{U,wt} - V_{U,d}\right) & \text{(5.7a)} \\ \dfrac{\mathrm{d}V_{W,d}}{\mathrm{d}t} = k\boldsymbol{V}_{wt}\left(V_{W,wt} - V_{W,d}\right) - g & \text{(5.7b)} \end{cases}$$

where $V_{U,wt}$ and $V_{W,wt}$ are the horizontal and vertical wind speeds, and $\boldsymbol{V}_{wt}$ the vector of the relative velocity between the wind and debris in the UoB Mobile Wind Tunnel.

5.3 Results

5.3.1 Numerical validation

Figure 5.4 shows the comparison between the experimental trajectory, obtained using a $0.002m$ Styrofoam bead subjected to steady horizontal winds of $5m/s$, and numerically calculated trajectories. Same results were found with different

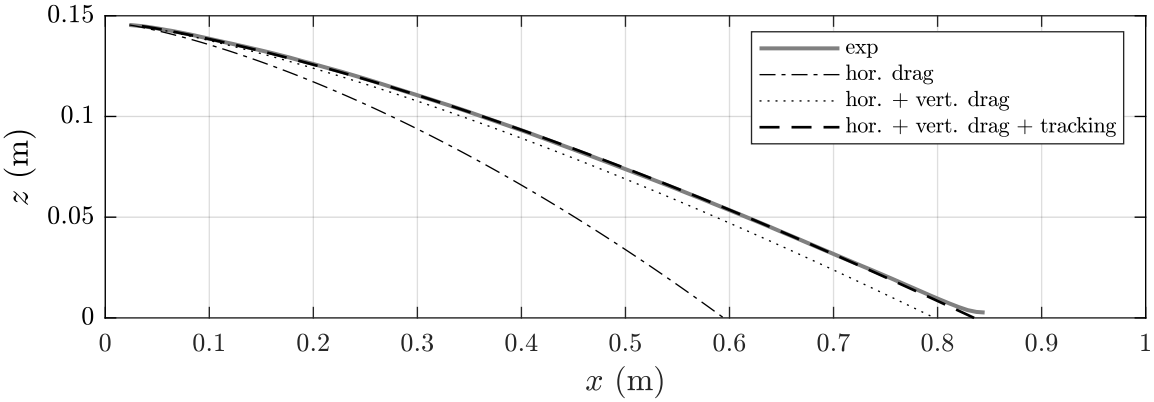


Figure 5.4: Comparison between experimental debris trajectories and different numerical methods subjected to uni-directional winds.

ball sizes but only one iteration is showed in Figure 5.4. When only considering the horizontal drag, the calculated trajectory shows that the debris impacts the ground plane much faster than experimentally, with an impact distance 29% shorter. When considering horizontal and vertical drag, Figure 5.4 shows good agreement with the experimental data, and the numerical and experimental trajectories match when incorporating the initial PTV velocities. Therefore, it shows that incorporating the experimental data into the model contributes to improving the early trajectory of the debris and ultimately to the location where the debris impacts the ground. However, although the present results provide a good validation for the numerical method applied to steady uni-directional winds, it is acknowledged that for tornado-like flow fields, where small scale turbulence is still not fully understood and may potentially have an influence, a variation of the local fields cannot be modelled and may result in some variations of the terminal location of the debris.

5.3.2 Low-rise building located at $1r_c$ for $S = 0.3$

The comparison between different debris flight configurations is shown in Figure 5.5. The Tachikawa number for the present results is 25. The debris trajectories obtained experimentally are shown in Figure 5.5 (a) and (c), while Figure 5.5 (b) and (d) show the attempt to numerically reproduce these trajectories. In both cases, visual similarities are observed and are quantified in this section. Figure 5.5 (a) and (c) illustrate the typical set of experimental data obtained using 3D-PTV when injecting 100 particles from the core radius position. Similar trajectory behaviours were found numerically when debris were released from the core radius location (Maruyama, 2011, Noda et al., 2013). In the present cases, the debris were

injected experimentally from the floor simulating the initiation of debris flight in a landscaped environment (i.e. no building), and from the top of a building. The tracking was stopped when the particles were falling to the ground after being airborne to reflect what could be observed during a full-scale event. However, it is worth noting that due to the elasticity of the Styrofoam bead, its light mass and the smooth floor surface in the tornado generator, the beads bounce when falling to the ground. For the sake of the current analysis, such motion has been neglected and is not considered further.

Figure 5.5 (a) shows that the particles are ejected outward from the vortex following a relatively straight line for a short period of time. The particles are then swirling back again around the vortex before falling to the ground. It also illustrates that a slight variation of the early stage trajectories can result in a large variation of the falling location. The variability observed in the trajectories could be due to the varying size of the beads, although it is most likely that the variation is due to the vortex wandering and/or to turbulent fluctuations of the local wind field. Figure 5.5 (c) shows the debris trajectories when injected from the top of the cubic model. It illustrates a greater variation of the early stage trajectories than without the model, resulting in a larger region where the debris falls. The larger variation can be attributed to the disturbance of the local flow field around the building model. This assumption can be supported by the initial velocity distributions, i.e. the first debris velocities calculated using 3D-PTV (Figure 5.6). It appears that debris are driven by positive tangential velocities in both situations (Figure 5.6 (a)); however, radial and vertical velocities have opposite signs between the two. As a result, an overall difference of 40 degrees in direction can be noticed

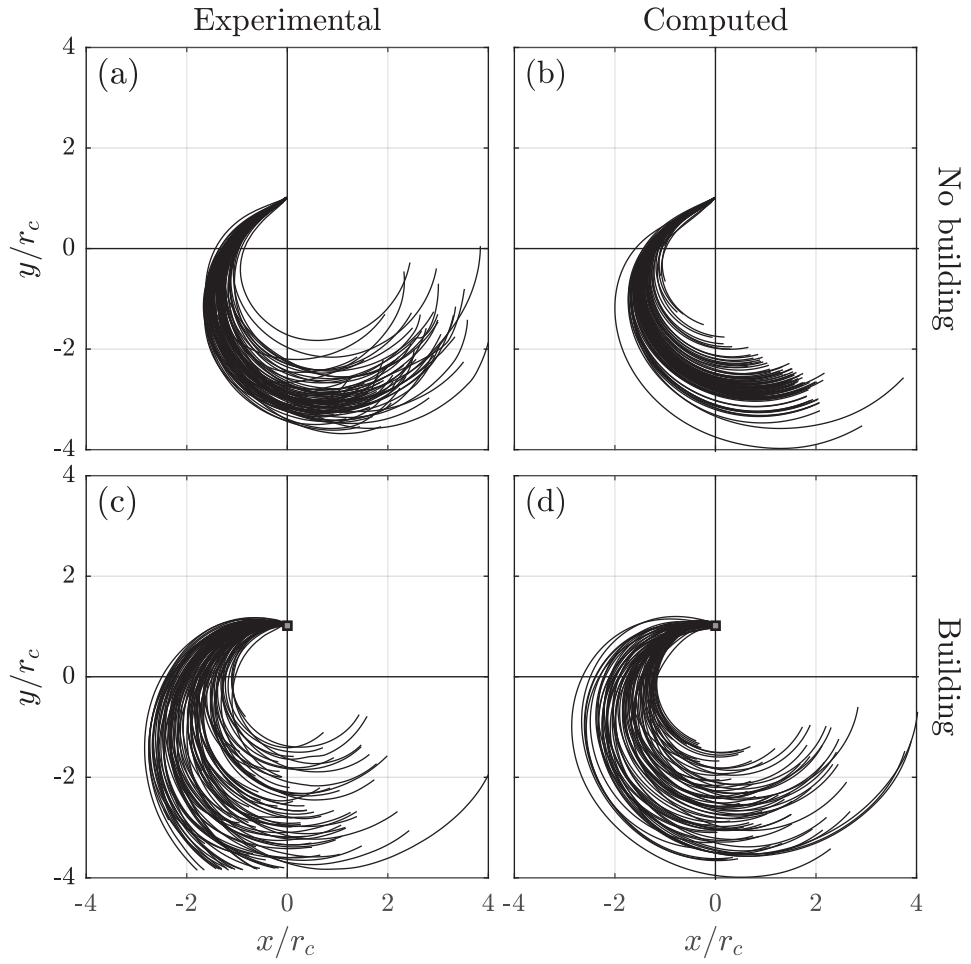


Figure 5.5: Top view of the experimental and numerical debris trajectories. Left column denotes the experimental trajectories (a-c), right column the computed trajectories (b-d). The top row denotes the trajectories when the building model is not included (a-b), the bottom row the trajectories when the building model is included (c-d).

when including the building into the flow field (Figure 5.6 (d)). Furthermore, Figure 5.6 (c) shows that debris are mainly driven by both positive and negative vertical velocities when released from the top of the building, which could be explained by potential flow separation. When debris are driven by negative vertical velocity, the debris falls quickly to the ground and is embedded further by strong

local tangential velocities, and therefore accounts for the closest trajectories to the core vortex. On the other hand, the debris tends to be ejected outwards from the core vortex and fall further, accounting for the longer trajectories to the core radius. Therefore, the risks with windborne debris initiated from a low-rise building are not only associated with long-range falling debris but also with possible short-range impacts at higher velocities.

Figure 5.5 (b) and (d) present the computed debris trajectories using experimental

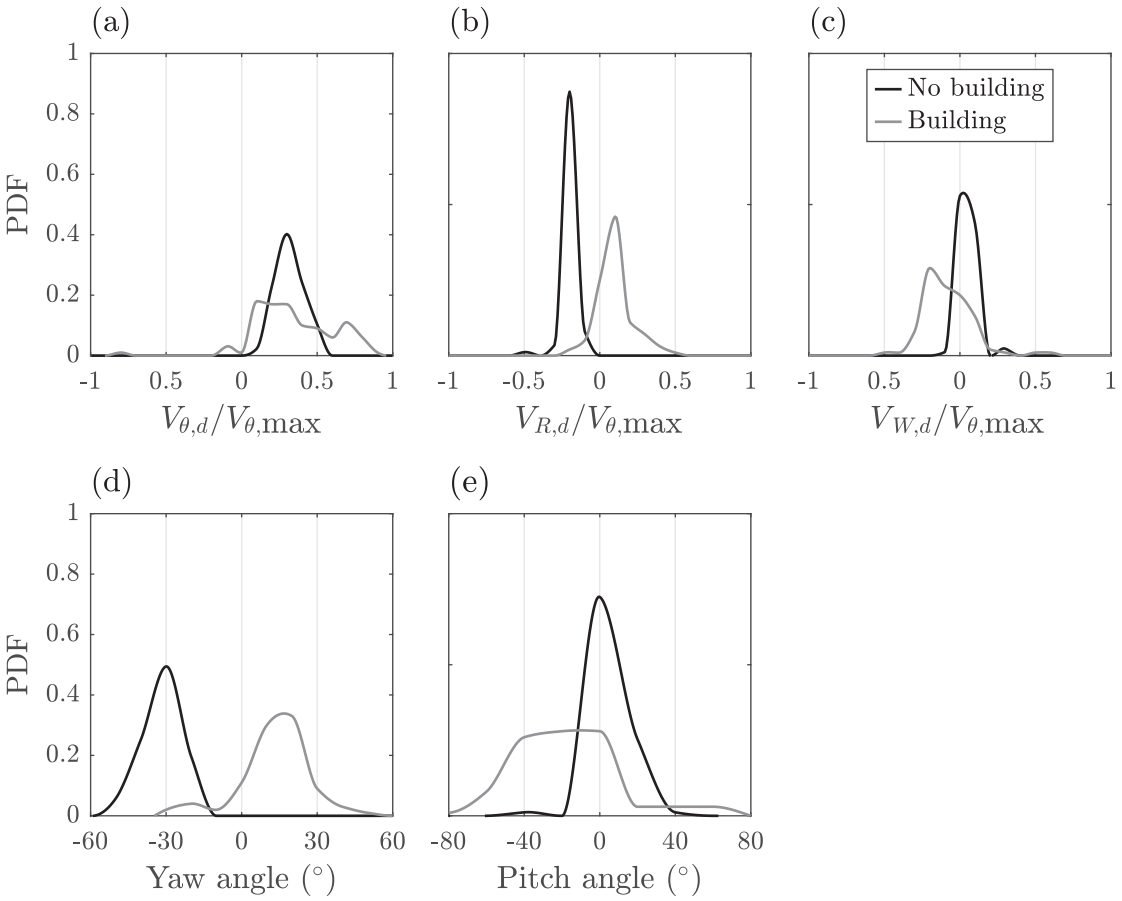


Figure 5.6: Distribution of debris initial tangential (a), radial (b), vertical (c) velocities, yaw (d) and pitch (e) angle, when the low-rise building model is and is not included in the tornado-like flow field.

Table 5.1: Comparison between wind and initial debris velocities, pitch and yaw angles, when the building model was included and not included in the simulations.

		$V_\theta/V_{\theta,max}$	$V_R/V_{\theta,max}$	$V_W/V_{\theta,max}$	Pitch (°)	Yaw (°)
No building	Wind	0.30	-0.20	0.04	25.8	4.01
	Debris	0.27	-0.16	0.04	30.7	7.10
Building	Wind	0.70	-0.44	0.27	-32.1	17.7
	Debris	0.38	0.11	-0.09	-16.7	-17.3

wind and PTV data. In both cases, the computed trajectories are in good agreement with the tracked trajectories. Although the flow field is assumed axisymmetric and does not include any turbulence, it shows that the present methodology can reproduce the trajectories variability. Table 5.1 compares the components of wind and initial debris velocities and shows that when the building is not included, the velocity components are matching wind and debris. This validates the assumption that debris flight is mainly a wind-driven process. When the building is included, large discrepancies are observed between wind and debris which could be explained by the fact that velocities are not measured exactly at the same position.

Figure 5.7 shows the debris flight analysis with normalised flight parameters determined from the debris trajectories (Figure 5.5). The flight distance (Figure 5.7 (a)) accounts for the cumulative local distance travelled by the debris, the flight time (Figure 5.7 (b)) accounts for the duration while the debris is airborne, V_{max} (Figure 5.7 (c)) accounts for the maximal velocity reached by the debris, and flight time to V_{max} (Figure 5.7 (d)) accounts for the duration taken by the debris to reach the maximal velocity. Overall, it shows that including a building model does not affect the flight behaviour of the debris in terms of flight distances. This corroborates

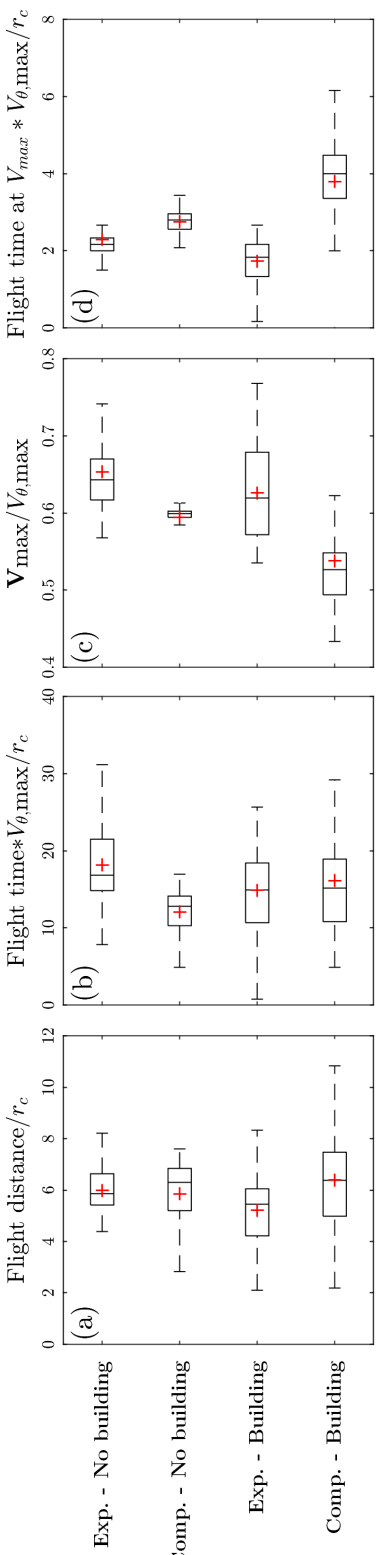


Figure 5.7: Debris flight analysis – the red cross denotes the mean value, the box the interquartile range, the vertical line the median and the whiskers the range from minimal to maximal values.

the assumption that the overall flow field is not affected by the building model, as discussed in section 4.9. The numerical simulations tend to reproduce some behaviour, although more variability is generally observed. The flight distance shows good agreement with experimental results and coincides with the debris trajectories overall behaviour (Figure 5.5), and so does the flight time. However, the numerical simulations show limitations in modelling the maximum velocity $V_{d,max}$, and therefore the flight time to reach V_{max} (Figure 5.7 (c) and (d)). This could be explained by the flow field variability (due to wandering and/or turbulence) that is dimmed after averaging and could result in a stronger instantaneous flow field at the time of the experiment.

5.3.3 Floor seeding at $0r_c$ for $S = 0.7$

In the previous chapter, Figure 4.20 and Figure 4.21 showed interesting debris trajectories when releasing the debris from the floor at the centre of the core vortex ($0r_c$) for $S = 0.7$. Since in the previous section, the numerical methodology showed a good capacity to reproduce similar experimental debris trajectories, it was considered appropriate to investigate the performance of the methodology when debris were released in a turbulent flow field. Figure 5.8 shows the comparison between experimental and computed trajectories with a Tachikawa number of 44 released at the core centre ($0r_c$) for $S = 0.7$ and reveals quite a few similarities. It shows that the computed trajectories are also scattered in all directions but tend to travel shorter distances compared to the experimental trajectories. Table 5.2 shows that the mean radial distance and flight distance of the computed trajectories, where it impacts the ground, is 45% and 33% smaller than experimentally. It also shows that the area affected by the debris is 49% smaller when trajectories are computed,

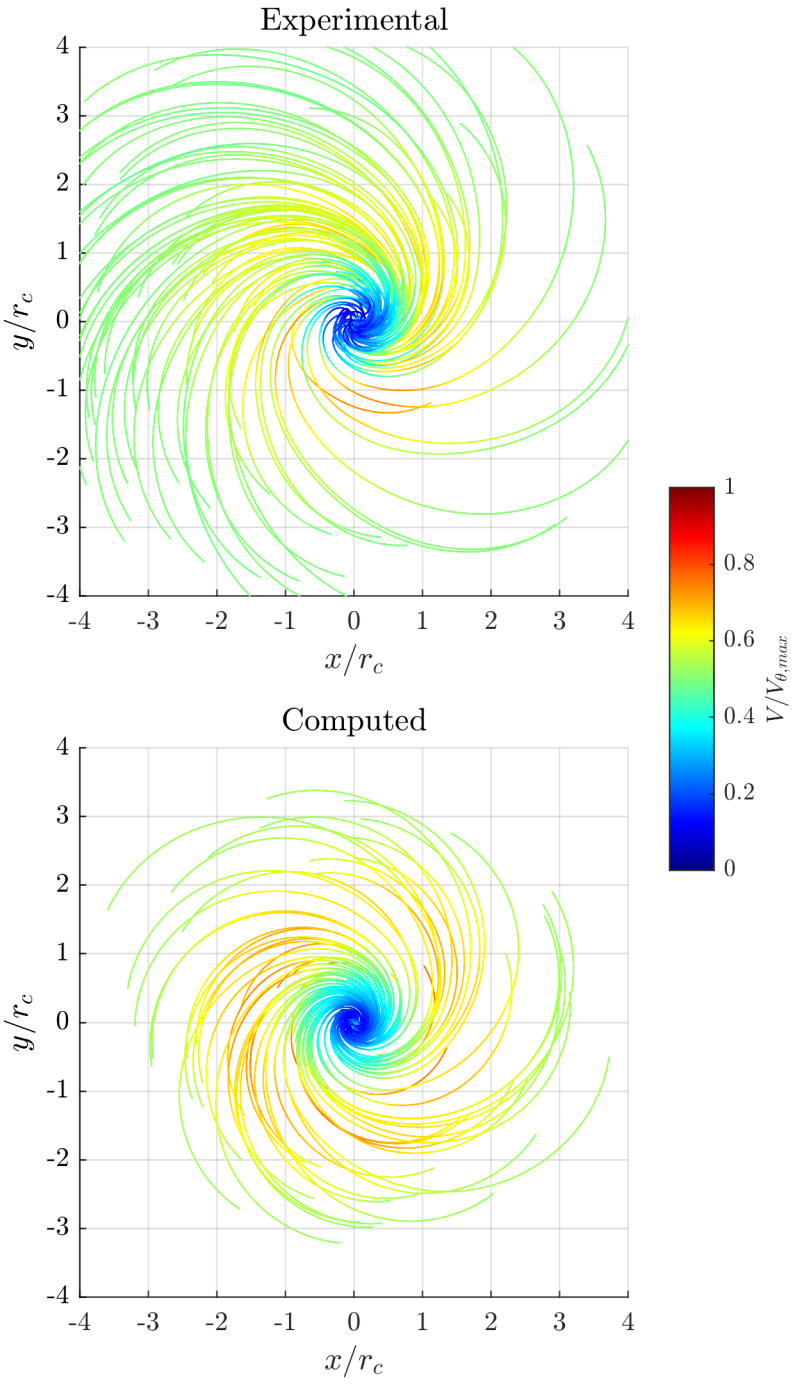


Figure 5.8: Comparison between experimental and computed trajectories released from the vortex centre ($0r_c$) for $S = 0.7$.

Table 5.2: Debris flight analysis and comparison between experimental and computed trajectories released from the vortex centre ($0r_c$) for $S = 0.7$.

(a)	mean radial distance	mean flight distance	mean debris area	mean maximum velocity
Experimental	3.67	6.98	22.66	0.52
Computed	2.02	4.69	11.41	0.61
Difference	-45%	-33%	-49%	+15%

which does reflect a mean radial distance about twice smaller. As observed in the previous section, the mean maximal velocity is overestimated at the moment and tends to confirm the current limitation of the model to correctly simulate the debris velocities. Nevertheless, considering the significant turbulence in the core vortex for $S = 0.7$ (see flow visualisation in Figure 4.4) and the fact wind data were obtained with invasive techniques (traverse system and Cobra probe), it shows the good potential of the present methodology to investigate debris flight numerically using experimental data.

5.3.4 Single debris with vortex wandering

An attempt to reproduce and understand the motion of single debris, as observed in Figure 4.18, was undertaken. In section 4.8.2, it was suggested that the way debris were ejected from swirling around the core vortex could be attributed to the vortex wandering. However, this was difficult to confirm as tracking single debris and measuring the vortex wandering at the same time was impractical. Therefore, the fluctuations of the vortex centre measured during the characterisation of the vortex wandering for $S = 0.3$ were incorporated into the model to simulate the vortex wandering. As a result, Figure 5.9 shows the comparison between single

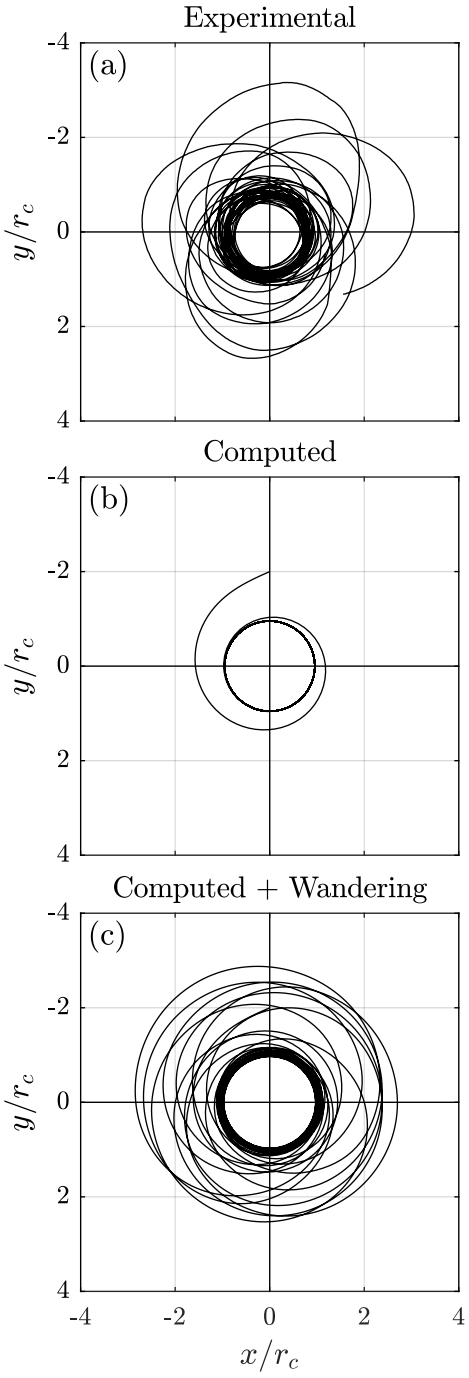


Figure 5.9: Single debris trajectories (a) experimental for $S = 0.30$, (b) computed and (c) computed included vortex wandering.

debris measured experimentally (Figure 5.9 (a)), computed (Figure 5.9 (b)) and computed with the vortex wandering included (Figure 5.9 (c)). Figure 5.9 (b) shows that when computing single debris (or more if needed) and released far from the centre ($2r_c$), the debris is embedded and moves towards the core radius before reaching a steady position around it. At this stage, if the debris is not disturbed from its equilibrium position, the debris will remain at the same radial position for the rest of the simulation. Therefore, it suggests that the annular ring around $1r_c$ as observed in Figure 5.9 (a), is associated with a low vortex wandering which keeps the debris in equilibrium around the core radius. On the other hand, Figure 5.9 (c) shows that incorporating the vortex wandering into the model replicates the debris ejection as observed experimentally but with more uniform radial extents due to the axisymmetric flow field used in the simulations. The annular ring at $1r_c$, appears to be broader than in Figure 5.9 (b) which confirms that this annular ring is most likely associated with small variations of the vortex centre position. However, an additional contribution could be attributed to intensifying/weakening of the vortex as previously observed in the simulator with surface pressure measurements (Gillmeier et al., 2017).

Figure 5.10 and Figure 5.11 reveal some hints on how debris get ejected outwards from the core vortex. Figure 5.10 (a) shows the single debris flight in the vertical plane and illustrates that the debris is lifted aloft when being ejected outwards, with height up to $0.5r_c$. Figure 5.11 (a) and (b) show the evolution of the debris radial and height positions, respectively, whereas Figure 5.11 (c) shows the retrieved vertical wind velocity the debris was exposed to during its flight. Figure 5.11 clearly establishes the local vertical wind velocity to be the cause of ejecting the debris outward. Each peak in vertical wind velocity (Figure 5.11 (c)) results

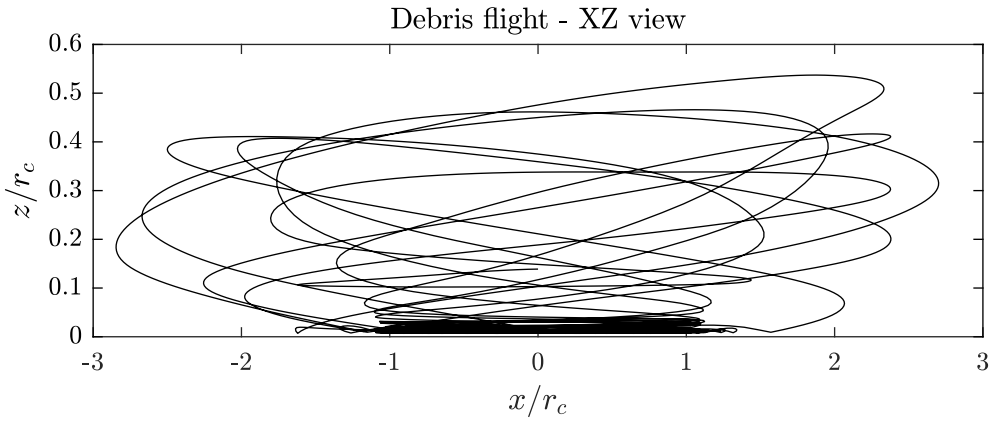


Figure 5.10: Vertical view (XZ plan) of single debris trajectories for $S = 0.30$ computed with vortex wandering.

in a peak in the radial and vertical position. Vertical tangential velocity profiles (Figure 3.14) showed for $S = 0.30$ and at the core radius position ($1r_c$), the maximum tangential velocity to be located at $z/h_0 = 0.025$, i.e. around $z/r_c = 0.17$. Therefore, it suggests that the variation in the local, vertical wind around the debris position lifts it sufficiently to reach higher vertical and tangential velocities, which force the debris to be ejected outward. Short spikes of vertical wind velocities in Figure 5.11 (c) (Revolutions = 13, 70 and 86) seem to corroborate this assumption, as they result in a slight deflection of the radial and vertical positions observed in Figure 5.11 (a) and (b), but not strong enough to be ejected outwards.

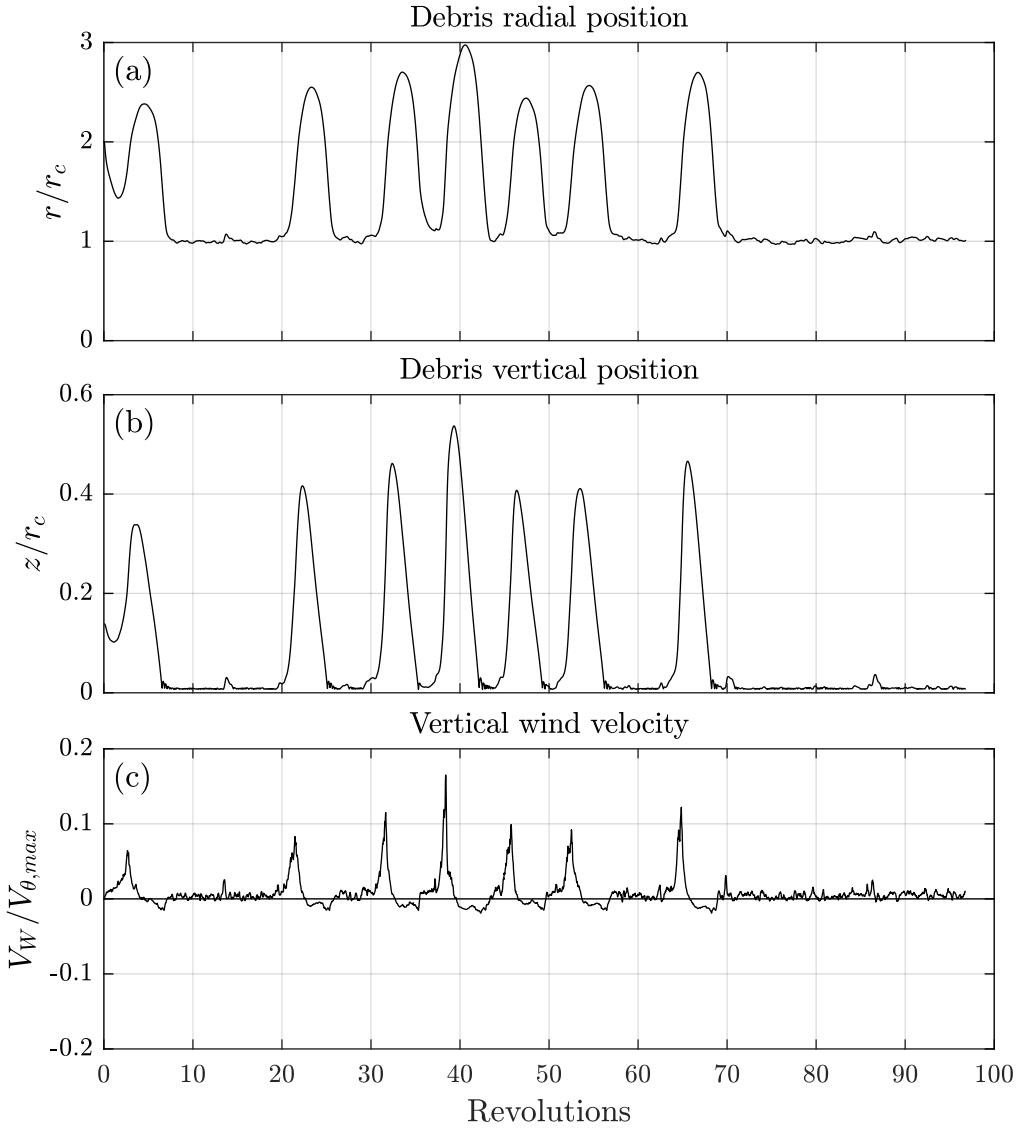


Figure 5.11: Evolution of (a) radial and (b) vertical position of single debris subjected to vertical wind velocities (c).

5.4 Concluding remarks

Physical and numerical simulations were undertaken to investigate the flight of debris in tornado-like vortices initiated with and without a low-rise building model. Numerical calculations were used to attempt reproducing the debris trajectories and flight behaviour. Using debris flight equations with wind and PTV experimental data, the computed trajectories show strong similarities with experimental trajectories. The debris flight analysis shows that the simulations could reproduce the overall trajectories but had limitations in simulating similar velocities. The limitations could be related to the experimental wind data used to compute the trajectories and not to the methodology itself. Finally, this numerical methodology presents advantages to investigating debris flight in tornadoes:

1. Gillmeier et al. (2018) showed that analytical vortex models could reproduce some of the behaviours observed in full scale and modelled tornadoes but fail to reproduce the complexity of the 3D flow field. Wind measurements help to describe the complexity that models fail to reproduce and therefore integrate a more "realistic" flow field to the study of debris flight.

2. Using bilinear interpolation to approximate the local wind field, the debris is affected by increases in the accuracy of the computed positions and velocities and does not require a fine measurement grid. It also significantly reduced the computational time compared to other methods (i.e. finding nearest neighbours, see Figure 5.1) and does not require high computational power.

3. The methodology also allows investigating any type of debris in tornado-like flow fields. By adjusting the debris flight equations to either compact

(Holmes, 2004) or plate (Holmes et al., 2006), a large range of debris types, sizes and densities (i.e. Tachikawa number) could be investigated.

4. The methodology could also be applied to full-scale tornado wind data. However, Doppler radars often fail to measure wind below 30m AGL (Wurman et al., 2013), which is where most of the debris are becoming airborne. When data are available, comparison and validation could be undertaken with full-scale data.

Although the methodology has many advantages, it also has limitations. The assumption of an axisymmetric flow field does not reflect the complexity of a tornado-like flow field. Volumetric wind measurements using neutral buoyancy tracers and laser illumination (Tomographic PIV, 3D-PTV, etc.) could help to retrieve instantaneous 3D flow field. Finally, the methodology only considers average flow fields. Turbulence could be incorporated into the simulation (Holmes, 2004) to recreate wind field fluctuations but would require a better understanding of the turbulence in tornadoes/tornado-like vortices.

Chapter 6

Analytical modelling of debris flight in tornado-like flow field

6.1 Introduction

In this chapter, five analytical vortex models were used to investigate the effect of vortex wandering on the flow field as well as the flight of debris with various Tachikawa numbers. Section 6.2 details the numerical methodology used in the present investigation. Section 6.3 analyses the introduction and effect of vortex wandering on an averaged flow field. Section 6.4 looks at the effect of the Tachikawa number on the computed debris flight using several vortex models. Section 6.5 focuses on debris flight using Baker and Sterling's two-cell model. Finally, concluding remarks are given in section 6.6.

6.2 Numerical methodology

For the present work, the same approach, as presented in section 5.2, was used here to compute debris trajectories. However, as identified in the previous chapters, the flow field measured experimentally appeared to indicate a two-cell vortex-like

structure. Therefore, the two-cell vortex model from Baker and Sterling (2017) will be used and detailed herein. As analytical vortex models are expressed dimensionlessly, the debris flight equations are also expressed in dimensionless form using the Tachikawa number.

6.2.1 Baker and Sterling two-cell vortex model

Baker and Sterling (2017) expressed the two-cell vortex model as a superposition of two flow fields: the first flow field consisting of the one-cell expression of the authors' model (see section 2.3) and the second an additional flow field representing a downdraft near the vortex core. The additional flow field is expressed as follows:

$$\begin{cases} \overline{V_R} = \dfrac{4\tilde{r}\tilde{z}}{\left(1+\tilde{r}^2\right)\left(1+\tilde{z}^2\right)} & \text{(6.1a)} \\ \overline{V_\theta} = 0 & \text{(6.1b)} \\ \overline{V_W} = -\dfrac{4\delta \ln\left(1+\tilde{z}^2\right)}{\left(1+\tilde{r}^2\right)^2} & \text{(6.1c)} \end{cases}$$

resulting in the following two-cell formulation of Baker and Sterling's model:

$$\begin{cases} \overline{V_R} = \dfrac{-4\overline{r}\overline{z}}{\left(1+\bar{r}^2\right)\left(1+\bar{z}^2\right)} + \dfrac{4\tilde{r}\tilde{z}}{\left(1+\tilde{r}^2\right)\left(1+\tilde{z}^2\right)} & \text{(6.2a)} \\ \overline{V_\theta} = \dfrac{K\bar{r}\left[\ln\left(1+\bar{z}^2\right)\right]}{\left(1+\bar{r}^2\right)} & \text{(6.2b)} \\ \overline{V_W} = \dfrac{4\delta \ln\left(1+\bar{z}^2\right)}{\left(1+\bar{r}^2\right)^2} - \dfrac{4\delta \ln\left(1+\tilde{z}^2\right)}{\left(1+\tilde{r}^2\right)^2} & \text{(6.2c)} \end{cases}$$

where $\overline{V_R} = V_R/V_{\theta,max}$, $\overline{V_\theta} = V_\theta/V_{\theta,max}$, $\overline{V_W} = V_W/V_{\theta,max}$, $\overline{r} = r/r_c$, $\overline{z} = z/z_{max}$, $\delta = z_{max}/r_c$, $K = S/0.347$, $\tilde{r} = \varepsilon_r\bar{r}$ and $\tilde{z} = \varepsilon_z\bar{z}$. ε_r and ε_z are scaling factors

in the radial and vertical direction and their values set to 0.3 and 1, respectively. These scaling factors give a downdraft located within the core vortex (Baker and Sterling, 2017).

6.2.2 Debris flight equations with Tachikawa numbers

Dimensionless debris flight equations were used to compute the 3D motion of debris, following the same methodology as described in section 5.2. The accelerations of the compact debris are defined as:

$$\begin{cases} \dfrac{\mathrm{d}\overline{V_\theta}}{\mathrm{d}\bar{t}} = K\overline{\boldsymbol{V}}(\overline{V_\theta} - \overline{V_{\theta,d}}) & \text{(6.3a)} \\ \dfrac{\mathrm{d}\overline{V_R}}{\mathrm{d}\bar{t}} = K\overline{\boldsymbol{V}}(\overline{V_R} - \overline{V_{R,d}}) & \text{(6.3b)} \\ \dfrac{\mathrm{d}\overline{V_W}}{\mathrm{d}\bar{t}} = K\overline{\boldsymbol{V}}(\overline{V_W} - \overline{V_{W,d}}) - 1 & \text{(6.3c)} \end{cases}$$

where K is the Tachikawa number, $\bar{t}$ represents the normalised time, $\overline{V_\theta}$ and $\overline{V_{\theta,d}}$ are the normalised tangential wind and debris velocities respectively, $\overline{V_R}$ and $\overline{V_{R,d}}$ the radial wind and debris velocities respectively, $\overline{V_W}$ and $\overline{V_{W,d}}$ the vertical wind and debris velocities respectively, and $\overline{\boldsymbol{V}}$ is the vector of the relative normalised velocity between the wind and debris defined as:

$$\overline{\boldsymbol{V}} = \sqrt{(\overline{V_\theta} - \overline{V_{\theta,d}})^2 + (\overline{V_R} - \overline{V_{R,d}})^2 + (\overline{V_W} - \overline{V_{W,d}})^2} \quad \text{(6.4)}$$

The maximal tangential velocity is used in the Tachikawa number and to normalise the different velocity components.

6.2.3 Simulated vortex wandering

The experimental investigation in section 4.8 revealed an effect of the vortex wandering on the debris trajectories. It showed that the lower the swirl ratio, the higher the vortex wandering, with the vortex centre randomly moving horizontally. Therefore, to assess the effect of the vortex wandering on the analytical vortex flow field, a horizontal random motion was introduced into the model to replicate similar behaviours observed experimentally. The horizontal random motion consists of a circularly bounded Gaussian random walk (Sadegh, 2016) characterised by a normal distribution of vortex centre position with a standard deviation and a confined radius. The confined radius defines the reflective boundary where the random walk is contained.

It is assumed here that if the vortex centre positions were measured experimentally for a significantly long period of time without any external perturbations, the vortex wandering would be circularly bounded within a certain radius. This assumption seems to be supported by PIV measurements in the ISU simulator (Hu et al., 2011). Therefore, for the present work, the random walk was generated to cover the whole confined area with a long timescale ($\bar{t} = 200,000$, which corresponds to about an hour at an experimental scale).

Values of the confined radius between 0 and 1, with 0.1 increments, were investigated and the same generated vortex wandering was introduced into the normalised Rankine, modified Rankine, Burgers-Rott, Sullivan and Baker and Sterling analytical models.

6.3 Effects of vortex wandering on velocity flow fields

6.3.1 Averaged tangential velocity profiles

The different analytical vortex models introduced in section 2.3 were used to investigate the effects of the vortex wandering on the averaged flow fields. The tangential velocity is analysed here for all models, and the velocity profiles show an increase in velocity from the vortex centre up to the core radius, followed by a decrease in velocity. Figure 2.16 in section 2.3 showed the difference in radial and vertical velocity profiles which limits the interpretation of vortex wandering effects between the models. The vortex wandering was introduced by means of a vortex centre displacement from $0r_c$ (no wandering) up to $1r_c$, and the velocity profiles were averaged to obtain time-averaged profiles.

Figure 6.1 shows the tangential velocity profiles for the different vortex models and vortex centre displacements. It is noticeably evident that when introducing vortex wandering in each individual vortex model, the larger the displacement, the more the maximal tangential velocity is reduced. However, the difference far from the core radius ($5r_c$) is less noticeable. For the Rankine model (Figure 6.1 (a)), it is interesting to point out that the discontinuity at $1r_c$, giving a non-physical sense to the Rankine model, is flattening out as vortex wandering is introduced. The maximum tangential velocity also drastically drops as the vortex displacement increases. This is not surprising considering the linear variation of the velocity from the centre where it is equal to zero, to the core radius where it is maximal. For the modified Rankine (Figure 6.1 (b)) and Burgers-Rott (Figure 6.1 (c)) models, the variations in the maximum tangential velocity are similar between the models but lower than for the Rankine model. For the Sullivan model (Figure 6.1 (d)),

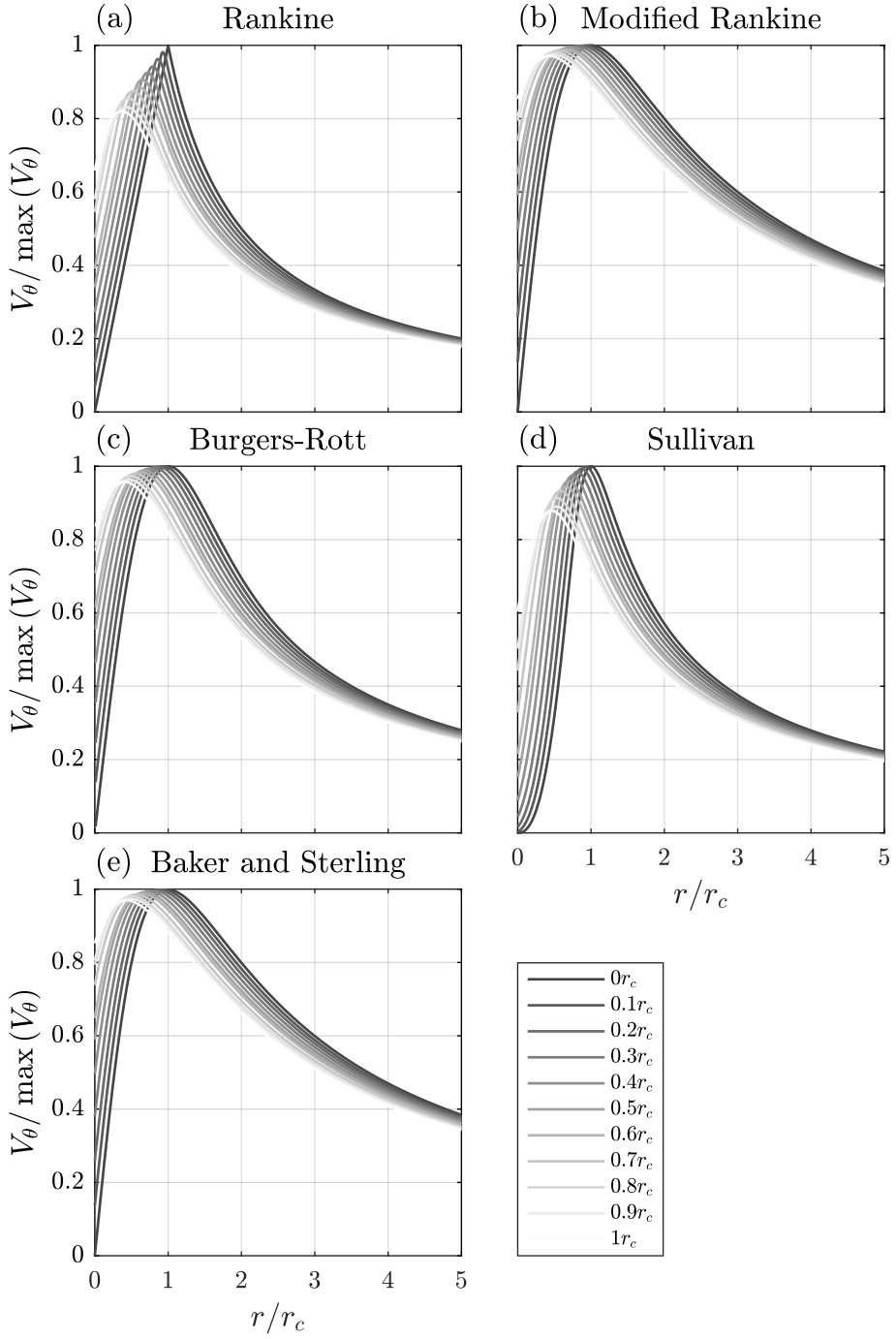


Figure 6.1: Averaged tangential velocities at $z/r_c = 1$ with vortex wandering up to $1r_c$ for (a) Rankine, (b) modified Rankine, (c) Burgers-Rott, (d) Sullivan and (e) Baker and Sterling analytical vortex models.

the fluctuation of the vortex centre position has a significant effect on the velocity profiles. This is not surprising as the tangential velocity slowly increases near the core centre ($r/r_c = 0$) before increasing to the maximal tangential velocity. Although the Sullivan model accounts for a two-cell vortex structure, the structure of the vortex in the Baker and Sterling model does not account for the same slow increase close to $r/r_c = 0$. It is worth noting that the expression of the tangential velocity in Baker and Sterling's model is the same for the one-cell and two-cell formulation (see Equation 6.2 (b)). Figure 6.1 (e) shows similar behaviour between Baker and Sterling's model and Burger-Rott and Sullivan models, with a slight decrease in maximal tangential velocity. This is principally due to the shape of the profile between the centre ($r/r_c = 0$) and the core radius ($r/r_c = 1$).

6.3.2 Variation in core radius size and maximum tangential velocity

Figure 6.2 (a) and (b) show, respectively, the maximum tangential velocity and core radius retrieved from the averaged velocity profiles in Figure 6.1. As discussed in the previous section, Figure 6.2 (a) shows that the maximum tangential velocity decreases as the vortex wandering increases, particularly for the Rankine and Sullivan models. When the vortex centre fluctuations are up to $1r_c$, the Rankine and Sullivan maximum tangential velocities difference is up to 19% and 11%, respectively. For the other models, they appear to be less sensitive, and only a difference up to 5% is observed for the maximum vortex displacement. Zhang and Sarkar (2012) showed a difference up to 15%, whereas Snow and Lund (1997) a difference of 15−50% in the maximum tangential velocity when vortex wandering occurs. Considering the differences were obtained experimentally for different swirl ratios, it cannot precisely be compared to the results shown in Figure 6.2. However, it

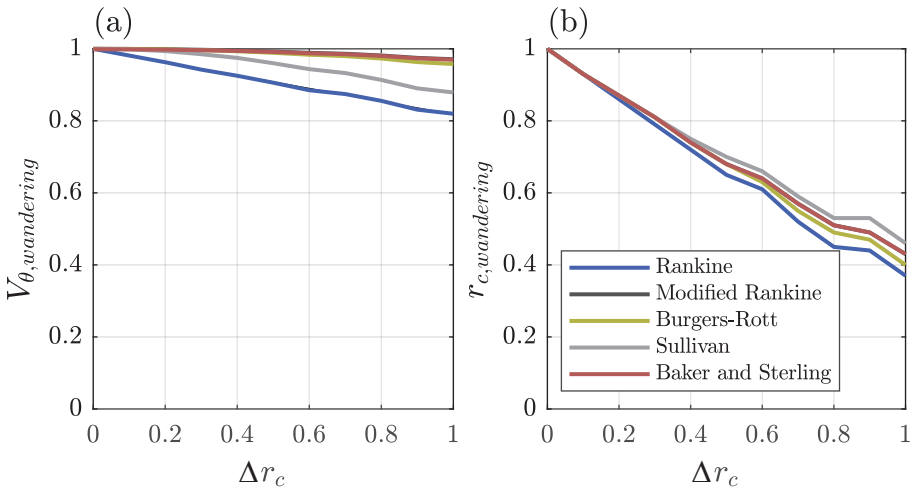


Figure 6.2: Effect of maximal fluctuation Δr_c of the vortex centre position on (a) the maximal tangential velocity and (b) the core radius.

confirms that great care must be taken when interpreting velocity profiles, or mapping when single-point measurements using probes are taken to measure the flow field in tornado-like vortex generators.

Figure 6.2 (b) shows a more significant effect on the core radius than for the maximum tangential velocity. Overall, all models are affected likewise by the introduction of vortex wandering with a somewhat linear decrease of the core radius size. The changes in gradient observed in Figure 6.2 (b) are most likely attributed to the randomness of vortex wandering. Therefore it is assumed that for a greater time scale than considered for the present work ($\bar{t} = 200,000$ here), the core radius size would decrease linearly. For the maximum fluctuation of $1r_c$, a difference of about $50-60\%$ of the core radius size is observed between the different models. Experimentally, in section 4.8, a difference of $17-44\%$ was found in the core radius size between wind and particle tracking measurements, whereas Zhang and Sarkar (2012) and Snow and Lund (1997) showed a difference of $18-29\%$ and up to 46%, respectively. However, as mentioned before, the experimental

measurements were carried out with different swirl ratios, and to date, there is no clear picture of how vortex wandering evolves with the swirl ratio. Therefore, it can be concluded that introducing a fluctuation of the centre positions shows to some extent some agreements, but cannot be used to explain all of the experimentally observed behaviour.

6.3.3 Tangential velocities at the vortex core centre

In section 3.7, horizontal velocity profiles measured using a Cobra probe in the simulator showed that for different swirl ratios the tangential velocity at the centre of the simulator, also assumed to be the centre of the simulated vortex, is not equal to zero. Similar behaviours were also measured by Gillmeier et al. (2018),Tang et al. (2018) and more marginally by Refan and Hangan (2018). Therefore, Figure 6.3 shows the variation in the tangential velocity for different vortex centre fluctuations. For the Rankine model, the central tangential velocity increases linearly up to 0.65 as vortex wandering increases. For the Sullivan model, it slowly

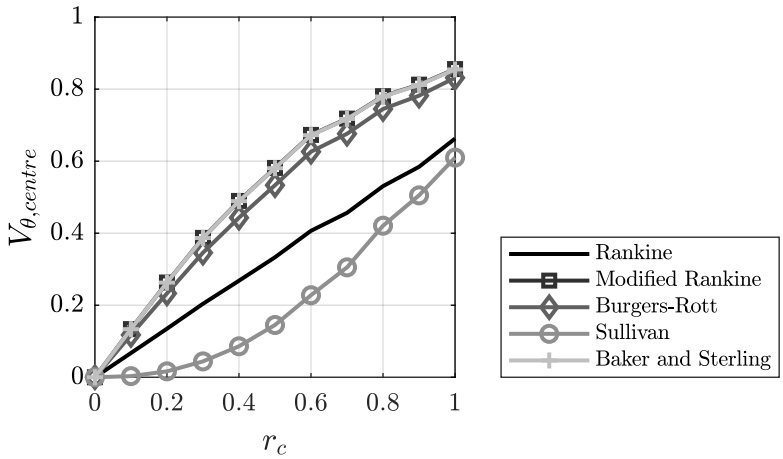


Figure 6.3: Effect of maximal fluctuation Δr_c of the vortex centre position on the tangential velocity at $r/r_c = 0$.

increases, due to the slow increase in velocity close to $r/r_c = 0$, up to 0.6. On the other hand, the central tangential velocity tends to increase more rapidly with the other models to reach up to about 0.8. The measurements presented in section 3.7 showed that normalised tangential velocities at the core centre varied between 0.2 ($S = 0.7$) and 0.40−0.45 ($S = 0.13$ and 0.30) for different swirl ratios and at the height where the maximum tangential velocity occurred. This agrees with errors observed in the estimation of the core radius, where the highest errors were observed for $S = 0.13$ and 0.30, than for $S = 0.7$ (see section 4.8). Therefore, the analysis presented here revealed that vortex wandering could significantly influence the estimation of the core radius and maximum tangential velocity. However, there is nothing indicating which analytical vortex models perform the best in reproducing full-scale or experimental behaviours.

6.4 Tachikawa number effect on debris flight

In this section, vortex models were used to investigate the flight of compact debris using a range of Tachikawa numbers. Table 6.1 presents some Tachikawa numbers and associated debris types found in the literature. The range of Tachikawa numbers investigated in tornado studies ranges from about 1 to 100; however, it is worth noting the studies reported in Table 6.1 have been carried out numerically or analytically. Sassa et al. (2009) looked experimentally at the behaviour of flying debris carried by a travelling tornado, but the data presented in the paper did not enable calculations of the Tachikawa number. Table 6.1 also shows that heavy compact debris were investigated in wind tunnel studies with Tachikawa numbers ranging from approximately 1.5 to 19.

Table 6.1: Brief review of Tachikawa numbers and associated debris types used in tornado and wind tunnel studies.

	Reference	Tachikawa number	Debris type
Tornado	Maruyama (2011)	0.7 <Ta <5.69	Wood plank / car
	Noda et al. (2013)	2 <Ta <100	Not specified
	Baker and Sterling (2018)	28 <Ta <50	Not specified
Wind tunnel	Holmes (2004)	Ta = 2.07	Wood sphere
	Holmes (2004)	Ta = 2.30	Stone sphere
	Karimpour and Kaye (2012*a*)	Ta = 1.59	Gravel
	Richards (2012)	Ta = 5	Steel sphere
	Richards (2012)	Ta = 18.8	Stone sphere

Therefore, a range of Tachikawa numbers from 1 to 100 was analytically investigated here. Based on the debris types reported in Table 6.1, Figure 6.4 shows the equivalent full-scale diameter of the compact debris against the Tachikawa number over the EF-scale range. The diameter was determined based on the maximum wind speed of the specific EF-scale and debris densities. It is assumed that for EF0-EF1 tornadoes, wood debris would most likely be easily embedded and be causing the maximum damage, whereas, for EF2-EF3 and EF4-EF5 tornadoes, stone and steel debris would respectively most likely be easily embedded. Those assumptions are not scientifically proven but help to put into perspective the range of Tachikawa numbers tested here against full-scale tornadoes.

Figure 6.5 shows the trajectories of debris released from $r/r_c = 1$ and $z/r_c = 1$, i.e. where the maximum tangential velocity is found, and calculated using the Burgers-Rott, Sullivan, Baker and Sterling vortex models. For the sake of simplicity, the debris trajectories are shown with a selection of Tachikawa numbers (K = 1, 2,

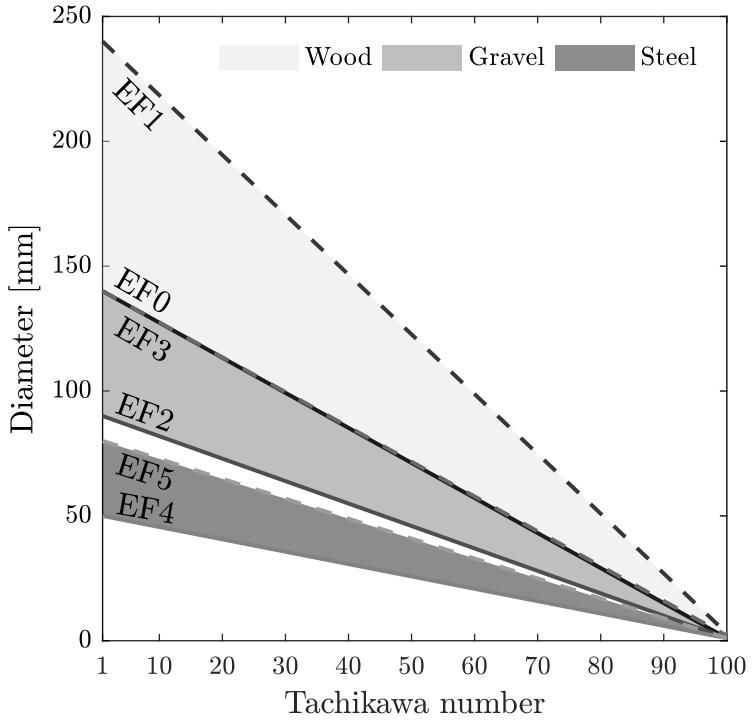


Figure 6.4: Estimated debris diameter based on the EF-scale for different debris types and Tachikawa numbers. Wood debris are more likely to become windborne with EF0-1 tornadoes (light grey), gravel with EF2-3 tornadoes (grey) and steel debris with EFF4-5 tornadoes (dark grey).

5, 10, 20, 40, 60, 80 and 100) corresponding to compact type debris, i.e., debris where the aerodynamic force coefficient would be largely unchanged with the angle of attack.

Debris trajectories using the Burgers-Rott model are shown in Figure 6.5 (a) and show that when releasing debris from $r/r_c = 1$ and $z/r_c = 1$, the debris are mainly swirling towards the vortex centre and lofted with only the heaviest debris (K = 1) impacting the ground. Vertical velocities in the Burgers-Rott model are radially constant but linearly increasing with height. It was found using Equation 6.3c that for K > 1.33 the vertical acceleration of the debris is solely positive. This explains why the trajectory for K = 2 is following a different flight than for 5 ≤ K ≤

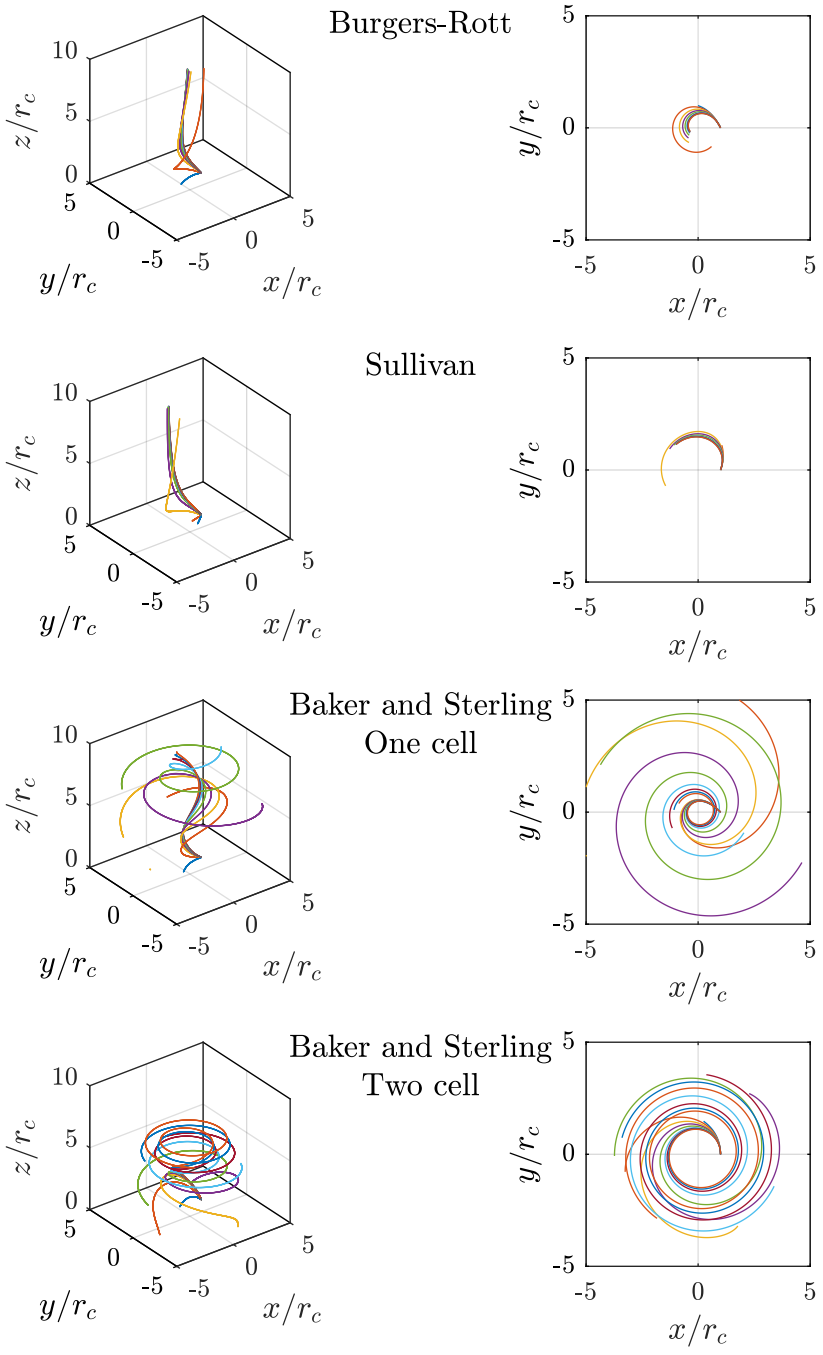


Figure 6.5: Debris released from $r/r_c = 1$ and $z/r_c = 1$ with K = 1, 2, 5, 10, 20. 40, 60, 80 and 100 and with (a) Burgers-Rott, (b) Sullivan, (c) Baker and Sterling one-cell and (d) Baker and Sterling two-cell vortex models.

100, with the debris slowly moving upward before significantly being moved aloft. Similar behaviours are observed for the Sullivan model (Figure 6.5 (b)), although the debris impacts the ground for K = 1 and 2. At $r/r_c = 1$ and $z/r_c = 1$, the radial and vertical components of the Sullivan model are positive and close to 0, respectively. Therefore, as soon as the debris is released, the debris is subjected to vertical velocity and depending on the Tachikawa number, it will be moved aloft or not. Nevertheless, Figure 6.5 (a) and Figure 6.5 (b) point out again the limitations of unbounded vortex models as discussed in section 2.3. Vertical axes on Figure 6.5 are shown up to $z/r_c = 10$, but the trajectories for the Burgers-Rott and Sullivan models are essentially continuing towards infinity.

Figure 6.5 (c) shows the debris trajectories using Baker and Sterling's one-cell model. Similar to Burgers-Rott and Sullivan, only debris with K = 1 impacts on the ground. However, the major difference with the former models is that for K $\geq$ 2 the debris are embedded aloft up to a temporary equilibrium height, where the debris stops moving upward and starts to slowly fall. Baker and Sterling (2017) showed that the significant parameters influencing whether the debris is flying or falling are the swirl ratio and the buoyancy parameter, i.e. the Tachikawa number to some extent. Here, the swirl ratio is fixed to $S = 1$; therefore, the flight of debris is solely dependent on the Tachikawa number. Compared to the Burgers-Rott and Sullivan models, debris flight using the one-cell formulation of Baker and Sterling's model shows significantly different trajectories for each Tachikawa number. For low Tachikawa numbers, debris tends to fly close to the core vortex whereas, for high Tachikawa, the debris are gradually flying away from the vortex. Similar behaviours were observed in Baker and Sterling (2017) for falling and flying

debris.

Debris trajectories using the two-cell formulation of Baker and Sterling's model are shown in Figure 6.5 (d) and show very different behaviours than observed in Figure 6.5 (c). Increasing the Tachikawa number shows that the debris are gradually flying further away from the core vortex and higher, while still impacting the ground within one revolution up to K = 20. For K > 20, the debris are reaching a temporary equilibrium height before falling, as observed with the one-cell formulation. However, the biggest difference between the two formulations is the fact debris are always being ejected outwards from the core vortex. This behaviour is typical for a two-cell vortex structure and confirms the possible two-cell structure for all swirl ratios, which was observed experimentally (see section 3.6).

Figure 6.6 shows the range of Tachikawa numbers when the debris are released from radial positions $r/r_c = 0.5$, 1 and 2 and height positions $z/r_c = 0.5$, 1 and 2, and impacting the ground within one revolution. It is undeniable that different analytical vortex models behave very differently when it comes to debris flight. Although released from the same height but from different radial positions, large discrepancies are observed between the models. The range of Tachikawa numbers of the debris impacting the ground generally increases with the radial distance for the Burger-Rott and Sullivan models, whereas it decreases for Baker and Sterling's one-cell model. Although Baker and Sterling's two-cell model seems to give a lower and more limited range of Tachikawa numbers, it is the only model showing consistency between the different release heights. Therefore, considering the similarities observed between experimental trajectories and Baker and Sterling's

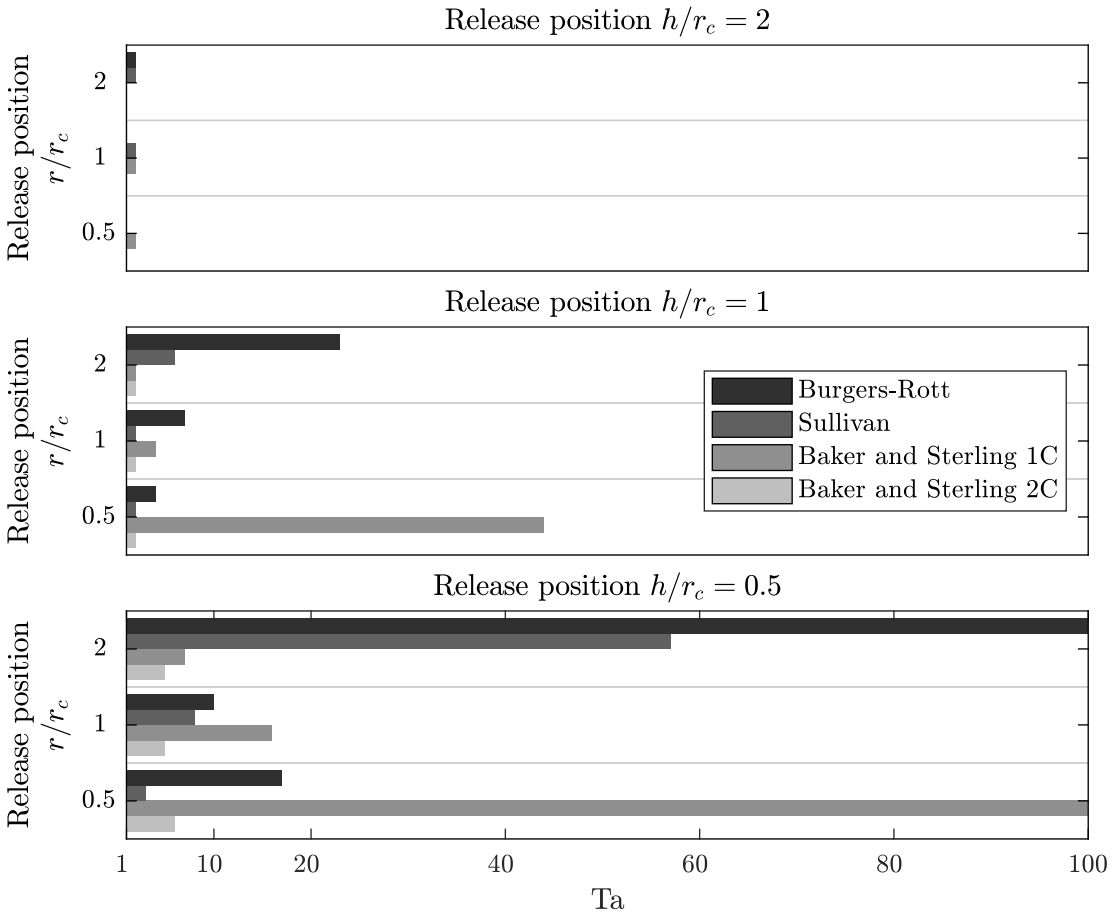


Figure 6.6: Comparison between different vortex models of the ranges of Tachikawa numbers when the debris is released for different radial and height positions and impacting the ground within one revolution.

two-cell model and the consistency for different release positions, it appears that Baker and Sterling's two-cell model is the most suitable for the study of debris flight. Moreover, full-scale two-cell structured tornadoes are more often observed than single-cell ones (Baker and Sterling, 2017).

6.5 Debris flight in Baker and Sterling's two-cell model

This section will now focus on Baker and Sterling's model as it appeared to better match the experimental flow field (Gillmeier et al. (2018); see section 3.7) as well as being more consistent with debris flight analysis (Figure 6.6).

6.5.1 Effect of Tachikawa numbers on impact velocity

Figure 6.7 shows the variation of the impact velocity of the debris against the Tachikawa number using Baker and Sterling models. The impact velocity was normalised using the wind velocity at the released position; therefore, it reflects whether the debris impacts the ground at a lower or higher velocity than initiated from. For both models, Figure 6.7 reveals that the ratio of impact and wind velocity clearly decreases non-linearly for most of the release positions as the Tachikawa number increases. Given the fact impact velocities were only considered when the debris reaches the ground within one revolution, it is most likely that some of the profiles would extend further if longer flights were considered. The condition to impact within one revolution was chosen to ensure the momentum at impact originates from the wind at the release position and to a lesser extent from built-up momentum during the debris flight. For the one-cell model (Figure 6.7 (a)), most of the debris impacting the ground are contained with Tachikawa numbers between 1 and about 10, i.e. mainly heavy debris. When the debris were released within the boundary layer ($z/r_c = 0.5$) and far from the centre ($r/r_c = 2$), the debris are impacting the ground up to K = 60. At this release position, it is also the only case where the impact velocity is greater than the initial wind velocity. For the two-cell model (Figure 6.7 (b)), a similar trend is observed than for the one-cell

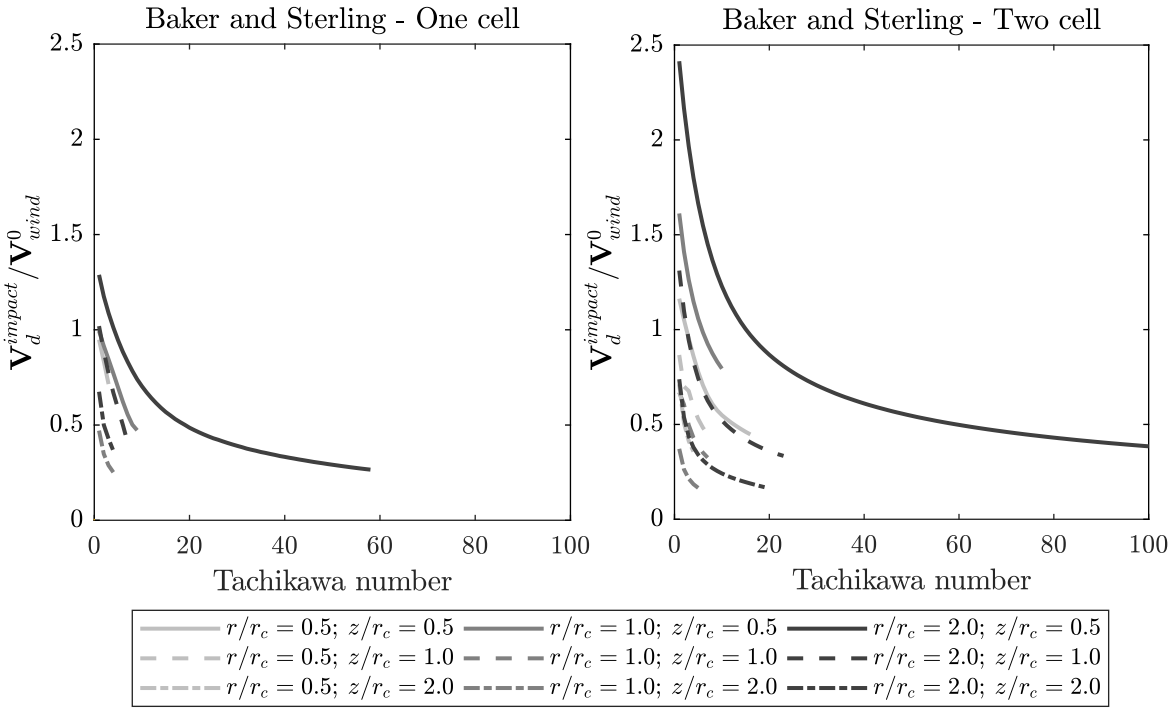


Figure 6.7: Relation between normalised initial impact debris velocities and Tachikawa number for Baker and Sterling's (a) one-cell and (b) two-cell vortex models and for debris impacting the ground within one revolution. The velocities are normalised by the wind velocity at the release location ($\boldsymbol{V}_{wind}^0$).

model, although some debris are now impacting the ground up to K = 100.

The biggest difference between the two models is the fact that more release positions are now showing impact velocities greater than the initial wind speeds, with velocity factors up to 2.5. It shows that not only debris initiated in strong winds can have significant impact momentum but also debris initiated further from the core vortex ($2r_c$ here) can also reach high velocities and potentially cause great damage. This behaviour can be attributed to the fact that vertical winds (for instance at $r/r_c = 2$, $z/r_c = 0.5$) are just strong enough to keep the debris airborne without being considerably moved aloft. Therefore, debris is dragged towards the

region of maximum velocities and the heavier the debris, the higher its impact velocity. Similar experimental behaviour was discussed in section 4.9 when debris were released from $r/r_c = 2$ with $S = 0.13$. However, due to the simplified nature of the model itself and the fact that it has not been validated against full-scale data to date, it is unclear whether the relationship between the Tachikawa number and the ratio of wind and impact velocities is dependent on the model itself. The same analysis for Burgers-Rott and Sullivan (not shown) did not depict any relationship at all. Nevertheless, Baker and Sterling's model is the only model including a representation of the boundary-layer and therefore gives some credit to be potentially representative of a full-scale event.

6.5.2 Effect of turbulence intensity and vortex wandering

Figure 6.8 shows 100 debris trajectories computed using Baker and Sterling's model with K = 5 and looking at the effect of the turbulence intensity and vortex wandering when the debris were released over time. Debris were released every $\Delta\bar{t} = 0.125$ for a duration $\bar{t} = 120$, which corresponds at full-scale to a few debris being initiated per second for several minutes. The turbulence intensity was introduced by incorporating into the calculations fluctuations to the initial debris tangential, radial and vertical velocities (same methodology as in section 5.2), and the standard deviation was calculated using the wind velocity vector at the release position. The vortex wandering was generated and introduced, as discussed in section 5.2. To ensure repeatability, the same set of generated random vortex wandering and turbulence intensities were used between each simulation, i.e. each row and column in Figure 6.8 uses the same repeatable random data. Figure 6.8 (a-d) shows

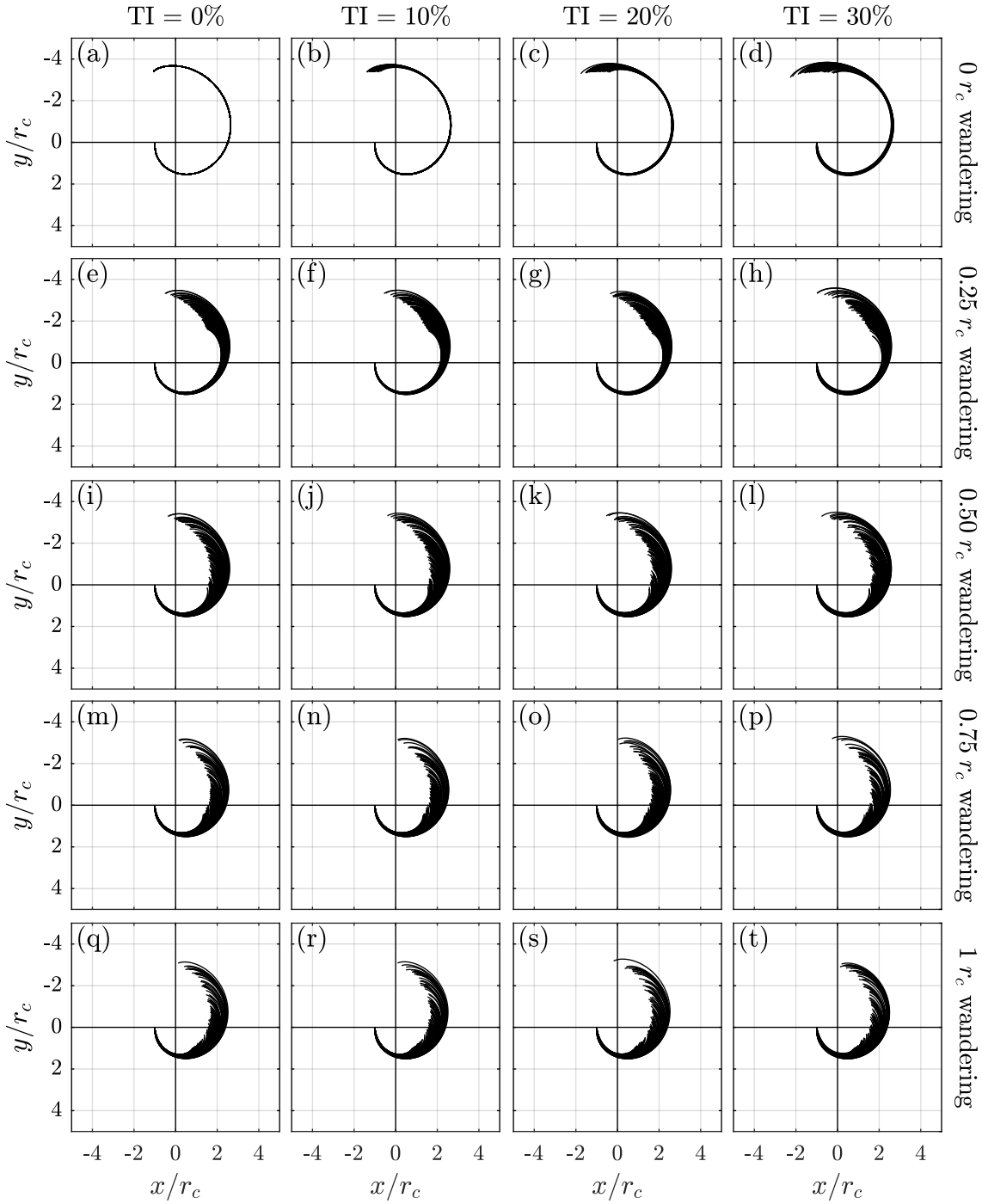


Figure 6.8: Effect of turbulence intensity and vortex wandering on 100 debris computed using Baker and Sterling's two-cell model and released from $r/r_c = 1$ and $z/r_c = 1$.

the effect on the trajectories of the turbulence intensity, only with no vortex wandering. Without any turbulence or wandering, the 100 debris unsurprisingly follow the same trajectories (Figure 6.8 (a)). When increasing the turbulence intensity, Figure 6.8 (b−d) shows little effect on the early stages of the debris trajectories, but some variations are observed in falling locations. The debris trajectories still follow the same main flight, as shown in Figure 6.8 (a) but the falling locations broaden as the turbulence increases, with debris simply falling closer and further. Holmes (2004) showed that incorporating turbulence into the simulated wind fields does not affect the mean trajectories over a certain amount of trajectory samples, but only adds variability into the horizontal velocity and displacement. Similar behaviour is observed here, although turbulence was only incorporated into the initial debris velocities and not into the simulated flow fields. To date, the poor understanding of turbulence in tornado-like flow fields and full-scale tornadoes limits the complexity of analytical vortex flow fields. However, introducing the vortex wandering appears to lower the effect of turbulence around the release position. Figure 6.8 (e−h) shows the debris trajectories when the vortex centre wanders up to $0.25r_c$, with turbulence intensity increasing from 0 to 30%. Although variabilities in the falling location without vortex wandering were observed, very modest variations are observed in the falling locations when the vortex is moving.

The same conclusion can be drawn when the vortex wandering is up to $0.5r_c$ (Figure 6.8 (i−l)), $0.75r_c$ (Figure 6.8 (m−p)) or $1r_c$ (Figure 6.8 (q−t)). Nevertheless, adding vortex wandering influences the falling locations of the debris with more debris falling quicker as the vortex displacement increases. Table 6.2 shows that in general, adding turbulence to the initial conditions has little effect on the mean flight distances, but the standard deviation only increases when no wandering

was introduced. However, introducing vortex wandering significantly decreases the mean flight distance and increases the standard deviation with a mean flight distance of about twice as low as when the vortex wanders up to $1r_c$. Therefore, the analysis suggests the variability in the falling locations, as observed in section 4.9, can be attributed to wind field variabilities, mainly due to the wandering of the vortex rather than turbulent velocity fluctuations around the release location.

Table 6.2: Normalised mean flight distance and standard deviation for different turbulence intensities and vortex wandering.

		Turbulence intensity (%)			
		0	10	20	30
$\Delta r_c/r_c$	0	11.4 ± 0.00	11.3 ± 0.14	11.3 ± 0.28	11.3 ± 0.40
	0.25	7.9 ± 1.03	7.9 ± 1.04	7.9 ± 1.03	8.0 ± 1.12
	0.5	6.8 ± 1.67	6.8 ± 1.66	6.8 ± 1.68	6.8 ± 1.71
	0.75	5.7 ± 1.56	5.7 ± 1.57	5.7 ± 1.57	5.8 ± 1.59
	1	5.0 ± 1.92	5.0 ± 1.92	5.0 ± 1.93	5.1 ± 1.97

6.6 Concluding remarks

The following conclusions can be drawn from the simulation and analysis of the flight of debris in analytical vortex models presented above:

1. Averaging the vortex model flow fields subjected to vortex wandering showed that the maximum tangential velocity and core radius size decreases for all vortex models as the vortex wandering increases. However, discrepancies were found between the models, but the modified Rankine, Burgers-Rott and Baker and Sterling tangential velocity components appear to perform the same way.

2. None of the models simulates similar trajectories when releasing debris from the same position. It was found that the range of Tachikawa numbers to be used for debris impacting the ground is limited. However, when releasing debris from different radial and height positions, Baker and Sterling's two-cell model appeared to have a more consistent range of Tachikawa numbers to be investigated.

3. Using Baker and Sterling's two-cell model, an effect of the Tachikawa number on the impact velocity was found. It showed that the impact velocity decreases non-linearly as the Tachikawa number as well as the impact velocity can be higher than the wind velocity the windborne debris originated from.

4. Also using Baker and Sterling's two-cell model, introducing turbulence intensity into the debris initial velocities as well as vortex wandering suggests that variations in the debris trajectories could be attributed to the vortex wandering.

Nevertheless, analytical vortex models also show limitations in modelling debris flight. Large differences in debris flight between the Burgers-Rott, Sullivan and Baker and Sterling models were found. The Burger-Rott and Sullivan models showed that they are not suitable for debris flights as the vertical components of the models are unbounded. The Baker and Sterling model gives better results, but the validation of the model against full-scale data is required before considering further analysis.

Chapter 7

Conclusions and recommendations for further work

7.1 Introduction

The main aim of this research was to explore tornado-like flow fields and investigate the flight of debris using physical and numerical simulations. This section summarises the main concluding remarks made in each chapter with a discussion of the different objectives listed in the introductory chapter. Recommendations for further work on the investigation of either the physical modelling of tornadoes or the flight of debris in tornadoes are suggested in section 7.3.

7.2 Conclusion

Objective 1: Characterise the vortex structure within the tornado simulator, using a velocity mapping with a high spatial resolution for different swirl ratios.

Chapter 3 focused on the physical modelling of tornado-like vortices using the UoB-TVG. The UoB-TVG was built during the early stages of this research; therefore, characterising the flow fields was crucial to understanding the performance of the

simulator. To do this, a traverse system and a control and data acquisition software were designed and developed to ease the mapping of different flow fields. Three swirl ratios were investigated (i.e. $S = 0.13$, 0.3 and 0.7) and wind velocity measurements revealed far more complex vortex structures than those idealised by conceptual views. For a low swirl ratio, for which a single cell structure is usually observed, a clear updraft could not be identified.

The flow visualisation already pointed out the large vortex wandering for this swirl ratio, which was confirmed and characterised in section 3.3. The medium and large swirl ratio depicted a clearer vortex structure. However, the flow field for S = 0.3 showed a clear recirculation, whereas, for this swirl ratio, a single cell vortex should be expected. This questions the formulation of the swirl ratio for Ward-type simulators as a function of the aspect ratio. Gillmeier et al. (2019) showed that two simulators with different geometric scales but the same aspect ratios and swirl ratios produce two significantly different flow fields. Therefore, it appears crucial that an accurate measurement of the vortex circulation is undertaken to correctly estimate the swirl ratio of tornado-like vortices. Nevertheless, some characteristics of the flow fields showed good similarities with other tornado simulators. The core radius was found to increase with height. For each swirl ratio, the maximal tangential velocities are located near the ground, and the radial profiles for each velocity component are consistent with height. Horizontal profiles of radial and vertical velocities are however different with height. The vertical profiles of radial, tangential and vertical velocities are also generally consistent with height for different radial locations and above the corner region.

Comparison with analytical vortex models confirmed the complexity of the flows but also the limitations of the vortex models to replicate tornado-like flow fields.

The tangential velocity was well represented by the models and has generally been in other tornado simulators. However, despite the fact the Burgers-Rott and Sullivan models have been expressed dimensionlessly, the models significantly overestimated the radial and vertical velocities. Baker and Sterling's model seems to better approach the experimental data, and Gillmeier et al. (2018) drew the same conclusions with another dataset. However, to date, these models are too simplistic to genuinely replicate tornado(-like) flow fields and still require some turbulent and time dependencies. Davies-Jones and Wood (2006) expressed a time-dependent version of the Burgers-Rott model. Although it has some credit to investigate developing tornado-like vortices, it did not account for the evolution of the vortex structure over time. Including some sort of turbulence into the vortex models seems somewhat delicate, as turbulent wind fields either experimentally or at full-scale are still unresolved. Therefore, using analytical vortex models remains the most straightforward way, but they are to date not realistically modelling tornadoes.

Objective 2: Develop a methodology to investigate the flight of debris using high-speed cameras and the Particle Tracking Velocimetry technique.

Obtaining experimental debris trajectories was a crucial milestone of this research work, as a gap in the literature was identified. Therefore, Chapter 4 focused on the experimental investigation of the flight of debris in the tornado simulator and was performed using the Particle Tracking Velocimetry technique. This technique is commonly used in air and water flow to characterise the flow field but has rarely been used to describe long and individual trajectories. In order to develop the

PTV system, three high-speed cameras were used, synchronised using a trigger device, and calibration targets were designed for the calibration of the system.
A thorough calibration of the PTV system was undertaken, and a good level of accuracy was achieved with marginal errors in position and velocity (submillimetre position errors and lower than 2% velocity errors). This allowed a good tracking of multiple debris released over time, enhanced by the development of different pre- and post-processing methodologies. Overall, individual debris were successfully tracked in 2D or 3D.
Individual debris flying freely in the simulator were first investigated for different debris sizes and swirl ratios. Debris were found to be flying close to the ground without being significantly lifted and swirled around the core vortex within radial distances up to twice the size of the core radius ($2r_c$). This seems to agree with measurements of the debris cloud of a full-scale tornado. In order to statistically assess the flight of debris, multiple debris were released into the different flow fields either from the ground or from a house model. In both cases, the debris were found to be flying up and then impacting the ground. Variabilities in the initial direction of the debris were discovered and appeared to be related to fluctuations of the local flow field around the release location. When the debris were released from the building model, similar flight characteristics were found but with a change up to 40 degrees in the initial debris direction. This indicated that, overall, the simulated flow field was not affected by the model, but only the local flow field around the building was fluctuating. Nevertheless, the region affected by impacting debris were found to be significantly larger when initiating the debris from the building model than from the ground. Debris released from the ground were also found to be travelling at distances of 3 up to 5 times the size of the core radius.

Therefore, the risk associated with windborne debris is not only limited to urban areas but could also be increased by long-distance travelling debris embedded in a landscaped environment.

Objective 3: Develop a methodology to numerically simulate the flight of debris, using analytical vortex models.

In chapters 5 and 6, debris trajectories were investigated numerically using either experimental data or analytical vortex models. The original objective was to focus on analytical models, but a robust method to compute trajectories from experimental data was also developed. Computer codes were designed and maintained to efficiently compute the debris trajectories from Holmes' debris flight equations. The data obtained from wind velocity mapping and PTV experiments were incorporated into the debris flight equations, and results were compared with PTV data. The methodology was shown to be accurate in reproducing strong similarities with experimental results and replicated surprisingly well a similar behaviour when the debris were released inside the core vortex in a highly turbulent flow field. The methodology has good potential to be used with different tornado(-like) flow fields and various types of debris.

The performance of five analytical vortex models to compute debris trajectories was evaluated. A parametric study was undertaken with debris initiated from different locations with Tachikawa numbers ranging from 1 to 100, i.e. from heavy to light debris. The analysis showed that none of the models simulate similar trajectories and the range of Tachikawa numbers that can be considered to investigate debris impact is rather limited, with mainly heavy debris impacting the ground.

Nevertheless, Baker and Sterling's two cell model appeared to be more consistent when releasing debris from different locations. The debris impact velocity seemed to have some sort of reciprocal relation to the Tachikawa number, with heavier debris impacting at a higher velocity than lighter debris. Finally, introducing turbulence and vortex wandering to the model seemed to confirm the experimental observation that variations in debris trajectories are related to the vortex wandering rather than small scale turbulence.

The question of using analytical vortex models for debris studies remains open. To date, the lack of full-scale data to validate the models keeps them at the theoretical stage. The fact that only the tangential velocity component is generally compared with experimental or full-scale data clearly limits the assessment of the models' performance. Baker and Sterling's model showed good promise in modelling experimental tornado-like flow fields but was only compared to data from a single tornado simulator. More comparisons, particularly with different tornado simulator flow fields, are needed before considering further analysis with regards to the flight of debris in tornadoes.

7.3 Recommendations for further work

The work presented in this thesis has shown good potential for investigating the flight of compact debris in tornadoes experimentally and numerically. However, further questions still need to be addressed in future studies to understand the interaction between debris and tornadoes with a more general scope.

The experimental techniques generally used to conduct wind measurements in tornado-like flow fields are usually not adapted for such a complex, three-dimensional

and transient flow field. Multi hole probes are useful to picture an averaged flow field but can be limited in highly turbulent flow fields. On the other hand, PIV is great for obtaining instantaneous and averaged flow fields but can only measure individual planes at a time. Therefore, volumetric wind measurements could retrieve instantaneous 3D flow fields and provide essential information about the structure of the flow field. Additionally, debris could also be tracked while measuring the 3D flow field, and therefore it would provide critical indications about the interaction between debris and tornado winds.

More debris types need to be investigated experimentally. The low Reynold number in the tornado simulator was a significant drawback for the examination of more debris types, as only Styrofoam beads appeared to suitably fly. Using a large tornado simulator will allow using different debris sizes and densities, with more realistic full-scale equivalents. Scaling the debris up to full-scale using the Tachikawa scaling gave some rather practical information but was dependent on a geometric scaling. Scaling is one of the critical challenges for tornado studies. Obtaining proper scaling is necessary to compare experimental and full-scale tornado flow fields. Baker and Sterling (2019) pointed out the limitations of tornado simulators to replicate realistic tornado-like flow fields. Full-scale data are challenging to collect due to the unpredictability of tornadoes and the associated risks, as noted in section 2.2.4. Wind data close to the surface, where the strongest winds are observed and critical for engineering and non-engineering structures, are generally still lacking. On the other hand, measuring wind components experimentally can bring a certain amount of uncertainty, especially when measuring near the surface. Therefore, establishing a general concept for scaling tornadoes appears to be imperative before further considering either physical modelling, wind loading or

debris studies.

Finally, it is essential to obtain more full-scale data and especially retrieve debris flight information during a tornado. The recent use of drones to get extremely close footage of tornadoes could be useful to obtain quality footage for photogrammetry analysis. Sassa et al. (2014) used mobile phone videos to perform photogrammetry analysis and retrieved flow field information of a full-scale tornado. Drone swarm, i.e. multiple drones flying in formation, could be used in that sense to obtain more video footage in a safe and controlled environment.

References

Adamczyk, A. A. and Rimai, L. (1988), 'Reconstruction of a 3-dimensional flow field from orthogonal views of seed track video images', *Experiments in Fluids* **6**(6), 380–386.

Akutina, Y., Mydlarski, L., Gaskin, S. and Eiff, O. (2018), 'Error analysis of 3D-PTV through unsteady interfaces', *Experiments in Fluids* **59**(3), 53.

Alexander, C. R. and Wurman, J. (2008), Updated mobile radar climatology of supercell tornado structures and dynamics, *in* '24th Conf. on Severe Local Storms, Savannah, GA, Amer. Meteor. Soc.', p. 19.4.

Anderson, C. E. (1985*a*), The Barneveld tornado: A new type of tornadic storm in the form of a spiral mesolow, *in* 'Preprints, 14th Conf. on Severe Local Storms, Amer. Meteor. Soc.', pp. 289–292.

Anderson, C. E. (1985*b*), The fall-out pattern for debris for the Barneveld, WI tornado: An F-5 storm, *in* '14th Conf. on Severe Local Storms, Amer. Meteor. Soc.', pp. 264–266.

Antonescu, B., Fairman, J. G. and Schultz, D. M. (2018), 'What is the Worst That Could Happen? Reexamining the 24–25 June 1967 Tornado Outbreak

over Western Europe', *Weather, Climate, and Society* **10**(2), 323–340. doi: 10.1175/WCAS-D-17-0076.1.

Antonescu, B., Schultz, D. M., Holzer, A. and Groenemeijer, P. (2016), 'Tornadoes in Europe: An Underestimated Threat', *Bulletin of the American Meteorological Society* **98**(4), 713–728. doi: 10.1175/BAMS-D-16-0171.1.

Arduino (2011), 'What is Arduino?'. [Last Accessed: 23/11/2019].
URL: *https://www.arduino.cc/en/guide/introduction*

Baker, C. J. (2007), 'The debris flight equations', *Journal of Wind Engineering and Industrial Aerodynamics* **95**(5), 329–353.

Baker, C. J. and Sterling, M. (2017), 'Modelling wind fields and debris flight in tornadoes', *Journal of Wind Engineering and Industrial Aerodynamics* **168**(February), 312–321.

Baker, C. J. and Sterling, M. (2018), 'A conceptual model for wind and debris impact loading of structures due to tornadoes', *Journal of Wind Engineering & Industrial Aerodynamics* **175**(February 2017), 283–291.

Baker, C. and Sterling, M. (2019), 'Are Tornado Vortex Generators fit for purpose?', *Journal of Wind Engineering and Industrial Aerodynamics* **190**, 287–292.

Baker, C., Sterling, M. and Jesson, M. (2020), 'The lodging of crops by tornadoes', *Journal of Theoretical Biology* **500**, 110309.
URL: *http://www.sciencedirect.com/science/article/pii/S0022519320301648*

Behr, R. A. and Minor, J. E. (1994), 'A survey of glazing system behavior in multi-story buildings during hurricane andrew', *The Structural Design of Tall Buildings* **3**(3), 143–161. doi: 10.1002/tal.4320030302.

Biwole, P. H., Yan, W., Zhang, Y. and Roux, J.-J. (2009), 'A complete 3D particle tracking algorithm and its applications to the indoor airflow study', *Measurement Science and Technology* **20**(11), 115403.

Bluestein, H. B. (2013), *Severe Convective Storms and Tornadoes: Observations and Dynamics*, Springer.

Bluestein, H. B., Snyder, J. C. and Houser, J. B. (2015), 'A Multiscale Overview of the El Reno, Oklahoma, Tornadic Supercell of 31 May 2013', *Weather and Forecasting* **30**(3), 525–552.
URL: *https://doi.org/10.1175/WAF-D-14-00152.1*

Bluestein, H. B. and Unruh, W. P. (1989), 'Observations of the Wind Field in Tornadoes, Funnel Clouds, and Wall Clouds with a Portable Doppler Radar', *Bulletin of the American Meteorological Society* **70**(12), 1514–1525. doi: 10.1175/1520-0477(1989)0702.0.CO;2.

Bodine, D. J. and Kurdzo, J. M. (2018), Ground-Based Radar Technologies for Tornado Observations, *in* Springer, ed., 'Remote Sensing of Clouds and Precipitation', springer r edn, pp. 65–112.

Bosbach, J., Kühn, M. and Wagner, C. (2009), 'Large scale particle image velocimetry with helium filled soap bubbles', *Experiments in Fluids* **46**(3), 539–547.

Bourriez, F., Sterling, M. and Baker, C. (2019), Windborne debris trajectories in tornado-like flow field initiated from a low-rise building, *in* '15th International Conference on Wind Engineering, Beijing, China, September 1-6, 2019'.

Bown, M. R., MacInnes, J. M., Allen, R. W. K. and Zimmerman, W. B. J. (2006), 'Three-dimensional, three-component velocity measurements using stereoscopic micro-PIV and PTV', *Measurement Science and Technology* **17**(8), 2175–2185.

Brooks, H. E. and Doswell, C. A. (2001), 'Normalized Damage from Major Tornadoes in the United States: 1890–1999', *Weather and Forecasting* **16**(1), 168–176. doi: 10.1175/1520-0434(2001)0162.0.CO;2.

Brooks, H. E., Doswell, C. A. and Kay, M. P. (2003), 'Climatological Estimates of Local Daily Tornado Probability for the United States', *Weather and Forecasting* **18**(4), 626–640. doi: 10.1175/1520-0434(2003)0182.0.CO;2.

Brooks, H. E., Lee, J. W. and Craven, J. P. (2003), 'The spatial distribution of severe thunderstorm and tornado environments from global reanalysis data', *Atmospheric Research* **67-68**, 73–94.

Brown, D. (1971), 'Close-range camera calibration', *Photogrammetric Engineering & Remote Sensing* **37**, 855–866.

Brown, R. A., Lemon, L. R. and Burgess, D. W. (1978), 'Tornado Detection by Pulsed Doppler Radar', *Monthly Weather Review* **106**(1), 29–38. doi: 10.1175/1520-0493(1978)1062.0.CO;2.

Burgers, J. M. (1948), A Mathematical Model Illustrating the Theory of Turbulence, Vol. 1, Elsevier, pp. 171–199.

Chang, T. P. K., Watson, A. T. and Tatterson, G. B. (1985), 'Image processing of tracer particle motions as applied to mixing and turbulent flow—I. The technique', *Chemical Engineering Science* **40**(2), 269–275.

Chernov, N. (2009), 'Circle Fit (Pratt method)'. MATLAB Central File Exchange. [Last Accessed: 22/01/2020].
URL: *https://www.mathworks.com/matlabcentral/fileexchange/22643-circle-fit-pratt-method*

Chiu, W. C. and Rib, L. N. (1956), 'The rate of dissipation of energy and the energy spectrum in a low-speed turbulent jet', *Eos, Transactions American Geophysical Union* **37**(1), 13–26. doi: 10.1029/TR037i001p00013.

Church, C. R., Snow, J. T. and Agee, E. M. (1977), 'Tornado Vortex Simulation at Purdue University', *Bulletin of the American Meteorological Society* **58**(9), 900–909. doi: 10.1175/1520-0477(1977)0582.0.CO;2.

Church, C. R., Snow, J. T., Baker, G. L. and Agee, E. M. (1979), 'Characteristics of Tornado-Like Vortices as a Function of Swirl Ratio: A Laboratory Investigation', *Journal of the Atmospheric Sciences* **36**(9), 1755–1776. doi: 10.1175/1520-0469(1979)0362.0.CO;2.

Colby, F. P. (1984), 'Convective Inhibition as a Predictor of Convection during AVE-SESAME II', *Monthly Weather Review* **112**(11), 2239–2252. doi: 10.1175/1520-0493(1984)1122.0.CO;2.

Courant, R., Friedrichs, K. and Lewy, H. (1928), 'Über die partiellen Differenzengleichungen der mathematischen Physik', *Mathematische Annalen* **100**(1), 32–74.

Crawford, K. (2012), Experimental and analytical trajectories of simplified debris models in tornado winds, Msc thesis, Iowa State University.

Davies-Jones, R. P. (1973), 'The Dependence of Core Radius on Swirl Ratio in a Tornado Simulator', *Journal of the Atmospheric Sciences* **30**(7), 1427–1430. doi: 10.1175/1520-0469(1973)0302.0.CO;2.

Davies-Jones, R. P. (2015), 'A review of supercell and tornado dynamics', *Atmospheric Research* **158-159**, 274–291.

Davies-Jones, R. P. and Wood, V. T. (2006), 'Simulated Doppler Velocity Signatures of Evolving Tornado-Like Vortices', *Journal of Atmospheric and Oceanic Technology* **23**(8), 1029–1048. doi: 10.1175/JTECH1903.1.

Diamond, C. J. and Wilkins, E. M. (1984), 'Translation Effects on Simulated Tornadoes', *Journal of the Atmospheric Sciences* **41**(17), 2574–2580. doi: 10.1175/1520-0469(1984)0412.0.CO;2.

Dias, S. (2011), 'An Increase in the Number of Tornado Reports in Brazil', *Weather, Climate, and Society* **3**(3), 209–217. doi: 10.1175/2011WCAS1095.1.

Doswell, C. A., Moller, A. R. and Brooks, H. E. (1999), 'Storm Spotting and Public Awareness since the First Tornado Forecasts of 1948', *Weather and Forecasting* **14**(4), 544–557. doi: 10.1175/1520-0434(1999)0142.0.CO;2.

Dunn, W. L. and Twisdale, L. A. (1979), 'A synthesized windfield model for tornado missile transport', *Nuclear Engineering and Design* **52**(1), 135–144.

FEMA-361 (2015), Safe Rooms for Tornadoes and Hurricanes: Guidance for Community and Residential Safe Rooms, Third Edition, Technical report.

Ferrel, W. (1861), 'The motions of fluids and solids relative to the Earth's surface', *American Journal of Science* **31**, 27–50.

FFmpeg (2000), 'About FFmpeg'. [Last Accessed: 08/02/2020].
URL: *https://www.ffmpeg.org/about.html*

Fiedler, B. H. and Rotunno, R. (1986), 'A Theory for the Maximum Windspeeds in Tornado-like Vortices', *Journal of the Atmospheric Sciences* **43**(21), 2328–2340. doi: 10.1175/1520-0469(1986)0432.0.CO;2.

French, M. M., Bluestein, H. B., PopStefanija, I., Baldi, C. A. and Bluth, R. T. (2013), 'Reexamining the Vertical Development of Tornadic Vortex Signatures in Supercells', *Monthly Weather Review* **141**(12), 4576–4601. doi: 10.1175/MWR-D-12-00315.1.

Frye, U., Ginger, J. and Mullins, P. (2009), Response of cladding to windborne debris impact, *in* '7th Asia-Pacific Conference on Wind Engineering, APCWE-VII'.

Fu, S., Biwole, P. H. and Mathis, C. (2015), 'Particle Tracking Velocimetry for indoor airflow field: A review', *Building and Environment* **87**, 34–44.

Fujita, T. T. (1971), Proposed characterization of tornadoes and hurricanes by area and intensity, Technical report, University of Chicago.

Fujita, T. T. (1973), 'Tornadoes around the World', *Weatherwise* **26**(2), 56–83. doi: 10.1080/00431672.1973.9931633.

Gillmeier, S. (2019), An investigation concerning the simulation of tornado-like vortices, Phd thesis, University of Birmingham.

Gillmeier, S., Sterling, M., Baker, C. and Hemida, H. (2017), An analysis of non-stationary processes in tornado-like vortices, *in* 'Physmod 2017 – International Workshop on Physical Modelling of Flow and Dispersion Phenomena Dynamics of Urban and Coastal Atmosphere – LHEEA - École Centrale de Nantes - France'.

Gillmeier, S., Sterling, M. and Hemida, H. (2019), 'Simulating tornado-like flows: the effect of the simulator's geometry', *Meccanica* **54**(15), 2385–2398.

Gillmeier, S., Sterling, M., Hemida, H. and Baker, C. J. (2018), 'A reflection on analytical tornado-like vortex flow field models', *Journal of Wind Engineering and Industrial Aerodynamics* **174**, 10–27.

Gorecki, P. and Selvam, R. P. (2015), 'Rankine combined vortex interaction with a rectangular prism', *International Journal of Computational Fluid Dynamics* **29**(1), 120–132. doi: 10.1080/10618562.2015.1010524.

Haan, F. L., Balaramudu, V. K. and Sarkar, P. P. (2010), 'Tornado-Induced Wind Loads on a Low-Rise Building', *Journal of Structural Engineering* **136**(1), 106–116. doi: 10.1061/(ASCE)ST.1943-541X.0000093.

Haan, F. L., Sarkar, P. P. and Gallus, W. A. (2008), 'Design , construction and performance of a large tornado simulator for wind engineering applications', **30**, 1146–1159.

Hadley, G. (1735), 'VI. Concerning the cause of the general trade-winds', *Philosophical Transactions of the Royal Society of London* **39**(437), 58–62. doi: 10.1098/rstl.1735.0014.

Hangan, H. and Kim, J. D. (2008), 'Swirl ratio effects on tornado vortices in relation to the Fujita scale', **11**.
URL: *http://doi.org/10.12989/WAS.2008.11.4.291 TT - Swirl ratio effects on tornado vortices in relation to the Fujita scale*

Holmes, J. D. (2004), 'Trajectories of spheres in strong winds with application to wind-borne debris', *Journal of Wind Engineering and Industrial Aerodynamics* **92**(1), 9–22.

Holmes, J. D., Baker, C. J. and Tamura, Y. (2006), 'Tachikawa number: A proposal', *Journal of Wind Engineering and Industrial Aerodynamics* **94**(1), 41–47.

Houze, R. A. (2014), Chapter 8 - Cumulonimbus and Severe Storms, *in* R. A. B. T. I. G. Houze, ed., 'Cloud Dynamics', Vol. 104, Academic Press, pp. 187–236.

Hu, H., Yang, Z., Sarkar, P. and Haan, F. (2011), 'Characterization of the wind loads and flow fields around a gable-roof building model in tornado-like winds', *Experiments in Fluids* **51**(3), 835.

Ishihara, T. and Liu, Z. (2014), 'Numerical study on dynamics of a tornado-like vortex with touching down by using the LES turbulent model', **19**.
URL: *http://doi.org/10.12989/WAS.2014.19.1.089 TT - Numerical study on dynamics of a tornado-like vortex with touching down by using the LES turbulence model*

Jones, T. A., McGrath, K. M. and Snow, J. T. (2004), 'Association between NSSL Mesocyclone Detection Algorithm-Detected Vortices and Tornadoes', *Weather and Forecasting* **19**(5), 872–890. doi: 10.1175/1520-0434(2004)0192.0.CO;2.

Kakimpa, B., Hargreaves, D. M. and Owen, J. S. (2012), 'An investigation of plate-type windborne debris flight using coupled CFD–RBD models. Part II: Free and constrained flight', *Journal of Wind Engineering and Industrial Aerodynamics* **111**, 104–116.
URL: *http://www.sciencedirect.com/science/article/pii/S0167610512002292*

Karimpour, A. and Kaye, N. B. (2012*a*), 'On the stochastic nature of compact debris flight', *Journal of Wind Engineering and Industrial Aerodynamics* **100**(1), 77–90.

Karimpour, A. and Kaye, N. B. (2012*b*), 'The critical velocity for aggregate blow-off from a built-up roof', *Journal of Wind Engineering and Industrial Aerodynamics* **107-108**, 83–93.
URL: *http://www.sciencedirect.com/science/article/pii/S0167610512000888*

Karstens, C. D., Samaras, T. M., Lee, B. D., Gallus, W. A. and Finley, C. A. (2010), 'Near-Ground Pressure and Wind Measurements in Tornadoes', *Monthly Weather Review* **138**(7), 2570–2588. doi: 10.1175/2010MWR3201.1.

Kerho, M. F. and Bragg, M. B. (1994), 'Neutrally buoyant bubbles used as flow tracers in air', *Experiments in Fluids* **16**(6), 393–400.

Kim, Y. C. and Matsui, M. (2017), 'Analytical and empirical models of tornado vortices: A comparative study', *Journal of Wind Engineering and Industrial Aerodynamics* **171**, 230–247.

Knox, J. A., Rackley, J. A., Black, A. W., Gensini, V. A., Butler, M., Dunn, C., Gallo, T., Hunter, M. R., Lindsey, L., Phan, M., Scroggs, R. and Brustad, S.

(2013), 'Tornado debris characteristics and trajectories during the 27 April 2011 super outbreak as determined using social media data', *Bulletin of the American Meteorological Society* **94**(9), 1371–1380.

Kolaas, J., Jensen, A. and Mielnik, M. (2013), 'Visualization and measurements of flows in micro silicon Y-channels', *The European Physical Journal E* **36**(2), 19.

Kordi, B. and Kopp, G. A. (2011), 'Effects of initial conditions on the flight of windborne plate debris', *Journal of Wind Engineering and Industrial Aerodynamics* **99**(5), 601–614.

Kosiba, K. A. and Wurman, J. (2013), 'The Three-Dimensional Structure and Evolution of a Tornado Boundary Layer', *Weather and Forecasting* **28**(6), 1552–1561. doi: 10.1175/WAF-D-13-00070.1.

Kuligowski, E. D., Lombardo, F. T., Phan, L. T., Levitan, M. L. and Jorgensen, D. P. (2014), Technical investigation of the May 22, 2011, tornado in Joplin, Missouri., Technical report, NIST NCSTAR.

Lee, A. J. H. (1974), 'A general study of tornado-generated missiles', *Nuclear Engineering and Design* **30**(3), 418–433.

Lee, J. J. and Samaras, T. M. (2004), Pressure measurements at the ground in an F-4 tornado, *in* 'Preprints, 22nd Conf. on Severe Local Storms, Hyannis, MA, Amer. Meteor. Soc.', p. 15.3.

Lee, W.-C. and Wurman, J. (2005), 'Diagnosed Three-Dimensional Axisymmetric Structure of the Mulhall Tornado on 3 May 1999', *Journal of the Atmospheric Sciences* **62**(7), 2373–2393. doi: 10.1175/JAS3489.1.

Leslie, F. W. (1977), 'Surface Roughness Effects on Suction Vortex Formation: A Laboratory Simulation', *Journal of the Atmospheric Sciences* **34**(7), 1022–1027. doi: 10.1175/1520-0469(1977)0342.0.CO;2.

Lewellen, W. S. (1962), 'A solution for three-dimensional vortex flows with strong circulation', *Journal of Fluid Mechanics* **14**(3), 420–432.

Liu, Z. and Ishihara, T. (2016), 'Study of the effects of translation and roughness on tornado-like vortices by large-eddy simulations', *Journal of Wind Engineering and Industrial Aerodynamics* **151**, 1–24.

LiveStormMedia (2019), '4-30-2019 Sulphur, Ok Tornado'. [Last Accessed: 03/05/2019].
URL: *https://www.youtube.com/watch?v=0JII2xXiGZY*

Luthi, B., Tsinober, A. and Kinzelbach, W. (2005), 'Lagrangian measurement of vorticity dynamics in turbulent flow', *Journal of Fluid Mechanics* **528**, 87–118.

Maas, H. G., Gruen, A. and Papantoniou, D. (1993), 'Particle tracking velocimetry in three-dimensional flows', *Experiments in Fluids* **15**(2), 133–146.

Malik, N. A., Dracos, T. and Papantoniou, D. A. (1993), 'Particle tracking velocimetry in three-dimensional flows', *Experiments in Fluids* **15**(4), 279–294.

Markowski, P. M. (2019), 'Tornado Formation'. [Last Accessed: 01/10/2019].
URL: *https://sites.psu.edu/tornadoes/*

Markowski, P. M. and Richardson, Y. P. (2009), 'Tornadogenesis: Our current understanding, forecasting considerations, and questions to guide future research', *Atmospheric Research* **93**(1), 3–10.

Markowski, P. M., Straka, J. M. and Rasmussen, E. N. (2002), 'Direct Surface Thermodynamic Observations within the Rear-Flank Downdrafts of Nontornadic and Tornadic Supercells', *Monthly Weather Review* **130**(7), 1692–1721. doi: 10.1175/1520-0493(2002)1302.0.CO;2.

Maruyama, T. (2011), 'Simulation of flying debris using a numerically generated tornado-like vortex', *Journal of Wind Engineering and Industrial Aerodynamics* **99**(4), 249–256.

McDonald, J. R. (1990), 'Impact resistance of common building materials to tornado missiles', *Journal of Wind Engineering and Industrial Aerodynamics* **36**, 717–724.

McDonald, J. R., Mehta, K. C. and Minor, J. E. (1974), 'Tornado-resistant design of nuclear power-plant structures', *Nucl Safety* **15**(4), 432–439.

Minor, J. E., McDonald, J. R. and Mehta, K. C. (1977), 'The tornado : an engineering-oriented perspective'.

Mishra, A. R., James, D. L. and Letchford, C. W. (2008*a*), 'Physical simulation of a single-celled tornado-like vortex , Part A : Flow field characterization', **96**, 1243–1257.

Mishra, A. R., James, D. L. and Letchford, C. W. (2008*b*), 'Physical simulation of a single-celled tornado-like vortex , Part B : Wind loading on a cubical model', **96**, 1258–1273.

Moncrieff, M. W. and Miller, M. J. (1976), 'The dynamics and simulation of tropical cumulonimbus and squall lines', *Quarterly Journal of the Royal Meteorological Society* **102**(432), 373–394. doi: 10.1002/qj.49710243208.

Mulder, K. J. and Schultz, D. M. (2015), 'Climatology, Storm Morphologies, and Environments of Tornadoes in the British Isles: 1980–2012', *Monthly Weather Review* **143**(6), 2224–2240. doi: 10.1175/MWR-D-14-00299.1.

Nasir, Z. (2017), Numerical modeling of tornado-like vortex and its interaction with bluff- bodies, Phd thesis, The University of Western Ontario.

NI (1986), 'What is LabVIEW?'. [Last Accessed: 24/11/2019].
URL: *https://www.ni.com/en-gb/shop/labview/labview-details.html*

Nishino, K., Kasagi, N. and Hirata, M. (1989), 'Three-Dimensional Particle Tracking Velocimetry Based on Automated Digital Image Processing', *Journal of Fluids Engineering* **111**(4), 384–391.

NOAA (1995), 'U.S. Tornado Climatology'. [Last Accessed: 12/10/2019].
URL: *https://www.ncdc.noaa.gov/climate-information/extreme-events/us-tornado-climatology*

NOAA (2011), 'An essential guide to tornadoes: Stay alert to stay alive'. [Last Accessed: 14/04/2020].
URL: *https://www.noaa.gov/stories/tornadoes-101*

NOAA (2016), 'America's deadliest year for tornadoes'. [Last Accessed: 22/06/2020].

URL: *https://www.noaa.gov/photo-story-americas-deadliest-year-for-tornadoes-2011*

NOAA (2019), 'TORUS: Targeted Observations by Radars and UAS of Supercells'. [Last Accessed: 26/10/2019].
URL: *https://www.nssl.noaa.gov/projects/torus/*

Noda, M., Masai, K., Ninomiya, M. and Nagao, F. (2013), 'Behavior of Flying Debris in Tornado-like Flow', *Journal of Wind Engineering* **38**(3), 63–73.

OpenPTV (2012), 'What is Open source Particle Tracking Velocimetry'. [Last Accessed: 16/01/2019].
URL: *https://www.openptv.net/*

Papantoniou, D. and Dracos, T. (1990), Lagrangian statistics in open channel flow by 3-D particle tracking velocimetry, *in* 'International Symposium on Engineering Turbulence Methods and Measurements', p. Volume 24.

Pelc, B. (2014), Development and performance of robust particle image velocimetry algorithms and investigation of a model tornado-like vortex: Kinematics and proper orthogonal decomposition, Phd thesis, University of Leeds.

Pratt, V. (1987), 'Direct Least-Squares Fitting of Algebraic Surfaces', *SIGGRAPH Comput. Graph.* **21**(4), 145–152.
URL: *https://doi.org/10.1145/37402.37420*

Racca, R. G. and Dewey, J. M. (1988), 'A method for automatic particle tracking in a three-dimensional flow field', *Experiments in Fluids* **6**(1), 25–32.

Rankine, W. J. M. (1882), *A Manual of Applied Physics*, 10th edn, Charles Griff and Co.

Refan, M. and Hangan, H. (2016), 'Characterization of tornado-like flow fields in a new model scale wind testing chamber', *Journal of Wind Engineering and Industrial Aerodynamics* **151**, 107–121.

Refan, M. and Hangan, H. (2018), 'Near surface experimental exploration of tornado vortices', *Journal of Wind Engineering & Industrial Aerodynamics* **175**(June 2017), 120–135.

Refan, M., Hangan, H. and Wurman, J. (2014), 'Reproducing tornadoes in laboratory using proper scaling', *Journal of Wind Engineering and Industrial Aerodynamics* **135**, 136–148.

Rhee, D. M. and Lombardo, F. T. (2017), Improved characterization of damage patterns from idealized tornado models, *in* '13th Americas Conference on Wind Engineering, ACWE 2017'. 2017 13th Americas Conference on Wind Engineering, ACWE 2017 ; Conference date: 21-05-2017 Through 24-05-2017.

Richards, P. J. (2012), 'Dispersion of windborne debris', *Journal of Wind Engineering and Industrial Aerodynamics* **104-106**, 594–602.

Richards, P. J., Williams, N., Laing, B., McCarty, M. and Pond, M. (2008), 'Numerical calculation of the three-dimensional motion of wind-borne debris', *Journal of Wind Engineering and Industrial Aerodynamics* **96**(10), 2188–2202.

Rose, S. F., Hobbs, P. V., Locatelli, J. D. and Stoelinga, M. T. (2004), 'A 10-Yr Climatology Relating the Locations of Reported Tornadoes to the Quadrants of Upper-Level Jet Streaks', *Weather and Forecasting* **19**(2), 301–309. doi: 10.1175/1520-0434(2004)0192.0.CO;2.

Rott, N. (1958), 'On the viscous core of a line vortex', *Zeitschrift für angewandte Mathematik und Physik 9* pp. 543–553.

Rotunno, R. (2013), 'The Fluid Dynamics of Tornadoes', *Annual Review of Fluid Mechanics* **45**(1), 59–84. doi: 10.1146/annurev-fluid-011212-140639.

Runstedtler, A. (2013), 'Inviscid flow arrangements in fluid dynamics'.

Ryzhkov, A. V., Schuur, T. J., Burgess, D. W. and Zrnic, D. S. (2005), 'Polarimetric Tornado Detection', *Journal of Applied Meteorology* **44**(5), 557–570. doi: 10.1175/JAM2235.1.

Sadegh, S. (2016), '2D random walk confined in a circular domain with reflective boundaries'. MATLAB Central File Exchange. [Last Accessed: 04/03/2020].
URL: *https://uk.mathworks.com/matlabcentral/fileexchange/60673-2d-random-walk-confined-in-a-circular-domain-with-reflective-boundaries*

Sarkar PP, Haan FL, Gallus WA, Kuai L, W. J. (2005), Velocity measurements in a laboratory tornado simulator and their comparison with numerical and full-scale data, *in* 'Proceedings of the 37th US-Japan panel on wind and seismic effects joint meeting, Tsukuba, Japan, May 16–18'.

Sassa, K., Miyagi, H. and Yamauchi, T. (2014), 'Measurement of Tsukuba tornado with particle image velocimetry', *27th Conf. on Severe Local Storms* (c), P177.

Sassa, K., Takemura, S. and Yamashita, K. (2009), 'The behavior of windborne debris accompanied by a traveling tornado', *7th Asia-Pacific Conference on Wind Engineering, APCWE-VII* .

Schanz, D., Schröder, A., Gesemann, S., Michaelis, D. and Wieneke, B. (2013), Shake The Box: A highly efficient and accurate Tomographic Particle Tracking Velocimetry (TOMO-PTV) method using prediction of particle positions, *in* 'PIV13; 10th International Symposium on Particle Image Velocimetry'.

Schlichting, H. and Gersten, K. (2000), *Boundary-Layer Theory*, Springer Berlin Heidelberg.

Schueth, A. and Weiss, C. C. (2018), Comparing observations and simulations of the streamwise vorticity current in a tornadic supercell storm, *in* 'Preprints, 29th Conference of Severe Local Storms, Amer. Meteor. Soc., Stowe, VT'.

Selvam, R. P. and Millett, P. C. (2003), 'Computer modeling of tornado forces on buildings', **6**.

Shnapp, R. and Liberzon, A. (2015), 'A comparative study and a mechanistic picture of resuspension of large particles from rough and smooth surfaces in vortex-like fluid flows', *Chemical Engineering Science* **131**, 129–137.

Simiu, E. and Cordes, M. (1976), Tornado-borne missile speeds Final report, Technical report, United States.

Snow, J. T. (1982), 'A review of recent advances in tornado vortex dynamics', *Reviews of Geophysics* **20**(4), 953–964. doi: 10.1029/RG020i004p00953.

Snow, J. T. and Lund, D. E. (1997), 'Considerations in Exploring Laboratory Tornadolike Vortices with a Laser Doppler Velocimeter', *Journal of Atmospheric and Oceanic Technology* **14**(3), 412–426. doi: 10.1175/1520-0426(1997)0142.0.CO;2.

Snow, J. T., Wyatt, A. L., McCarthy, A. K. and Bishop, E. K. (1995), 'Fallout of Debris from Tornadic Thunderstorms: A Historical Perspective and Two Examples from VORTEX', *Bulletin of the American Meteorological Society* **76**(10), 1777–1790. doi: 10.1175/1520-0477(1995)0762.0.CO;2.

Snyder, W. H. and Lumley, J. L. (1971), 'Some measurements of particle velocity autocorrelation functions in a turbulent flow', *Journal of Fluid Mechanics* **48**(1), 41–71.

Song, F. and Ou, J. (2010), 'Windborne debris damage prediction analysis', *Frontiers of Architecture and Civil Engineering in China* **4**(3), 326–330.

Sullivan, R. D. (1959), 'A Two-Cell Vortex Solution of the Navier-Stokes Equations', *Journal of the Aerospace Sciences* **26**(11), 767–768. doi: 10.2514/8.8303.

Tachikawa, M. (1983), 'Trajectories of flat plates in uniform flow with application to wind-generated missiles', *Journal of Wind Engineering and Industrial Aerodynamics* **14**(1), 443–453.

Tachikawa, M. (1988), 'A method for estimating the distribution range of trajectories of wind-borne missiles', *Journal of Wind Engineering and Industrial Aerodynamics* **29**(1), 175–184.

Tang, Z., Feng, C., Wu, L., Zuo, D. and James, D. L. (2018), 'Characteristics

of Tornado-Like Vortices Simulated in a Large-Scale Ward-Type Simulator', *Boundary-Layer Meteorology* **166**(2), 327–350.

TFI (2011), Turbulent Flow Instrumentation - Cobra Probe - Getting started guide. Technical report, Turbulent Flow Instrumentation, Technical report.

TORRO (1975), 'The International Tornado Intensity Scale'. [Last Accessed: 22/06/2020].
URL: *http://www.torro.org.uk/tscale.php*

Trapp, R. J. (2000), 'A Clarification of Vortex Breakdown and Tornadogenesis', *Monthly Weather Review* **128**(3), 888–895.
URL: *https://doi.org/10.1175/1520-0493(2000)128%3C0888:ACOVBA%3E2.0.CO http://0.0.0.2*

Trapp, R. J. and Davies-Jones, R. P. (1997), 'Tornadogenesis with and without a Dynamic Pipe Effect', *Journal of the Atmospheric Sciences* **54**(1), 113–133. doi: 10.1175/1520-0469(1997)0542.0.CO;2.

Trapp, R. J., Stumpf, G. J. and Manross, K. L. (2005), 'A Reassessment of the Percentage of Tornadic Mesocyclones', *Weather and Forecasting* **20**(4), 680–687. doi: 10.1175/WAF864.1.

Twisdale, L. A., Dunn, W. L. and Davis, T. L. (1979), 'Tornado missile transport analysis', *Nuclear Engineering and Design* **51**(2), 295–308.

Umbach, D. and Jones, K. N. (2003), 'A few methods for fitting circles to data', *IEEE Transactions on Instrumentation and Measurement* **52**(6), 1881–1885.

Vickery, J. P., Skerlj, F. P., Lin, J., Twisdale, A. L., Young, A. M. and Lavelle, M. F. (2006), 'HAZUS-MH Hurricane Model Methodology. II: Damage and Loss Estimation', *Natural Hazards Review* **7**(2), 94–103. doi: 10.1061/(ASCE)1527-6988(2006)7:2(94).

Wang, H., Li, X., Shao, X., Wang, B. and Lin, Y. (2017), 'A colour-sequence enhanced particle streak velocimetry method for air flow measurement in a ventilated space', *Building and Environment* **112**, 77–87.

Ward (1972), 'The exploration of certains features of tornado dynamics using a laboratory model'.

Wesolek, E. and Mahieu, P. (2011), 'The F4 tornado of August 3, 2008, in Northern France: Case study of a tornadic storm in a low CAPE environment', *Atmospheric Research* **100**(4), 649–656.

Willneff, J. (2003), A spatio-temporal matching algorithm for 3D particle tracking velocimetry, Phd thesis, Institute of Technology, Germany.

Wills, J. A. B., Lee, B. E. and Wyatt, T. A. (2002), 'A model of wind-borne debris damage', *Journal of Wind Engineering and Industrial Aerodynamics* **90**(4), 555–565.

Winn, W. P., Hunyady, S. J. and Aulich, G. D. (1999), 'Pressure at the ground in a large tornado', *Journal of Geophysical Research Atmospheres* **104**(D18), 22067–22082. doi: 10.1029/1999JD900387.

Wood, V. T. and Brown, R. A. (2011), 'Simulated Tornadic Vortex Signatures of Tornado-Like Vortices Having One- and Two-Celled Structures', *Journal of*

Applied Meteorology and Climatology **50**(11), 2338–2342. doi: 10.1175/JAMC-D-11-0118.1.

Wood, V. T. and White, L. W. (2011), 'A New Parametric Model of Vortex Tangential-Wind Profiles: Development, Testing, and Verification', *Journal of the Atmospheric Sciences* **68**(5), 990–1006. doi: 10.1175/2011JAS3588.1.

Wurman, J. and Alexander, C. R. (2005), 'The 30 May 1998 Spencer, South Dakota, Storm. Part II: Comparison of Observed Damage and Radar-Derived Winds in the Tornadoes', *Monthly Weather Review* **133**(1), 97–119. doi: 10.1175/MWR-2856.1.

Wurman, J., Alexander, C., Robinson, P. and Richardson, Y. (2007), 'Low-Level Winds in Tornadoes and Potential Catastrophic Tornado Impacts in Urban Areas', *Bulletin of the American Meteorological Society* **88**(1), 31–46. doi: 10.1175/BAMS-88-1-31.

Wurman, J., Kosiba, K. and Robinson, P. (2013), 'In Situ, Doppler Radar, and Video Observations of the Interior Structure of a Tornado and the Wind–Damage Relationship', *Bulletin of the American Meteorological Society* **94**(6), 835–846. doi: 10.1175/BAMS-D-12-00114.1.

Wurman, J. M. (1999), Preliminary results from the Radar Observations of Tornadoes and Thunderstorms Experiment (ROTATE-98/99), *in* 'Preprints, 29th Conf. on Radar Meteorology, Montreal, QC, Canada, Amer. Meteor. Soc.', pp. 613–616.

Wurman, J. M. (2011), The DOW mobile multiple-Doppler network, *in* '30th Conf. on Radar Meteorology, Amer. Meteor. Soc.', pp. 95–97.

Wurman, J., Straka, J., Rasmussen, E., Randall, M. and Zahrai, A. (1997), 'Design and Deployment of a Portable, Pencil-Beam, Pulsed, 3-cm Doppler Radar', *Journal of Atmospheric and Oceanic Technology* **14**(6), 1502–1512. doi: 10.1175/1520-0426(1997)0142.0.CO;2.

Ying, S. J. and Chang, C. C. (1970), 'Exploratory Model Study of Tornado-Like Vortex Dynamics', *Journal of the Atmospheric Sciences* **27**(1), 3–14. doi: 10.1175/1520-0469(1970)0272.0.CO;2.

Zhang, W. and Sarkar, P. P. (2012), 'Near-ground tornado-like vortex structure resolved by particle image velocimetry (PIV)', *Experiments in Fluids* **52**(2), 479–493.

Ziehl-Abegg (2010), 'Technical Data - Axial Fans Series FC'. [Last Accessed: 19/11/2019].

Zrnic, D. S., Doviak, R. J., Burgess, D. W. and Brown, R. A. (1977), 'Probing tornadoes with a pulse doppler radar', *Quarterly Journal of the Royal Meteorological Society* **103**(438), 707–720. doi: 10.1002/qj.49710343813.